



Guan, Debao (2021) *Mathematical modelling of cardiac function: constitutive law, fibre dispersion, growth and remodelling*. PhD thesis.

<https://theses.gla.ac.uk/82424/>

Copyright and moral rights for this work are retained by the author

A copy can be downloaded for personal non-commercial research or study, without prior permission or charge

This work cannot be reproduced or quoted extensively from without first obtaining permission in writing from the author

The content must not be changed in any way or sold commercially in any format or medium without the formal permission of the author

When referring to this work, full bibliographic details including the author, title, awarding institution and date of the thesis must be given

Enlighten: Theses

<https://theses.gla.ac.uk/>
research-enlighten@glasgow.ac.uk

**Mathematical modelling of cardiac function: constitutive law,
fibre dispersion, growth and remodelling**

Debao Guan

Submitted in fulfilment of the requirements for the
Degree of Doctor of Philosophy

School of Mathematics & Statistics
College of Science and Engineering
University of Glasgow



University
of Glasgow

August 2021

Abstract

The heart is an immensely complex living organ. Myocardium has continually been undergoing adaptive or maladaptive response to surrounding environments, in which the significant importance of growth and remodelling (G&R) has been valued. This PhD project intends to study mechanics modelling of myocardium towards predictive stress/strain-driven growth. Constitutive laws and fibre structures in myocardium work together to determine the mechanical clues which trigger the growth mechanically. Therefore, this project includes two parts: (1) constitutive characterization of myocardium, and (2) myocardial G&R.

Constitutive laws and myofibre architectures hold the key to accurately model the biomechanical behaviours of the heart. In the first part of this thesis, we firstly perform an analysis using combinations of uniaxial tension, biaxial tension and simple shear from three different sets of myocardial experimental tissue studies to investigate the descriptive and predictive capabilities of a general invariant-based model that is developed by Holzapfel and Ogden, denoted the HO model. We aim to reduce the constitutive law using the Akaike information criterion to maintain its mechanical integrity whilst achieve minimal computational cost. Our study shows that single-mode tests are insufficient to determine the myocardium responses. It is also essential to consider the transmural fibre rotation within the myocardial samples. We conclude that a competent myocardial material model can be obtained from the general HO model using Akaike information criterion analysis and a suitable combination of tissue tests.

Secondly, we develop a neonatal porcine bi-ventricle model with three different myofibre architectures for the left side of the heart. The most realistic one is derived from ex vivo diffusion tensor magnetic resonance image, and the other two simplifications are based on the rule-based methods. We show that the most realistic myofibre architecture model can achieve better cardiac pump functions compared to those of the rule-based models under the same pre/after loads. Our results also reveal that when the cross-fibre contraction is included, the active stress seems to play a dual role: the sheet-normal component enhances the ventricular contraction while the sheet component does the opposite. This study highlights the importance of including myofibre dispersion in cardiac modelling if rule-based methods are used, especially in personalized model. To further describe the detailed fibre distribution, discrete fibre dispersion method is employed to compute passive response because of its advantages in excluding compressed fibres. An additive active stress method that includes cross-fibre active stress is proposed according to

the generalised structure tensor method. We find that end-systolic volumes of simulated heart models are much more sensitive to dispersion parameter than end-diastolic volumes.

G&R is the focus in the second part of this thesis. An updated reference approach is employed to track the evolution of the reference configuration during G&R, in which the nodal positions and the fibre structure are updated at the beginning of each new growth cycle. Moreover, the homogenised constrained mixture theory is used to describe the G&R process of each constituent within myocardium, which are the ground matrix, collagen network and myofibres. Our models can reproduce the eccentric growth driven by fibre stretch at the diastole, concentric growth driven by fibre stress at the systole, and heterogeneous growth after acute myocardium infarction. Ventricular wall G&R mainly occurs in endocardium, in which the myocyte is the primary responder for the G&R process. G&R laws of collagen fibre have significant impacts on G&R of heart. For example, purely remodeled collagen network without new deposition causes increasingly softer heart wall, leading to excessive heart dilation. Finally, the effects of fibre dispersion on G&R is investigated by including fibre dispersion model in the G&R of infarction model. Highly dispersed fibre structure in the infarcted zone significantly reduces the pump function.

This thesis has been focusing on mathematical modelling of biomechanical behaviours of myocardium, firstly on the nonlinear cardiac mechanics including constitutive laws and fibre structures, and then on the G&R process of heart under different pathological conditions. These studies support to choose suitable constitutive laws and fibre architectures in G&R model and illustrate the underlying mechanism of mechanical triggers in G&R. It presents the potential for understanding the mechanics of heart failure and reveal hidden roles of different constituents in myocardium.

Contents

Abstract	i
Acknowledgements	xxii
Declaration	xxiii
Publication list	xxiv
Abbreviations	xxv
1 Introduction	1
2 Literature Review	4
2.1 Structure and function of heart	4
2.1.1 Structure at cellular level	6
2.1.2 Tissue level structure and function	7
2.2 Constitutive models of passive myocardium	8
2.2.1 Passive tension experiments of myocardium	9
2.2.2 Phenomenological constitutive models	12
2.2.3 Micro-structurally informed models	16
2.3 Active contraction models of myocardium	19
2.3.1 Active stress approach	20
2.3.2 Active strain approach	20
2.3.3 Hill's three-element approach	21
2.4 Fibre structure in modelling myocardium	22
2.4.1 Construction of fibre structure	22
2.4.2 Consideration of fibre dispersion	24
2.4.3 Collagen fibre recruitment under fibre dispersion	26
2.4.4 Myofibre active stress under fibre dispersion	29
2.5 Growth and remodelling	29
2.5.1 The volumetric growth theory	31
2.5.2 Constrained mixture theory	33

2.6	Myocardium infarction	36
2.6.1	Experimental measurements of MI	37
2.6.2	Mathematical modelling of MI	38
I	Constitutive laws and fibre structures of myocardium	40
3	Constitutive law: reduction of the general Holzapfel–Ogden model based on ex-vivo experiments	41
3.1	Introduction	41
3.2	Method	43
3.2.1	The general HO model	43
3.2.2	Selected myocardial experiments	43
3.2.3	Effective fibre contribution	47
3.2.4	Parameter estimation	49
3.2.5	Reduced HO models	50
3.2.6	Optimal combination of experiments through predictive analysis	52
3.3	Results	53
3.3.1	The general HO strain energy function	53
3.3.2	Reduced strain energy functions based on AIC analysis	55
3.3.3	Optimal combination of experimental tests	60
3.4	Discussion	61
3.5	Conclusion	67
4	Myofibre architecture: mapping among different geometries and its dispersion on contraction	69
4.1	Introduction	69
4.2	Method	71
4.2.1	Geometry and Fibre Construction	71
4.2.2	Constitutive Model	74
4.2.3	Boundary conditions and implementations	78
4.3	Results	81
4.3.1	No cross-fibre active tension	82
4.3.2	RBM ^{uni} with cross-fibre active tension	83
4.3.3	Parameter sensitivity and inference study of myocardial property	86
4.4	Discussion	88
4.5	Conclusion	92

5	Fibre dispersion: its effects on cardiac mechanics from diastole to systole	93
5.1	Introduction	93
5.2	Method	95
5.2.1	DT-MRI acquisition protocol	95
5.2.2	Passive stress	95
5.2.3	Active stress	97
5.2.4	Estimation in the eigenvector space: the AI approach	98
5.3	Results	103
5.3.1	Uniaxial test on multi-element strip	104
5.3.2	Comparison between Algorithms	107
5.3.3	The dynamic rabbit bi-ventricle model	109
5.3.4	The human LV model	113
5.4	Discussion	116
5.5	Conclusion	121
II	Growth and remodelling in left ventricle	122
6	Growth and remodelling: a framework based on the constrained mixture theory	123
6.1	Introduction	123
6.2	Methodology of updated Lagrangian constrained mixture G&R framework . . .	125
6.2.1	Homogenised constrained mixture model	125
6.2.2	Updated reference configuration framework	126
6.2.3	Strain energy functions	130
6.2.4	Application to human in vivo heart model	131
6.3	Verification of the homogenised constrained mixture model	132
6.3.1	Homogenised constrained mixture approach	132
6.3.2	Volumetric growth approach	134
6.3.3	Verification results	135
6.4	Comparison of maintaining and relieving residual stress during G&R	137
6.4.1	With residual stress before and after growth	137
6.4.2	Without residual stress before and after growth	141
6.4.3	Comparison results	142
6.4.4	Discussion	145
6.5	Effects of different G&R properties of constituents on eccentric and concentric growths	146
6.5.1	Methods in eccentric and concentric G&R	146
6.5.2	Eccentric growth results	147
6.5.3	Concentric growth results	152

6.5.4	Discussion	155
6.6	Conclusion	159
7	Growth and remodelling in infarcted left ventricle	160
7.1	Introduction	160
7.2	G&R of MI model without fibre dispersion	162
7.2.1	Definition of the MI region	162
7.2.2	Growth and remodelling patterns in MI model	162
7.2.3	Results	164
7.2.4	Discussion	167
7.3	G&R of MI model with fibre dispersion	168
7.3.1	Fibre dispersion structure after MI	168
7.3.2	Numerical implementation	169
7.3.3	Results	171
7.3.4	Discussion	175
7.4	Conclusion	177
8	Summary and future work	178
8.1	Summary	178
8.2	Future work	180
8.2.1	Constitutive modelling of myocardium from ex vivo to in vivo	180
8.2.2	A biophysically detailed active tension model based on Hill model	181
8.2.3	Patient-specific G&R model based on experimental data	182

List of Tables

2.1	Summary of passive experiments on myocardium, including uniaxial tension, biaxial tension, simple shear and confined compression. Size of specimen in $a \times b \times c$ form is length \times width \times thickness, and $a \times b$ form is length \times diameter. ($a : b$) in biaxial tension denotes loading ratios along two vertical loading orientations. (ij) in simple shear test refers to shear in the j direction within the ij plane.	11
2.2	Summary of phenomenological SEFs describing passive mechanical responses of myocardium. Please note, strain components E_{ij} with $i, j \in \{f, s, n\}$ are with respect to the $\mathbf{f}_0 - \mathbf{s}_0 - \mathbf{n}_0$ fibre system, whilst E_{11} and E_{22} refer to the two orthogonal loading orientations in the biaxial tension tests.	13
2.3	Summary of structurally informed models for describing passive mechanical responses of myocardium	18
2.4	Summary of active contraction models. The active stress expressions listed in active stress model, the constructions of active strain tensor are expressed in active strain model, and the active SEF is showed in Hill's three-element model.	22
2.5	Summary of published methods that consider collagen fibre recruitment under fibre dispersion during passive deformations.	28
3.1	The estimated parameters for the reduced HO models fitting to corresponding experimental studies.	59
3.2	Relative and absolute errors for the reduced HO models when fitting to corresponding experimental studies.	59
3.3	The average value <i>avg</i> and standard deviation <i>std</i> of optimized parameters from 100 random generated initial starts in interval (0.001, 50).	68
4.1	Average myofibre rotation angles ($^\circ$) at endocardium and epicardium according to the AHA17 definition, and the set of angles for the RV.	74
4.2	Parameter values for the time varying elastance active tension constitutive model.	76

4.3	Parameter values for the lumped circulatory model as shown in Fig. 4.5. C_V is the viscous resistance coefficient, and k is the stiffness of the grounded spring. Corresponding values for the equivalent Windkessel model is also listed for reference including the resistance (R) and the compliance (C). Note that the compliances of the RA and LA are not constant but varied to ensure constant EDP, which are not listed here.	81
4.4	Parameter values for passive properties of the LV and RV myocardium.	81
4.5	Summary of fibre rotation angles from published experimental modelling studies. RVFW: right ventricle free wall.	91
5.1	Parameters of rabbit myocardium by fitting to the experimental data in [1] and parameters for human LV model adopted from [2]. Contractility T_a was manually determined by achieving a physiological EF within 50% ~ 75%.	106
5.2	Fibre rotation angles at different regions of the rabbit heart adopt from [3].	110
5.3	Parameter values for the lumped circulatory model as shown in Fig. 5.8 (d) and Fig. 5.12 (c). C_V is the viscous resistance coefficient, and k is the stiffness of the grounded spring.	110
6.1	Parameters in simulations of G&R	133
7.1	Summary of main indices associated with G&R and cardiac pumping function in MI models without and with fibre dispersions at the fifth growth cycle.	172

List of Figures

1.1	Schematic for the organization of the project	2
2.1	(a) Simple anatomy diagram of the human heart (https://en.wikipedia.org/wiki/Heart). (b) Pressure-Volume loop of the LV presenting the different phases in a complete heart cycle.	5
2.2	Structural hierarchy. Human heart graph from Sommer et al. [4], myofibre network graph from Ahmad et al. [5], and collagen fibre network graph from Avazmohammadi et al. [6]. All figures are reprinted with permission.	6
2.3	Sketch of a LV with inside fibres (red lines) and a cubic sample cut from the ventricular wall (left). The layered organization of myocytes and the collagen fibres between the sheets referred to a right-handed orthonormal coordinate system with fibre axis \mathbf{f}_0 , sheet axis \mathbf{s}_0 and sheet-normal axis \mathbf{n}_0 in the reference configuration (middle). A cube model with orthogonal \mathbf{f}_0 , \mathbf{s}_0 and \mathbf{n}_0 represents a material point of myocardium when using constitutive laws (right).	9
2.4	(a) Sketches of uniaxial tension tests along mean fibre direction (MFD) and cross-fibre direction (CFD), respectively. f_1 is the loading force along the MFD, and f_2 is along the CFD. L is the initial length of specimen, and λ_1 and λ_2 are stretch ratios. (b) A sketch of a sample with fibres (red dash lines), which is stretched along the two orthogonal directions (MFD and CFD) in fibre-normal plane during a biaxial test. (c) A sketch of all six possible shear modes, \mathbf{f}_0 , \mathbf{s}_0 and \mathbf{n}_0 denote the fibre, sheet and normal directions in the reference configuration, respectively. (ij) refers to shear in the j direction within the ij plane, where $i \neq j \in \{\mathbf{f}, \mathbf{s}, \mathbf{n}\}$	10

- 2.5 Sketch of active contraction models with different arrangements of passive elements (spring) and active contractile elements (red box). (a) Active stress model consists of a passive spring element in parallel with a contractile element. (b) Active strain model is composed of a contractile element in series with a passive spring element. (c) Hill's three-element model also has two parallel branches, in which one branch only has a passive spring element and another branch has a contractile element in series with a passive element. \mathbf{F} denotes total deformation gradient tensor and is decomposed into elastic tensor (\mathbf{F}_e) and active strain tensor (\mathbf{F}_a). σ_t is total Cauchy stress, σ_a is active stress, and σ_p is passive stress. 19
- 2.6 (a) Bi-ventricular canine model is reconstructed directly from DT-MRI and inside fibre structure (red lines) is mapped from same DT-MRI data. Then, it warps into porcine heart by atlas-based methods, together with inside fibre structure. (b) Definition of linear rotation from epicardium to endocardium and its application in single LV model with rotation angles from endocardium (60°) to epicardium (-60°). Single LV graph is cited from Wang et al. [7] with the permission to be reprinted. 23
- 2.7 Fibre dispersion in measurement and its definition in mathematical model. (a) Measured intensity of fiber orientations through-the-thickness from Sommer et al. [4], showing the existence of fibre dispersion around mean fibre direction. The measurable intensity can be expressed by PDF $\rho(\Theta)$ (b), and spatial disperse fibre in mathematical model can be denoted by two polar angles Θ and Φ (c), and its distribution is controlled by the PDF. (d) Four representative fibre dispersion distributions around the mean fibre direction (red arrow), from the left to the right is respective isotropic dispersion, in-plane isotropic dispersion, transversely isotropic dispersion, and general dispersion. 25
- 2.8 Projected stacks of multiphoton images as viewed from abluminal side (images are cited from Cheng et al. [8] with the permission to be reprinted). Top graphs showed collagen fibre deformation from the toe, transition and high stress regimes with increasing strain, and the bottom graph denoted corresponding progressive mechanical loading curves through different segments. 27
- 2.9 Schematic description of G&R of heart. From the cross section view as cut from the black dash line on heart, normal heart respectively proceeds concentric growth associated with wall thickening in response to pressure overload and eccentric growth associated with ventricular dilation in response to volume overload. 30

- 2.10 Schematic description of the volumetric growth theory, in which total deformation gradient tensor \mathbf{F} is decomposed into \mathbf{F}_g and \mathbf{F}_e . Firstly, LV model grows into new incompatible and stress-free intermediate configuration \mathcal{B}_1 by growth tensor \mathbf{F}_g , in which myocardium grows along myocyte (myofibre) θ_f and cross myocyte θ_s directions. Then, all tissues emerged into new compatible LV model in \mathcal{B}_2 by elastic deformation tensor \mathbf{F}_e 31
- 2.11 Schematic description of homogenised constrained mixture growth theory. The configuration before growth $\kappa(0)$ is assumed to be stress-free, $\kappa(s)$ is current configuration after G&R, and $\kappa(\tau)$ is a intermediate configuration with time $\tau \in (0, s)$. Under total deformation gradient tensor $\mathbf{F}(s)$, growth and part remodelling occurs from $\kappa(0)$ to $\kappa(\tau)$ via $\mathbf{F}(\tau)$ and the other part remodelling and external loading occurs from $\kappa(\tau)$ to $\kappa(s)$ via $\mathbf{F}_\tau(s)$. A grown and remodelled constituent i in $\kappa(\tau)$ is treated as the deposition in $\kappa_n^i(\tau)$ via a pre-strain tensor $\mathbf{F}_{\text{pre}}^i(\tau)$ from fictitious incompatible stress-free intermediate configuration $\kappa'(\tau)$ to $\kappa(\tau)$. Then all deposited constituents perform remodelling and loading deformations. $\mathbf{F}_{\text{gr}}^i(0)$ is the fictitious inelastic G&R tensor for each constituent from $\kappa(0)$ to $\kappa'(\tau)$, and $\mathbf{F}_e^{i(\tau)}(s)$ represents its elastic deformation tensor from $\kappa'(\tau)$ to $\kappa(s)$ 35
- 2.12 A myocardial infarction sketch from https://en.wikipedia.org/wiki/Myocardial_infarction 36
- 3.1 (a) A sketch of all six possible shear modes, \mathbf{f}_0 , \mathbf{s}_0 and \mathbf{n}_0 denote the fibre, sheet and normal direction, respectively. (ij) refers to shear in the j direction within the ij plane, where $i \neq j \in \{f, s, n\}$. (b) A sketch of the sample with fibres (red dash lines), which is stretched along the two orthogonal directions (MFD and CFD) in fibre-normal plane during a biaxial test. (c) Sketches of uniaxial tension tests along the MFD and CFD, respectively. f_1 is the loading force along the MFD, and f_2 is along the CFD. L is the initial length of specimen, and λ_1 and λ_2 are stretch ratios. (d) The recorded image in a biaxial tensile specimen in [9]. The four white markers in the centre of the experimental sample in (d) are also shown in (e), in which the solid rectangle represents the initial shape, and the deformed shape is shown using dashed lines. (f) Transmural variation of \mathbf{f}_0 (red dash lines) and \mathbf{n}_0 (green dot lines) along the thickness of myocardium. $\mathbf{e}_1, \mathbf{e}_2, \mathbf{e}_3$ in Cartesian coordinate system represent the MFD, CFD and sheet (transmural) directions, respectively. A_i is the cross-sectional area perpendicular to \mathbf{e}_i axis. 44

3.2	Schematic illustration of normal and shear forces for the marked region in a bi-axial test sample. The stress and strain fields in the central region (the red colour) are general considered homogeneous, while the tissue outside of the region-of-interest also stretch the central region, thus the measured force along \mathbf{e}_1 is $f_{11} + f_{12}$ and the measured force along \mathbf{e}_2 is $f_{21} + f_{22}$	46
3.3	Schematic illustration of the effective area (blue) when the fibre direction is θ under uniaxial loading in the MFD test. The collagen fibres (red dot line) within the region enclosed by the two blue dashed lines are defined as effective fibres that are stretched both sides. The effective fibre ratio is defined by rectangle area dividing blue effective area.	48
3.4	(a) depicts the 3D FE bi-ventricle mesh geometry with boundary condition that applies pressure in LV inner surface (red surface). Pressure linearly increases from 0 to 4 mmHg in a period of 0.5s. (b) describes the myofibre distribution in the ventricle wall, which rotates from epcardium to endocardium (60° to -60°).	52
3.5	Comparison of the fitting results with and without considering fiber effective ratio (α). (a) fitting the general HO model to Dokos's data, (b)-(d) describe the differences in uniaxial, biaxial and simple shear tests in Ahamd's data.	54
3.6	Comparison of the First P-K stress, including shear (red) and not including shear (blue) using same SEF. (a) is for Sommer et al. biaxial test and a minimum shear angle of 6° is introduced. Below 6° there is no good fit, above it is not supported by Sommer et al. experiments. (b) is for Ahmad et al. biaxial test, corresponding to Fig. 3.8 (e)	55
3.7	Comparison between descriptive ability of the general HO and the HO2009 models for the three experimental studies. (a): Dokos's simple shear tests; (b) and (c): Sommer's biaxial tension and simple shear tests; (d-f): Ahmad's uniaxial, biaxial tension and simple shear tests.	56
3.8	Descriptive capability of reduced HO models. (a) Change of η when dropping the terms associated with the invariants for the different three experiments. The fitting results for the HO-D model (b), and (c-d) the HO-S model, and (e-g) the HO-A model.	58
3.9	The differences of FE bi-ventricle model using the HO2009, HO-A and general HO models for Ahmad et al. data. (a) the PV curve in diastolic filling, (b) the displacement differences between the general HO and HO2009 models, and (c) the displacement differences between the general HO and HO-A models.	60
3.10	δ values that are computed according to Algorithm 1, where the cases whose average (<i>avg</i>) $\delta \geq 0.8$ are marked in red. (a) In Dokos et al. experiments, case 25 ((fs)+(fn)+(ns)) is the optimal case which has few tests while meeting the criterion, (b) shows the corresponding fitting curves using case 25.	61

3.11	In Sommer et al. experiments, Case 20 ((1:1)+(nf)) is the optimal case in (a), the corresponding fitting curves are shown in (b) and (c).	62
3.12	In Ahmad et al. experiments, case ALL is the only one which satisfies the criterion. The other cases are corresponding to certain combinations to be discussed in the text.	62
3.13	The rest four loading protocols ((1:0.75), (0.75:1), (1:0.5) and (0.5:1)) for Sommer et al. biaxial tests. (a) compares the First P-K stress including shear (solid lines) or not (dash lines) as in Fig. 3.6 (a). (b) is the comparison between the general HO model and HO2009 model in Fig. 3.7 (b). (c) is fitting results using the reduced HO model (HO-S) in Fig. 3.8 (c). (d) is the simulated results according to optimised combinations (1:1)+(nf) in Fig. 3.11 (b).	63
3.14	Only using biaxial tests in Sommer et al. data, we compute δ by fitting the HO-S model to one individual stretch ratio and predicting the remained experimental data from other stretch ratios. Only (1:1) and (1:0.75) meet $\delta \geq 0.8$ whilst (1:0.5) and (0.5:1) have $\delta \leq 0.4$	65
3.15	Stress distribution when fibre direction is 10° in uniaxial tensile along MFD as shown in Fig. 3.3. The green area enclosed by the two dashed lines is the effective area with higher stress while the blue area (the right bottom and left upper corners) is the ineffective area with much lower stress.	65
4.1	(a) The reconstructed bi-ventricle neonatal heart geometry from a 3D CT data (263,972 linear tetrahedral elements and 50,640 nodes). Local coordinate system, $\mathbf{f}_0, \mathbf{s}_0, \mathbf{n}_0$ are the conventional fibre-sheet-normal system, in which \mathbf{f}_0 is the mean fibre direction, \mathbf{s}_0 is the sheet direction in general along the transmural direction from endocardium to epicardium, and \mathbf{n}_0 is the sheet-normal direction. $\mathbf{c}_0, \mathbf{r}_0, \mathbf{l}_0$ are the local circumferential-radial-longitudinal system. (b) The reconstructed canine heart (252,713 linear tetrahedral elements and 49,460 nodes) with corresponding DT-MRI fibres. (c) Displacement vectors (\mathbf{u}) for warping the canine geometry to the porcine heart, coloured by the magnitude of \mathbf{u}	71
4.2	Myofibre rotation angle definition (a), which is the angle between \mathbf{f}_0^{\parallel} and \mathbf{c}_0 . \mathbf{f}_0^{\parallel} (in-plane) and \mathbf{f}_0^{\perp} (out-of-plane) are the projections of \mathbf{f}_0 in $\mathbf{c}_0 - \mathbf{l}_0$ and $\mathbf{l}_0 - \mathbf{r}_0$ planes, respectively, (b) AHA 17 segments definition in a bullseye view and (c) in the porcine model. Three different myofibre architectures are generated, they are (d) LDDMM derived, (e) RBM ¹⁷ and (f) RBM ^{uni}	73
4.3	An unit vector $\mathbf{M}(\Theta, \Phi)$ representing a fibre direction defined by Θ and Φ with respect to a Cartesian system $\mathbf{e}_1, \mathbf{e}_2$ and \mathbf{e}_3 . The plane spanned by \mathbf{e}_2 - \mathbf{e}_3 is in-plane whilst out-of-plane is \mathbf{e}_1 - \mathbf{e}_2 . The mean myofibre direction is along \mathbf{e}_3	77

4.4	Fibre dispersion quantified from the DT-MRI dataset. (a) shows the in-plane angle Θ and (b) the out-of-plane angle Φ across the LV ventricular wall; (c) is the in-plane dispersion distribution with fitted $\rho_{ip}(\Theta, b_1)$ and (d) is the out-of-plane dispersion distribution with fitted $\rho_{op}(\Phi, b_2)$; (e) a 3D surface plot defined by the vector $\rho(\Theta, b_1, \Phi, b_2)\mathbf{f}(\Theta, \Phi)$ with $\rho(\Theta, b_1, \Phi, b_2) = \rho_{ip}(\Theta, b_1)\rho_{op}(\Phi, b_2)$. The negative angle in (a) suggests the in-plane fibre vector lies in the fourth quadrant ($+\mathbf{c}_0$ and $-\mathbf{l}_0$), and similarly in (b) for the out-of-plane fibre vector, which lies in the fourth quadrant of plane ($-\mathbf{l}_0$ and $+\mathbf{r}_0$). All values are used for determining the in-plane and out-of-plane dispersions in (c) and (d).	79
4.5	Schematic of the bi-ventricular model coupled with a circulatory system. MV: mitral valve; AV: aortic valve; RA: right atrium; TV: tricuspid valve; PV: pulmonary valve; LA: left atrium; RA: right atrium; Ao: aorta; Sys: systemic circulation; Pul: pulmonary circulation; and PA: pulmonary artery. Grounded spring with a stiffness (k) is tuned to provide the appropriate PV response (i.e., compliance) for that cavity. C_V is viscous resistance coefficient to describe resistance between cavities. One-direction flow through valves is controlled by setting fluid exchanging properties between the cavities.	80
4.6	Simulated pump functions from cases LDDMM, RBM ¹⁷ and RBM ^{uni} , including (a) PV loops of LV and RV, (b) LV and RV EFs, (c) stress distribution across the wall at end-systole, and (d) apex twist angle.	83
4.7	Myofibre stress and strain distributions at end-systole for cases LDDMM, RBM ¹⁷ and RBM ^{uni} , respectively. The solid lines in (d), (e), and (f) are the long-axis which links the LV basal centre and the LV apex, and the longitudinal axis is represented by the dash line passing the LV basal centre and perpendicular to the basal plane.	84
4.8	Pump functions with varied n_s and n_n in case RBM ^{uni} . $n_f = 1.0$ for all simulations. (a) PV loops of LV and RV, and (b) EFs for LV and RV.	84
4.9	Pump function comparisons between case LDDMM and case RBM ^{uni} with cross-fibre contraction. (a) PV loops, (b) apex twist angle, (c) intramural stress across the entire LV wall and (d) myofibre stress distribution from case RBM ^{uni} with cross-fibre contraction at end-systole.	85
4.10	Predicted EFs with literature-based myofibre rotation angles [7] and dispersion parameters [4] using case RBM ^{uni} . The results are to be compared with the LDDMM case in Fig.4.7 (b), which has the mean fibre rotation angles $40^\circ \sim -30^\circ$, and EFs of 51.92% (LV) and 55.47% (RV).	86

4.11	Myocardial material parameter sensitivity study, including a , b , a_f , b_f , a_n , b_n , a_{fs} , b_{fs} , a_{fn} , b_{fn}) and the active parameter (T_{\max}). (a) normalized EDV and ESV values of the LV and (b) the RV with respect to the corresponding baseline values; (c) EF values. The baseline values of LV and RV are from the simulation with parameter values in Table 3 (the main text).	87
4.12	Relative errors in EDV (a) and EF (b) of the LV when inferring reasonable model parameters by matching targeted EDV ($V_0 + 1$) mL with V_0 the initial value and EF 52%.	87
5.1	(a) Surface plot of $\rho(\Theta, b_1, \Phi, b_2)\mathbf{M}(\Theta, \Phi)$ in the fibre system \mathbf{f}_0 , \mathbf{n}_0 and \mathbf{s}_0 with an unit vector \mathbf{M} (red) representing the fibre direction defined by Θ and Φ . (b) Illustration of a discrete triangular discretization of the unit hemisphere domain centralised with the mean fibre direction \mathbf{f}_0 (the red arrow) with N representative fibre directions \mathbf{M}_q (blue arrows) at the centroid of each triangular surface.	96
5.2	(a) Fibre directions (\mathbf{M}) defined using the eigenvectors (\mathbf{v}_1 , \mathbf{v}_2 and \mathbf{v}_3) of the right Cauchy-Green tensor \mathbf{C} with the two fibre angles θ and ϕ . (b) The stretched fibres Ω^e of (x, y) represented by the shaded area for case 2 and (c) case 3.	100
5.3	Surface plots of $\rho(\Theta, b_1, \Phi, b_2)\mathbf{M}(\Theta, \Phi)$ for different combinations of b_1 and $b_2 \in \{0, 1, 2, 4, 6, 8\}$ (a), and (b) a uniaxially stretched strip with linearly rotated fibres represented by red arrows.	105
5.4	Inference of rabbit myocardial passive property from the equibiaxial experimental data of Lin and Yin [1]. Red circles and blue squares are measured data along the mean fibre direction and the cross-fibre direction, respectively, and the solid lines are the final fitted result.	106
5.5	Relative errors of evaluating Eq. (5.4) using $N = 40$, $N = 160$ and $N = 640$ with different b_1 and b_2 combinations (a), the relative error is calculated in relate to the analytical value (1.0). (b) Stress-stretch responses of the uniaxial tension in four dispersion cases by using human (blue lines) and rabbit (red lines) material parameters, respectively. (c) Contours of stresses at the maximum stretch when using rabbit material parameters and (2) the human material parameters.	107
5.6	Compression tests with $b_1 = b_2 = 1$ and $b_1 = b_2 = 2$, respectively. A maximum of 20% compression is applied along the mean fibre direction, the negative values mean the resultant compressive stress.	108
5.7	A single element model with non-rotationally symmetric fibre distribution under uniaxial stretching (a), and (b) stretch-stress responses using Algorithm 5.1 (the black line), Algorithm 5.2 (the red cycles) and Algorithm 5.3 (the blue squares).	108

5.8	The reconstructed bi-ventricle rabbit heart geometry from a DT-MRI data (296785 linear tetrahedral elements and 55957 nodes). (a) An example DT-MRI rabbit heart with delineated ventricular wall enclosed by the red lines; (b) Four regions are defined for the rabbit heart with different colors, \mathbf{f}_0 , \mathbf{s}_0 , \mathbf{n}_0 are the fibre-sheet-normal system, in which \mathbf{f}_0 is the mean fibre direction, \mathbf{s}_0 is the sheet direction, in general along the transmural direction from endocardium to epicardium, and \mathbf{n}_0 is the sheet-normal direction; (c) Rule-based fibre architecture with fibre rotation angles defined in Table 5.2; (d) A schematic illustration of the bi-ventricular rabbit model coupled with a circulatory system. MV: mitral valve, AV: aortic valve, RA: right atrium, TV: tricuspid valve, PV: pulmonary valve, LA: left atrium, RA: right atrium, Ao: aorta, Sys: systemic circulation, Pul: pulmonary circulation and PA: pulmonary artery. Grounded spring with a stiffness of k is tuned to provide the appropriate PV response (i.e., compliance) for the corresponding cavity. C_V is the viscous resistance coefficient for describing resistance between cavities. Flow through valves is realized by only allowing uni-directional fluid exchanging between two cavities.	109
5.9	Myofibre stress (σ_{ff}) distributions with deformed shapes at end of diastole (top) and end of systole (bottom) in the rabbit bi-ventricle model for case 1 ($b_1 = b_2 = 0$), case 2 ($b_1 = 0, b_2 = 2$), case 3 ($b_1 = 2, b_2 = 0$), case 4 ($b_1 = b_2 = 2$), and case 5 without fibre dispersion.	111
5.10	Systolic function for the five cases with different dispersed fibres in the rabbit heart model. (a) PV loops; (b) long-axis shortening, and the long axis is defined as the line segment between the LV basal centre and the apex (the black line in Fig. 5.9); (c) average myofibre stress σ_{ff} in the middle ventricle enclosed by the black rectangle in Fig. 5.9, and (d) the apex twist angles.	112
5.11	Relative differences of ESV and EDV values with different dispersion parameters compared to case 5. (a) EDV differences of the rabbit LV and (b) RV, (c) ESV differences of the rabbit LV and (d) RV, respectively.	113
5.12	A human LV model with 133,042 linear tetrahedral elements and 26,010 nodes (a) and its fibre architecture (b) generated by the rule-based method with fibre rotation angles from -60° at epicardium to 60° at endocardium. (c) A schematic illustration of the human LV model with a circulation system, and the definitions of various symbols are same as those in Fig. 5.8 (d).	114
5.13	Myofibre stress distributions (σ_{ff}) at the end of diastole (top) and at the end of systole (bottom) for the human LV model with different combinations of b_1 and b_2	114

5.14	Systolic function for the five cases in the human LV model. (a) PV loops; (b) long-axis shortening, the long-axis is defined as the link between the LV basal centre and the apex (the black line in Fig. 5.13); (c) average myofibre stress σ_{ff} in the middle ventricle indicated by the black rectangle in Fig. 5.13, and (d) the apex twist angles.	116
5.15	Relative differences of EDV (a) and ESV (b) with different dispersion parameters compared to case 5 for the human LV model. The contour lines indicate $\pm 5\%$ difference, and the white dot is the measured dispersion ($b_1 = 4.5, b_2 = 3.9$) from Sommer et al [4].	116
5.16	Fitting results to an equal-biaxial tension test in Sommer et al. [4] using Eq.(1).	117
6.1	Scheme of G&R and loading process for each constituent in one numerical cycle. \mathcal{B}_1 is the updated reference configuration. Growth tensor (\mathbf{G}^i) firstly converts \mathcal{B}_1 to the incompatible configuration \mathcal{B}_2 , and inelastic remodelling (\mathbf{F}_{ir}^i) further remodels the \mathcal{B}_2 to the compatible or incompatible configuration \mathcal{B}_3 , then elastic remodelling (\mathbf{F}_{er}^i) merger all constituents to the compatible state \mathcal{B}_4 , finally the configuration \mathcal{B}_5 is the loading state according to external loads.	125
6.2	Scheme to update reference configuration and proceed a numerical simulation cycle that includes a updating reference configuration step, a growth step and a loading step.	127
6.3	(a) Meshed network of human LV model (133,042 linear tetrahedral elements and 26,010 nodes) and three element circles at base, medium and apex positions. Inside fibre distribution was constructed by the rule based method from -60° at epicardium to 60° at endocardium. (b) Sketch of the human LV model with a circulation system, same as the Fig. 5.12 (c). (c) Meshed network of simple ring model (1,925 linear hexadecimal elements and 2,772 nodes) and fibres also rotates from endocardium (60°) to epicardium (-60°).	131
6.4	Scheme of G&R when relieving residual stress before growth at beginning of each updated growth cycle. The configuration \mathcal{B}_1 is stress-free and grows to the new stress-free and incompatible configuration \mathcal{B}_2 , which turns to be the compatible state again \mathcal{B}_3 by elastic remodelling, finally cardiac dynamics in the \mathcal{B}_4 is achieved by applying external loadings in the \mathcal{B}_3	133
6.5	Scheme of volumetric growth without residual stress at beginning of growth. The configuration \mathcal{B}_1 is stress-free and grows to the incompatible stress-free configuration \mathcal{B}_2 . Then, it turns to be the compatible state \mathcal{B}_3 by elastic remodelling, which is finally loaded to \mathcal{B}_4	134
6.6	(a) Grown LV anatomical diagrams and their inside growth ratio distributions in the final growth cycle. With respect to growth cycles, average values of total growth ratio (b) and incremental growth ratio (c) of the whole LV.	136

6.7	Residuals stress is estimated at compatible geometry after growth in the final growth cycle. (a) Distribution of fibre stress component along fibre S_{11} at medium of LV, (b) mean transmural stress along wall thickness, and (c) open angle under mean residual stress in the ring model.	137
6.8	Scheme of G&R with residual stress before and after growth. \mathcal{B}_1 is real compatible state with residual stress and grows to incompatible state \mathcal{B}_2 that turns to be compatible \mathcal{B}_3 then is loaded to \mathcal{B}_4 . Fictitious incompatible stress free configurations \mathcal{B}_{-1} , \mathcal{B}_0 and \mathcal{B}_5 are included to depict equivalent fictitious G&R paths. \mathcal{B}_{-1} converts to \mathcal{B}_1 by residual deformation tensor \mathbf{F}_{r0}^i . After polar decomposition of \mathbf{F}_{r0}^i , intermediate \mathcal{B}_0 is from rotation of \mathcal{B}_{-1} then is stretched to \mathcal{B}_1 . Growing from \mathcal{B}_0 by equivalent growth, \mathcal{B}_5 merges into \mathcal{B}_3 by equivalent residual stress or turns to \mathcal{B}_4 by total equivalent elastic deformation.	138
6.9	Growth increments with (a) and without (b) residual stress. Configurations \mathcal{B}_0 , \mathcal{B}_1 , \mathcal{B}_2 and \mathcal{B}_5 refer from Fig. 6.8. Red squares represent stress-free state whilst residual stress in blue squares. Fibre length in \mathcal{B}_0 is l_0 , stretch ratio from \mathcal{B}_0 to \mathcal{B}_1 is p_f , growth ratio from \mathcal{B}_1 to \mathcal{B}_2 is ϑ_f and fictitious growth ratio from \mathcal{B}_0 to \mathcal{B}_5 is ϑ'_f . When relieving residual stress from \mathcal{B}_2 to \mathcal{B}_5 , growth increment with pre-stretch induced by residual stress in (a) needs to remove the pre-stretch by p_f^{-1} , whilst stress free increment keeps same length in (b).	140
6.10	Scheme of G&R without residual stress before and after growth. Stress-free \mathcal{B}_1 grows and remodels to \mathcal{B}_3 that turns to \mathcal{B}_4 after dropping residual stress. Then, all constituents share same external loads to \mathcal{B}_5	141
6.11	(a) grown LV anatomical diagrams and their inside growth ratio distributions in the final growth cycle. With respect to growth cycles, average values of total growth ratio (b) and incremental growth ratio (c) of the whole LV.	142
6.12	With respect to growth cycles n , average total θ^f and incremental ϑ^f growth ratios at each layers from endocardium (layer 1) to epicardium (layer 5) in maintaining residual stress model (a,b) and in relieving residual stress model (c,d).	143
6.13	Mean fibre angles variations around endocardium (a) and epicardium (b).	144
6.14	With respect to growth cycle, (a) unloaded LV volumes and (b) loaded LV volumes with EDP (16 mmHg).	144
6.15	Residual stress is estimated at compatible geometry after growth in the final growth cycle. (a) Distribution of fibre stress component along fibre S_{11} at medium of LV, (b) mean transmural stress along wall thickness, and (c) open angle under mean residual stress in the ring model.	145
6.16	Growth of myofibre in eccentric growth. (a) Growth ratio distribution in the final grown heart models. With respect to growth cycle, (b) mean total growth ratio and (c) mean incremental growth ratio.	148

6.17	In eccentric growth, average total (top) and incremental (bottom) growth ratios of myofibre at each layers from endocardium to epicardium with respect to growth cycle (n).	149
6.18	In eccentric growth, variations of volume fractions of constituents in CF-NG-PR case (a), in CF-NG-ER case (b), and in CF-GAM case (c). Using volume fractions (VF) in the final growth cycle, uniaxial tension test provides stress-stretch lines for each case comparing to no growth (NG) case.	149
6.19	In eccentric growth, residuals stress is estimated at compatible geometry after growth in the final growth cycle. For three cases, (a) cross-sectional view of fibre stress component along fibre S_{11} distribution at the medium of LV, (b) mean transmural stress along wall thickness, and (c) opening angle under mean residual stress in the ring model.	150
6.20	In eccentric growth, with respect to growth cycles, PV loops in (a) CF-NG-PR, (b) CF-NG-ER and (c) CF-GAM cases. Black solid line is the normal case with EDP 8 mmHg, blue dash line is the first loading step after applying volume overload with EDP 16 mmHg, red dot line is the ending of growth, and grass thin lines are medium growth cycles. Their corresponding EFs are in (d) and SVs in (e).	151
6.21	In concentric growth, for three types of G&R of collagen fibre, (a) growth ratio distributions in the final grown heart models. With respect to growth cycles, (b) mean total growth ratio and (c) mean incremental growth ratio. (d) Average total (top) and incremental (bottom) growth ratios at each layers from endocardium to epicardium with respect to growth cycles (n).	153
6.22	In concentric growth, variations of volume fractions of constituents in CF-NG-PR case (a), in CF-NG-ER case (b), and in CF-GAM case (c). Using volume fractions (VF) in the final growth cycle, uniaxial tension test provides stress-stretch lines for each case comparing to no growth (NG) case.	154
6.23	In concentric growth, residuals stress is estimated at compatible geometry after growth in the final growth cycle. For three cases, (a) cross-sectional view of fibre stress component along fibre S_{11} distribution at the medium, (b) mean transmural stress along wall thickness, and (c) opening angles under mean residual stress in the ring model.	155

6.24	In concentric growth, with respect to growth cycles, PV loops in (a) CF-NG-PR, (b) CF-NG-ER and (c) CF-GAM cases. Black solid line is the normal case, blue dash line is the first loading step after applying pressure overload by aortic stenosis, pink dot line is the step with maximum pressure, brown dash-dot line is the step with maximum EF and red line is ending of growth. Their corresponding EFs are in (d) and SV in (e). (f) Updated PV loop with bigger EDP 12 mmHg in the CF-NG-PR case.	156
7.1	LV model and its medium cross-section where MI region is denoted by the red color and remote healthy region is in blue color. (a) Infarction degree (\mathcal{I}) distribution in LV where $\mathcal{I} = 1$ is the infarction zone and $\mathcal{I} = 0$ is remote healthy zone. Medium border zone connects infarcted zone and remote healthy zone with linear varying volume fractions of myofibre and collagen fibre (b).	162
7.2	G&R of MI model without fibre dispersion. Comparing to the initial LV before growth, grown geometry and distributions of total growth ratios of myofibres along fibre (θ^f) and sheet (θ^s) direction are shown in (a). Cauchy stress component along fibre in (b), and logarithm strain component along fibre in (c) at ED and ES at the final numerical cycle. Average total (θ^i) and incremental (ϑ^i) growth ratios of the non-MI zone with respect to growth cycles are plotted in (d) and (e), respectively.	164
7.3	Variations of PV loop, EF, SV and wall thickness with G&R. Comparing to the normal PV loop, four representative loops are adopted in (a), which are the first cycle, the second cycle having the maximum ESP, the fourth cycle having the maximum EDV, and the last cycle. EF in (b), and SV in (c). Wall thickness in (d) covers the average thickness of the non-MI zones and the MI zone.	166
7.4	Residual stresses at healthy, border, and MI zones, respectively. Three transverse cutting positions pass through the healthy, the border, and the MI zones, respectively. (a) Cross-sections with distribution of Cauchy stress component along fibre. (b) Average transmural residual stress distributions at the three zones.	167
7.5	G&R of MI model with fibre dispersion. All non-MI zones use the same dispersion ($b_1 = 4.5, b_2 = 3.9$), and three general cases are in the MI zone, which are $b_1 = 1.0 \& b_2 = 1.0$, $b_1 = 2.0 \& b_2 = 2.0$, and $b_1 = 4.5 \& b_2 = 3.9$. (a) Their distributions of total growth ratios along fibre (θ^f) direction on the top and along sheet (θ^s) direction on the bottom. Average growth ratios θ^f and θ^s of non-MI zones in three case 1 (b), case 2 (c), and case 3 (d), respectively.	172
7.6	Fibre stress distributions at ED (the top) and ES (the bottom) after G&R of MI model with three cases of fibre dispersion.	173

7.7 (a) Comparison of residual stress between MI models with three cases of fibre dispersion, at the healthy zone (the top), at the border zone (the medium), and at the MI zone (the bottom). The right denotes positions of the three cross-sections.
(b) Three cases' average transmural residual stress distributions at the three zones. 174

7.8 Variations of PV loop, EF, and SV using the MI models with fibre dispersion in the first five cycles. (a) PV loops of case $b_1 = 1.0$ & $b_2 = 1.0$, (b) PV loops of case $b_1 = 2.0$ & $b_2 = 2.0$, and (c) PV loops of case $b_1 = 4.5$ & $b_2 = 3.9$. Their EFs in (d), SVs in (e), and wall thickness in (f). 175

Acknowledgements

It is a genuine pleasure to express my deep sense of thanks and gratitude to all people who provided helps and supports during my PhD.

I would like to express my deep gratitude and respect to my supervisors Dr. Hao Gao and Prof. Xiaoyu Luo for their valuable guidance over this project. They all showed great patience to help me to explore new fields and learn new knowledge. Prof. Xiaoyu Luo can always share wide views on researching and offer instructive suggestions. Dr. Hao Gao spends a lot of effort into in my researching program, for which I am deeply grateful. He has taught me the methodology for conducting research correctly, presenting works clearly, and writing papers effectively. I am also very grateful for his care and help in life. Prof. Raymond Ogden has been serving as the reviewer of my annual report during my PhD. I am impressed by his profound knowledge and benefit a lot from his academic suggestions. The SIMULIA Living Human Heart Project was the first project I joined when I started my PhD, from which I learned a lot of methods for constructing the heart modes in this thesis.

I sincerely appreciate Chinese Scholarship Council who provides the funding to support my study and life abroad. I am very excited to witness the great development of China and wish my motherland better and better.

I really enjoy the positive research atmosphere in School of Mathematics and Statistics, where researchers can communicate freely and cooperate closely. In particular, I would like to show my great thanks to my colleagues and friends Xin Zhuan, Liuyang Feng, Mihaela Paun, Yalei Yang, Yingjie Wang, etc. They all have given me a lot of helps in my life and study.

In the past four years, my dear friends Xin Xin, Mingzhe Wei, Yuheng Wang, Yongjie Wang, Shuting Zhang, and Ruochen Dong have been accompanying me like my family members. I deeply cherish the friendship with them and wish them all the best in the future.

In China, my family gives their unconditional loves and efforts to support me and I love them very much. Chen Chen, Chen Dong, Hongbiao Duan, etc. are the best friends to plan the future and share a joyful life.

There are so many friends to thank and so many stories to remember. I will take all my gratitude in my heart and bless all the people I love and love me.

Declaration

I, Debao Guan, declare that this thesis titled, ‘Mathematical modelling of cardiac function: constitutive law, fibre dispersion, growth and remodelling’ and the work presented in it are my own.

I confirm that:

- This work was done wholly or mainly while in candidature for a research degree at this University.
- Where any part of this thesis has previously been submitted for a degree or any other qualification at this University or any other institution, this has been clearly stated.
- Where I have consulted the published work of others, this is always clearly attributed.
- Where I have quoted from the work of others, the source is always given. With the exception of such quotations, this thesis is entirely my own work.
- I have acknowledged all main sources of help.
- Where the thesis is based on work done by myself jointly with others, I have made clear exactly what was done by others and what I have contributed myself.

Signed:

Date:

Publication list

- Journal publications based on this thesis:

1. **Guan, D.**, Ahmad, F., Theobald, P., Soe, S., Luo, X. and Gao, H., 2019. On the AIC-based model reduction for the general Holzapfel–Ogden myocardial constitutive law. *Biomechanics and modeling in mechanobiology*, 18(4), pp.1213-1232.
2. **Guan, D.**, Yao, J., Luo, X. and Gao, H., 2020. Effect of myofibre architecture on ventricular pump function by using a neonatal porcine heart model: from DT-MRI to rule-based methods. *Royal Society Open Science*, 7(4), p.191655.
3. **Guan, D.**, Zhuan, X., Holmes, W., Luo, X. and Gao, H., 2021. Modelling of fibre dispersion and its effects on cardiac mechanics from diastole to systole. *Journal of Engineering Mathematics*, 128(1), pp.1-24.
4. **Guan, D.**, Luo, X. and Gao, H., 2020. Constitutive Modelling of Soft Biological Tissue from Ex Vivo to in Vivo: Myocardium as an Example. *In International Conference by Center for Mathematical Modeling and Data Science, Osaka University. Springer, Singapore*, pp.3-14.

Abbreviations

G&R	Growth and remodelling
HO model	Holzapfel and Ogden model
LV	Left ventricle
RV	Right ventricle
LVFW	Left ventricle free wall
RVFW	Right ventricle free wall
FE	Finite element
DT-MRI	Diffusion tensor magnetic resonance imaging
LDDMM	large deformation diffeomorphic metric mapping
SEF	Strain energy function
MFD	Mean fibre direction
CFD	Cross fibre direction
RBM	Rule-based method
3D	Three-dimensional
2D	Two-dimensional
PDF	Probability density function
AI	Angular integration
GST	Generalised structure tensor
DFD	Discrete fibre dispersion
MI	Myocardium infarction
EF	Ejection fraction
ED	End diastole
EDV	End-diastolic volume
EDP	End-diastolic pressure
ES	End systole
ESV	End-systolic volume
ESP	End-systolic pressure
PV	Pressure-volume
SV	Stroke volume
P-K	Piola-Kirchhoff
AIC	Akaike information criterion

Chapter 1

Introduction

The heart is an essential organ of a living body whose primary function is to generate the pressure gradient to pump blood into all organs, which requires myocardium to operate systematically. Heart disease is the leading killer worldwide, responsible for about 40% of all deaths each year. The incidence of heart failure, such as induced by heart attacks, has remained persistently high due to the maladaptive growth and remodelling (G&R). There are more heart diseases survivors who also come with a subsequent rise in heart failures. Myocardial G&R can be broadly defined as variations in heart geometry and function in response to an imbalanced mechanical environment. To account for these changes, mathematical models of G&R are proposed according to continuum mechanics [10].

Stress/strain-driven G&R depends on the mechanical response and deformation of a heart model, which is determined by constitutive laws and fibre structures together. The direct measurement of in vivo ventricular wall stress has not been achieved. Hence, constitutive laws are proposed to predict the stress-strain relationships in myocardium, such as the invariants-based or strain-based phenomenological models and micro-structural analysis models. The classic invariant-based constitutive law proposed by Holzapfel and Ogden [11] exhibits a strong descriptive and predictive capability when fitting a set of simple shearing experimental data and is widely used in simulating cardiac dynamics [12, 13]. To the author's best knowledge, however, no analysis has shown whether it is sufficiently descriptive and predictive for other tissue examinations of the myocardium. In fact, for any constitutive law, this analysis is important for clinically useful computational simulations.

Myocardium is a type of fibre-reinforced material, and fibre rotates from endocardium to epicardium in a helix structure. In the three-dimensional (3D) finite element (FE) model, fibre structure plays a critical role in deforming the whole heart model. Currently, there are two main approaches to construct fibre structure. Rule-based approach is easy to implement by defining fibre direction according to fibre position in ventricular wall [7, 14]. Atlas mapping approach is to map the measured realistic fibre direction from image data to corresponding geometry [12, 15]. Recently, the concept of fibre dispersion are prevalent with the proofs of

dispersed fibres in experiments [4, 5]. Excluding compressed fibres that do not produce stress response is a challenging task when considering fibre dispersion around the mean fibre direction. Lots of studies have proposed ample approaches to incorporate fibre dispersion into previous passive constitutive laws [16–20]. However, few studies tried to quantify active tensions in myocardium with fibre dispersion structure [21] and to explore the effects of fibre dispersion on the cardiac pump function.

Kinematic growth theory has been widely used to elucidate G&R of fibrosis tissues [22]. It is based on multiplicative decomposition of total deformation gradient tensor \mathbf{F} , such as $\mathbf{F} = \mathbf{F}_e \mathbf{F}_g$, according to the concept of plasticity. \mathbf{F}_g is inelastic growth deformation gradient tensor that describes changes in shape and size of the stress-free and compatible tissue. Growth leads the tissue into a new incompatible and stress-free intermediate configuration. In subsequent step, elastic deformation gradient tensor \mathbf{F}_e assembles all growing and original constituents into new compatible state, in which residual stress may be generated. However, the kinematic growth theory is unable to directly account for the G&R of individual constituents within myocardium, such as the turnovers or deformations of myofibres and collagen fibres that play the crucial role in adaptive and maladaptive process of heart. Additionally, considering the important effect of reference configuration types [23], simulations of G&R basing on fix reference configuration may not match biological growth. The recent homogenised constrained mixture theory makes it possible to describe individual G&R process of each constituent who has its own mechanical constitutive law and fibre structure. However, the requirement to tracking the evolution of reference configuration is tough to be achieved in numerical computations. Identifying appropriate growth laws for each constituent under specific pathological conditions is also an arduous challenge. Until now, the constrained mixture model were often used to study vascular G&R [24] and barely in cardiac problems.

In summary, intentions of this thesis can be divided into two parts. Part one is to demonstrate continuum mechanics of myocardium, including constitutive laws and fibre structures, and part two is to explore G&R of heart under various pathological conditions. The organization for the thesis is schemed in Fig. 1.1 and details are:

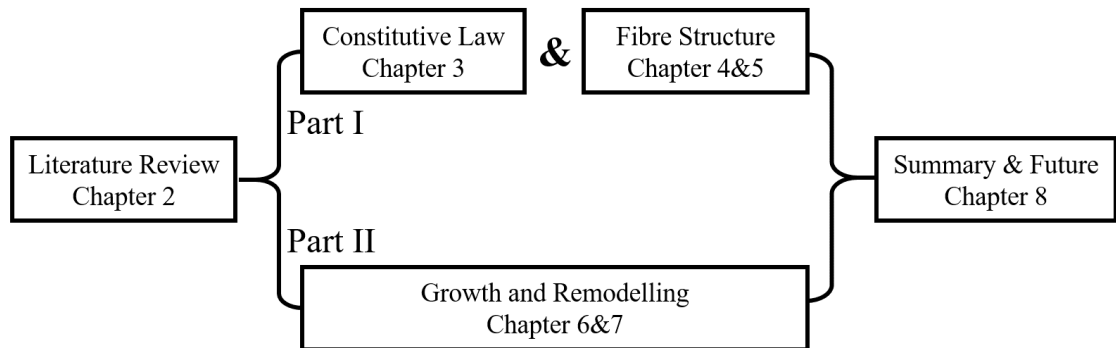


Figure 1.1: Schematic for the organization of the project

- **Chapter 2** reviews the general background knowledge about the general structure of myocardium, constitutive mechanical laws for myocardium, approaches to construct fibre architecture and its dispersion, and G&R framework. It systemically covers the main research topics of myocardial mechanics.
- **Chapter 3** aims to reduce the constitutive law by using the Akaike information criterion to maintain its mechanical integrity whilst achieving minimal computational cost. It also investigates the optimal combinations of tissue tests. For example, it shows that one shear responses plus one biaxial stretch are sufficient to describe human myocardial mechanical properties satisfactorily.
- **Chapter 4** develops a neonatal porcine bi-ventricle model with three different myofibre architectures. The most realistic one is derived from ex vivo diffusion tensor magnetic resonance image, and the other two simplifications are based on the rule-based method. Results highlight the importance of including myofibre dispersion in cardiac modelling if rule-based methods are used, especially in personalized models.
- **Chapter 5** employs three types of FE models, a multi-element strip, a bi-ventricular rabbit heart and a single LV human heart, to study the effects from different fibre dispersions that are characterized by in-plane and out-of-plane dispersion parameters. General structure tensor method and discrete fibre dispersion method are used to compute dispersed active and passive stresses, respectively.
- **Chapter 6** couples the homogenised constrained mixture G&R theory to the updated reference configuration framework. It studies the G&R processes under various physiological and pathological conditions, such as aortic stenosis and mitral regurgitation. Different biomechanical cues are considered to deepen our understanding of the onset of maladaptation.
- **Chapter 7** investigates G&R of heart with myocardium infarction and the impact of fibre dispersion in G&R process. Different fibre dispersion structures are integrated into the infarcted zone and non-infarcted zones.
- **Chapter 8** is the summary of this thesis and future development of G&R in heart, which includes a constitutive model from ex vivo to in vivo, a biophysically detailed active tension model, and validations of G&R based on experimental data.

Chapter 2

Literature Review

This PhD project includes two parts, cardiac mechanics that includes constitutive modelling and fibre structure and G&R of myocardium that studies G&R processes of heart under various physiological and pathological conditions. On the one hand, myocardium is a fibre-reinforced material where constitutive laws and fibre structures are essential to elaborate its mechanical properties. Constitutive laws describe the relations between mechanical responses and deformations of myocardium after calibration using experimental data, which may predict stress/strain clues for myocardial remodelling induced by abnormal loading of heart. Then, acting as the main load-bearing constituents in myocardium, myofibre and collagen fibre structures with supplementary fibre dispersion play a crucial role in determining the overall mechanical responses of a heart model and shed light on the fundamental principles of cardiac functions. On the other hand, mechanical clues from cardiac dynamics drive G&R. Classic volumetric growth cannot explain the individual G&R of constituents in myocardium. To overcome this limitation, the homogenised constrained mixture theorem is developed here by coupling an updated reference configuration framework.

Therefore, we review relative concepts and models to describe biomechanics of myocardium. The first part is the brief illustration of myocardial structure and function, ranging from cell to tissue. Then, based on the myocardial structure, passive and active models in cardiac biomechanics are respectively introduced. Subsequently, the significant importance of myofibre and collagen fibre architectures in modelling myocardial mechanical behaviours is evaluated. The final part briefly summarizes two primary G&R theories and the G&R of heart after MI.

2.1 Structure and function of heart

Heart is the centre of the circulatory system of a body, whose primary task is to pump blood with oxygen and nutrients to all organs. As shown in Fig. 2.1 (a), a heart consists of four chambers that regulate oxygen-poor or oxygen-rich blood throughout the four valves. Briefly, the right atrium transports the oxygen-free blood, collected from the systemic circulation, into

the right ventricle (RV) by the tricuspid valve. Then the blood is pumped into the lung through the pulmonary valve. Simultaneously, the left atrium pours the oxygen-enriched blood from the pulmonary circulation into the left ventricle (LV) through the mitral valve, and LV further pumps the blood into all organs of body through the aortic valve. One heart cycle can be divided into four phases: ventricular filling, isovolumetric contraction, ejection and isovolumetric relaxation. For example, in LV (Fig. 2.1 (b)), at the beginning of contraction, the mitral valve closes, and the LV pressure increases while the LV cavity volume remains constant. Once LV pressure exceeds aortic pressure, the aortic valve opens, and ejection starts. LV volume decreases with increasing pressure to a peak value, after which LV pressure decreases as reduction of active tension in myocardium. The aortic valve will close when LV pressure is lower than the pressure in the aorta, which marks end of ejection process, then the isovolumetric relaxation starts, during which LV pressure falls quickly. When LV pressure falls below left atrium pressure, the mitral valve will open again, and the LV begins the filling phase.

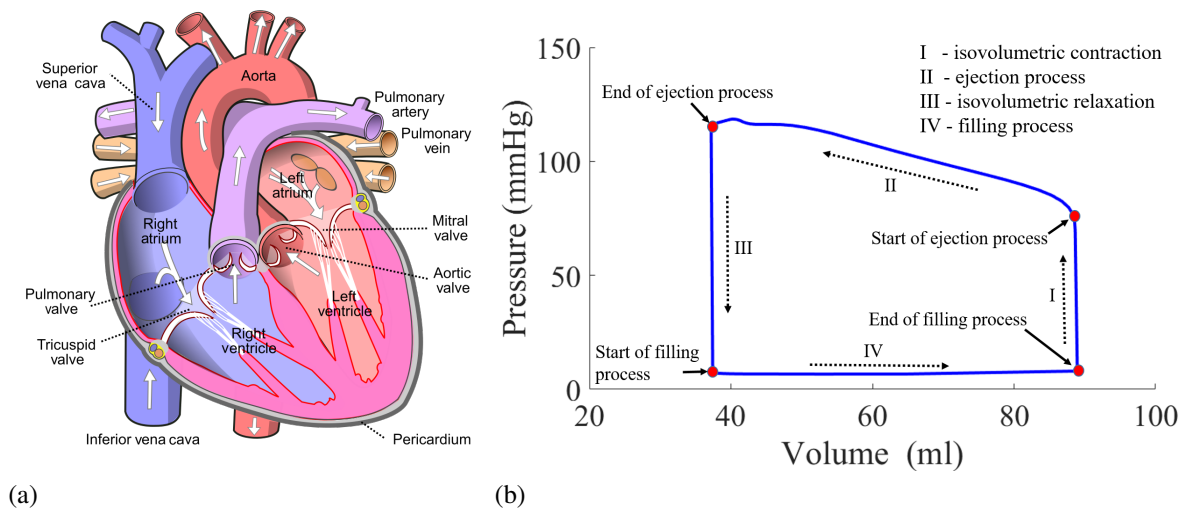


Figure 2.1: (a) Simple anatomy diagram of the human heart (<https://en.wikipedia.org/wiki/Heart>). (b) Pressure-Volume loop of the LV presenting the different phases in a complete heart cycle.

The structural hierarchy of a heart is briefly depicted in Fig. 2.2. Myocardium is the main constituent of the heart wall that has three layers: the outer thin layer (epicardium), the middle thick layer (myocardium), and the inner thin layer (endocardium). In myocardium, myofibre (bundles of myocytes) accounts for 70% of myocardium by volume [25] and has a lower passive stress response with increasing strain than collagen fibre that only takes 2.6%, followed by ground matrix (27.4%). If myocardium is analogous to reinforced concrete, ground matrix is the concrete, and myofibres and collagen fibres are two types of rebar inside. The contractile capability of myofibre is generated by the internal contraction unit, i.e. sarcomere, which is triggered by an electrical signal for active tension generation. Collagen fibre is the main constituent to bear a tensile load, such as providing passive stress to prevent excessive expansion

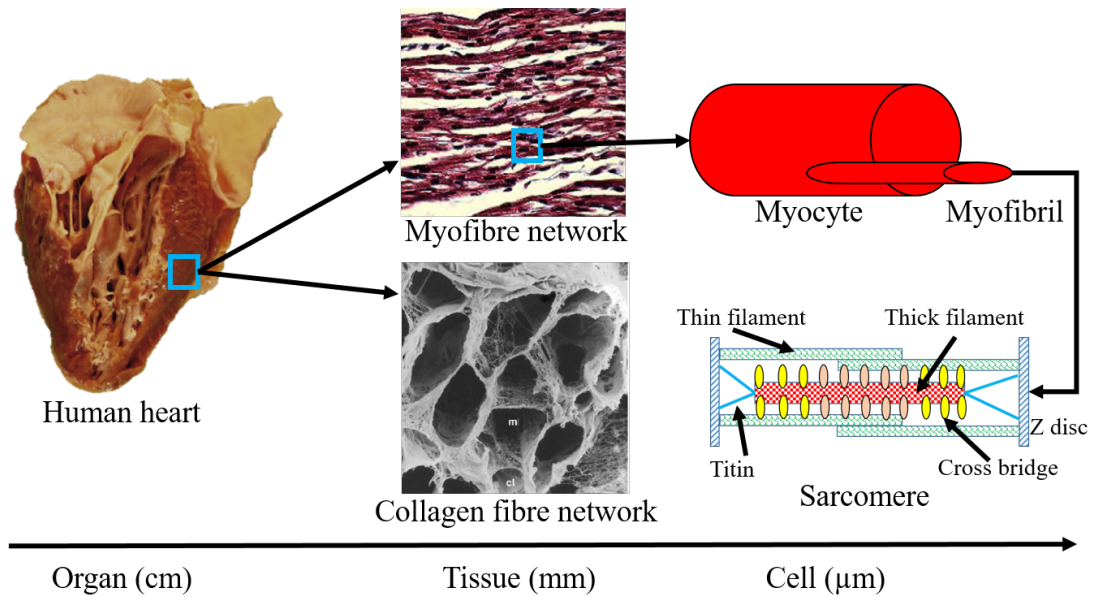


Figure 2.2: Structural hierarchy. Human heart graph from Sommer et al. [4], myofibre network graph from Ahmad et al. [5], and collagen fibre network graph from Avazmohammadi et al. [6]. All figures are reprinted with permission.

of heart during diastole. Therefore, architectures of myofibres and collagen fibres have critical importance in the regulation of cardiac functions. This section aims to provide myocardial microstructure details that are involved in mechanical models.

2.1.1 Structure at cellular level

Myocardium is a type of muscle tissue consisting of myofibres and collagen fibres surrounded by ground matrix. Inside the cardiomyocytes, there are many myofibrils arranged in parallel along their longitudinal direction. The microstructure of myofibril is constituted by the systematic assembly of sarcomeres that are the basic units for myocyte contraction (Fig. 2.2). The sarcomere has a symmetric structure where thin actin filaments are parallel to thick myosin filament. Z discs at both ends are anchored to only one end of the thin filament and connect to both ends of the thick filament by elastic protein titin. Regulated by action potential prorogation, cross bridges on thick myosin filament can bind thin actin filament and pull both ends towards the centre, resulting in relative sliding and generating a force that leads active contraction.

Collagen in myocardium contains two main types: thick cord-like parallel fibrils that have high tensile strength and account for 85% of fibrillar collagen, and fine network of fibrils that accounts for 15% [26]. Following the division of cardiac fibrillar collagen network [27], endomysium surrounds and interconnects individual myocytes, perimysium surrounds and connects groups of myocytes, and epimysium is the connective tissue surrounding the entire muscle [28]. Collagen fibres are responsible for maintaining the extracellular matrix where myocytes can obtain mechanical support and anchors.

The ground matrix is a mixture composed of fibroblasts, elastin, and other molecules. In this thesis, all the remaining components in myocardium after removing myofibres and collagen fibres are collectively referred to as the ground matrix. Maintained by fibroblasts in tissue, it surrounds the myocytes to provide structural support and acts as the ground substance to construct the architecture of myocardium.

2.1.2 Tissue level structure and function

Within the heart wall, the main characteristic of myofibre structure is transmural rotation from endocardium to epicardium with a helical angle [29]. It is an idealized description due to the fact that organizations of fibre and sheet are highly complex and various with respect to regions. However, diffusion tensor magnetic resonance imaging (DT-MRI) makes it feasible to capture 3D myofibre directions, followed by the observations of inclination angles in various regions [30] and the twisted laminar surfaces throughout the ventricular wall [31].

The ground matrix surrounds the myofibres and the collagen fibres, and transfers the load throughout the myocardial wall. It is able to regulate the stiffness of myocardium by varying the inside contents, such as increasing collagen content to stiffen myocardium. In addition, ground matrix integrates myofibres and collagen fibres, resulting in anisotropic mechanical properties in myocardium. For example, different stress responses along the mean fibre direction and the cross-fibre direction in biaxial tension test [4], in which non-zero force occurs at the cross-fibre direction may be explained by mechanical support of ground matrix or rotated fibres. In addition, the overall composition of the ground matrix is one suspected reason [32] that leads to myocardial elastic anisotropy varying with muscle depth [33].

Collagen fibres in myocardium are initially in crimped state [34] and cannot bear load until they are straighten, resulting in higher strains of loaded myocardium. For instance, in the passive tension test of myocardium, low-stress response regime is governed by the myofibres alone before the engagement of collagen fibres, after which collagen fibres and their interactions with myofibres determine the higher stress response. Therefore, collagen fibres play as the scaffold to protect myofibres and ground matrix from excessive deformation.

At tissue level, the interaction of myofibre and collagen fibres was early described by a strut structure [27,35], in which collagen fibres act as the intermediary to connect myofibres to myofibres, and myofibres to capillaries perpendicularly. Later, high-precision imaging technologies, such as scanning electron microscopy and reticulum-staining techniques, found that collagen fibre structure is analogous to a honeycomb where weaved fibrillar sheath structure surrounding myofibres and capillaries [36, 37]. Currently, the sheath structure representation is widely accepted and used for constitutive modelling. Nevertheless, myofibres and collagen fibres are usually assumed to share the same direction, and both rotate from endocardium to epicardium with a helix structure. Advanced image techniques demonstrate that fibres are dispersed in space along a mean direction [4,30]. Moreover, the dispersions of myofibres and collagen fibres may

have deviation [5].

2.2 Constitutive models of passive myocardium

Stress or strain in myocardium has significant importance on both physiological and pathological processes, such as hypertrophy and myocardial infarction [38–40]. Constitutive models describe the relationships between kinematics and stress of a material in general. The in vivo kinematics of ventricular wall, i.e. its deformations, can be quantitatively measured by imaging techniques, whilst direct measurement of in vivo wall stress has not been achieved, which are commonly derived from constitutive functions. Thus, the choice of constitutive laws determines the accurate prediction of myocardial stress. Over the years, many models have been proposed to illustrate myocardial constitutive behaviours, ranging from linear elastic to hyperelastic, from isotropic to anisotropic, and from phenomenological to micro-structurally informed constitutive laws [11]. Nowadays, treating myocardium as an anisotropic, hyper-elastic material is a prevalent practice in developing constitutive laws. For the passive behaviour of myocardium, the constitutive function is also called strain energy function (SEF) because it is in the form of pseudoelastic stored energy density function \mathscr{W} .

Under external loading, one material point \mathbf{X} in myocardium in the reference configuration moves to a new position $\mathbf{x} = \mathbf{x}(\mathbf{X}, t)$ in the deformed configuration at time t , and the deformation gradient tensor $\mathbf{F} = \frac{\partial \mathbf{x}}{\partial \mathbf{X}}$ denotes the deformation of the material point. Then the Cauchy stress caused by deformation can be computed by a SEF \mathscr{W} through

$$\boldsymbol{\sigma} = J^{-1} \mathbf{F} \frac{\partial \mathscr{W}}{\partial \mathbf{F}} - p \mathbf{I}, \quad (2.1)$$

where $J = \det(\mathbf{F}) = 1$ enforces the incompressibility constraint, \mathbf{I} is the identity tensor, and p is the Lagrange multiplier. In addition, the left and right Cauchy-Green tensors ($\mathbf{B} = \mathbf{F}\mathbf{F}^T$ and $\mathbf{C} = \mathbf{F}^T\mathbf{F}$), and the Green-Lagrange strain tensor ($\mathbf{E} = (\mathbf{C} - \mathbf{I})/2$) are often involved in calculating stress.

Constitutive models always assume myocardium as a continuum, and variables in \mathscr{W} usually are measurable in tissue level. They are divided into two categories according to their description scales. The first category is the phenomenological model, which treats myocardium as a lumped continuum element of its constituents, in which all variables are derived from the deformations of the whole myocardium and do not account for structural information of its compositions. In contrast, micro-structurally informed models are based on volume fractions, microstructures and deformations of constituents within myocardium, generally on sub-tissue scales, such as myofibre bundles. Both types of models for the constitutive behaviours of myocardium are briefly summarized below.

2.2.1 Passive tension experiments of myocardium

Parameters in constitutive laws are determined by fitting them to experimental data. The prevalent approach is to choose a model that best fits the existing data, which ensures the model's descriptive capability whilst its predictive capability in general loading condition may be not sufficient. Schmid et al. [41, 42] proposed three metrics to evaluate the parameter estimation process, which are goodness of fit, determinability and variability. The goodness of fit is the ability of a model to reproduce experimental data. Determinability exhibits how sensitive material parameters are to disturbances in the data values. Variability describes the varied range of material parameters for a given constitutive law. However, it remains a great challenge to determine the exact formulations of constitutive laws and estimate their parameters according to limited experimental data.

The orthonormal basis in myocardium is composed by the mean fibre direction \mathbf{f}_0 , the sheet direction \mathbf{s}_0 along the transmural direction from endocardium to epicardium, and the sheet-normal direction \mathbf{n}_0 defined by $\mathbf{n}_0 = \mathbf{f}_0 \times \mathbf{s}_0$, as shown in Fig. 2.3 (left). At tissue level, the mean fibre direction can be identified by measuring fibre distributions on the top and bottom surfaces of a specimen when using histological analysis in experiments [4, 5], as shown in Fig. 2.3 (middle). Alternatively, DT-MRI can provide more detailed mean fibre direction at each local pixel by computing the first eigenvector of the acquired diffusion tensor, whilst it is difficult to distinguish the sheet and the sheet-normal directions by the second and third eigenvectors [43–45]. The distribution of \mathbf{f}_0 derived from DT-MRI can be mapped back to the geometry reconstructed from the same DT-MRI data. In the literature [7, 46], the sheet direction \mathbf{s}_0 is usually approximated by the transmural direction. Each material point of the myocardium can be assume as a cube with the orthogonal \mathbf{f}_0 , \mathbf{s}_0 and \mathbf{n}_0 (Fig. 2.3 (right)) when using constitutive law models.

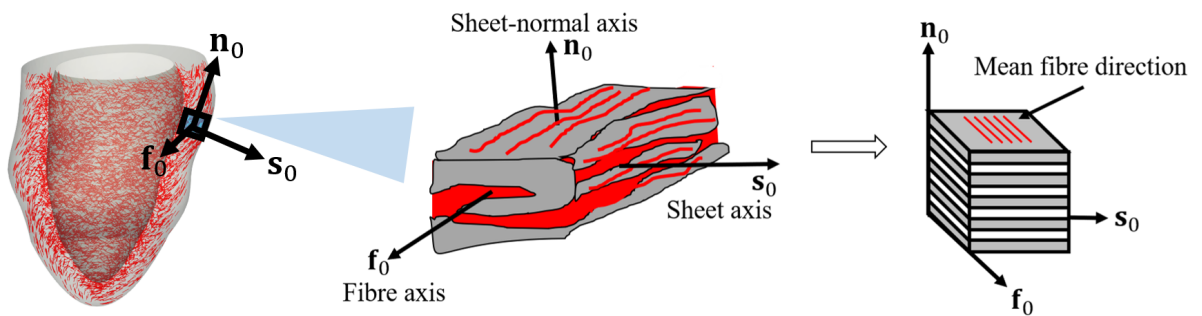


Figure 2.3: Sketch of a LV with inside fibres (red lines) and a cubic sample cut from the ventricular wall (left). The layered organization of myocytes and the collagen fibres between the sheets referred to a right-handed orthonormal coordinate system with fibre axis \mathbf{f}_0 , sheet axis \mathbf{s}_0 and sheet-normal axis \mathbf{n}_0 in the reference configuration (middle). A cube model with orthogonal \mathbf{f}_0 , \mathbf{s}_0 and \mathbf{n}_0 represents a material point of myocardium when using constitutive laws (right).

The passive tension test of myocardium is usually performed on tissue level because the setup and operation of experiments are more manageable than those on the cell level. Assuming

cut specimen of myocardium as a homogenous body, these measurable variables, such as stress and strain, can illustrate the underlying principles of the constitutive behaviour of myocardium. Typical tests include uniaxial tension, biaxial tension, and simple shear, as shown in Fig. 2.4 and existed studies are summarized in Table 2.1.

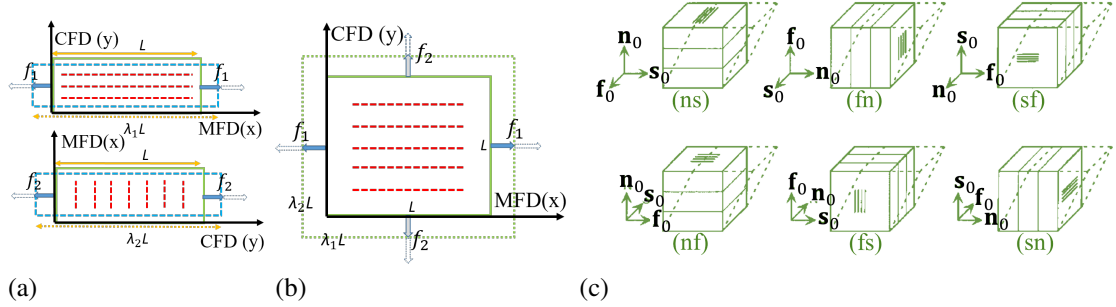


Figure 2.4: (a) Sketches of uniaxial tension tests along mean fibre direction (MFD) and cross-fibre direction (CFD), respectively. f_1 is the loading force along the MFD, and f_2 is along the CFD. L is the initial length of specimen, and λ_1 and λ_2 are stretch ratios. (b) A sketch of a sample with fibres (red dash lines), which is stretched along the two orthogonal directions (MFD and CFD) in fibre-normal plane during a biaxial test. (c) A sketch of all six possible shear modes, f_0 , s_0 and n_0 denote the fibre, sheet and normal directions in the reference configuration, respectively. (ij) refers to shear in the j direction within the ij plane, where $i \neq j \in \{f, s, n\}$.

Strong anisotropy and transmural variations of fibres (collagen fibres and myofibres) in myocardium were early found in active and passive tests of the mechanical behaviour of human myocardium [56]. Subsequent studies also report the similar conclusions. For example, the equal-biaxial tension test was performed to investigate the influences of biaxial constraint resulted by glutaraldehyde crosslinking on mechanical propitiates of bovine pericardium [50]. The anisotropic extensibility was evaluated by computing an anisotropy index according to biaxial stress-strain responses. Dokos et al. [55] performed six types of simple shear tests using specimens from porcine heart. Variations of the nonlinear response of simple shear tests along different micro-structural axes of the myocardial sample reported the orthotropic properties of myocardium. Under the same shear amount, shear along the cross-fibre direction had higher stress response, especially shear along the sheet direction producing the biggest shear stress, followed by shear cross sheet direction, while shear cross sheet-normal direction experienced the lowest shear stress. Later, Sommer et al. [4] examined the biaxial and shear properties of human myocardium, and also reported the underlying fibre structure of the ventricular wall. More biaxial tension protocols were designed by controlling biaxial strain ratios, such as 1:1, 1:0.75 and 1:0.5, and six shear modes were also performed. Existed experimental data has showed myocardium is a nonlinear, orthotropic, viscoelastic and history-dependent soft biological material that undergoes large deformations. In addition, considering their previous work [57], matching and comparing mechanical responses and inside fibre structures of myocardial samples reflected the strong correlation between inside fibre structures and mechanical properties of myocardial

Uniaxial tension test				
	Species	Size (mm)	Position	Loading
Ahmad et al. [9]	Porcine	$15 \times 5 \times 3$	LV, RV	Stress
McEvoy et al. [47]	Porcine	3×6	LV	Strain
Demer et al. [48]	Dog	$30 \times 30 \times 2$	LV	Strain
Kakaletsis et al. [49]	Sheep	$- \times - \times 8$	RV	Strain
Biaxial tension test				
	Species	Specimen size	Position	Loading
Langdon et al. [50]	Calve	$30 \times 30 \times 4.4$	Pericardium	Strain (1:1)
Sommer et al. [4]	Human	$25 \times 25 \times 2.3$	LV	Strain (1:1; 1:0.75; 1:0.5)
Ahmad et al. [9]	Porcine	$15 \times 15 \times 3$	LV, RV	Stress (1:1)
Demer et al. [48]	Dog	$30 \times 30 \times 2$	LV	Strain (1:1)
Yin et al. [51]	Canine	$40 \times 40 \times 2$	LV	Strain (1:0.5, 1:1, 1:2)
Choi et al. [52]	Canine	$40 \times 40 \times -$	Pericardium	Strain (1:1)
Hill et al. [53]	Rat	-	RV	Strain (1:1)
Vélez-Rendón et al. [54]	Rat	-	RV	Strain (1:0.5; 1:0.25; 1:1)
Simple shear test				
	Species	Specimen size	Position	Types
Dokos et al. [55]	Porcine	$3 \times 3 \times 3$	LV	(fs),(fn),(sf),(sn),(nf),(ns)
Ahmad et al. [9]	Porcine	$3 \times 3 \times 3$	LV, RV	(sf),(sn)
Sommer et al. [4]	Human	$4 \times 4 \times 4$	LV	(fs),(fn),(sf),(sn),(nf),(ns)
Kakaletsis et al. [49]	Sheep	$- \times - \times 8$	RV	(fs),(fn),(sf),(sn),(nf),(ns)
Compression test				
	Species	Specimen size	Position	Loading
McEvoy et al. [47]	Porcine	3×6	LV	Strain
Kakaletsis et al. [49]	Sheep	$- \times - \times 8$	RV	Strain

Table 2.1: Summary of passive experiments on myocardium, including uniaxial tension, biaxial tension, simple shear and confined compression. Size of specimen in $a \times b \times c$ form is length \times width \times thickness, and $a \times b$ form is length \times diameter. ($a : b$) in biaxial tension denotes loading ratios along two vertical loading orientations. (ij) in simple shear test refers to shear in the j direction within the ij plane.

samples. Recently, Ahmad et al. [9] combined uniaxial tension, biaxial tension and simple shear tests on neonatal porcine cardiac samples that were cut from the anterior and posterior free walls of LV and RV. Results not only provided a baseline for describing mechanical characteristics of immature cardiac tissue but also indicated relative changes in constitutive behaviours caused by tissue maturation. Nevertheless, the volume compressibility in passive-excised porcine myocardium was also investigated by applying both tensile and confined compression on myocardial tissue [47], quantifying the compressibility by a joint experimental-computational approach. The fundamental mechanics, microstructure, and constitutive behaviour of mature RV myocardium were studied by comprehensive mechanical tests, including uniaxial tension/compression and six simple shear modes, and histology-based microstructural analysis [49], reporting the softer RV myocardium with inside dispersed fibre structure.

2.2.2 Phenomenological constitutive models

The choice of phenomenological constitutive models depends on their included variables that quantify the deformations of myocardium. Often, kinematic invariants of the right Cauchy–Green deformation tensor \mathbf{C} are employed in SEF \mathscr{W} to represent the anisotropic properties of myocardium. In addition, after considering the physical interpretation of kinematic invariants, a single item in \mathscr{W} can reflect the mechanical properties of a constituent. SEFs can also be formulated using the components of the Green–Lagrange strain tensor \mathbf{E} that are easy to be measured or controlled in experiments. Published phenomenological SEFs are listed in Table 2.2 where both invariant-based and strain component-based models are further subdivided into transversely isotropic models that only have one fibre family and orthotropic models that include two or three fibres families.

Invariant-based models

There are many constitutive laws that use strain invariant-based orthotropic or transversely isotropic constitutive laws to characterize passive myocardial tissue. Transversely isotropic models were first proposed to account for the anisotropic mechanics of myocardium, based on the idealization that all types of fibres are always aligned and share the same mechanical properties, i.e. only one fibre family. Their mean fibre direction is identified as \mathbf{f}_0 in the reference configuration, and the corresponding SEF employs the functional form $\mathscr{W}(I_1, I_2, I_3, I_4, I_5)$, where I_1, I_2, I_3 account for isotropic ground matrix contributions and I_4, I_5 account for anisotropic fibre contributions. These variants can be derived according to the right Cauchy–Green tensor \mathbf{C} and fibre direction \mathbf{f}_0 , such as

$$I_1 = \text{tr}(\mathbf{C}), \quad I_2 = \frac{1}{2} \{ [\text{tr}(\mathbf{C})]^2 - \text{tr}(\mathbf{C}^2) \}, \quad I_3 = \det(\mathbf{C}), \quad (2.2)$$

and

$$I_4 = \mathbf{f}_0 \cdot (\mathbf{C}\mathbf{f}_0), \quad I_5 = \mathbf{f}_0 \cdot (\mathbf{C}^2\mathbf{f}_0). \quad (2.3)$$

Reduced forms $\mathscr{W}(I_1, I_4)$ are commonly used in transversely isotropic models [63–66], although the important contributions of the I_5 term in fitting to simple shear tests were demonstrated in [67]. For a reduced $\mathscr{W}(I_1, I_4)$, the Cauchy stress is

$$\boldsymbol{\sigma} = 2\mathscr{W}_1\mathbf{B} + 2\mathscr{W}_4\mathbf{f} \otimes \mathbf{f} - p\mathbf{I}, \quad (2.4)$$

where $\mathbf{f} = \mathbf{F}\mathbf{f}_0$ is the deformed fibre and $\mathscr{W}_i = \frac{\partial \mathscr{W}}{\partial I_i}$. More choices of reduced \mathscr{W} were developed, such as polynomial forms developed by Humphrey et al. [58], Fung-type exponential forms put forward by Lin & Yin [1], and additive exponential terms proposed by Kerckhoffs et al. [60] and Humphrey et al. [59].

Later, histological analysis of the microstructure of myocardium supports the existence of

Invariant-based models: $\mathcal{W}(I_i)$		
Transverse isotropic	Lin & Yin [1]	$\mathcal{W} = a_1[\exp(Q) - 1]$ $Q = a_2(I_1 - 3)^2 + a_3(I_1 - 3)(I_4 - 1) + a_4(I_4 - 1)^2$
	Humphrey et al. [58]	$\mathcal{W} = a_1(\sqrt{I_4} - 1)^2 + a_2(\sqrt{I_4} - 1)^3 + a_3(I_1 - 3) + a_4(I_1 - 3)(\sqrt{I_4} - 1) + c_5(I_1 - 3)^2$
	Humphrey & Yin [59]	$\mathcal{W} = a_1\{\exp[a_2(I_1 - 3)] - 1\} + a_3\{\exp[a_4(\sqrt{I_4} - 1)] - 1\}$
	Kerckhoffs et al. [60]	$\mathcal{W} = a_1\{\exp[a_2(I_1 - 3)^2 + a_3(I_2 - 2I_1 + 3)] - 1\} + a_4\{\exp[a_5(I_4 - 1)^2] - 1\} + a_6(I_3 - 1)^2$
Orthotropic	Schmid et al. [42]	$\mathcal{W} = \sum_{i=1,2} \frac{a_i}{2b_i} \{\exp[b_i(I_i - 3)^2] - 1\} + \sum_{i=f,s,n} \frac{a_i}{2b_i} \{\exp[b_i(I_{4i} - 1)^2] - 1\}$
	Holzapfel & Ogden [11]	$\mathcal{W} = \frac{a_1}{2b_1} \{\exp[b_1(I_1 - 3)] - 1\} + \frac{a_{fs}}{2b_{fs}} \{\exp(I_{8fs}^2) - 1\} + \sum_{i=f,s} \frac{a_i}{2b_i} \{\exp[b_i(I_{4i} - 1)^2] - 1\}$
Strain component-based models: $\mathcal{W}(E_{ij})$		
Transverse isotropic	Guccione et al. [61]	$\mathcal{W} = a_1[\exp(Q) - 1]$ $Q = 2a_2(E_{ff} + E_{ss} + E_{nn}) + a_3E_{ff}^2 + a_4(E_{nn}^2 + E_{ss}^2 + E_{sn}^2 + E_{ns}^2) + a_5(E_{sf}^2 + E_{fs}^2 + E_{fn}^2 + E_{nf}^2)$
	Yin et al. [51]	$\mathcal{W} = a_1[\exp(a_2E_{11}^n + a_3E_{22}^n) - 1]$
	Choi et al. [52]	$\mathcal{W} = a_1\{\exp(a_2E_{11}^2) + \exp(a_3E_{22}^2) + \exp(a_4E_{11}E_{22}) - 3\}$
Orthotropic	Schmid et al. [41]	$\mathcal{W} = a_{ff}[\exp(b_{ff}E_{ff}^2 - 1)] + a_{ss}[\exp(b_{ss}E_{ss}^2 - 1)] + a_{nn}[\exp(b_{nn}E_{nn}^2 - 1)] + a_{fn}\{\exp[b_{fn}(\frac{E_{fn} + E_{nf}}{2})^2] - 1\} + a_{fs}\{\exp[b_{fs}(\frac{E_{fs} + E_{sf}}{2})^2] - 1\} + a_{sn}\{\exp[b_{sn}(\frac{E_{sn} + E_{ns}}{2})^2] - 1\}$
	Costa et al. [39]	$\mathcal{W} = a_1[\exp(Q) - 1]$ $Q = a_2E_{ff}^2 + a_3E_{ss}^2 + a_4E_{nn}^2 + 2a_5E_{fs}^2E_{sf}^2 + 2a_6E_{fn}^2E_{nf}^2 + 2a_7E_{sn}^2E_{ns}^2$
	Hunter et al. [62]	$\mathcal{W} = \frac{k_{ff}E_{ff}^2}{ a_{ff} - E_{ff} ^{b_{ff}}} + \frac{k_{fn}E_{fn}^2}{ a_{fn} - E_{fn} ^{b_{fn}}} + \frac{k_{nn}E_{nn}^2}{ a_{nn} - E_{nn} ^{b_{nn}}} + \frac{k_{fs}E_{fs}^2}{ a_{fs} - E_{fs} ^{b_{fs}}} + \frac{k_{ss}E_{ss}^2}{ a_{ss} - E_{ss} ^{b_{ss}}} + \frac{k_{ns}E_{ns}^2}{ a_{ns} - E_{ns} ^{b_{ns}}}$

Table 2.2: Summary of phenomenological SEFs describing passive mechanical responses of myocardium. Please note, strain components E_{ij} with $i, j \in \{f, s, n\}$ are with respect to the $\mathbf{f}_0 - \mathbf{s}_0 - \mathbf{n}_0$ fibre system, whilst E_{11} and E_{22} refer to the two orthogonal loading orientations in the biaxial tension tests.

sheets, which consists of locally parallel myofibres and is interconnected by a spatial network of collagen fibres [31, 68, 69]. Therefore, myocardium may be not isotropic in cross-fibre planes as reported in the six simple shear tests [55]. To describe orthotropic properties of myocardium, orthonormal base is $\mathbf{f}_0 - \mathbf{s}_0 - \mathbf{n}_0$. Then, the orthotropic properties can be characterised by the material directions, such as the SEF \mathcal{W} including two more deformation invariants I_6 and I_7 to describe

mechanical characteristics along the sheet direction

$$I_6 = \mathbf{s}_0 \cdot (\mathbf{C}\mathbf{s}_0), \quad I_7 = \mathbf{s}_0 \cdot (\mathbf{C}^2\mathbf{s}_0). \quad (2.5)$$

To reduce \mathscr{W} forms, the attributes of myocardium aligning the sheet-normal direction may be integrated into the ground matrix by adjusting material parameters or expression forms. In addition, invariant I_8 is defined as [11]

$$I_8 = \mathbf{f}_0 \cdot (\mathbf{C}\mathbf{s}_0) = \mathbf{s}_0 \cdot (\mathbf{C}\mathbf{f}_0), \quad (2.6)$$

which represents the interaction between two fibre families along fibre and sheet directions, respectively.

A prominent reduced orthotropic SEF $\mathscr{W}(I_1, I_4, I_6, I_8)$ has been proposed by Holzapfel and Ogden [11] according to the simple shear data from [55]. It has one term related to the matrix responses, two terms related to the two fibres families along fibre (\mathbf{f}_0) and sheet (\mathbf{s}_0) directions, and a final term for interaction between the two families of fibres

$$\mathscr{W} = \frac{a_1}{2b_1} \{\exp[b_1(I_1 - 3)] - 1\} + \sum_{i=f,s} \frac{a_i}{2b_i} \{\exp[b_i(I_{4i} - 1)^2] - 1\} + \frac{a_{fs}}{2b_{fs}} \{\exp(b_{fs}I_{8fs}^2) - 1\}, \quad (2.7)$$

where $a_1, b_1, a_f, b_f, a_s, b_s, a_{fs}, b_{fs}$ are material parameters.

The Holzapfel and Ogden (HO) model and its variation have been widely used in the cardiac modelling community, such as the LivingHeart Project [70]. Goktepe et al. [71] developed a general constitutive and algorithmic approach for the computational modelling of passive myocardium using the HO model, which is embedded in a non-linear FE method. Wang et al. [7] studied the fibre orientation on LV diastolic mechanics using the HO model and further extended it to include residual stresses [72]. Gao et al. [2] implemented the HO model into an immersed boundary framework combined with FE to study LV biomechanics both in diastole and systole. Simplified forms of the HO model were also used by Asner et al. [73] with personalized ventricular dynamics derived from in vivo data. General structural tensors accounting for collagen fibre dispersion were introduced by Eriksson et al. [21], followed by Melnik et al. [74] recent extension, accounting for fibre dispersion in the coupling term between the fibre and sheet directions. Inverse estimation of unknown parameters in the HO model from in vivo data was first investigated by Gao et al. [13], and later by Nikou et al. [75], and by Palit et al. [76]. The HO model has also been applied to simulate various heart diseases, such as myocardial infarction [2, 70].

No study has previously investigated the descriptive and predictive capability of HO-type SEFs. A competent constitutive law should be able to describe as many deformation modes (uniaxial, biaxial, simple shear, etc.) as possible in qualitative point and then from quantitative point with acceptable errors of simulation with respect to the experimental data [77], and with least terms. Mechanical properties of myocardium are traditionally measured by a single series

of either uniaxial [56], biaxial tests [48], or simple shear deformations [55], despite it being demonstrated that combined biaxial data (with different loading protocols) and simple shear data (with various loading directions) are required to adequately capture the tissue's direction-dependent nonlinear response [11]. For example, Holzapfel et al. [11], and Schmid et al. [42] both only used simple shear data of [55] to demonstrate the good descriptive capability of selected constitutive laws. Only recently Sommer et al. [4] have performed both biaxial and shear tests on similar human myocardial samples, whilst Ahmad et al. [9] reported their experiments on neonatal porcine myocardium samples with uniaxial, biaxial and shear tests.

Fung-type models

Another widely-used approach employs strain components directly or strain invariants when developing such constitutive laws. For instance, Guccione et al. [61] used a transverse isotropic exponential Fung-type hyperelastic material model to characterize the equatorial region of the canine LV, in which the SEF consists of six strain components. Based on an idealized cylindrical coordinate system consisting of fibre (\mathbf{f}_0), cross-fibre (\mathbf{c}_0) and radial (\mathbf{r}_0) axes, it assumes the same constitutive behaviour of myocardium aligning \mathbf{c}_0 and \mathbf{r}_0 directions and accounts for their coupling contributions. This model has been extensively used in FE simulations because of its highly tractable implementation.

Another simple Fung-type SEF is designed to describe biaxial behaviour of myocardium and only includes two axial strain components [51] along fibre and cross-fibre directions, respectively. This form facilitates identifying material parameters whilst limiting the predictive capability for tissue behaviour as debated in [78]. Moreover, it did not consider the interaction between two perpendicular directions, which played an important role in reproducing biaxial mechanical responses of the RV myocardium [53].

Following subsequent evidence supporting the orthotropic mechanical responses along local orthotropic material axes, Hunter et al. [62] firstly proposed the so-called pole-zero model, a spatial orthotropic strain component-based model based on the orthogonal material base $\mathbf{f}_0 - \mathbf{s}_0 - \mathbf{n}_0$. It contains six strain components, the strains along material axes and shears within material planes. Corresponding eighteen parameters can be divided into three categories: the limiting strains or poles representing physical properties of tissue, the parameters describing the curvature of stress-strain relationships, and the parameters weighting contributions of each term to total SEF. However, excepting equi-biaxial tension tests, it was not suitable to describe or predict other types of deformation as mentioned in [79].

In a followed study, Costa et al. [39] extended the transversely isotropic Fung-type relation to accounting for the orthotropy. Based on $\mathbf{f}_0 - \mathbf{s}_0 - \mathbf{n}_0$ coordinate system, it separates the attributes along the sheet and sheet-normal directions that governs the anisotropy in the cross-fibre plane. Moreover, the updated model includes shear stiffness between any two adjacent material planes whilst ignoring the coupling terms between any two orthogonal directions.

Later, to decouple the material parameters from the single exponential function in Costa et al. [39], separated Funy-type law was proposed by Schmid et al. [41], which was in the additive form of six exponential functions of strain components, such as $a[\exp(bE_{ij}^2) - 1]$. There were also no coupling terms to account for interactive behaviours between material axes. Nevertheless, to exhibit strong stiffness at large stretches and avoid an infinite slope in pole-zero model, replacing $a[\exp(bE_{ij}^2) - 1]$ by $a\text{IntTan}(bE_{ij}^2)$ was also investigated, where $\text{IntTan}(x)$ is the first five terms of the Taylor series expansion of the indefinite integral of $\text{Tan}(x)$ [41].

2.2.3 Micro-structurally informed models

The phenomenological models quantitatively describe myocardial constitutive behaviours whilst failing to account for its compositional material and structural properties. Therefore, the micro-mechanical mechanisms are unlikely derived from these models, which involve functions and architectures of myofibres and collagen fibres, as well as their coupling, under physiological or pathological conditions.

Micro-structurally informed models attempt to bridge the constitutive mechanical behaviour of myocardium and the microstructural mechanisms of myocardial constituents, using compositional SEFs. In idealization, myocardium is divided into a continuous ground matrix and embedded myofibres and collagen fibres. Hence, total SEF \mathcal{W} is usually the sum of their contributions [80], such as

$$\mathcal{W} = \phi^g \mathcal{W}^g + \phi^m \mathcal{W}^m + \phi^c \mathcal{W}^c + \mathcal{W}^{\text{int}}, \quad (2.8)$$

where \mathcal{W}^i is constitutive laws to describe mechanical characteristics of ground matrix (g), myofibre (m), collagen fibres (c), and the interaction (int) between myofibre and collagen fibres. ϕ^i is volume fractions or mass for each constituent. Please note that no volume fraction is assigned for the last interaction term because of unavailable information. Thus, Avazmohammad et al. [6, 80] assumed the \mathcal{W}^{int} absorbed the fraction value and were still useful to estimate the interactive contribution to the total energy.

To estimate effective contribution for each type of fibre, one approach employs the angular integration of each fibre's contribution following a spatial distribution map $\rho(\mathbf{M})$, where \mathbf{M} is a unit vector representing fibre (myofibre and collagen fibre) orientation in the reference configuration. The energy function for each fibre is usually expressed by fibre stretch, such as $w^f(I^M)$ where $I^M = \mathbf{M} \cdot (\mathbf{C}\mathbf{M})$. Hence, the total fibre strain energy is

$$\mathcal{W}^f = \int_{\mathbb{S}} \rho(\mathbf{M}) w^f(I^M) dS, \quad (2.9)$$

where \mathbb{S} is the surface of the unit sphere in three dimensions. For the case of collagen fibres, they are crimped in the stress-free state and do not produce force until fully straightened. Thus, the actual deformation contributing to energy function in an individual fibre is $I^{M*} = I^M / \lambda_s^2$ where λ_s is compression-tension switch stretch. The gradual recruitment of undulated collagen fibres

can be accounted by a truncated function $D(\lambda_s)$. Finally, total energy of collagen fibres can be expressed as

$$\mathcal{W}^f = \int_{\mathcal{S}} \rho(\mathbf{M}) \int_1^{\sqrt{I^M}} D(\lambda) w^f\left(\frac{I^M}{\lambda_s^2}\right) d\lambda dS, \quad (2.10)$$

where λ is the integral variable in fibre stretch space. Some representative structural models are summarized in Table. 2.3.

Lanir et al. [83] developed a general multi-axial theory for the constitutive relations in fibrous connective tissues while considering micro-structures and thermodynamics. Then Horowitz et al. [81] proposed a model that illustrated the distributions of myofibres and collage fibres, in which collagen fibres symmetrically surround and connect adjacent myofibres. They are both expressed in a spherical coordinate system and ascribed linear stress-strain relations.

Humphrey & Yin [82] extended their previous phenomenological transverse isotropic model [59] to a simple structural model by treating myocardium as a layered composite from endocardium to epicardium and assuming transverse isotropy in each layer with the mean fibre direction. It avoids the definition for fibre distribution and consideration of gradual recruitment of collagen fibres. Total fibre energy contributions are the integration of layered fibre energy along ventricular wall thickness. Later, in this concept, Sacks & Chuong [84] developed a similar constitutive relation for passive RVFW that replaces fibre energy function in each layer from exponential form [59] to polynomial form [85].

Three orthogonal fibre-sheet-normal families fibres were considered by Hunter et al. [62] who used the pole-zero descriptor $(aE_n^2/(b - E_n)^c)$ to estimate strain energy of all families fibres. Each family fibre has a Gaussian distribution around its mean fibre direction in the fibrous connective tissue. Total fibre energy is the sum of the contributions of the three families fibres where the effect of gradual fibre recruitment is ignored.

Recently, Krishnamurthy et al. [86] proposed a multi-scale model that elaborated cross-bridge and myofilament lattice structure and investigated the effect of fibre dispersion on myocardial contractility. Sacks et al. [87] developed a rigorous full structural model (i.e. explicitly incorporating various features of the collagen fibre architecture) for exogenously cross-linked soft tissues, which made an extension to the collagenous structural constitutive model, meaning the uncross-linked collagen fibre responses could be mapped to the cross-linked configuration. Based on Sacks' study, Avazmohammadi et al. [6] proposed a fibre-level constitutive model for the passive mechanical behaviour of the RVFW, which explicitly separated the mechanical contributions of myocytes and collagen fibre ensembles whilst accounting for their mechanical interactions. Xi et al. [25] only discussed the collagen fibre distribution with gradual recruitment, whilst the energy functions of ground matrix and myofibre were in phenomenological form. The volume fraction of each constituent is denoted before the respective term's SEF that only illustrates the compositional constitutive behaviours. Li et al. [88] developed a discrete approach that divides the continuous fibre space into finite elementary areas and assumes each area

associating one uniform fibre bundle, i.e. representative fibre. It contributes to the total stress weighted by its corresponding density distribution determined from the corresponding distribu-

General expression	Reference
$\mathcal{W} = \mathcal{W}^m + \mathcal{W}^c$ $\mathcal{W}^m = \int_{-\pi/24}^{\pi/24} \rho^m w^{m*} d\alpha,$ $\mathcal{W}^c = \int_{-\pi/24}^{\pi/24} \int_0^{2\pi} \int_0^{\rho^i} \rho^c w^{c*} J d\phi d\theta d\alpha$ $w^i = a_i \varepsilon^i, \quad D^i(x) = \frac{1}{\sqrt{2\pi\sigma^i}} \exp\left[-\frac{(m^i-x)^2}{2(\sigma^i)^2}\right]$ $w^{i*} = \int_0^{\varepsilon^i} D^i(x) w^i(x) dx, \quad i = m, c \text{ and } \varepsilon \text{ is the fibre strain}$	Horowitz et al. [81]
$\mathcal{W} = \mathcal{W}^g + \mathcal{W}^f$ $\mathcal{W}^g = a_1 \{\exp[b_1(I_1 - 3)] - 1\}, \quad \mathcal{W}^f = \int_{r_{\text{endo}}}^{r_{\text{epi}}} w dr$ $w = a_2 \{\exp[b_2(\sqrt{I_4} - 1)^2] - 1\}$	Humphrey & Yin [82]
$\mathcal{W} = \mathcal{W}^f + \mathcal{W}^s + \mathcal{W}^n$ $\mathcal{W}^f = \int_{-\pi/2}^{\pi/2} \rho^f \frac{a_f E_f^2}{(b_f - E_f)^{c_f}} d\theta, \quad \mathcal{W}^s = \int_{-\pi/2}^{\pi/2} \rho^s \frac{a_s E_s^2}{(b_s - E_s)^{c_s}} d\theta,$ $\mathcal{W}^n = \int_0^{2\pi} \int_0^{\pi/2} \rho^n \frac{a_n E_n^2}{(b_n - E_n)^{c_n}} d\phi d\theta,$ $E_i = \frac{1}{2}(I_{4i} - 1) \text{ where } i = f, s, n.$ $\rho^f(\theta) = \frac{1}{\sqrt{2\pi\sigma^f}} \exp\left[-\frac{\theta^2}{2(\sigma^f)^2}\right], \quad \rho^s(\theta) = \frac{1}{\sqrt{2\pi\sigma^s}} \exp\left[-\frac{\theta^2}{2(\sigma^s)^2}\right]$ $\rho^n(\phi, \theta) = \frac{1}{2\pi\sigma^{n1}\sigma^{n2}} \exp\left[-\frac{1}{2}\left(\frac{\phi^2}{(\sigma^{n1})^2} + \frac{\theta^2}{(\sigma^{n2})^2}\right)\right]$	Hunter et al. [62]
$\mathcal{W} = \phi^g \mathcal{W}^g + \phi^m \mathcal{W}^m + \phi^c \mathcal{W}^c + \phi^i \mathcal{W}^i$ $\mathcal{W}^g = \frac{a_g}{2} (I_1 - 3),$ $\mathcal{W}^m = \frac{1}{H} \int_0^H \int_{-\pi/2}^{\pi/2} \rho^m(\theta, z) w^m(I^m) d\theta dz,$ $\mathcal{W}^c = \frac{1}{H} \int_0^H \int_{-\pi/2}^{\pi/2} \rho^c(\theta, z) w^{c*}(I^c) d\theta dz,$ $\mathcal{W}^i = \frac{1}{H} \int_0^H \int_{-\pi/2}^{\pi/2} \int_{-\pi/2}^{\pi/2} \rho^m \rho^c w^{i*}(I^m, I^c) d\theta^m d\theta^c dz,$ $w^m = \frac{a_1^m}{2a_2^m} \{\exp[a_2^m(\sqrt{I^m} - 1)^2] - 1\},$ $w^c = \frac{a^c}{2} (\sqrt{I^c}/\lambda_s - 1)^2, \quad w^{c*} = \int_{\lambda_{lb}}^{\lambda_{ub}} D(\lambda_s) w^c(I^c) d\lambda_s,$ $w^i = \frac{k_1}{2k_2} \{\exp[k_2(I^m + I^c/\lambda_s^2 - 2)] - [k_2(I^c/\lambda_s^2 - 1) + 1] \exp[k_2(I^m - 1)]\},$ $w^{i*} = \int_{\lambda_{lb}}^{\lambda_{ub}} D(\lambda_s) w^i(I^m, I^c) d\lambda_s,$ $D(\lambda_s) = \frac{y^{\alpha-1}(1-y)^{\beta-1}}{B(\alpha, \beta)(\lambda_{ub} - \lambda_{lb})}.$	Avazmohammadi et al. [6]
$\mathcal{W} = \phi^g \mathcal{W}^g + \phi^m \mathcal{W}^m + \phi^c \mathcal{W}^c,$ $\mathcal{W}^g = \frac{a_1}{2} (I_1 - 3), \quad \mathcal{W}^m = a_2 \{\exp[a_3(\sqrt{I^m} - 1)^2] - 1\},$ $\mathcal{W}^c = \frac{a_4}{2} \int_0^{2\pi} \int_0^{\pi} \int_0^{\varepsilon_c} D(x) \frac{\varepsilon_c - x}{1+2x} \rho(\theta, \phi) dx d\phi d\theta,$ $D(x) = \frac{1}{a_5} \frac{1}{\sqrt{2\pi\sigma_c}} \exp\left[-\frac{(m_c - x)^2}{2\sigma_c^2}\right].$	Xi et al. [25]
$\mathcal{W} = \mathcal{W}^g + \mathcal{W}^f,$ $\mathcal{W}^g = \frac{a_1}{2} (I_1 - 3), \quad \mathcal{W}^f = \sum_{n=1}^m \rho_n w_n,$ $w_n = \frac{a_2}{2b_3} \{\exp[b_3(I_c/\lambda_s^2 - 1)^2] - 1\}.$	Li et al. [17]

Table 2.3: Summary of structurally informed models for describing passive mechanical responses of myocardium

tion function. The energy function for each representative fibre is an invariant-based exponential function.

2.3 Active contraction models of myocardium

Cardiac contraction is a synergistic reaction process among different components. Briefly, the electrical signals produced by self-excitable cells in sinoatrial node make up voltage waves travelling along Purkinje fibres. Varying potential in cardiac cells changes concentrations of calcium, potassium, sodium, etc., which control the shortening of myocytes then resulting in contraction of heart. Finally, blood with rich oxygen is pumped through arteries into all tissues and organs in body. Hence, any disorder in the above cooperation might threaten life. However, due to the complexity of heart, especially due to the difficulties associated with in vivo experiments, cognition to functions of heart is a difficult task.

Active contraction in myocardium is usually simulated by the cardiac electromechanics that mainly includes three parts: action potential model based on a system of ordinary differential equations in terms of ion concentrations, reaction-diffusion model to describe the propagation of electrical excitation, and the continuum mechanics model to predict the deformation of myocardium.

Currently, there are three common approaches to incorporate the active tension into the total mechanics of myocardium: active stress approach, active strain approach and Hill's three-element approach. Their respective definitions can be demonstrated by the sketch with different arrangements of passive elements and active contractile elements, as shown in Fig. 2.5.

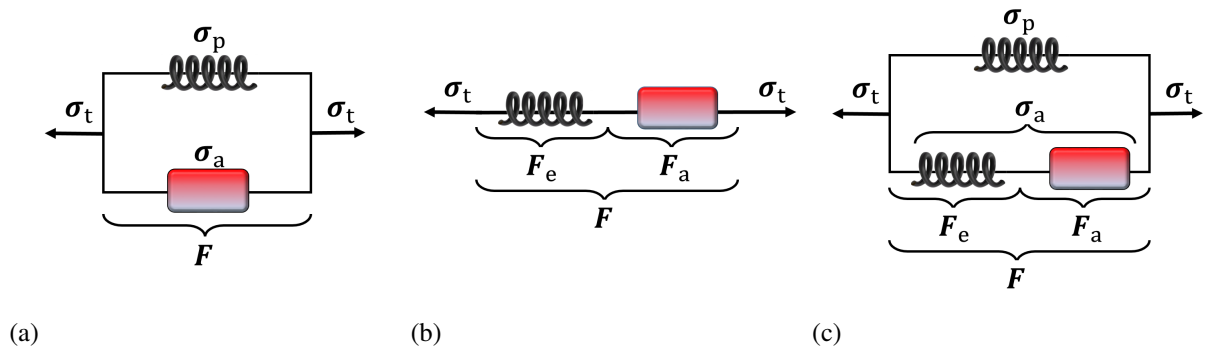


Figure 2.5: Sketch of active contraction models with different arrangements of passive elements (spring) and active contractile elements (red box). (a) Active stress model consists of a passive spring element in parallel with a contractile element. (b) Active strain model is composed of a contractile element in series with a passive spring element. (c) Hill's three-element model also has two parallel branches, in which one branch only has a passive spring element and another branch has a contractile element in series with a passive element. \mathbf{F} denotes total deformation gradient tensor and is decomposed into elastic tensor (\mathbf{F}_e) and active strain tensor (\mathbf{F}_a). σ_t is total Cauchy stress, σ_a is active stress, and σ_p is passive stress.

2.3.1 Active stress approach

The prevalent approach to account for active tension in total stress is to directly add the active stress generated by contraction of myocardium to the passive stress, as demonstrated in Fig. 2.5(a) where the passive spring element is parallel with the active contractile element. In this model, both active and passive elements share the same deformation \mathbf{F} . The additive form of total Cauchy stress (σ_t) can be expressed as

$$\begin{aligned}\sigma_t &= \sigma_p + \sigma_a, \\ \sigma_p &= J^{-1} \mathbf{F} \frac{\partial \mathcal{W}_p}{\partial \mathbf{F}}, \\ \sigma_a &= n_f T_a \hat{\mathbf{f}} \otimes \hat{\mathbf{f}} + n_s T_a \hat{\mathbf{s}} \otimes \hat{\mathbf{s}} + n_n T_a \hat{\mathbf{n}} \otimes \hat{\mathbf{n}},\end{aligned}\tag{2.11}$$

where passive stress σ_p is derived from a SEF as reviewed in the section 2.2, active stress σ_a consists of total active tension T_a , unit deformed fibre orientation vectors $\hat{\mathbf{f}}$, $\hat{\mathbf{s}}$ and $\hat{\mathbf{n}}$, and fractions along each direction n_f , n_s , and n_n . T_a is the active tension generated along the myofibre direction, which can be described by a time-varying elastance model [89–91]. For instance, $n_f = 1$ and $n_s = n_n = 0$ indicates active stress only along myofibre direction [2, 46], and non-zero n_s and n_n denote the dispersed active tension when considering fibre dispersion around the mean fibre direction [14, 15]. In addition, some studies used non-unit deformed fibre vectors directly such as $\sigma_a = T_a \mathbf{f} \otimes \mathbf{f}$ [91].

Easy implementation and abundant experimental data for the parameters calibration make active stress approach popular in personalized cardiac modelling [2, 21, 91, 92]. However, it hard to obtain a simple expression of SEF due to the complex forms of the active tension function, in particular when it is modelled as a set of ordinary differential equations [93–95]. Coupling two stress tensors from different concepts also may result in the limitation on mathematical convexity [96].

2.3.2 Active strain approach

Active strain approach is inspired by the theories of plasticity, tissue growth and morphogenesis. Kondaurov and Nikitin [97] firstly proposed this framework and then was developed by Taber [98] and others [99–102]. The key is the multiplicative decomposition of the deformation gradient tensor $\mathbf{F} = \mathbf{F}_e \mathbf{F}_a$ (Fig. 2.5 (b)). \mathbf{F}_a is active strain contribution that stores no elastic energy and is usually formulated via prescribed myocardial contraction that can be fictitiously imagined as plastic distortion of tissue. The elastic deformation \mathbf{F}_e , undermined by \mathbf{F}_a , accounts for the elastic energy and preserves the compatibility of the soft tissue. Finally, the derivation of the original passive SEF with respect to the \mathbf{F}_e is used to estimate total stress [101–103], in which active and passive stresses are inseparable.

The total Cauchy stress in this case is computed by

$$\boldsymbol{\sigma}_t = J_{\mathbf{F}_e}^{-1} \mathbf{F}_e \frac{\partial \mathcal{W}_p(\mathbf{F}_e)}{\partial \mathbf{F}_e}, \quad (2.12)$$

where $\mathbf{F}_e = \mathbf{F} \mathbf{F}_a^{-1}$, and \mathbf{F}_a is usually defined in the reference configuration, such as [101]

$$\mathbf{F}_a = \mathbf{I} + \gamma_f \mathbf{f}_0 \otimes \mathbf{f}_0 + \gamma_s \mathbf{s}_0 \otimes \mathbf{s}_0 + \gamma_n \mathbf{n}_0 \otimes \mathbf{n}_0, \quad (2.13)$$

where γ_f , γ_s , and γ_n are contractile strains along respective axial directions. For them, a prescribed time varying curve is easy to be implemented [101, 104], and more physiological and complex approaches have been proposed to calculate those by cardiac potential from cell level [103, 105, 106].

2.3.3 Hill's three-element approach

The hybrid approach [105] is inspired by the classic Hill's three-element model [107], which combines the active stress and active strain approaches, as shown in Fig. 2.5 (c). There are two parallel branches to denote passive and active responses, respectively. The parallel branch with only one passive spring element accounts for all the passive response of the myocardium. The contractile element in series with a passive element in another parallel branch characterises the mechanics of myocardium contraction. This approach keeps the advantages in mathematical convexity whilst separating active and passive contributions in total stress.

Same as the active stress approach, total stress is the sum of active and passive components. Passive stress is derived from passive SEF (\mathcal{W}_p) with respect to total deformation gradient tensor \mathbf{F} . The active stress tensor is calculated by derivation of additive active SEF (\mathcal{W}_a) with respect to \mathbf{F}_e that is determined by \mathbf{F}_a using the active strain approach. Thus, total Cauchy stress is expressed as

$$\begin{aligned} \boldsymbol{\sigma}_t &= \boldsymbol{\sigma}_p + \boldsymbol{\sigma}_a, \\ \boldsymbol{\sigma}_p &= J^{-1} \mathbf{F} \frac{\partial \mathcal{W}_p}{\partial \mathbf{F}}, \\ \boldsymbol{\sigma}_a &= J_{\mathbf{F}_e}^{-1} \mathbf{F}_e \frac{\partial \mathcal{W}_a(\mathbf{F}_e)}{\partial \mathbf{F}_e}, \end{aligned} \quad (2.14)$$

where $\mathbf{F}_e = \mathbf{F} \mathbf{F}_a^{-1}$. Three types of active contraction models are summarized in Table 2.4.

Through reviewing the studies employing the active strain approach, different assumptions are made to describe active strain tensor. Transversely isotropic models with the determinant of \mathbf{F}_a being one [101, 110] cannot produce physiological ejection fraction (EF) and wall thickening with myofibre contraction in the physiological range. However, the transversely isotropic model with contraction only occurring along myofibre orientation [96] is able to overcome the above

Active stress model	
General expression	Reference
$\boldsymbol{\sigma}_a = n_f T_a \hat{\mathbf{f}} \otimes \hat{\mathbf{f}} + n_s T_a \hat{\mathbf{s}} \otimes \hat{\mathbf{s}} + n_n T_a \hat{\mathbf{n}} \otimes \hat{\mathbf{n}}$	Guan et al. [15]
$\boldsymbol{\sigma}_a = n_f T_a \hat{\mathbf{f}} \otimes \hat{\mathbf{f}}$	Gao et al. [2]
$\boldsymbol{\sigma}_a = T_a \mathbf{f} \otimes \mathbf{f} + n_s T_a \mathbf{s} \otimes \mathbf{s}$	Sack et al. [91], Genet et al. [92]
$\boldsymbol{\sigma}_a = S_a \left(\frac{k_f}{1-2k_f} \mathbf{I} + \frac{1-3k_f}{1-2k_f} \hat{\mathbf{f}} \otimes \hat{\mathbf{f}} \right)$	Eriksson et al. [21]
Active strain model	
General expression	Reference
$\mathbf{F}_a = \mathbf{I} + \gamma_f \mathbf{f}_0 \otimes \mathbf{f}_0 + \gamma_s \mathbf{s}_0 \otimes \mathbf{s}_0 + \gamma_n \mathbf{n}_0 \otimes \mathbf{n}_0$	Rossi et al. [108], Quarteroni et al. [103], Barbarotta et al. [101], Göktepe et al. [105]
$\mathbf{F}_a = f_1 \mathbf{I} + f_2 \int_{\omega} \cos^2 \beta \mathbf{A} \rho(\mathbf{a}) d\omega$	Pandolfi et al. [109]
$\mathbf{F}_a = \gamma_1 \mathbf{f}_0 \otimes \mathbf{f}_0 + \gamma_2 (\mathbf{I} - \mathbf{f}_0 \otimes \mathbf{f}_0)$	Barbarotta et al. [101], Gjerald et al. [110], Giantesio et al. [104]
$\mathbf{F}_a = \mathbf{I} - \gamma \mathbf{f}_0 \otimes \mathbf{f}_0$	Ambrosi et al. [96], Cansız et al. [106]
Hill's three-element model	
General expression	Reference
$\mathcal{W}_a = \frac{1}{2} \eta (I_{4f}^e - 1)^2$	Göktepe et al. [105]

Table 2.4: Summary of active contraction models. The active stress expressions listed in active stress model, the constructions of active strain tensor are expressed in active strain model, and the active SEF is showed in Hill's three-element model.

limitations because it does not change elastic properties in transverse orientations. Alternatively, the orthotropic model [108] can also capture the physiological wall thickening in cardiac systole by defining different contraction amounts along fibre and sheet directions. It assumes the contraction of myofibre pushes the enlargement along sheet direction that forces rearrangement of collagen sheet, thus increasing wall thickness. The multiplicative decomposition of deformation gradient tensor signifies the sequential order between active distortion and elastic deformation. In fact, however, active contraction does produce force simultaneously with elastic deformation as exhibited in an isometric contraction experiment of muscle [111].

2.4 Fibre structure in modelling myocardium

2.4.1 Construction of fibre structure

The spatial architecture of myofibres plays a central role in electrical propagation, myocardial expansion and contraction [112]. Early studies relied on fibre dissections and histological slices [113] to determine local fibre structure. Currently, the cardiac fibres can be imaged via DT-MRI [43] that allows a direct description of the 3D myofibre architecture. To reconstruct myofibres in computational models, two different approaches have been developed. One is directly mapping myofibres from ex/in vivo datasets to the models, i.e. reconstructing directly from DT-MRI [91], or using atlas-based methods to warp DT-MRI data into different models [44], as

shown in Fig. 2.6 (a). The other approach is the rule-based method (RBM), in which myofibres rotates from endocardium to epicardium with prescribed angles concerning the circumferential direction (Fig. 2.6 (b)), varying linearly across the wall in most of the studies [7, 114, 115].

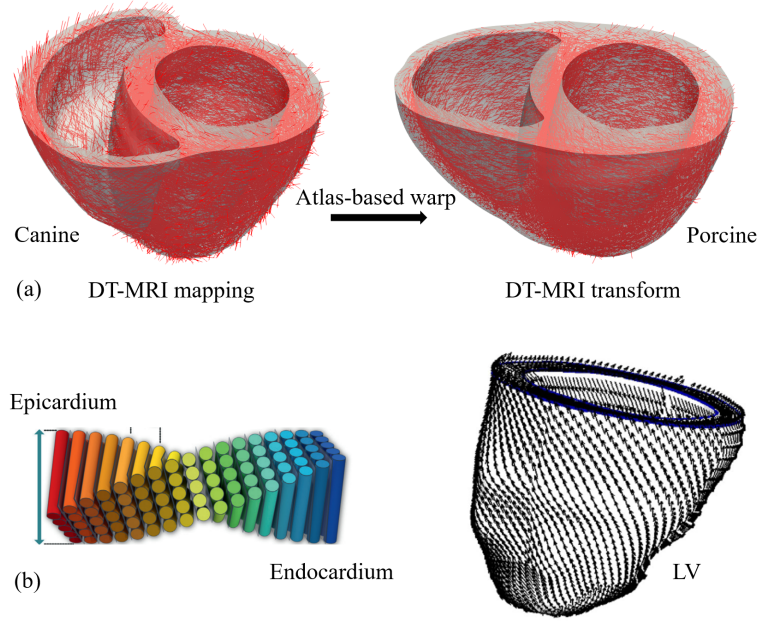


Figure 2.6: (a) Bi-ventricular canine model is reconstructed directly from DT-MRI and inside fibre structure (red lines) is mapped from same DT-MRI data. Then, it warps into porcine heart by atlas-based methods, together with inside fibre structure. (b) Definition of linear rotation from epicardium to endocardium and its application in single LV model with rotation angles from endocardium (60°) to epicardium (-60°). Single LV graph is cited from Wang et al. [7] with the permission to be reprinted.

One key step in RBM is to parameterise wall thickness (\bar{e}) in order to assign local fibre angles, from $\bar{e} = 0$ at endocardial surface to $\bar{e} = 1$ at epicardial surface. With measured fibre angles at endocardium θ^{endo} and epicardium θ^{epi} , the local fibre angle can then be assigned by varying linearly or nonlinearly with \bar{e} . For example, the linear case, fibre angle (θ) at thickness \bar{e} is

$$\theta = (1 - \bar{e})\theta^{\text{endo}} + \bar{e}\theta^{\text{epi}}. \quad (2.15)$$

Bayer et al. [116] proposed a Laplace-Dirichlet RBM, in which the circumferential-radial-longitudinal directions and normalized wall thickness are determined by solving a series of Laplace equations. They demonstrated that the Laplace-Dirichlet rule-based fibre could achieve almost identical electrical activation patterns in a whole heart model as a DT-MRI based model. Additionally, regionally-varied RBM has been developed to take into account spatial variations [21], in which myofibre rotation angles are regionally dependent.

Three dimensional FE mechanics models of the heart have been used extensively to investigate the role of myofibre architecture in cardiac function under normal and abnormal function,

including ischaemia, ventricular pacing, myofibre disarray, and heart failure. For example, by using a rule-based approach for myofibre reconstruction in an LV model, Wang et al. [7] found that changes in myofibre rotation angle can dramatically affect the stress and strain distributions during diastole. Using a bi-ventricular model, Patil et al. [117] also demonstrated that changes in myofibre angle could significantly affect myofibre stress-strain distribution within the LV wall in diastole. Pluijmert et al. [118] found that a change of 8° in myofibre orientation along transmural direction can cause a considerable increase in cardiac pump work (17%). In a recent study, Gil et al. [119] compared three different myofibre architectures in an electromechanics bi-ventricular model, one was from a DT-MRI dataset [120], the other two were reconstructed using a rule-based approach [114] with histologically measured myofibre angles [121]. Their results showed that the model with realistic myofibre structure from DT-MRI produces functional scores much closer to healthy ranges than rule-based approaches. Using the polynomial chaos expansion method, Rodriguez-Cantano et al. [122] studied the uncertainty in myofibre orientation and demonstrated that a realistic myofibre structure is necessary for a personalized cardiac model, such as DT-MRI acquired myofibres.

2.4.2 Consideration of fibre dispersion

Micro-structurally informed constitutive modelling in soft tissue has attracted tremendous interest in this area since its introduction in the 1970s [123]. With advanced imaging techniques, such as DT-MRI, detailed 3D fibre distribution for the whole organ, such as the heart, can be acquired in ex/in vivo [5, 30]. Existing measurements have shown that fibres in myocardium are dispersed in space with a predominant mean fibre direction [4, 5], as the measurement in Fig. 2.7 (a) and a sketch of probability distribution in Fig. 2.7 (b). Constitutive modelling of soft tissue with dispersed fibres has found that dispersed collagen fibres can significantly affect the overall mechanical response of the soft tissue [20, 124].

To incorporate fibre dispersion into its constitutive law, one way is to assume a probability density function (PDF) concerning the mean fibre direction (\mathbf{f}_0), as shown in Fig. 2.7 (c) where the spatial disperse fibre \mathbf{M} is determined by two polar angles Θ and Φ , such as

$$\mathbf{M}(\Theta, \Phi) = \sin \Theta \cos \Phi \mathbf{s}_0 + \sin \Theta \sin \Phi \mathbf{n}_0 + \cos \Theta \mathbf{f}_0, \quad (2.16)$$

where Θ is the angle between \mathbf{f}_0 and \mathbf{M} , and Φ is the angle between \mathbf{s}_0 and the projected vector of \mathbf{M} in the \mathbf{s}_0 - \mathbf{n}_0 plane. Fibre dispersion is described by PDF $\rho(\Theta, \Phi)$, and

$$\int_{\mathbb{S}} \rho(\Theta, \Phi) dS = 1 \quad (2.17)$$

where \mathbb{S} is the surface of the unit spherical fibre dispersion domain. Four illustrative fibre dispersion cases are listed in Fig. 2.7 (d). Then the SEF for the tissue can be the summarization of

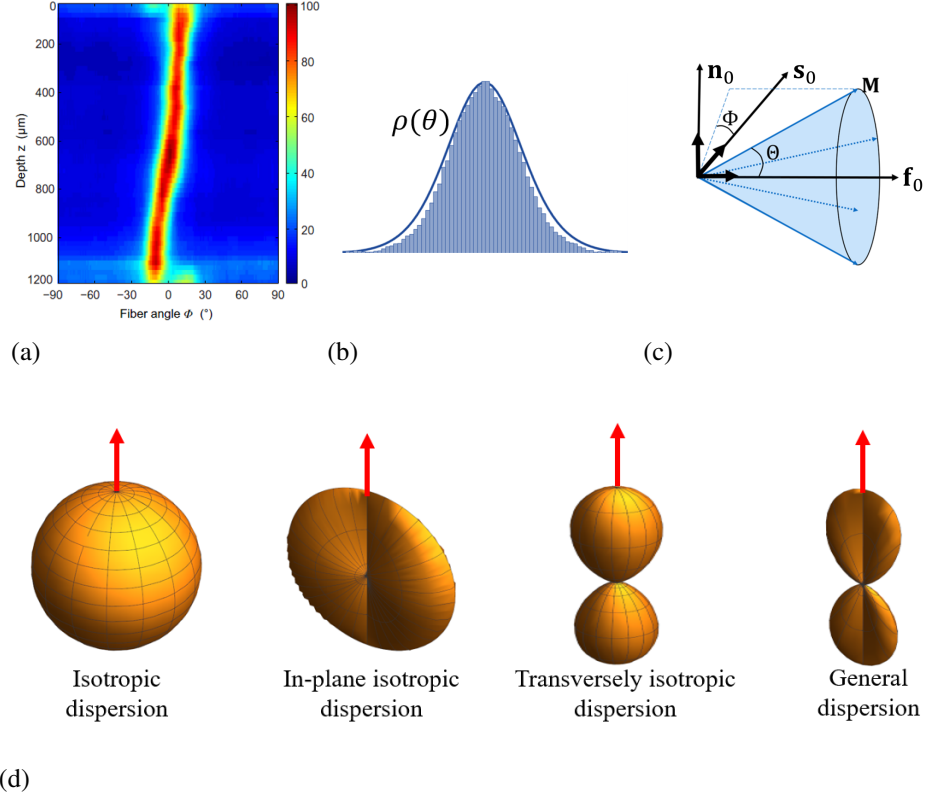


Figure 2.7: Fibre dispersion in measurement and its definition in mathematical model. (a) Measured intensity of fiber orientations through-the-thickness from Sommer et al. [4], showing the existence of fibre dispersion around mean fibre direction. The measurable intensity can be expressed by PDF $\rho(\Theta)$ (b), and spatial disperse fibre in mathematical model can be denoted by two polar angles Θ and Φ (c), and its distribution is controlled by the PDF. (d) Four representative fibre dispersion distributions around the mean fibre direction (red arrow), from the left to the right is respective isotropic dispersion, in-plane isotropic dispersion, transversely isotropic dispersion, and general dispersion.

each fibre contribution along with other constituents.

Broadly speaking, there are two approaches for counting collagen fibre contributions: (1) the angular integration (AI) approach [123], in which the stress from each fibre is added together, that is

$$\boldsymbol{\sigma} = J^{-1} \int_{\mathbb{S}} \rho(\Theta, \Phi) \mathbf{F} \frac{\partial \mathcal{W}(\Theta, \Phi)}{\partial \mathbf{F}} dS, \quad (2.18)$$

where $\mathcal{W}(\Theta, \Phi)$ is the SEF with respect to dispersed fibres, and (2) the other one is the generalised structure tensor (GST) approach, which was first proposed by Gasser et al. [20]. By assuming a rotational symmetry for the fibre distribution around the mean fibre direction, Gasser et al. [20] derived a κ -model based on a modified squared mean fibre stretch, that is

$$\mathbf{H} = \int_{\mathbb{S}} \rho(\Theta, \Phi) \mathbf{M} \otimes \mathbf{M} dS = \begin{pmatrix} \kappa & & \\ & \kappa & \\ & & 1 - 2\kappa \end{pmatrix} = \kappa \mathbf{I} + (1 - 3\kappa) \mathbf{f}_0 \otimes \mathbf{f}_0, \quad (2.19)$$

where the unit first eigenvector is same as the \mathbf{f}_0 with $1 - 2\kappa \geq \kappa$, and the reset two unit eigenvectors are \mathbf{n}_0 and \mathbf{s}_0 , respectively. Then total dispersed fibre stress is

$$\boldsymbol{\sigma}_f = 2J^{-1} \frac{\partial \mathcal{W}_f(I_{4f}^*)}{\partial I_{4f}^*} \mathbf{F}\mathbf{H}\mathbf{F}^T, \quad (2.20)$$

where $I_{4f}^* = \kappa I_1 + (1 - 3\kappa)I_{4f}$. Later, Holzapfel and co-workers employed this GST approach to depicting mechanical responses of various soft tissues (arterial walls, myocardium, etc.) [19, 21, 124]. Recently, Melnik [74] further extended the GST model to a coupled invariant from two fibre families in the HO model.

2.4.3 Collagen fibre recruitment under fibre dispersion

In soft tissue mechanics, it is often considered that collagen fibres will not bear load under compressed state, thus excluding compressed fibres is necessary, or the so-called tension-compression switch [125]. Because of the wavy structure of the collagen network in the soft tissue, collagen fibres are initially crimped and gradually recruited to bear the loading with increased stretch [8, 126]. Recently, Cheng et al. [8] assessed collagen fibre recruitment in bladder tissue using advanced bioimaging. The low resistance in the toe regime, i.e. the low stretch regime, can be explained by the no-discernible recruitment of collagen fibres. Collagen fibre states at different stretch regimes are briefly shown in Fig. 2.8.

A straight fibre under compression will buckle and cannot support load because of its crimped configuration [17, 127]. This assumption is also necessary for reasons of stability as discussed in [127]. Including recruitment into the SEF would be more physiologically relevant compared to the simple tension-compression switch [128]. Another way to take into account the crimped wavy collagen fibre network is to adopt a multiscale approach from the nanoscale up to the macro-scale using homogenisation techniques as in [129].

Such exclusion is simple when fibres are not dispersed by simply zeroing out fibre stress if compressed, but can be challenging when fibres are dispersed because a stretched domain needs to be determined at each loading step according to its PDF. With a dispersed fibre distribution, exclusion of compressed fibres in the AI approach is relatively simple by only adding stress contribution from each stretched fibre [63, 130, 131] compared to the GST approach. For example, Federico et al. [131] excluded compressed fibres from a planar von Mises distribution using a Heaviside function with a value of 1 when the fibre is stretched, otherwise zero. In general, the AI approach will require significant computational resources to consider each fibre's contribution at each loading step for each location. On the contrary, the GST approach can be much more computational efficient because of one evaluation of the fibre potential derivative with the precomputed structural tensor.

In recent years, a few studies have tried to address the compressed fibre exclusion in GST. When firstly developing the GST model, Gasser et al. [20] suggested that only include fibre

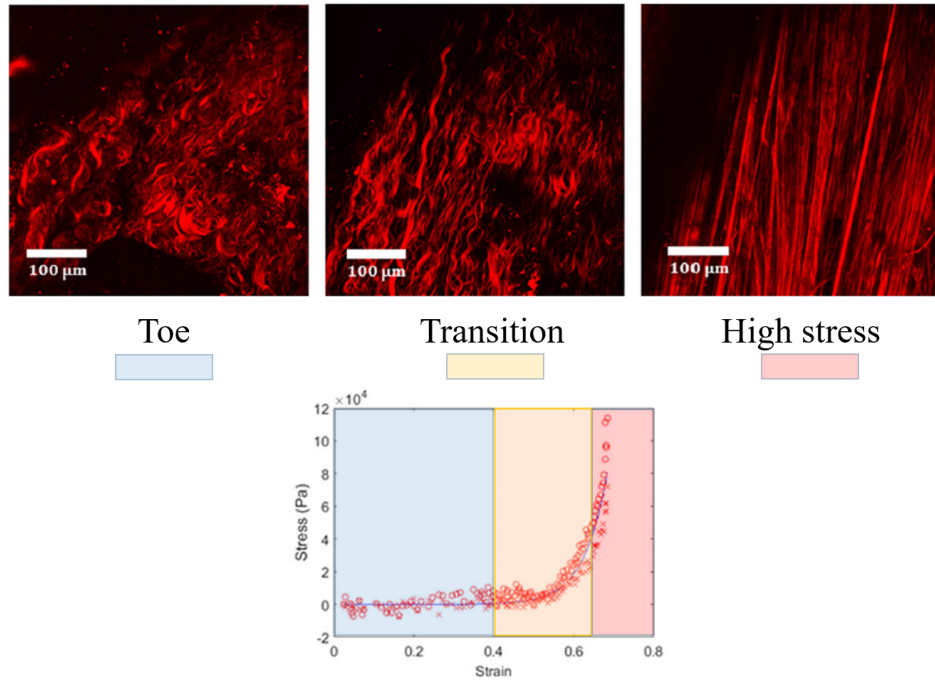


Figure 2.8: Projected stacks of multiphoton images as viewed from abluminal side (images are cited from Cheng et al. [8] with the permission to be reprinted). Top graphs showed collagen fibre deformation from the toe, transition and high stress regimes with increasing strain, and the bottom graph denoted corresponding progressive mechanical loading curves through different segments.

contribution when the mean squared fibre stretch is greater than 1. However, as being discussed extensively in the literature [125, 132], even though the mean fibre stretch is less than 1, there is a portion of fibres being stretched depending on the deformation state, thus, the original GST treatment will redistribute the fibre tensile stress over all the fibres. Significant different consequence may happen if the formulation of the squared mean fibre stretched is based on the volumetric/isochoric split as discussed in [133]. To exclude compressed fibres in GST, Melnik et al. [132] introduced a Heaviside function into the integration of the structure tensor that only includes the stretched fibres. In a recent study, Holzapfel and Ogden [134] modified the original κ model [20] to have κ only depending on the stretched fibre domain, rather than the whole PDF. They further compared this modified κ model with an AI model, and concluded that both the GST and the AI models have equivalent predictive power for characterizing various fibre-reinforced soft tissues. In a similar way, Li et al. [135] proposed a general fibre invariant by integrating $(I_4 - 1)^2$ only over each stretched fibre.

In both the AI and GST approaches, to exclude compressed fibres under complex dynamics will generally require a two-dimensional (2D) integration over a unit sphere at each computational location at each loading step, except for some special cases where analytical solutions may exist. The numerical realization of this 2D integration over a unit sphere may require hundreds of integrations, thus the computational demand can be very high [136]. To improve the

computational efficiency of this 2D integration of stretched fibres in FE simulation, Li et al. [17] developed a discrete fibre dispersion (DFD) model. Instead of integrating fibre contributions from thousands of fibres over a unit sphere, the DFD method will firstly divide this unit sphere into finite triangles, then each triangle in the sphere surface will associate one uniform fibre bundle that will contribute to the total stress weighted by its corresponding density distribution determined from the corresponding PDF. Li et al. [17] further demonstrated that the computational demand was significantly reduced for excluding compressed fibres in their DFD approach, a speed-up of 224 times was observed in their study than using a traditional AI approach. A brief summary of published methods that consider collagen fibre recruitment under fibre dispersion is listed in Table 2.5.

AI approach	
General expression	Reference
$W_{\text{aniso}} = \frac{1}{\pi} \int_{-\pi/2}^{\pi/2} w_f(\lambda_f^2) \rho_{2D}(\theta) d\theta$ $w_f(\lambda_f^2) = \int_1^{\lambda_f} d_1(\lambda_a) w_f^*\left(\frac{\lambda_f^2}{\lambda_a^2}\right) d\lambda_a, \quad 1 = \int_1^{\infty} d_1(\lambda_a) d\lambda_a$ <p>Abrupt commences</p> $w_f^*(\lambda_t^2) = \frac{\eta}{\gamma} \left[e^{\gamma(\lambda_t^2-1)} - 1 \right], \text{ and } d_1(\lambda_a) = \delta[\lambda - \lambda_{a1}]$ <p>Gradual commences</p> $w_f^*(\lambda_t^2) = \frac{\eta}{2} (\lambda_t^2 - 1), \text{ and } d_1(\lambda_a) = \begin{cases} \Gamma_{PDF} & \lambda_a \geq \lambda_{a1} \\ 0 & \lambda_a < \lambda_{a1} \end{cases}$	Hill et al. [128]
$\sigma^e = J^{-1} \int_0^{2\pi} \int_0^\pi \mathcal{H}(I_n - 1) \mathbf{F} \frac{\partial \mathcal{W}(\theta, \phi)}{\partial \mathbf{F}} \sin \phi d\phi d\theta,$ <p>and $\mathcal{H}(I_n - 1) = \begin{cases} 1 & I_n > 1 \\ 0 & I_n \leq 1 \end{cases}$</p>	Ateshian et al. [130]
$\mathcal{W} = \int_{\Omega} \rho(\Theta, \Phi) \mathcal{H}(I_4 - 1) \mathcal{W}^*(\Theta, \Phi) d\Omega,,$ <p>and $\mathcal{H}(I_4 - 1) = \begin{cases} 1 & I_4 > 1 \\ 0 & I_4 \leq 1 \end{cases}$</p>	Federico et al. [131]
$\Psi_f = \frac{1}{2\pi} \iint_{\Omega} \rho(\Theta, \Phi) \Psi_n(\bar{I}_4(\Theta, \Phi)) \sin \Theta d\Theta d\Phi$ $\Omega = \{(\Theta, \Phi) \in \mathbb{S} \mid I_4(\Theta, \Phi) > 1\}$	Li et al. [63]
GST approach	
General expression	Reference
$\mathbf{H} = \int_{\Omega} \rho(\Theta, \Phi) \mathbf{M} \otimes \mathbf{M} d\Omega,$ $I_{4f}^* = \kappa I_1 + (1 - 3\kappa) I_{4f}, \text{ and } \mathcal{W}_{\text{aniso}} = \mathcal{W}_f(I_{4f}^*)$	Gasser et al. [20]
$\mathbf{H} = \oint_{\cup} \rho(\mathbf{m}_0) \chi(\mathbf{m}_0 \otimes \mathbf{m}_0 : \mathbf{C}) \mathbf{m}_0 \otimes \mathbf{m}_0 d\omega,$ <p>and $\chi(I_f) = \begin{cases} 1, & I_f = \mathbf{m}_0 \otimes \mathbf{m}_0 : \mathbf{C} > 1, \\ 0, & I_f = \mathbf{m}_0 \otimes \mathbf{m}_0 : \mathbf{C} \leq 1. \end{cases}$</p>	Melnik et al. [132]
DFD approach	
General expression	Reference
$\Psi_f = \sum_{n=1}^m \rho_n \Psi_n(I_{4n}), \text{ and } \Psi_n(I_{4n}) = \begin{cases} f(I_{4n}) & \text{if } I_{4n} \geq 1 \\ 0 & \text{if } I_{4n} < 1 \end{cases}$	Li et al. [17]

Table 2.5: Summary of published methods that consider collagen fibre recruitment under fibre dispersion during passive deformations.

2.4.4 Myofibre active stress under fibre dispersion

Myofibres do not align perfectly along one direction at any location within a ventricular wall but dispersed as reported by Ahmad et al. [5], who measured in-plane and out-of-plane myofibres and collagen fibres dispersion using two-photon-excited fluorescence and second harmonic generation microscopy on neonatal heart samples. This also agrees with the historical experimental findings from Lin and Yin [1], who measured around 40% cross-fibre active stress in rabbit myocardium. Until now, very few studies included fibre dispersion in active contraction models for the myocardium.

To take into account active contraction caused by dispersed myofibres, Guccione and co-workers introduced cross-fibre active contraction in cardiac models [90, 92] based on experiments by Lin and Yin [1]. Recently, Sack et al. [91] inversely determined cross-fibre contraction ratio in a healthy porcine heart and a failing heart. It has been argued that cross-fibre active contraction may be related to myofibre dispersion. However, no detailed studies reported this connection. Eriksson et al. [21] incorporated myofibre dispersion in both the passive and active mechanics in an electromechanically-coupled idealised LV model. Their model, based on the κ -model [20], showed that large dispersion in the diseased heart could significantly affect ventricular pump function. On the other hand, Ahmad's study [5] demonstrated that in-plane dispersion is different from out-of-plane dispersion, which suggests the rotational symmetry assumption used in the κ -model may not be appropriate. Therefore, for the active stress formulation, a better approach would be to use the non-symmetric dispersion model.

2.5 Growth and remodelling

Heart disease is the leading killer worldwide, responsible for about 40% of all deaths each year [137]. The incidence of heart failure, such as after a heart attack, has remained persistently high due to the maladaptive G&R of heart. There are more heart disease survivors, suffering a subsequent rise in heart failure. Myocardium responds to internal or external environmental changes, such as mechanical loading conditions, by adaptably altering its structure or function. These adaption processes are generally referred to as G&R.

Growth indicates an increase in the number (via proliferation, hyperplasia, or migration) or size (via hypertrophy) of cells, leading to an increase in mass. The mass density or material properties may or may not be changed during the growth process. Remodelling demonstrates structural changes by reorganizing existing components (for example, changing myofibre or collagen fibre orientations) or by synthesizing new components with different structures. The remodelling process also may or may not change the mass density, whilst it does change the material properties such as stiffness [138].

G&R can further be classified as adaptive and maladaptive categories. The former is that heart is still able to maintain normal cardiac functions after G&R, which is a beneficial compen-

satory mechanism and usually occurs at an early stage of heart diseases. Maladaptive G&R due to persistent pathological stimuli gradually makes the heart pump function into a more severe and non-reversible diseased state. For example, when the heart is subjected to chronic overload conditions, ventricular dysfunction occurs after initial compensatory hypertrophy failing, finally resulting in heart failure. It means that the heart is unable to pump sufficient blood to meet body's need.

There are two typical types of pathological overloads: pressure overload and volume overload, as the sketch shown in Fig. 2.9. As for the former, common causes are aortic stenosis or systemic hypertension, which force LV to overcome more resistance when it pumps blood into the aorta or normalises the systemic circulation. Under normal heart rate, sufficient stroke volume (SV) is maintained by higher LV contractile force that results higher systolic wall stress. This high wall stress in systole has been considered to be one mechanical clue to trigger G&R in pressure overload condition. For example, Grossman et al. [139] found the wall thickening in the LV with increased systolic tension, usually denoted as concentric growth. In volume overload, LV may experience a dramatic pressure increase in diastolic filling, such as due to mitral valve regurgitant [140]. Excessive blood in LV results further excessive stretch of myocytes as the wall becomes thinner, which triggers myocyte slippage and elongation of myofibres, hence stretch of fibre may be one mechanical clue to estimate eccentric G&R of LV under volume overload.

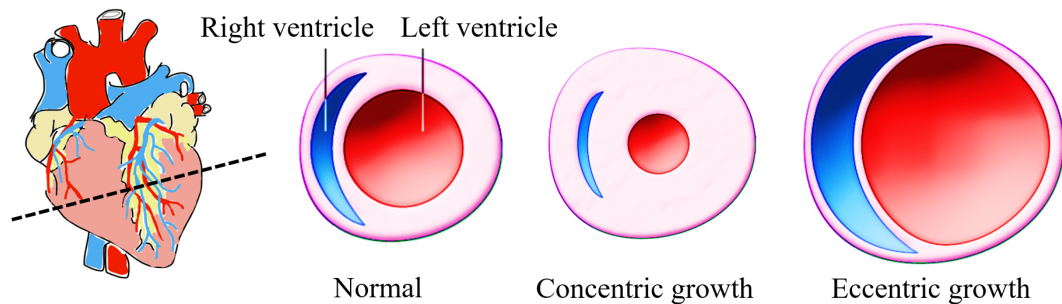


Figure 2.9: Schematic description of G&R of heart. From the cross section view as cut from the black dash line on heart, normal heart respectively proceeds concentric growth associated with wall thickening in response to pressure overload and eccentric growth associated with ventricular dilation in response to volume overload.

The current prevalent theories to elaborate G&R in soft tissue are volumetric growth theory [141] and constrained mixture theory [138]. Volumetric growth theory is a phenomenological approach that treats myocardium as a continuum mixture and does not account for G&R processes of its constituents. In contrast, constrained mixture theory aims to explain the G&R of individual constituents, which allows different growth laws for different constituents.

2.5.1 The volumetric growth theory

Kinematic growth theory is commonly used to study G&R in soft tissue. Rodriguez et al. [10] firstly proposed the volumetric growth by multiplicatively decomposing the total deformation gradient tensor \mathbf{F} , such as $\mathbf{F} = \mathbf{F}_e \mathbf{F}_g$, which is originally based on the concept of plasticity. Here, \mathbf{F}_g is an inelastic growth tensor that describes changes in shape of a material point. Derived \mathbf{F}_e is an elastic tensor to quantify stress response. As shown in Fig. 2.10, \mathbf{F} , including G&R and external loads, converts the LV from a compatible configuration \mathcal{B}_0 to another compatible configuration \mathcal{B}_2 . After decomposition, growth tensor (\mathbf{F}_g) leads the LV into a new incompatible and stress-free intermediate configuration \mathcal{B}_1 . Subsequently, elastic deformation gradient tensor \mathbf{F}_e assembles all grown and original constituents into the final compatible state \mathcal{B}_2 , in which residual stress may be generated.

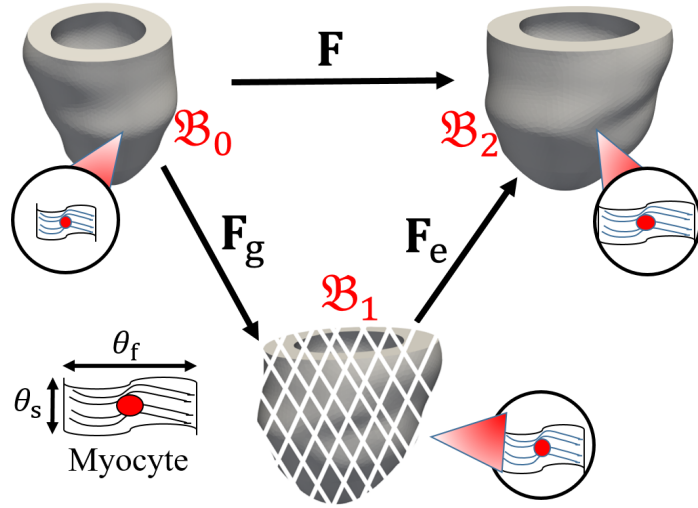


Figure 2.10: Schematic description of the volumetric growth theory, in which total deformation gradient tensor \mathbf{F} is decomposed into \mathbf{F}_g and \mathbf{F}_e . Firstly, LV model grows into new incompatible and stress-free intermediate configuration \mathcal{B}_1 by growth tensor \mathbf{F}_g , in which myocardium grows along myocyte (myofibre) θ_f and cross myocyte θ_s directions. Then, all tissues emerged into new compatible LV model in \mathcal{B}_2 by elastic deformation tensor \mathbf{F}_e .

The evolution of growth tensor is usually formulated according to the layered myofibre architecture, such as

$$\mathbf{F}_g = \theta_f \mathbf{f}_0 \otimes \mathbf{f}_0 + \theta_s \mathbf{s}_0 \otimes \mathbf{s}_0 + \theta_n \mathbf{n}_0 \otimes \mathbf{n}_0, \quad (2.21)$$

where θ_f , θ_s and θ_n are respective growth ratios along each principal axial orientation. $\theta_f > 1.0$, $\theta_s = \theta_n = 1.0$ is the so-called fibre growth in eccentric growth, $\theta_s > 1.0$, $\theta_f = \theta_n = 1.0$ is the so-called cross-fibre growth in concentric growth, and $\theta_f = \theta_s = \theta_n > 1.0$ is the isotropic volume growth. These growth ratios are determined by specific growth laws that defines the relationships between growth ratios and stimuli cues, such as through a set of ordinary differential equations for fibre growth driven by stretch or cross-fibre growth driven by stress [141].

The elastic stress of the grown tissue is calculated only with respect to the elastic tensor \mathbf{F}_e , that is

$$\boldsymbol{\sigma}_p = J_{\mathbf{F}}^{-1} \mathbf{F} \frac{\partial \mathcal{W}(\mathbf{F})}{\partial \mathbf{F}} = J_{\mathbf{F}_e}^{-1} \mathbf{F}_e \frac{\partial \mathcal{W}(\mathbf{F}_e)}{\partial \mathbf{F}_e}, \quad (2.22)$$

in which $J_{\mathbf{F}}^{-1} = \det(\mathbf{F})$ and $J_{\mathbf{F}_e}^{-1} = \det(\mathbf{F}_e)$.

The volumetric growth framework was firstly applied into cardiac mechanics by Kroon et al. [23], who used the isotropic growth tensor to study the impact of two different reference configurations: fixed reference throughout the entire growth process and updated reference after each growth increment. They found that the growth stimulus significantly depended on the types of the reference configuration, therefore, choosing the reference configuration is critical to simulate growth.

Later, Göktepe et al. [141] investigated the eccentric growth induced by serial sarcomere deposition and the concentric growth by parallel sarcomere deposition. They provided anisotropic growth tensors and growth multipliers were estimated by a set of ordinary differential equations. Phenomenological thresholds of fibre stretch and stress were used to trigger eccentric and concentric growth, respectively.

Recently, Lee et al. [142] developed a framework of volumetric strain-driven finite growth to predict reverse growth in response to fibre stretch below the threshold of a critical fibre stretch. The model was embedded in an electromechanical model of heart [143] that included active contraction of myocardium to exam myocardial infarction. They also adopted the framework of updated reference in FE computation.

Kerckhoffs et al. [140] studied a more complex growth law where growth multipliers in orthotropic growth tensors are expressed in sigmoidal functions with respect to stimulus for fibre axial or radial growth. The model not only was able to reproduce primary physiological responses under conditions of pressure overload and volume overload but also showed wall thickening in pressure overload induced by a strain-based stimulus.

In contrast to existing single or biventricular models, Genet et al. [144] applied volumetric growth to a four-chamber human heart model to explore its availability in describing or predicting the patient-specific heart failure progression, which is achieved by using the Living Heart Project developed by ABAQUS company. In addition, lumped model to briefly describe circulation was attached to a time-varying elastance model, where Witzenburg and Holmes [145] introduced growth laws from Kerckhoffs et al. [140]. The model was implemented in MATLAB with high computing efficiency and was able to predict both the time course and different patterns of G&R in pressure overload, volume overload and even post-infarction remodelling.

Recently, based on experimental data of porcine heart, Peirlinck et al. [146] coupled machine learning and the multiscale data from a porcine heart model with volume overload. They have claimed the approach will contribute to a new generation of multiscale growth model that can explain the interplay of different scale contributors to heart failure.

In summary, volumetric growth theory is an elegant approach to describe G&R, with the

advantages of simple concept and convenient computational implementation. However, there are limitations. For example, the theory was initially applied in a stress-free configuration that is impossible for the living tissue. The fact that added or lost mass of different constituents is assembled into a common one compatible geometry causes stress inside the body. Additionally, a single phenomenological evolution law of \mathbf{F}_g cannot distinguish the different G&R patterns of multiple constituents in soft tissue. Moreover, the constant density of tissue is always assumed during both elastic deformation and G&R. Therefore, although the volumetric growth theory can characterise overall G&R progression, important information such as different biological constituents' adaptation and response are missed.

2.5.2 Constrained mixture theory

Mixture theory

Here, we introduce the basic idea of mixture theory, involving the mass density, displacement and stress etc. of a body and its constituents. In a homogenised concept, position \mathbf{x} in the current configuration \mathcal{B}_t of a body is the comprehensive results of multiple constituents simultaneously. In other words, each constituent shares the same current position as the body, that is

$$\mathbf{x} = \hat{\mathbf{x}}^i(\mathbf{X}^i, t), \quad i = 1, 2, \dots, N \quad (\text{no sum on } i), \quad (2.23)$$

where \mathbf{X}^i is the position of constituent i in the reference configuration, and N is the number of constituents in the body. Hence, the displacement \mathbf{u}^i and velocity \mathbf{v}^i of each constituent can be defined as

$$\mathbf{u}^i = \hat{\mathbf{x}}^i - \mathbf{X}^i, \quad \text{and} \quad \mathbf{v}^i = \frac{\partial \hat{\mathbf{x}}^i}{\partial t}. \quad (2.24)$$

In continuum mechanics, mass and linear momentum should keep conserved. Energy is ignored here because of G&R is assumed as a nearly isothermal process and underlying metabolism is not considered [138]. The governing equations of mass balance for constituents i (left) and for the mixture body (right) are

$$\frac{\partial \rho^i}{\partial t} + \text{div}(\rho^i \mathbf{v}^i) = m^i, \quad \text{and} \quad \frac{\partial \rho}{\partial t} + \text{div}(\rho \mathbf{v}) = \sum m^i, \quad (2.25)$$

where ρ^i is the mass density of constituent i , m^i is its mass production per time per volume, conserved mass can be achieved by changing the mass density of each constituent with the constraint $\sum m^i = 0$. ρ and \mathbf{v} are variables of the mixture and are defined by

$$\rho = \sum_{i=1}^N \rho^i, \quad \text{and} \quad \mathbf{v} = \frac{1}{\rho} \sum_{i=1}^N \rho^i \mathbf{v}^i. \quad (2.26)$$

For constituent i , governing equations of linear momentum balance requires

$$\operatorname{div}(\boldsymbol{\sigma}^i) + \rho^i \mathbf{b}^i + \mathbf{p}^i + m^i \mathbf{v}^i = \rho^i \mathbf{a}^i, \quad (2.27)$$

where $\boldsymbol{\sigma}^i$ is the homogenised Cauchy stress, \mathbf{b}^i is the body force, \mathbf{p}^i is a momentum exchange between constituents such as drag induced by solid particles moving through a fluid or fluid moving through a porous solid, $m^i \mathbf{v}^i$ is a momentum from the mass production, and \mathbf{a}^i is the acceleration. The balances of momentum exchanges and mass productions between the constituents are maintained by the constraint $\sum_{i=1}^N (\mathbf{p}^i + m^i \mathbf{v}^i) = \mathbf{0}$. Hence, the linear momentum balance equation for the constrained mixture is

$$\sum_{i=1}^N \operatorname{div}(\boldsymbol{\sigma}^i) + \rho^i \mathbf{b}^i + \mathbf{p}^i + m^i \mathbf{v}^i = \sum_{i=1}^N \rho^i \mathbf{a}^i, \quad \Rightarrow \quad \operatorname{div}(\boldsymbol{\sigma}) + \rho \mathbf{b} = \rho \mathbf{a}, \quad (2.28)$$

where the quantities of the mixture body typically can be defined as

$$\boldsymbol{\sigma} = \sum_{i=1}^N \boldsymbol{\sigma}^i, \quad \mathbf{b} = \frac{1}{\rho} \sum_{i=1}^N \rho^i \mathbf{b}^i, \quad \text{and} \quad \mathbf{a} = \frac{1}{\rho} \sum_{i=1}^N \rho^i \mathbf{a}^i. \quad (2.29)$$

There are more constraints relative to the deformations of body. In the sub-tissue level, we can assume each constituent having incompressibility. In tissue level, the mixture body is also incompressible and its volume is the sum of volumes of constituents. Identification of appropriate constraints for G&R of constituents or mixture body will be a challenging task.

As growing and remodelling, the changes in stiffness of the tissue indicates the evolution of microstructure, which requires updated reference configuration to derived current stresses [138]. In other words, reference configurations of constituents and mixture body evolve with G&R, and their deformations are defined with respect to respective current configurations. In fact, the traction of the evolved configuration of each constituent is a complicated process, particularly when residuals stress makes the unloading body in a stressed state.

Homogenised constrained mixture theory

Constrained mixture theory was proposed by Humphrey and Rajagopal et al. [138] to explain the deposition and degradation of individual constituents within a tissue. As shown in Fig. 2.11, if deformation gradient tensors of the whole tissue from the reference configuration at time $t = 0$ to the configuration at time s and τ are $\mathbf{F}(s)$ and $\mathbf{F}(\tau)$, respectively, then $\mathbf{F}(s)$ can be decomposed into two parts: $\mathbf{F}(\tau)$ that contains all growth and part of remodelling information and $\mathbf{F}_\tau(s) = \mathbf{F}(s)\mathbf{F}^{-1}(\tau)$ that describes the rest remodelling and all external loading deformations.

An important hypothesis is that a grown and remodelled constituent i in $\kappa(\tau)$ is treated as the deposition from the stress-free incompatible configuration $\kappa_n^i(\tau)$ via a pre-strain tensor

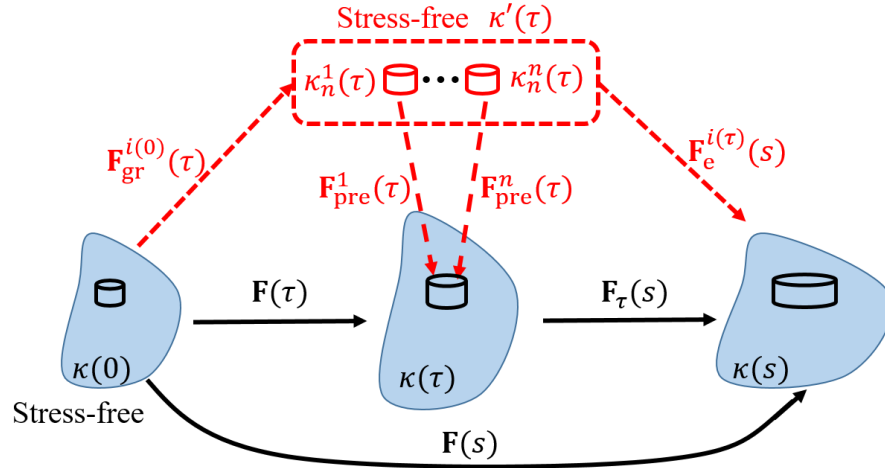


Figure 2.11: Schematic description of homogenised constrained mixture growth theory. The configuration before growth $\kappa(0)$ is assumed to be stress-free, $\kappa(s)$ is current configuration after G&R, and $\kappa(\tau)$ is a intermediate configuration with time $\tau \in (0, s)$. Under total deformation gradient tensor $\mathbf{F}(s)$, growth and part remodelling occurs from $\kappa(0)$ to $\kappa(\tau)$ via $\mathbf{F}(\tau)$ and the other part remodelling and external loading occurs from $\kappa(\tau)$ to $\kappa(s)$ via $\mathbf{F}_\tau(s)$. A grown and remodelled constituent i in $\kappa(\tau)$ is treated as the deposition in $\kappa_n^i(\tau)$ via a pre-strain tensor $\mathbf{F}_{\text{pre}}^i(\tau)$ from fictitious incompatible stress-free intermediate configuration $\kappa'(\tau)$ to $\kappa(\tau)$. Then all deposited constituents perform remodelling and loading deformations. $\mathbf{F}_{\text{gr}}^i(0)$ is the fictitious inelastic G&R tensor for each constituent from $\kappa(0)$ to $\kappa'(\tau)$, and $\mathbf{F}_e^{i(\tau)}(s)$ represents its elastic deformation tensor from $\kappa'(\tau)$ to $\kappa(s)$.

$\mathbf{F}_{\text{pre}}^i(\tau)$ from fictitious incompatible stress-free intermediate configuration $\kappa'(\tau)$ to $\kappa(\tau)$. Then, all deposited constituents perform remodelling and loading deformations together. Therefore, the deformation of each constituent can be demonstrated by the fictitious path $\kappa(0) \rightarrow \kappa'(\tau) \rightarrow \kappa(s)$, such as

$$\mathbf{F}(s) = \mathbf{F}_e^{i(\tau)}(s) \mathbf{F}_{\text{gr}}^{i(0)}(\tau), \quad (2.30)$$

where $\mathbf{F}_{\text{gr}}^{i(0)}(\tau)$ denotes the inelastic G&R process from the compatible stress-free $\kappa(0)$ to the incompatible stress-free $\kappa'(\tau)$. Hence, the individual elastic deformation gradient tensor for constituent i from $\kappa'(\tau)$ to compatible configuration at time s is

$$\mathbf{F}_e^{i(\tau)}(s) = \mathbf{F}(s) \mathbf{F}^{-1}(\tau) \mathbf{F}_{\text{pre}}^i(\tau). \quad (2.31)$$

The homogenised constrained mixture model [147] aims to define an effective, temporally homogenised elastic deformation gradient \mathbf{F}_e^i and inelastic G&R deformation gradient \mathbf{F}_{gr}^i for every constituent during G&R process, thus, Eq. (2.30) can be rewritten as

$$\mathbf{F} = \mathbf{F}_e^i \mathbf{F}_{\text{r}}^i \mathbf{F}_{\text{g}}^i, \quad \text{and} \quad \mathbf{F}_{\text{gr}}^i = \mathbf{F}_{\text{r}}^i \mathbf{F}_{\text{g}}^i, \quad (2.32)$$

where \mathbf{F} is total deformation gradient tensor of the whole mixture body, \mathbf{F}_g^i , \mathbf{F}_r^i , and \mathbf{F}_e^i are respective inelastic growth tensor, inelastic remodelling tensor, and elastic deformation tensor of constituent i , respectively.

Constrained mixture model was often used to study vascular G&R [24] and barely in cardiac problems. There are two categories of hybrid approaches based on constrained mixture model: volumetric constrained mixture model and homogenised constrained mixture model. Alford et al. [24] coupled kinematic growth theory to constrained mixture theory to model G&R of aorta. 3D FE simulations were performed by Wan et al. [148] who used pre-determined distribution functions to calculate local homeostatic pre-stretch in a thick-walled aorta model. In the concept of the homogenised constrained mixture, Braeu et al. [149] designed tensional homeostasis as stimulus and constant density in studying G&R of cylindrical artery model.

2.6 Myocardium infarction

Myocardium infarction (MI) is a common heart attack disease and has high mortality worldwide, such as the proportion of in-hospital deaths about 8.1% in UK [150]. Even though more patients survive after MI, the incidence of post-MI heart failure continue to rise, which are caused by maladaptive G&R of heart. MI indicates the damage of heart muscle, usually death of myocytes in an area of the myocardium due to the decreased or stopped supply of oxygen, causing the dysfunction of heart, as shown in Fig. 2.12. Occlusion or pathology of coronary circulation is the primary cause of MI.

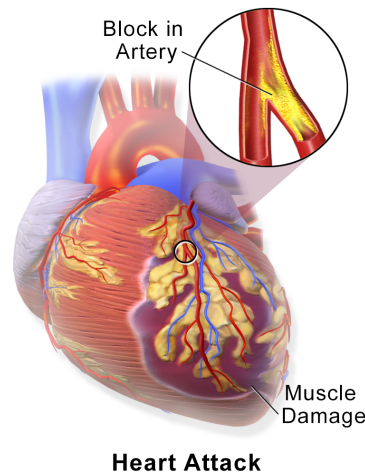


Figure 2.12: A myocardial infarction sketch from https://en.wikipedia.org/wiki/Myocardial_infarction

The healing after acute MI involves four main phases with respect to time, acute ischemia occurs the first minutes to hours after MI, necrotic or dying of myocardium occurs during the first a few days, MI region becomes fibrosis after weeks or months, and final remodelling phase of the whole heart begins after months. The remodelling of heart after MI is a comprehensive

process regulated by mechanical, neuro-hormonal and genetic factors [151], in which the heart may be sequentially subjected to eccentric dilation, thinning of infarct zone, hypertrophy of healthy region, and fibrosis infarct muscle, causing the risk of heart failure or rupture.

2.6.1 Experimental measurements of MI

The G&R of collagen fibre in MI scar have gradually become a fascinating study topic. Current imaging technologies, such as late gadolinium enhanced MRI, are able to precisely determine MI size and location in a heart, commonly in an anterior location. MI size is negatively correlated with cardiac contractile capability. For instance, a larger anterior MI can lead to significant LV dilation and even heart failure. Myocytes in the MI region are degraded and replaced by grown collagen fibres, whose remodelling structure varies with MI position [152].

Collagen fibre structure in MI region

After MI, the dead myocytes are gradually replaced by newly grown collagen fibres, resulting in a fibrous scar. The increased content of collagen has been measured [153, 154]. However, the studies about collagen fibre structure of mean orientation in the MI region have not yet reached a consistent conclusion, which may be associated with measurement methods, experimental species, and observation time.

For instance, early measurement on dog LV found obliquely alighted mean collagen fibre directions in MI scar, in which shifted angle with respect to circumferential direction was $-14.0 \pm 3.5^\circ$ at sub-epicardium, $-12.7 \pm 2.1^\circ$ at sub-endocardium, and $-1.4 \pm 0.4^\circ$ at mid-myocardium [153]. Ultrasonic backscatter method was used to measure the transmural shift of collagen fibre orientation in healthy and MI regions of human heart, and found rotated mean collagen fibre orientation in the MI region ($14.6 \pm 1.5^\circ$) is 59% bigger than that in the healthy region ($9.2 \pm 0.7^\circ$) [155]. In the rat hearts, MI near the equator of the LV was stretched mainly along the circumferential direction and remodelling process orientated grown collagen fibres circumferentially, however, randomly alighted collagen occurred when MI located at the apex where stretch of MI scar was in both the circumferential and longitudinal directions [152].

In contrast, DT-MRI for rat heart at four weeks after MI demonstrated that transmural courses of myofibre orientation angles in the MI region were similar to those in remote healthy zone, and newly grown collagen fibres in the MI region might maintain the original orientation of myofibres they replaced [156].

Observed remodelling process

Remodelling process is the compensatory procedure in response to the loss of LV normal pumping function from about 2-5 days after acute MI. MI zone undergoes regional dilation and thinning, although MI perfusion may cause additional myocardial necrosis. The remote healthy

region activates compensatory expansion to decrease LV diastolic pressure and increase cardiac blood output, however, a continuous LV expansion can cause LV dysfunction. If the LV functions return to normal conditions, such as enough stroke volume under healthy heart rate, by the remodelling process, then this is so-called compensatory G&R, otherwise decompensatory G&R [157].

For instance, in the measurements of infarct collagen and LV topography in 132 dogs with coronary artery ligation [158], LV cavity dilation emerged in the first 7 days, and then the infarct shrank and thinned as well as collagen deposited up to 6 weeks. During the remodelling process after MI, the LV regional shape distortion was mainly induced by thinned infarcted segment and collagen deposition.

Mckay et al. [159] compared LV remodelling process of 30 patients at the first acute MI and 2 weeks late by monitoring changes of geometry and haemodynamic. Their results proved that infarcted size determined the magnitude of the remodelling process, and the remodelling could reduce LV diastolic pressure and increase cardiac blood output at the expense of a significant enlarged LV cavity.

Remodelling process after MI reperfusion were tracked in 66 patients at baseline (1 week), early stage (4 months), and late stage (14 months), and mean infarct size, evaluated by late gadolinium enhanced cardiac magnetic resonance, were 25 ± 17 g, 17 ± 12 g, and 15 ± 11 g, respectively [160]. This fact shows that the remodelling process is continuous and substantially reduces infarct size at the early state.

The variations of main representative mechanical indexes appear in sequence. Loss of contraction of MI segment causes both systolic and diastolic dysfunction, with decreased EF, increased LV end-systolic volume (ESV), end-diastolic volume (EDV) and end-diastolic pressure (EDP). For instance, the analysis of LV EDP of 744 acute MI patients over three years after MI reported that the mean LV EDP is 23 ± 9 mmHg and 75% of patients' LV EDP was higher than 15 mmHg [161]. Then, peripheral mechanisms are activated, such as adjusting the sympathetic nervous system and circulating catecholamine, to maintain a normal arterial pressure and blood condition, which leads to increased end-systolic pressure (ESP) and EDP with increased wall stresses, eventually progressive dilation and thinning. If the mature MI scar fails to resist the elevated wall stress, LV rupture may occur. In the MI segment, myocytes' degradation accounts for most wall thinning, and myocyte stretch and reduced intercellular space lead to further thinning.

2.6.2 Mathematical modelling of MI

Passive material properties of infarcted and remote healthy myocardium are usually described by phenomenological constitutive laws, such as strain-based Fung-type SEF or invariant-based Holzapfel-Ogden SEF [12]. Tissue in the MI region is much stiffer than that in the remote healthy region, while the border zone is the transition zone [143]. The MI zone is usually modelled as a pure passive soft tissue without contractility, the border zone has diminished

contractility depending on the distance to the MI zone [46], and normal contractile capability is in remote healthy and border regions.

Wenk et al. [162] established a treatment model for infarcted sheep LV by injecting calcium hydroxyapatite-based tissue filler. Based on 3D ultrasound images at the end-diastole and the end-systole, the passive parameters and maximum active tension were inversely estimated. Their results showed that injection of filler increased the matrix stiffness in the MI region and reduced both diastolic and systolic wall stress in the LV, especially in the MI region.

Based on MRI, Fomovsky et al. [163] used a FE model of a dog LV with a large anteroapical MI to simulate cardiac dynamics and investigate the effect of collagen fibre orientation in the MI zone on LV pumping function. They reported that the best stroke volume could be achieved when the MI zone had high longitudinal stiffness and low circumferential stiffness. Their study showed the potential for therapies to improve LV pumping functions by modifying collagen fibre structure in the MI zone.

Recent studies [2, 164] estimated the prognosis of MI according to patient-specific LV models constructed by MRI at the end-diastole and the end-systole. The stiffness of the myocardium in the MI zone was 50 times of that in the remote healthy zone, and the active tension decreased from the remote healthy region to zero in the MI zone.

Growth and remodelling models post-MI

The living tissue can grow or remodel in response to an altered environment, such as changes in mass or biomechanical property. In myocardium, myofibre and collagen fibre undergo G&R when their surrounding environments vary. Moreover, G&R of myocardium plays a critical role in MI healing and the recovery of LV pump function post-MI. Thus, mathematical modelling of G&R contributes to understanding the underlying mechanism of LV pump function adaption post-MI.

Rouillard et al. [165] proposed an agent-based model for the G&R of collagen fibre in the MI zone during the healing process. Their results showed that the level of anisotropy of collagen fibre in scar could be reduced when fibroblasts aligned themselves in the orientation of the greatest strain/stretch. Lee et al. [143] developed an integrated electromechanical-growth heart model to predict G&R after MI, in which the growth of myocardium was modelled using the classical volumetric growth approach. The updated reference framework was further used but without considering the growth-induced residual stress in the cardiac G&R process, in which growth or shrinkage depended on the elastic stretch of fibre. The coupled cardiac electromechanics model to produce the potential of the entire cardiac cycle was solved by a system of ordinary differential equations and partial differential equations. It also explained the separation of the timescale between growth and elastic deformation. These models have shown significant importance in understanding the G&R process after MI and assessing treatment therapies.

Part I

Constitutive laws and fibre structures of myocardium

Chapter 3

Constitutive law: reduction of the general Holzapfel–Ogden model based on ex-vivo experiments

3.1 Introduction

Cardiac diseases remain a major public health burden, especially the adverse remodelling of cardiac function after acute myocardial infarction. Studies have demonstrated that stress/strain in myocardium can have great effects on pathological processes such as hypertrophy, and myocardial infarction [38–40]. Accurate prediction of myocardial stress relies on the choice of constitutive laws. Determining the constitutive laws and their parameters from limited experimental data, however, remains a great challenge for the cardiac modelling community.

In general, biological tissue, including myocardium, mainly consists of proteins such as collagen, elastin and ground substance. Published in vitro/ex vivo experimental tests of the mechanical behaviour of human myocardium [4, 55, 56] have shown strong anisotropy and transmural variations. These results showed it is a nonlinear, anisotropic (orthotropic), viscoelastic and history-dependent soft biological material.

Over the years, a number of models have been developed to describe myocardial mechanical properties, ranging from linear elastic to hyper-elastic, from isotropic to anisotropic, and from phenomenological to micro-structurally-based constitutive laws [11]. Nowadays, it is a common practice to characterize myocardium as an anisotropic, hyper-elastic material. Based on the simple shear data from [55], Holzapfel and Ogden proposed a simplified formulation (HO2009) derived from a more general strain-invariants based material model (the general HO model) [11]. The HO2009 model and its variation have been widely used in the cardiac modelling community [2, 70]. However, there has been no analysis to show if it has both adequate descriptive and predictive capabilities for other tissue tests of myocardium. Indeed, such an analysis is important for any constitutive laws for clinically useful computational simulations.

In this chapter, our aim is to reduce the general HO model to maintain its mechanical integrity whilst achieve minimal computational cost. A competent constitutive law should have descriptive and predictive capabilities for different tissue tests. By competent, we mean the model has least terms but is still able to describe and predict experimental data. We also intend to find the optimal combination of experiments for each species of tissues that uses minimal mechanical tests.

This chapter first considers the descriptive capabilities of the general and specific HO models proposed in [11], using Dokos’ simple shear data of porcine myocardium [55], Sommer’s biaxial and simple shear data of human myocardium [4], and Ahmad’s uniaxial, biaxial and simple shear data of neonatal porcine myocardium [9]. Secondly, the Akaike information criterion (AIC) [41, 166, 167] is used to analyze the goodness-of-fit of the general HO model to the experimental data, with AIC values determined when excluding different strain invariants. Based on the AIC analysis, reduced HO models for different experimental studies are then proposed by excluding those strain invariants with little contribution to the overall goodness-of-fit. Finally, we use predictive capability of the reduced HO models to find the optimal combination of experiments for each species of tissues that uses the least mechanical tests.

We propose three different reduced HO models based on the three sets of experimental data, and they all retain similar descriptive and predicative capability as the general HO model. Our results show that one shear responses and one biaxial stretch can sufficiently describe the human myocardial mechanical properties in Sommer’s experiments [4]. Our study shows that single-state tests (i.e., simple shear or stretching only) are insufficient to determine the myocardium responses. Finally, it is also important to consider the transmural fibre rotation within the myocardial samples, that is excluding un-stretched fibres using the ‘effective fibre ratio’, which depends on the sample size, shape, local myofibre architecture, and loading conditions. We conclude that a competent myocardium material model can be obtained from the general HO model using AIC analysis and calibrated from a suitable combination of tissue tests. In particular, the reduced HO model based on biaxial and simple shear data of human myocardium [4] shall be used in subsequent human heart studies, which has less unknown parameters than the general HO model, and is informed by the human myocardial experiments.

This chapter is based on the published paper *Guan, D., Ahmad, F., Theobald, P., Soe, S., Luo, X. and Gao, H., 2019. On the AIC-based model reduction for the general Holzapfel–Ogden myocardial constitutive law. Biomechanics and modeling in mechanobiology, 18(4), pp.1213-1232.*

3.2 Method

3.2.1 The general HO model

To characterize the mechanical behaviours of myocardium, the general HO strain energy function proposed by Holzapfel and Ogden [11] is employed in this study, which is

$$\begin{aligned} \Psi = & \frac{a}{2b} \exp[b(I_1 - 3)] + \sum_{i=f,s,n} \frac{a_i}{2b_i} \{ \exp[b_i(\max(I_{4i}, 1) - 1)^2] - 1 \} \\ & + \sum_{ij=fs,fn,sn} \frac{a_{ij}}{2b_{ij}} [\exp(b_{ij}I_{8ij}^2) - 1], \end{aligned} \quad (3.1)$$

where $a, b, a_i, b_i, a_{ij}, b_{ij}$ are the 14 material constants, $I_1 = \text{trace}(\mathbf{F}^T \mathbf{F})$, representing the overall squared stretch, I_{4f} , I_{4s} and I_{4n} are squared stretches along each direction,

$$I_{4f} = \mathbf{f}_0 \cdot (\mathbf{F}^T \mathbf{F} \mathbf{f}_0), \quad I_{4s} = \mathbf{s}_0 \cdot (\mathbf{F}^T \mathbf{F} \mathbf{s}_0), \quad I_{4n} = \mathbf{n}_0 \cdot (\mathbf{F}^T \mathbf{F} \mathbf{n}_0),$$

in which $\mathbf{f}_0, \mathbf{s}_0, \mathbf{n}_0$ are the initial fibre, sheet and normal directions. The $\max()$ in (Eq. (3.1)) will ensure the collagen fibres can only bear the load when stretched but not in compression. I_{8fs} , I_{8fn} and I_{8sn} are invariants representing the coupling between two different directions,

$$I_{8fs} = \mathbf{f}_0 \cdot (\mathbf{F}^T \mathbf{F} \mathbf{s}_0), \quad I_{8fn} = \mathbf{f}_0 \cdot (\mathbf{F}^T \mathbf{F} \mathbf{n}_0), \quad I_{8sn} = \mathbf{s}_0 \cdot (\mathbf{F}^T \mathbf{F} \mathbf{n}_0).$$

3.2.2 Selected myocardial experiments

In this study, the experimental data are taken from three ex vivo myocardial biomechanical studies: [55] investigating porcine myocardium; [4] investigating human myocardium; and, [9] investigating neonatal porcine myocardium. These are briefly summarized below. For details please refer to the original papers.

- Dokos et al. [55] published shear data of passive myocardium from porcine hearts with six different shear modes, shown in Fig. 3.1 (a) where (ij) is used to refer to shear in the j direction within the ij plane, where $i \neq j \in \{f, s, n\}$. Myocardial samples were cut from adjacent regions in the left lateral ventricular mid-wall with a size of $\sim 3 \times 3 \times 3$ mm.
- Sommer et al. [4] performed similar six shear-mode experiments, with samples from human hearts (size: $\sim 4 \times 4 \times 4$ mm), They also performed biaxial testing with different stretch ratio (1:1, 1:0.75, 1:0.5, 0.75:1, 0.5:1) along the mean fibre direction (MFD) and the cross-fibre direction (CFD) (Fig 3.1 (b)). MFD is the average angle of the dominant orientation of collagen fibres on the upper and lower surfaces of each sample [57], with CFD perpendicular to MFD. Square specimens with dimensions $\sim 25 \times 25 \times 2.3$ mm were used in biaxial tests, with tension applied along the MFD and CFD. They recorded

the collagen fibre rotation within samples, which was $14.8 \pm 6.9^\circ$ per mm depth in the transmural direction.

- Ahmad et al. [9] performed uniaxial (Fig. 3.1 (c)), biaxial and simple shear experiments on myocardial samples from neonatal porcine left and right ventricular free walls. Sample dimensions were $\sim 15 \times 5 \times 3$ mm for uniaxial tests, $\sim 15 \times 15 \times 3$ mm for biaxial tests and $\sim 3 \times 3 \times 3$ mm for simple shear tests. Shearing was only performed in the sheet–fibre and sheet–normal planes, whilst the MFD was determined based on the external surface texture and not the average angle of the dominant orientation of collagen fibres as in [57].

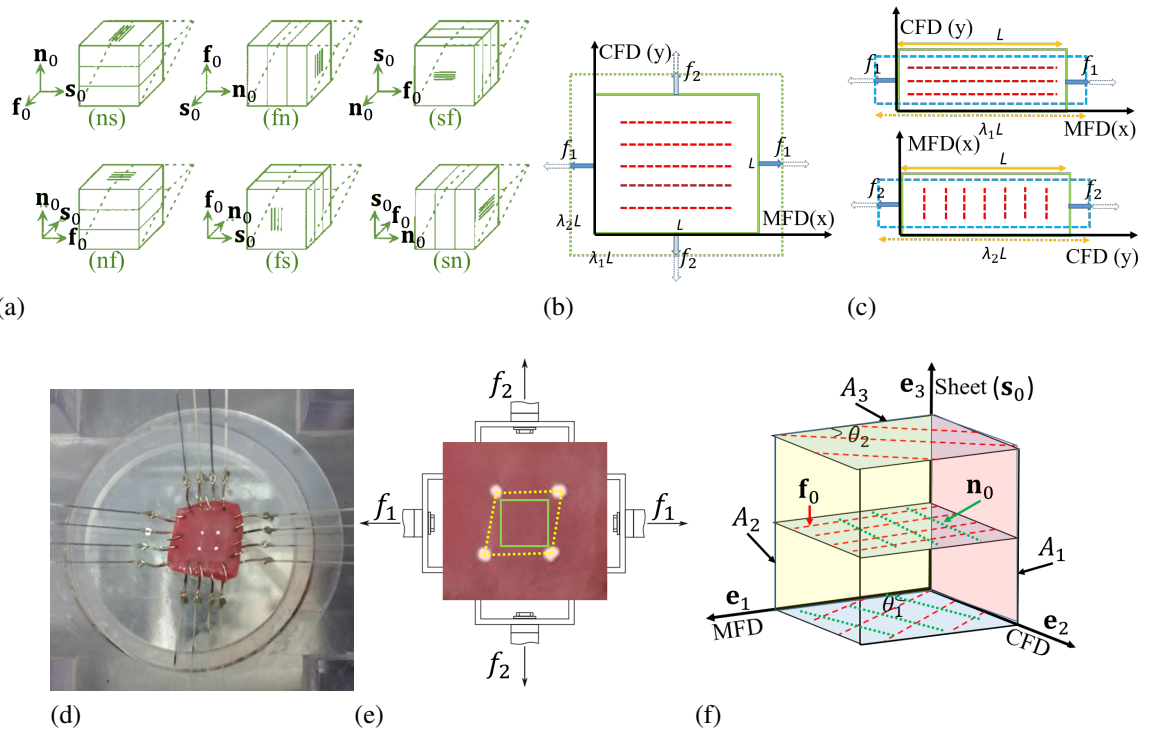


Figure 3.1: (a) A sketch of all six possible shear modes, \mathbf{f}_0 , \mathbf{s}_0 and \mathbf{n}_0 denote the fibre, sheet and normal direction, respectively. (ij) refers to shear in the j direction within the ij plane, where $i \neq j \in \{f, s, n\}$. (b) A sketch of the sample with fibres (red dash lines), which is stretched along the two orthogonal directions (MFD and CFD) in fibre-normal plane during a biaxial test. (c) Sketches of uniaxial tension tests along the MFD and CFD, respectively. f_1 is the loading force along the MFD, and f_2 is along the CFD. L is the initial length of specimen, and λ_1 and λ_2 are stretch ratios. (d) The recorded image in a biaxial tensile specimen in [9]. The four white markers in the centre of the experimental sample in (d) are also shown in (e), in which the solid rectangle represents the initial shape, and the deformed shape is shown using dashed lines. (f) Transmural variation of \mathbf{f}_0 (red dash lines) and \mathbf{n}_0 (green dot lines) along the thickness of myocardium. \mathbf{e}_1 , \mathbf{e}_2 , \mathbf{e}_3 in Cartesian coordinate system represent the MFD, CFD and sheet (transmural) directions, respectively. A_i is the cross-sectional area perpendicular to \mathbf{e}_i axis.

In the following, we refer these three sets of experiments as Dokos’ data, Sommer’s data and Ahmad’s data. Let \mathbf{e}_1 , \mathbf{e}_2 , \mathbf{e}_3 in Cartesian coordinate system represent the MFD, CFD and sheet

(transmural) directions, and assume that the test sample is incompressible ($\det(\mathbf{F}) = 1$ where \mathbf{F} is deformation gradient tensor). To make use of the experiments, it is convenient to use the first Piola–Kirchhoff (P-K) stress \mathbf{P} , which is related to the applied force components f_{ij} in the tests and Cauchy stress tensor $\boldsymbol{\sigma}$ as

$$\mathbf{P} = \begin{bmatrix} P_{11} & P_{12} & P_{13} \\ P_{21} & P_{22} & P_{23} \\ P_{31} & P_{32} & P_{33} \end{bmatrix} = \begin{bmatrix} \frac{f_{11}}{A_1} & \frac{f_{12}}{A_2} & \frac{f_{13}}{A_3} \\ \frac{f_{21}}{A_1} & \frac{f_{22}}{A_2} & \frac{f_{23}}{A_3} \\ \frac{f_{31}}{A_1} & \frac{f_{32}}{A_2} & \frac{f_{33}}{A_3} \end{bmatrix}, \quad \boldsymbol{\sigma} = \mathbf{P}\mathbf{F}^T, \quad (3.2)$$

where A_i is the cross-sectional area perpendicular to \mathbf{e}_i axis as shown in Fig. 3.1 (f).

Uniaxial tests

For uniaxial stretch experiments along MFD, we have

$$\mathbf{F} = \begin{bmatrix} \lambda_1 & 0 & 0 \\ 0 & \frac{1}{\sqrt{\lambda_1}} & 0 \\ 0 & 0 & \frac{1}{\sqrt{\lambda_1}} \end{bmatrix} \quad \text{and} \quad \sigma_{11} = \lambda_1 \frac{f_1}{A_1} = \lambda_1 P_{11}, \quad (3.3)$$

in which λ_1 is the stretch ratio, f_1 is the applied force along MFD direction, and in this case $f_1 = f_{11}$, σ_{11} is the Cauchy stress component, and A_1 is the reference cross-section area perpendicular to MFD. Similarly, for uniaxial stretch along CFD

$$\mathbf{F} = \begin{bmatrix} \frac{1}{\sqrt{\lambda_2}} & 0 & 0 \\ 0 & \lambda_2 & 0 \\ 0 & 0 & \frac{1}{\sqrt{\lambda_2}} \end{bmatrix} \quad \text{and} \quad \sigma_{22} = \lambda_2 \frac{f_2}{A_2} = \lambda_2 P_{22}, \quad (3.4)$$

where the applied force $f_2 = f_{22}$. The two pairs of unloading faces are stress-free.

Biaxial tests

For the shear-free biaxial test along MFD and CFD, since $A_1 = A_2 = A$, then

$$\mathbf{F} = \begin{bmatrix} \lambda_1 & 0 & 0 \\ 0 & \lambda_2 & 0 \\ 0 & 0 & \frac{1}{\lambda_1 \lambda_2} \end{bmatrix} \quad \text{and} \quad \sigma_{11} = \lambda_1 \frac{f_1}{A} = \lambda_1 P_{11}, \quad \sigma_{22} = \lambda_2 \frac{f_2}{A} = \lambda_2 P_{22}. \quad (3.5)$$

Again, in this case, we have $f_1 = f_{11}$, $f_2 = f_{22}$. The unloading top and bottom faces are stress-free.

If shear exists in the biaxial test as in Fig. 3.1 (e), $\gamma_{12} \neq 0$ and $\gamma_{21} \neq 0$, then

$$\mathbf{F} = \begin{bmatrix} \lambda_1 & \gamma_{12} & 0 \\ \gamma_{21} & \lambda_2 & 0 \\ 0 & 0 & \frac{1}{\lambda_1 \lambda_2 - \gamma_{12} \gamma_{21}} \end{bmatrix} \quad \text{and} \quad \sigma_{11} = \lambda_1 P_{11} + \gamma_{12} P_{12}, \quad \sigma_{22} = \lambda_2 P_{22} + \gamma_{21} P_{21}. \quad (3.6)$$

Here, we follow the similar assumption from Sommer's biaxial study [57], in which the sum of forces along the directions \mathbf{e}_1 and \mathbf{e}_2 are defined as

$$f_1 = f_{11} + f_{12}, \quad \text{and} \quad f_2 = f_{21} + f_{22}, \quad (3.7)$$

in which f_1 and f_2 are the measured forces, f_{11} , f_{12} , f_{21} and f_{22} are unknown forces which are the equivalent forces being imposed to the region-of-interest (red color) as shown in Fig. 3.2. Note that for the bi-axial test, the marked region in Fig. 3.2 is assumed to deform homogeneously. Although conventional biaxial soft tissue tests consider shear stress to be zero [78], given that Sommer's experimental data is used in this chapter, thus the same assumption about f_1 and f_2 is adopted here (Eq. (3.7)). We remark that future studies shall explore how to measure shear and normal forces separately.

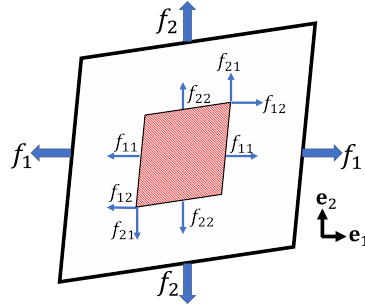


Figure 3.2: Schematic illustration of normal and shear forces for the marked region in a bi-axial test sample. The stress and strain fields in the central region (the red colour) are general considered homogeneous, while the tissue outside of the region-of-interest also stretch the central region, thus the measured force along \mathbf{e}_1 is $f_{11} + f_{12}$ and the measured force along \mathbf{e}_2 is $f_{21} + f_{22}$.

According to the maximum shear amounts in Ahmad's and Sommer's data, we further assume the shear in Eq. (3.6) increases linearly with stretch, that is

$$\gamma_{12} = k_1 \frac{\lambda_1 - 1}{\lambda_1^{\max} - 1}, \quad \text{and} \quad \gamma_{21} = k_2 \frac{\lambda_2 - 1}{\lambda_2^{\max} - 1}, \quad (3.8)$$

where k_1 and k_2 are the maximum values of γ_{12} and γ_{21} , λ_1^{\max} and λ_2^{\max} are maximum stretches along the two loading directions in the experiments.

Finally, the relationship between the first P-K stress components and the applied forces are

$$\begin{aligned}\frac{f_1}{A} &= \frac{f_{11}}{A} + \frac{f_{12}}{A} = P_{11} + P_{12} = (\boldsymbol{\sigma}\mathbf{F}^{-\text{T}})_{11} + (\boldsymbol{\sigma}\mathbf{F}^{-\text{T}})_{12}, \\ \frac{f_2}{A} &= \frac{f_{21}}{A} + \frac{f_{22}}{A} = P_{21} + P_{22} = (\boldsymbol{\sigma}\mathbf{F}^{-\text{T}})_{21} + (\boldsymbol{\sigma}\mathbf{F}^{-\text{T}})_{22}.\end{aligned}\quad (3.9)$$

Using Eq. (3.9), we can predict the applied forces using a chosen SEF and the prescribed deformation gradient tensor which consists of stretches (λ_1, λ_2) and shears $(\gamma_{12}, \gamma_{21})$, then by matching the predicted forces from a chosen SEF to the measured forces f_1 and f_2 , a set of material parameters can be obtained, see details in section 3.2.4.

Simple shear tests

For the simple shear tests, Fig. 3.1 (a), we have

$$\begin{aligned}(\text{ns}): \quad \mathbf{F} &= \begin{bmatrix} 1 & 0 & 0 \\ 0 & 1 & 0 \\ 0 & \gamma_{32} & 1 \end{bmatrix} & (\text{fn}): \quad \mathbf{F} &= \begin{bmatrix} 1 & 0 & 0 \\ \gamma_{21} & 1 & 0 \\ 0 & 0 & 1 \end{bmatrix} & (\text{sf}): \quad \mathbf{F} &= \begin{bmatrix} 1 & 0 & \gamma_{13} \\ 0 & 1 & 0 \\ 0 & 0 & 1 \end{bmatrix} \\ (\text{nf}): \quad \mathbf{F} &= \begin{bmatrix} 1 & \gamma_{12} & 0 \\ 0 & 1 & 0 \\ 0 & 0 & 1 \end{bmatrix} & (\text{fs}): \quad \mathbf{F} &= \begin{bmatrix} 1 & 0 & 0 \\ 0 & 1 & 0 \\ \gamma_{31} & 0 & 1 \end{bmatrix} & (\text{sn}): \quad \mathbf{F} &= \begin{bmatrix} 1 & 0 & 0 \\ 0 & 1 & \gamma_{23} \\ 0 & 0 & 1 \end{bmatrix}\end{aligned}\quad (3.10)$$

and in this case, the stress components are determined from

$$\boldsymbol{\sigma}_{ij} = P_{ij} = \frac{f_{ij}}{A}, \quad i \neq j \in \{1, 2, 3\}.\quad (3.11)$$

For each loading mode in Fig. 3.1 (a), the unloading faces are stress-free.

3.2.3 Effective fibre contribution

The rotation of collagen fibres from epicardium to endocardium plays a significant role in the myocardial mechanical response. Thus, it is necessary to consider fibre rotation in tested samples when fitting constitutive laws to experimental data. We further assume collagen fibres (along with myocytes) only lie in the $\mathbf{f}_0 - \mathbf{n}_0$ plane. Considering a myocardial sample with linearly rotated fibres from θ_1 to θ_2 as shown in Fig. 3.1 (f), the local fibre angle related to the MFD with a depth of h is

$$\theta(h) = \frac{\theta_2 - \theta_1}{H_0} h + \theta_1,\quad (3.12)$$

where H_0 is the total thickness of the sample, and the local $\mathbf{f}_0 - \mathbf{n}_0 - \mathbf{s}_0$ system is

$$\mathbf{f}_0 = (\cos \theta, \sin \theta, 0), \quad \mathbf{n}_0 = (-\sin \theta, \cos \theta, 0) \quad \text{and} \quad \mathbf{s}_0 = (0, 0, 1).$$

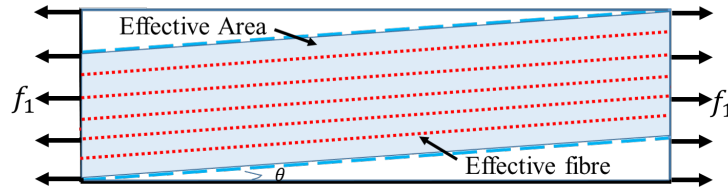


Figure 3.3: Schematic illustration of the effective area (blue) when the fibre direction is θ under uniaxial loading in the MFD test. The collagen fibres (red dot line) within the region enclosed by the two blue dashed lines are defined as effective fibres that are stretched both sides. The effective fibre ratio is defined by rectangle area dividing blue effective area.

Different to the 3D FE simulations, the method in this chapter is to treat a whole specimen as a material point to reproduce the stress-strain relationships in the measurements by using the SEF. However, the above typical experiments were performed on tissue level with different loading conditions, which involved different amounts of fibre recruitment when including fibre rotation in the specimen. Because collagen fibres can only bear the load when stretched, to further describe the effective fibre amount under different deformations, factors based on analysis of deformations are coupled to the initial strain energy function (Eq. (3.1)), that is

$$\Psi(\theta) = \psi_1 + \alpha_{4f}(\theta)\psi_{4f} + \alpha_{4s}(\theta)\psi_{4s} + \alpha_{4n}(\theta)\psi_{4n} + \psi_{8fs} + \psi_{8fn} + \psi_{8sn}, \quad (3.13)$$

in which ψ_i is the strain energy term associated with the invariant of I_i in Eq. (3.1). Values of $\alpha_{4f}(\theta)$, $\alpha_{4s}(\theta)$ and $\alpha_{4n}(\theta)$ will depend on the experimental loading conditions and the fibre structure of tested samples, but not for I_{8fs} , I_{8fn} and I_{8sn} which are dependent on the angles between different directions. For example, in an uniaxial test along the MFD as shown in (Fig. 3.3), only when fibres are attached to both ends (the most left and right sides), or in the shaded area in Fig. 3.3, can they be stretched along the MFD and contribute to the stress response. If the fibres have one or two stress-free ends (e.g. the unshaded area in Fig. 3.3), they will not be stretched and not contribute to the stress response. $\alpha_{4f}(\theta)$ is defined as the ratio between the shaded blue area and the total area of the sample as shown in Fig. 3.3, denoting the effective fibre ratio. Similarly, collagen aligned in the CFD may contribute to the stress response depending on the size of the sample, the fibre angle and the experimental set-up. Collagen in the sheet direction are not stretched, which means they do not contribute to the uniaxial test; therefore, for the uniaxial test in Fig. 3.3, the effective fibre ratios are

$$\begin{aligned} \alpha_{4f}(\theta) &= \begin{cases} 1 - \frac{L_0}{W_0} |\tan(\theta)| & \text{for } -\theta_0 < \theta < \theta_0, \\ 0 & \text{for others,} \end{cases} \\ \alpha_{4n}(\theta) &= \begin{cases} 1 - \frac{L_0}{W_0} |\cot(\theta)| & \text{for } \frac{\pi}{2} - \theta_0 < \theta < \frac{\pi}{2} \text{ or } -\frac{\pi}{2} < \theta < -\frac{\pi}{2} + \theta_0, \\ 0 & \text{for others,} \end{cases} \\ \alpha_{4s}(\theta) &= 0. \end{aligned} \quad (3.14)$$

where W_0 and L_0 are the width and length of the tested sample in the $\mathbf{f}\text{-}\mathbf{n}$ plane, and $\theta_0 = \arctan \frac{W_0}{L_0}$. In biaxial tests, because the four sides are stretched along two directions simultaneously in the fibre-normal plane, thus

$$\alpha_{4f}(\theta) = \alpha_{4n}(\theta) = 1, \quad (3.15)$$

and $\alpha_{4s}(\theta) = 0$ because the fibre in \mathbf{s} direction is compressed.

There are six different shear modes, fibre effective ratio will be different in every shear mode. If assuming the fibre rotation is from $-\frac{\pi}{4}$ to $\frac{\pi}{4}$ and the specimen is a cube, then we have

$$(fs) : \quad \alpha_{4f}(\theta) = \begin{cases} 1 - |\tan(\theta)| & \text{for } -\frac{\pi}{4} < \theta < \frac{\pi}{4} \end{cases} \quad \alpha_{4s}(\theta) = \alpha_{4n}(\theta) = 0, \quad (3.16)$$

$$(fn) : \quad \alpha_{4f}(\theta) = \begin{cases} 1 - |\tan(\theta)| & \text{for } 0 \leq \theta < \frac{\pi}{4} \\ 0 & \text{for } -\frac{\pi}{4} < \theta < 0 \end{cases} \quad \alpha_{4s}(\theta) = \alpha_{4n}(\theta) = 0, \quad (3.17)$$

$$(sf) : \quad \alpha_{4s}(\theta) = \begin{cases} 1 & \text{for } -\frac{\pi}{4} \leq \theta < \frac{\pi}{4} \end{cases} \quad \alpha_{4f}(\theta) = \alpha_{4n}(\theta) = 0, \quad (3.18)$$

$$(sn) : \quad \alpha_{4s}(\theta) = \begin{cases} 1 & \text{for } -\frac{\pi}{4} \leq \theta < \frac{\pi}{4} \end{cases} \quad \alpha_{4f}(\theta) = \alpha_{4n}(\theta) = 0, \quad (3.19)$$

$$(nf) : \quad \alpha_{4n}(\theta) = \begin{cases} 0 & \text{for } 0 \leq \theta < \frac{\pi}{4} \\ 1 - |\tan(\theta)| & \text{for } -\frac{\pi}{4} < \theta < 0 \end{cases} \quad \alpha_{4f}(\theta) = \alpha_{4s}(\theta) = 0, \quad (3.20)$$

$$(ns) : \quad \alpha_{4n}(\theta) = \begin{cases} 1 - |\tan(\theta)| & \text{for } -\frac{\pi}{4} < \theta < \frac{\pi}{4} \end{cases} \quad \alpha_{4f}(\theta) = \alpha_{4s}(\theta) = 0. \quad (3.21)$$

The first P-K stress tensor in a myocardium layer ($\det(\mathbf{F}) = 1$) with a specific fibre angle θ is

$$\mathbf{P}^\theta = \mathbf{F} \frac{\partial \Psi(\theta)}{\partial \mathbf{F}} \mathbf{F}^{-T} - p \mathbf{F}^{-T}. \quad (3.22)$$

Because the local fibres in a test sample rotate from θ_1 to θ_2 transmurally (as shown in Fig. 3.1 (f)), the total first P-K stress tensor for the sample is approximated as:

$$\mathbf{P} = \frac{1}{\theta_2 - \theta_1} \int_{\theta_1}^{\theta_2} \mathbf{P}^\theta d\theta. \quad (3.23)$$

3.2.4 Parameter estimation

For Dokos et al. study, all six shear experiments are used for formulating (Eq. (3.24)). For Sommer et al. study, we fit the SEFs using both the biaxial and simple shear tests. All three modes of experimental data from Ahmad et al. study are combined together. Material parameters are estimated using a non-linear least square minimization function (*fmincon* from MatLab, MathWorks 2017) with upper and lower limits of the parameter values, and the involved loss function is

$$L(\beta) = \sum_{n=1}^N [\mathcal{P}^{n,\text{pre}}(\beta) - \mathcal{P}^{n,\text{exp}}]^2, \quad (3.24)$$

where β denotes the set of unknown parameters, N is the total number of data points, $\mathcal{P}^{n,\text{pre}}$ are the model-prediction values, and $\mathcal{P}^{n,\text{exp}}$ are the experimental values. Please note $\mathcal{P} = P_{11}$ or $\mathcal{P} = P_{22}$ in the uniaxial tests, $\mathcal{P} = P_{11} + P_{12}$ or $\mathcal{P} = P_{21} + P_{22}$ in the biaxial tests, and $\mathcal{P} = P_{ij}$ in the simple shear tests with $i \neq j \in \{1, 2, 3\}$.

The relative and absolute difference of the area-under-the-curve between the experimental and fitted stress-strain curves ($\text{err}^{\text{Relative}}$, $\text{err}^{\text{Absolute}}$) are introduced to quantitatively describe the goodness-of-fit,

$$\begin{aligned}\text{err}^{\text{Relative}} &= \frac{\sum_{n=1}^N \Delta \lambda_n |P_n(\beta) - P_n^{\text{exp}}|}{\sum_{n=1}^N \Delta \lambda_n P_n^{\text{exp}}}, \\ \text{err}^{\text{Absolute}} &= \sum_{n=1}^N \Delta \lambda_n |P_i(\beta) - P_n^{\text{exp}}|,\end{aligned}\tag{3.25}$$

in which $\Delta \lambda_n$ is the stretch increment. A value of 0 indicates a perfect fitting.

3.2.5 Reduced HO models

Some of the invariants may be excluded in the general HO model when applied to human myocardium, whilst still achieving a good agreement with experimental data. For example, Holzapfel and Ogden [11] reported that after dropping I_{4n} , I_{8fn} and I_{8sn} from the general HO model, they could still fit the six shear tests [55] very well; hence, they proposed an 8-parameter HO model (HO2009),

$$\begin{aligned}\Psi &= \frac{a}{2b} \exp[b(I_1 - 3)] + \sum_{i=f,s} \frac{a_i}{2b_i} \{\exp[b_i(\max(I_{4i}, 1) - 1)^2] - 1\} \\ &+ \frac{a_{fs}}{2b_{fs}} [\exp(b_{fs} I_{8fs}^2) - 1].\end{aligned}\tag{3.26}$$

The reason for excluding I_{8fn} and I_{8sn} is because the two shear responses marked as (nf) and (ns) were not distinguishable based on Dokos et al. data. There lacks, however, a study investigating whether the general HO and HO2009 can fit all other myocardial experiments well, such as human myocardium in [4].

Reducing the general HO model (Eq. (3.1)) is advantageous, as so many strain invariants and material parameters prevent efficient personalized cardiac simulations. Furthermore, multiple sets of optimal material parameters from limited experimental data can lead to different simulation results for a given boundary-value problem [168]. To derive a simplified but competent SEF, the AIC analysis [169] is employed in this study to reduce the general HO model, which is defined as

$$\text{AIC} = N \ln \left[\frac{1}{N} L(\beta) \right] + 2K,\tag{3.27}$$

where K is the number of model parameters. AIC is typically used for model selection by considering both the model complexity and the loss function. The best model is the one with

the lowest AIC value. This approach has previously been used by [41] to compare five different myocardial SEFs. Note the AIC in (Eq. (3.27)) is negative when the fitting is good. Therefore, for any two different models and the same experimental data, the one with the more negative AIC value suggests a better fitting. Similar AIC values represent comparable models. In this study, we consider various reduced forms of Eq. (3.1). This allows us to drop the terms in Eq. (3.1) that make little change in the AIC value. This way we can select the simplest SEF that fits to the test data. To this end, we introduce the AIC ratio:

$$\eta = \frac{\text{AIC}_{\text{reduced}}^{\text{model}}}{\text{AIC}_{\text{general}}^{\text{model}}} \quad (3.28)$$

where η represents the ratio of AIC values of a reduced and the general HO model for the same experimental data. The more negative AIC, the better goodness-of-fit. The closer to 1 of η , the more accurate approximation of the reduced HO model to the general HO model.

We aim to simplify the general HO model with a subset of strain invariants, $\mathbb{I} = \{I_{4f}, I_{4s}, I_{4n}, I_{8fs}, I_{8fn}, I_{8sn}\}$, for effectively characterizing different experimental studies. The steps for reducing the general HO model are

- Step 1: Initialize the reduced HO model that is the same as the general HO model, and $\eta = 1$;
- Step 2: Compute a η_i value while removing the term with one invariant I_i in the subset \mathbb{I} from the reduced model;
- Step 3: Repeat step2 k times (k is the length of \mathbb{I}) when iterating through all I_i in the subset \mathbb{I} ;
- Step 4: Compare all η_i values. If the greatest η_i is bigger than a predetermined threshold ε , the reduced HO model is updated by dropping the term with I_i , the subset \mathbb{I} is updated by deleting the I_i and the computation goes to step 2. Otherwise, the computation stops.

In this study, we chose ε to be 0.95.

We further compare the modelling accuracy between the general and various reduced HO models using a 3D FE bi-ventricular model, which is reconstructed from 3D computed tomography (CT) data. Details of the data acquisition can be found in [9]. The 3D CT data is first segmented using Seg3D¹, then the boundary contours are exported into SolidWorks (Dassault Systemes, MA USA) for 3D geometry reconstruction, and then meshed with ICM (ANSYS, Inc. PA USA). Finally, explicit Abaqus (Dassault Systemes, MA USA) is used for the FE simulation. User-subroutines are implemented for different strain energy functions. Diastolic filling

¹<http://www.sci.utah.edu/cibc-software/seg3d.html>

in the LV (Fig. 3.4 (a)) is simulated with layered myofibre rotating from the epicardial to endocardial surface (Fig. 3.4 (b)), with rotation angles measured from experimental studies using a rule-based approach [7].

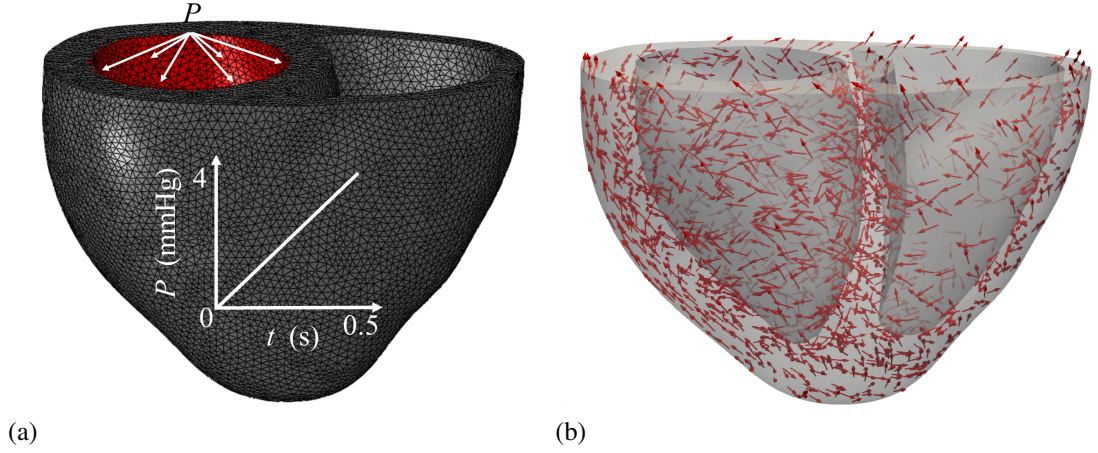


Figure 3.4: (a) depicts the 3D FE bi-ventricle mesh geometry with boundary condition that applies pressure in LV inner surface (red surface). Pressure linearly increases from 0 to 4 mmHg in a period of 0.5s. (b) describes the myofibre distribution in the ventricle wall, which rotates from epicardium to endocardium (60° to -60°).

3.2.6 Optimal combination of experiments through predictive analysis

Likewise, we can use AIC method to determine the optimal combination of experiments using minimum tests. For a given SEF, we firstly fit it to a subset of experimental data with N_s data points, then use it to predict the remaining points ($N - N_s$). We introduce a similar AIC ratio

$$\delta = \frac{\text{AIC}_{\text{subset}}^{\text{exp}}}{\text{AIC}_{\text{all}}^{\text{exp}}}. \quad (3.29)$$

where $\text{AIC}_{\text{subset}}^{\text{exp}}$ and $\text{AIC}_{\text{all}}^{\text{ext}}$ are computed using parameters optimised from a subset or all combinations of experimental data, respectively. We don't consider cases when δ becomes negative. Hence, δ denotes the AIC change of using different combinations of experiments for a same model. We choose the criterion for the best combination to be the minimum group of tests which satisfies $\delta \geq 0.8$. This corresponds to about 5% change of the relative error in Eq. (3.25)). The pseudo-code for this analysis is listed in Algorithm 1.

Algorithm 3.1 The predictive analysis for determining the optimal combination with minimal tests

Data:

Λ : number of total tests of experimental data;
 m : m combinations of the tests used for model fitting;
 k : case number;

Result: δ_k : δ value for case k .

Initialization: $k = 0$

Through Λ : $\beta_{\text{opt}}^{\text{all}} = \operatorname{argmin}_{\beta} \{L(\beta) = \sum_{i=1}^{N_s} [P_i(\beta) - P_i^{\text{exp}}]^2\}$

and $\text{AIC}_{\text{all}}^{\text{exp}} = N \ln \left[\frac{1}{N} L(\beta_{\text{opt}}^{\text{all}}) \right] + 2K$

for $m=1$ to Λ : **do**

for $\Lambda^* = 1 : \binom{\Lambda}{m}$ **do**

$k = k+1$;

$\beta_{\text{opt}} = \operatorname{argmin}_{\beta} \{L(\beta) = \sum_{i=1}^{N_s} [P_i(\beta) - P_i^{\text{exp}}]^2\}$,

$\text{AIC}_{\text{subset}}^{\text{exp}} = N \ln \left[\frac{1}{N} L(\beta_{\text{opt}}) \right] + 2K$

$\delta_k = \frac{\text{AIC}_{\text{subset}}^{\text{exp}}}{\text{AIC}_{\text{all}}^{\text{exp}}}$

end

end

We considered any combinations of

1. Dokos et al. simple shear: $\Lambda = \{(fs), (fn), (sf), (sn), (nf), (ns)\}$;
2. Sommer et al. data:
 $\Lambda = \{1 : 1, 1 : 0.75, 0.75 : 1, 1 : 0.5, 0.5 : 1, (fs), (fn), (sf), (sn), (nf), (ns)\}$;
3. Ahmad et al. data: $\Lambda = \{\text{MFD}, \text{CFD}, 1 : 1(\text{equal force}), (sf), (sn)\}$.

3.3 Results

3.3.1 The general HO strain energy function

Fig. 3.5 (a) shows the results by fitting the general HO model to the Dokos et al. shear tests. Improved agreement can be found when including the effective fibre ratio (AIC: -589.3) compared to without (AIC: -464.7), whilst the mean relative error also decreases from 15.9% to 9.3%. When fitting all test data from Ahmad et al. study with the effective fibre ratio, the AIC value is reduced significantly from -338.5 to -1170.3 (shown in Figs. 3.5(b – d)), whilst the relative errors for the uniaxial test along the MFD decrease from 36.06% to 4.25%, and from 26.76% to 6.97% for the biaxial test along the CFD.

In Ahmad et al. data, we estimate $k_1 = 0.18$ and $k_2 = 0.05$ using markers for the sample angle changes (Fig. 3.1 (d,e)). In the Sommer et al.'s data [4], no information on the shear

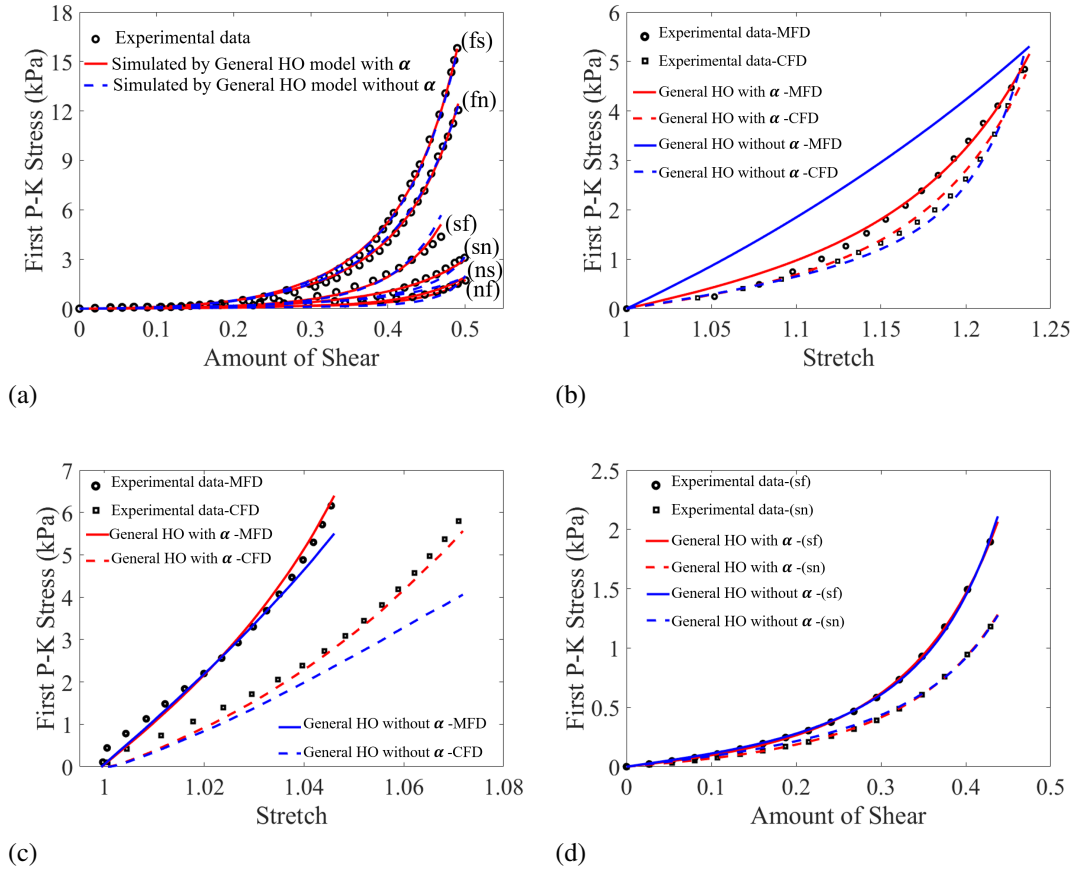


Figure 3.5: Comparison of the fitting results with and without considering fiber effective ratio (α). (a) fitting the general HO model to Dokos's data, (b)-(d) describe the differences in uniaxial, biaxial and simple shear tests in Ahmad's data.

measurements is available. However, we assume the maximum shear angles in both MFD and CFD in Sommer et al. biaxial tests are around 6° , i.e. $k_1 = k_2 \approx 0.1$ [57, 170], which is necessary for a good fit to their experiments. As for Ahmad et al. and Sommer et al. biaxial test, the difference of with and without shear for the same model in Fig. 3.6 indicates inclusion of the shear component is critical when fitting biaxial experimental tests, since for fibre-reinforced material, it is almost impossible to conduct biaxial tests without inducing shear [171].

Fig. 3.7 (a) demonstrates that both the general HO (AIC: -589.3) and HO2009 (AIC: -559.3) models can fit Dokos et al. shear test data very well, while noticeable differences can be found when fitting the two material models to Sommer et al. data (Figs. 3.7(b, c), where only plotting one set (MFD:CFD=1:1) experimental data, whilst the rest four sets have similar results and are included in Fig. 3.13. Better agreement is achieved for the general HO model (AIC: -1102.6) than the HO2009 model (AIC: -849.5). Figs. 3.7(d, e, f) show the results when fitting the two models to Ahmad's data. Again, much better agreement can be found when using the general HO model (AIC: -1170.3) compared to the HO2009 model (AIC: -423.1), in particular the HO2009 model fails to fit the shear test in (Fig. 3.7 (f)).

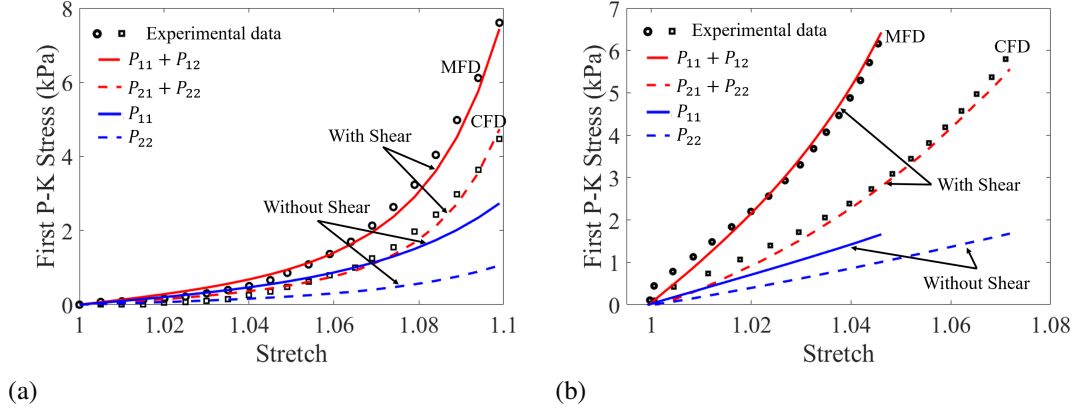


Figure 3.6: Comparison of the First P-K stress, including shear (red) and not including shear (blue) using same SEF. (a) is for Sommer et al. biaxial test and a minimum shear angle of 6° is introduced. Below 6° there is no good fit, above it is not supported by Sommer et al. experiments. (b) is for Ahmad et al. biaxial test, corresponding to Fig. 3.8 (e)

3.3.2 Reduced strain energy functions based on AIC analysis

Although the general HO model can fit the three selected experimental studies very well as shown in Fig. 3.7, it includes seven invariants with fourteen unknown parameters, which can be extremely challenging to obtain a unique solution when fitting to limited experimental data. A reduced form, such as the HO2009 model, is desirable for constructing personalized models [2, 75, 76]. However, since HO2009 is derived from fitting the Dokos et al. data only, if such a model fails to describe other experimental data, we need to have strategies in place to derive a better reduced model with test data available for tissues of interests.

In this work, alternative reduced SEFs are identified from the general HO model for selected experimental studies based on the AIC analysis. Fig. 3.8 (a) reports η values when individually excluding each invariant from the general HO model (Eq. (3.1)) and fitting to three experimental studies. For Dokos et al. data, I_{4n} , I_{8fn} and I_{8sn} have much less contribution to the agreement compared to I_{4f} , I_{4s} and I_{8fs} , because η remains more than 0.95 when dropping these terms. This means I_{4n} , I_{8fn} and I_{8sn} can be dropped from (Eq. (3.1)), and it can now be denoted as HO-D, which actually equates to the HO2009 model (Eq. (3.26)). In other words, η is reduced by 3% when using the HO-D model (HO2009) to replace the general HO model. Similarly, invariants I_{4s} , I_{8fn} and I_{8sn} may be excluded from the general HO model when fitting to Sommer et al. biaxial and simple shear data. This gives us a reduced SEF for Sommer's data (HO-S) at a 4% of drop in η ,

$$\Psi = \frac{a}{2b} \exp[b(I_1 - 3)] + \sum_{i=f,n} \frac{a_i}{2b_i} \{ \exp[b_i(\max(I_{4i}, 1) - 1)^2] - 1 \} + \frac{a_{fs}}{2b_{fs}} [\exp(b_{fs} I_{8fs}^2) - 1]. \quad (3.30)$$

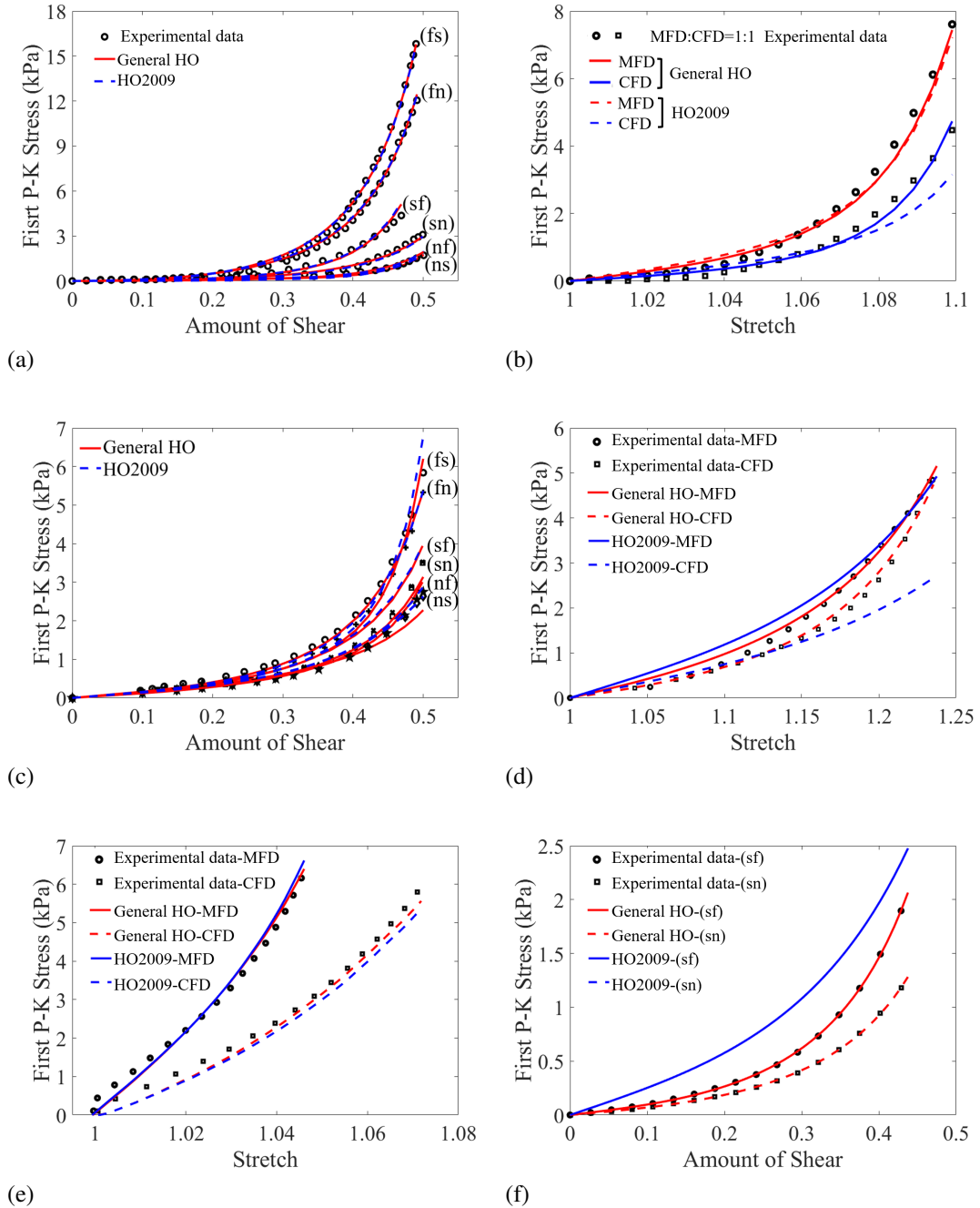


Figure 3.7: Comparison between descriptive ability of the general HO and the HO2009 models for the three experimental studies. (a): Dokos's simple shear tests; (b) and (c): Sommer's biaxial tension and simple shear tests; (d-f): Ahmad's uniaxial, biaxial tension and simple shear tests.

Fig. 3.8 (c) is the fitting results of the HO-S model to various biaxial tests with different stretch ratios, and fitting results to the shear tests in Fig. 3.8 (d). Notice, good agreement for Sommer's biaxial data can only be achieved when a small amount of shear is included. The reduced model

for Ahmad et al. data in Fig. 3.8 (a), (HO-A), is similarly determined

$$\begin{aligned} \Psi = & \frac{a}{2b} \exp[b(I_1 - 3)] + \sum_{i=f,n} \frac{a_i}{2b_i} \{ \exp[b_i(\max(I_{4i}, 1) - 1)^2] - 1 \} \\ & + \sum_{ij=fs,fn} \frac{a_{ij}}{2b_{ij}} [\exp(b_{ij}I_{8ij}^2) - 1], \end{aligned} \quad (3.31)$$

in which I_{4s} , and I_{sn} are excluded from the general HO model, and the η is only reduced by 0.015. Figs. 3.8(e - g) show the fitting results to the uniaxial stretch, biaxial stretch and simple shear tests, respectively. Again, the HO-A model has good descriptive capability for Ahmad et al. experiments. All estimated parameters for the HO-D (HO2009), HO-S and HO-A models and the fitting errors with their corresponding experimental data, can be found in Tables 3.1 and 3.2.

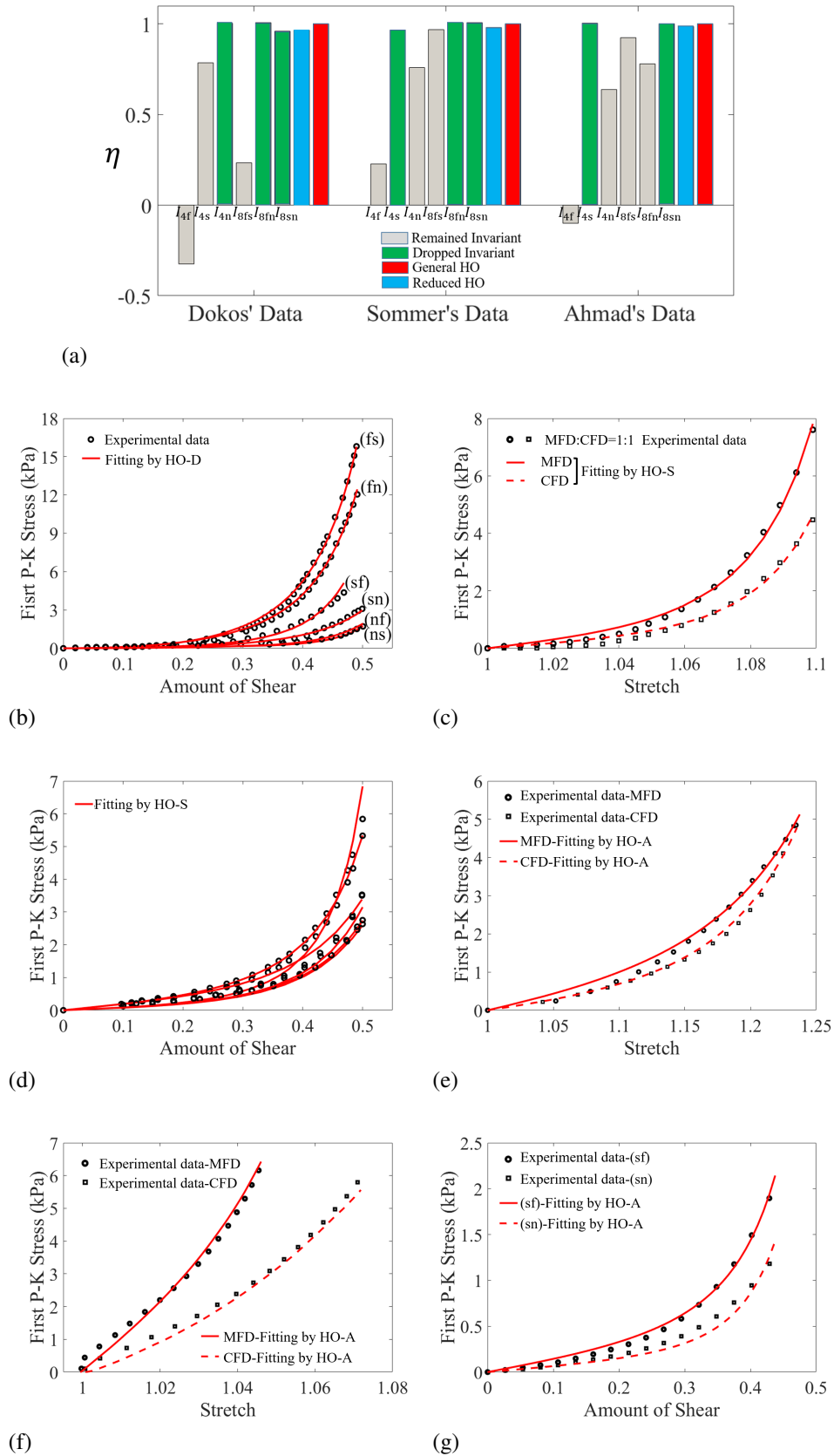


Figure 3.8: Descriptive capability of reduced HO models. (a) Change of η when dropping the terms associated with the invariants for the different three experiments. The fitting results for the HO-D model (b), and (c-d) the HO-S model, and (e-g) the HO-A model.

		a (kPa)	b	a_f (kPa)	b_f	a_s (kPa)	b_s	a_n (kPa)	b_n	a_{fs} (kPa)	b_{fs}	a_{fn} (kPa)	b_{fn}	a_{sn} (kPa)	b_{sn}
Dokos et al	HO-D	0.073	15.529	25.992	9.348	4.822	0.001	-	-	0.178	16.740	-	-	-	-
Sommer et al	HO-S	0.809	7.474	1.911	22.063	-	-	0.227	34.802	0.547	5.691	-	-	-	-
Ahmad et al	HO-A	0.075	18.143	7.067	1.339	-	-	2.745	4.497	1.859	4.066	3.541	8.222	-	-

Table 3.1: The estimated parameters for the reduced HO models fitting to corresponding experimental studies.

Experiment	Model	Relative Error (%) and Absolute Error (kPa)																Mean	
		(fs)	(fn)	(sf)	(sn)	(nf)	(ns)	1:1		1:0.75		0.75:1		1:0.5		0.5:1			
Dokos et al	HO-D	%:	2.96	4.43	12.55	12.10	13.37	16.87											10.38
		kPa:	0.12	0.14	0.14	0.11	0.08	0.10											
Sommer et al	HO-S		1:1		1:0.75		0.75:1		1:0.5		0.5:1		(fs)	(fn)	(sf)	(sn)	(nf)	(ns)	
		%:	MFD	CFD	MFD	CFD	MFD	CFD	MFD	CFD	MFD	CFD	6.39	15.10	12.34	21.92	5.31	8.54	14.32
		kPa:	0.18	0.13	0.16	0.10	0.15	0.06	0.16	0.07	0.14	0.08	0.11	0.23	0.13	0.22	0.05	0.08	0.13
			Uniaxial		Biaxial		Simple shear												
Ahmad et al	HO-A	%:	4.72	4.08	5.95	6.96	7.15	14.61											7.24
		kPa:	0.02	0.01	0.04	0.04	0.001	0.005											

Table 3.2: Relative and absolute errors for the reduced HO models when fitting to corresponding experimental studies.

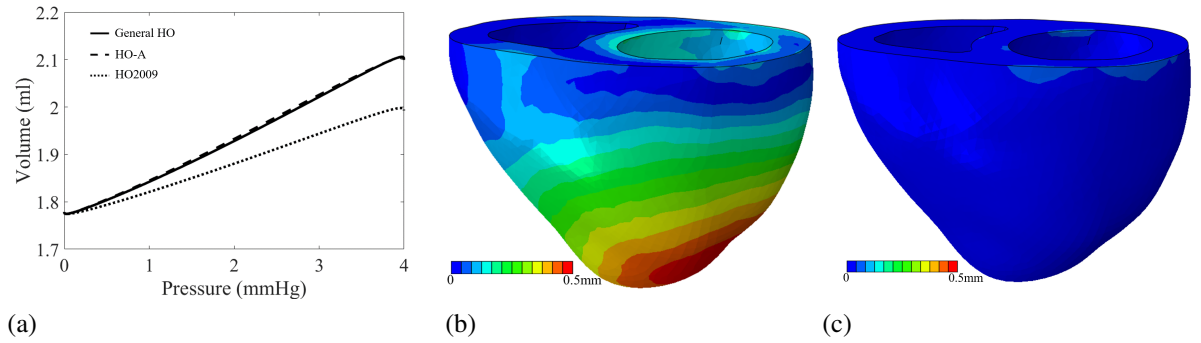


Figure 3.9: The differences of FE bi-ventricle model using the HO2009, HO-A and general HO models for Ahmad et al. data. (a) the PV curve in diastolic filling, (b) the displacement differences between the general HO and HO2009 models, and (c) the displacement differences between the general HO and HO-A models.

Fig. 3.9 (a) describes the LV pressure-volume (PV) relationship from the 3D FE bi-ventricle model using the general HO, HO2009 and HO-A models with parameters determined from Ahmad et al. study. Nearly identical PV relationships can be found between the general HO and HO-A models; however, the ventricle is stiffer when using the HO2009 model even though the parameters are determined using the same experimental data. This appears to indicate that the HO2009 model cannot effectively characterize Ahmad et al. myocardial samples. We further compare the displacement differences among different material models based on Ahmad et al. data. The displacement differences between the general HO and HO-A models are nearly negligible (Fig. 3.9 (c)), but large discrepancies exist for the HO2009 model (Fig. 3.9 (b)).

3.3.3 Optimal combination of experimental tests

To find the optimal combination of tissue tests, we use reduced HO models and a random initialization strategy to get the average value of δ , $avg(\delta)$, and its corresponding standard deviation, std .

Combinations from Dokos et al. data As shown in Fig. 3.10 (a), in addition to all tests, case 25 ((fs) + (fn) + (ns)), case 42 ((fs) + (fn) + (sf) + (sn)), case 57 ((fs) + (fn) + (sf) + (sn) + (nf)) meet the criterion of $avg(\delta) \geq 0.8$. Clearly, case 25 is the optimal combination.

Combinations from Sommer et al. data Fig. 3.11 (a) displays partial $avg(\delta)$ values of Sommer et al. AIC analysis when combining different biaxial and simple shear test data using the HO-S model, for clarity, only group 1, 2, 3, 5 and 6 are shown. The best combination is case 20 ((1:1)+(nf)). In particular, case 562 ((1:1)+(1:0.75)+(0.75:1)+(1:0.5)+(0.5:1)) is the combination of all biaxial data and has negative δ value, suggesting using biaxial data only cannot predict the simple shear responses. Likewise, using simple shear tests only, case 1484 ((fs) + (fn) + (sf) + (sn) + (nf) + (ns)), is unable to predict biaxial data. Therefore, both biaxial and simple shear test data are needed when characterizing myocardial properties. This agrees

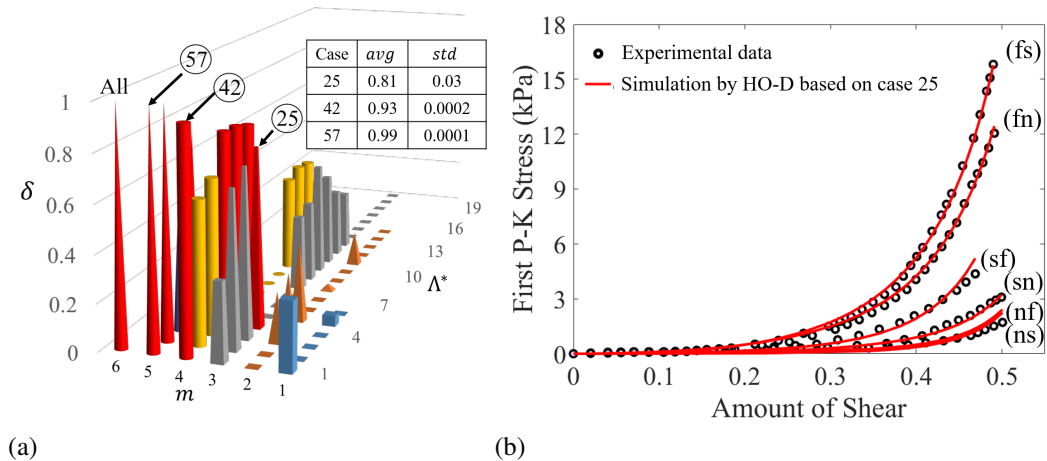


Figure 3.10: δ values that are computed according to Algorithm 1, where the cases whose average (*avg*) $\delta \geq 0.8$ are marked in red. (a) In Dokos et al. experiments, case 25 ((fs)+(fn)+(ns)) is the optimal case which has few tests while meeting the criterion, (b) shows the corresponding fitting curves using case 25.

with the observation by Holzapfel and Ogden [11]. Figs. 3.11(c) and (d) show the stress of biaxial tests and simple shear tests with parameters determined from stress responses in (1:1)+(nf).

Combinations from Ahmad et al. data In Fig. 3.12, apart from all tests, none of other combinations meet $\delta \geq 0.8$ in Ahmad et al. study. The fitting curves using all the tests are already in Fig. 3.8 (e,g,f).

3.4 Discussion

This study focuses on a rational reduction of the general HO model for the myocardial tissue responses. Three different myocardial experiments are selected, including Dokos et al. study on porcine myocardium over a decade ago [55], Sommer et al. study on human myocardium published several years ago [4], and the very recent experimental data from [9] on neonatal porcine myocardium [9]. To our best knowledge, these are the most comprehensive myocardial mechanical experiments. [55] is the first presenting simple shear tests to characterize the direction-dependent myocardial mechanical property, which has driven new developments in SEF and led to the extensive use of the HO2009 model [11]. [4] included biaxial and simple shear tests, with both needed for characterizing an orthogonal hyperelastic material [11]. We show, for the first time, that the general HO model is very good as describing stress responses from different deformation types as shown in Fig. 3.7.

A number of studies have used the HO-based SEFs (mostly HO2009 model) to construct personalized biomechanical models [2, 70, 73]. The widely successful application of the HO-type models suggests it is good for characterizing myocardial mechanical properties and provides the natural starting-point to optimise the general HO model for specific tissue types, aiming to

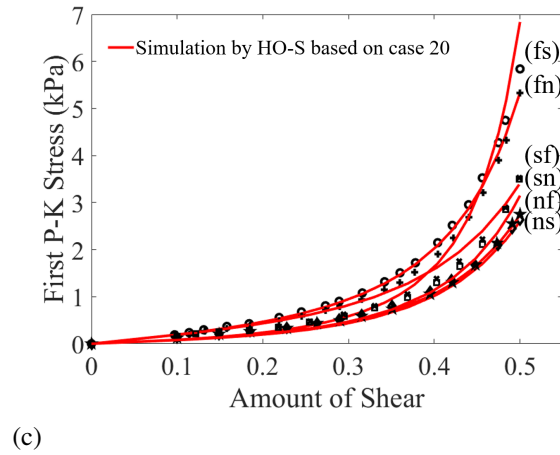
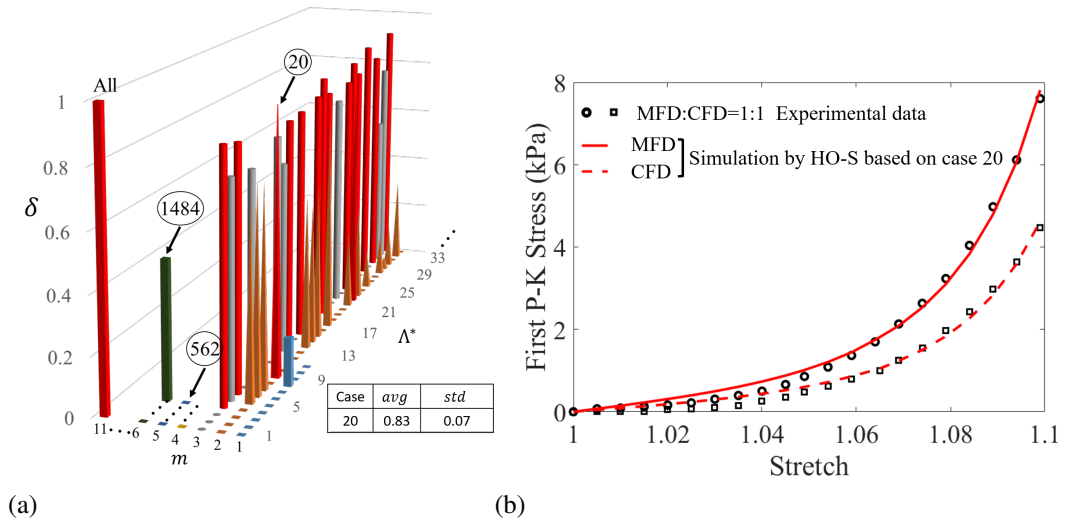


Figure 3.11: In Sommer et al. experiments, Case 20 ((1:1)+(nf)) is the optimal case in (a), the corresponding fitting curves are shown in (b) and (c).

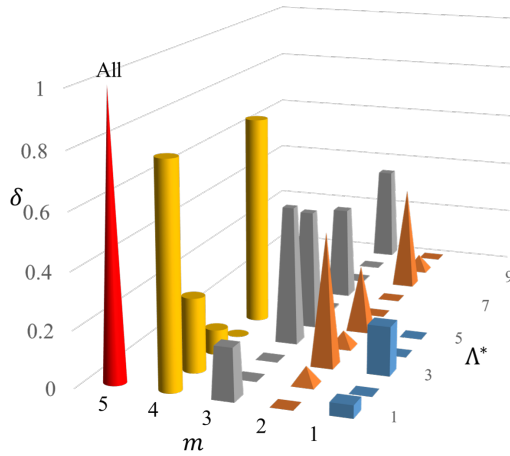


Figure 3.12: In Ahmad et al. experiments, case ALL is the only one which satisfies the criterion. The other cases are corresponding to certain combinations to be discussed in the text.

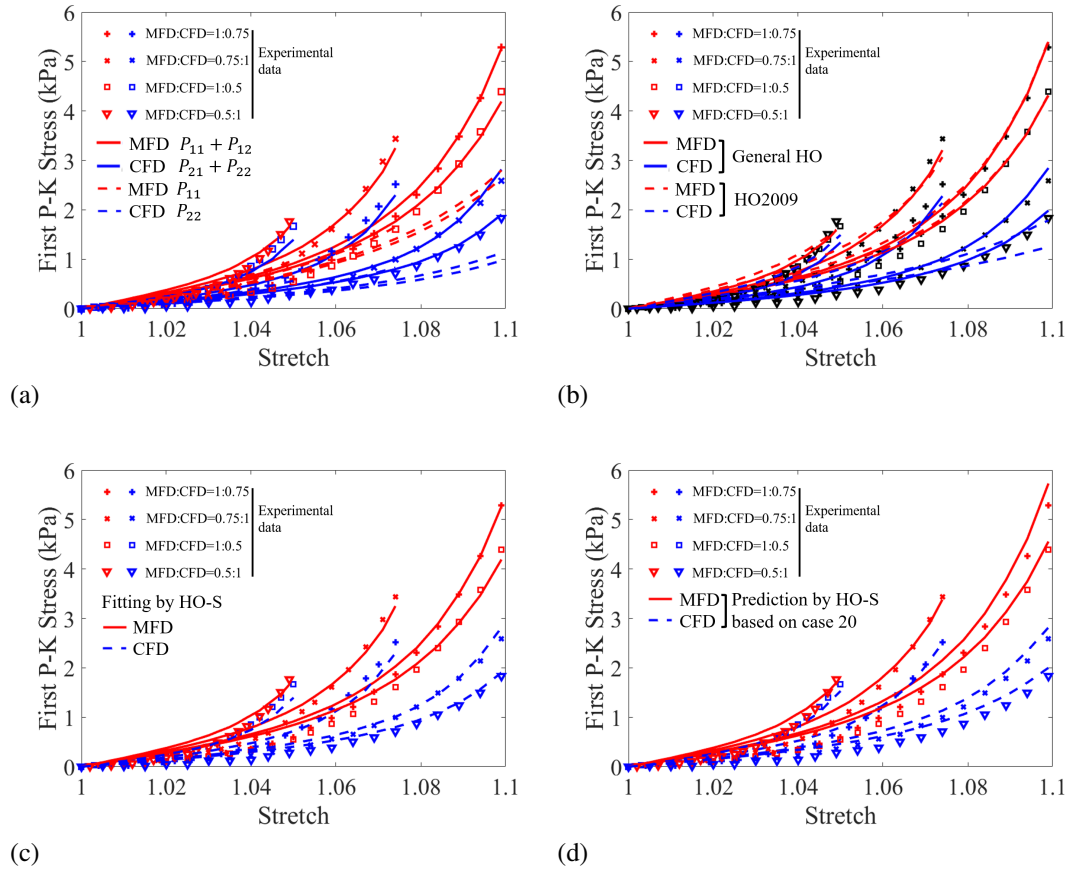


Figure 3.13: The rest four loading protocols ((1:0.75), (0.75:1), (1:0.5) and (0.5:1)) for Sommer et al. biaxial tests. (a) compares the First P-K stress including shear (solid lines) or not (dash lines) as in Fig. 3.6 (a). (b) is the comparison between the general HO model and HO2009 model in Fig. 3.7 (b). (c) is fitting results using the reduced HO model (HO-S) in Fig. 3.8 (c). (d) is the simulated results according to optimised combinations (1:1)+(nf) in Fig. 3.11 (b).

achieve the least terms and yet retaining sufficient descriptive and predictive capability. However, it has been recognized that the HO2009 model has its limitations (Fig. 3.7). This is because their model reduction is based on Dokos et al. simple shear data only, which did not include all responses of the myocardial tissues.

In the past several decades, efforts have been made to develop a SEF with fewest terms, whilst accurately describing the test data and predicting the dynamics [172]. A simplified but competent material model not only reduces computational cost, but is also easy to implement and personalize from limited test data. In this study, the AIC analysis is employed to systematically reduce the general HO model, whilst maintaining good descriptive and predictive capabilities. An invariant is excluded from the general HO model if it causes only a small change in the resultant AIC value. For instance, Fig. 3.8 (a) suggests that I_{4n} , I_{8fn} and I_{8sn} could be excluded when fitting to the Dokos et al. data, which is the same formulation as the HO2009 model. Other approaches can also be used for model reduction and selection, such as parameter sensitivity analysis by setting those insensitive parameters to constant values or zero [173].

Interestingly, the reduced HO models are different for the selected experimental studies. Presumably this is because these tests were for different species and ages, Dokos et al. [55] used adult porcine myocardium, Ahmad et al. [9] used the neonatal porcine myocardium, and Sommer et al. [4] worked on human myocardium. When fitting to the biaxial tests only from Sommer et al. data, the general HO model can be simplified to a reduced form consisting of only I_1 and I_{4f} , similar to the findings reported in [11]. This is because in the biaxial tests, collagen fibres are only stretched in fibre-normal plane, but not in the sheet direction, thus $\max(I_{4s}, 1) = 1$ and $I_{8fs} = 0$. When fitting to the biaxial and simple shear tests together, the term with I_{4n} needs to be included, which is different from the reduced formulation when fitting only to Dokos et al. data. One reason is that the shear responses along (fs) and (fn) are closer to each other in Sommer et al. human myocardium, than in Dokos et al. porcine myocardium. This is similar to shear responses along (sf) and (sn), and along (nf) and (ns), which suggests there may be a difference in passive myocardial properties between human and porcine myocardium. The reduced HO model from Ahmad et al. data needs to incorporate I_{8fn} , which might be explained by: (1) the asymmetric fibre structure in relation to the stretching axis; and (2) limited test data with only 2 shear responses, 2 biaxial tests and 2 uniaxial tests. There is, however, no conclusion as to the number of tests required with different deformation types to fully characterize myocardium.

The AIC analysis can also be used to choose the best combination of experiments. As shown in Fig. 3.10-3.12, different combinations of test data affect the prediction accuracy. Specifically, within the shear responses (Fig. 3.10 (a)), the groups containing (fs) and (fn) always have better predictive capability than other groups. One reason is that the shear responses along (fs) and (fn) are much stiffer than other directions in both Dokos et al. and Sommer et al. data. For the biaxial test, most combinations have good predictive capability, which suggests that not all the biaxial tests in Sommer et al. data are needed to fit the general HO model or the HO-S model. For instance, one stretching ratio with 1(MFD):0.75(CFD) from Sommer et al. biaxial tests has good predictions for other stretching ratios. But if the stretch ratio is largely non-equal, such as 1(MFD):0.5(CFD) or 0.5(MFD):1(CFD), the prediction is poor (see Fig. 3.14), partially because the material response with lower stretch ratios is still within the toe regime with non-stretched collagen fibres [8, 174]. Prediction between different deformation types are poor, as shown in Fig. 3.11 (a), using biaxial tests only (case 563) and simple shear only (case 1484). This might be because one experiment type is inadequate to capture the non-linearity and anisotropy of myocardium. [9] included simple shear, biaxial and uniaxial tests, which allows investigation of uniaxial data in characterizing myocardium property. However, even with Ahmad et al. data, the predictions of uniaxial tests using the two biaxial and simple shear tests (case 25) are poor. As discussed in [11], biaxial tests are insufficient for characterizing a hyperelastic anisotropic material. When using stress responses from both the simple shear and biaxial tests, the least test data for the HO-S model with good prediction is one shear tests along (nf), together with a biaxial test 1(MFD):1(CFD). Our results presented here suggest uniaxial tests are still needed

for an experiment like Ahmad et al. study, whilst further studies may be needed for experiments like Sommer et al. study using uniaxial tests.

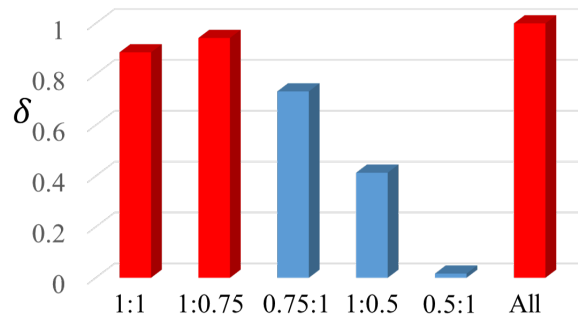


Figure 3.14: Only using biaxial tests in Sommer et al. data, we compute δ by fitting the HO-S model to one individual stretch ratio and predicting the remained experimental data from other stretch ratios. Only (1:1) and (1:0.75) meet $\delta \geq 0.8$ whilst (1:0.5) and (0.5:1) have $\delta \leq 0.4$.

In general, the stiffness aligned to the collagen fibre direction is much greater than the extracellular matrix, which is considered homogeneous and isotropic. Many studies have demonstrated the importance of excluding compressed fibres which cannot bear load [66, 134]. Here we use a simpler approach, effective fibre ratios, to consider this effect. Because of the gradual fibre rotation transmurally, we assume the collagen fibres will experience the same deformation as the extracellular matrix only when both ends are stretched. A simplified FEM model based on Fig. 3.3 is simulated under uniaxial stretch along the MFD (Fig. 3.15), showing that the stress is much higher in the effective fibre area. The inclusion of the effective fibre ratio is also supported by Fig. 3.5, where the goodness-of-fit for the general HO model is much better than without it. The effective fibre ratio is a geometrical effect and depends on the sample size, loading direction and the local collagen fibre structures. It does not affect the fit to biaxial tests since the in-plane collagen fibres will be physically stretched at both ends, but will affect the fit to the uniaxial and simple shear tests.

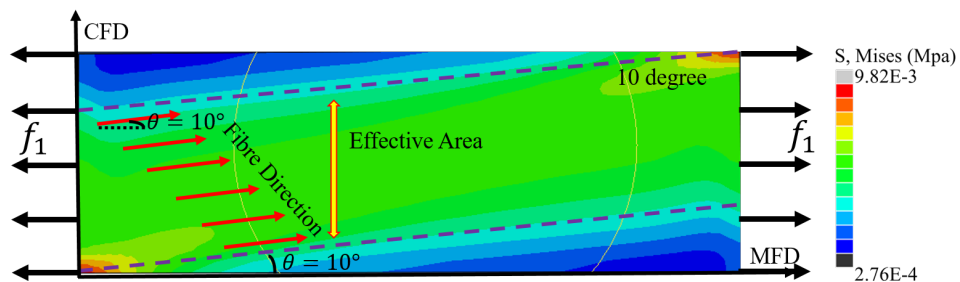


Figure 3.15: Stress distribution when fibre direction is 10° in uniaxial tensile along MFD as shown in Fig. 3.3. The green area enclosed by the two dashed lines is the effective area with higher stress while the blue area (the right bottom and left upper corners) is the ineffective area with much lower stress.

This chapter also demonstrates that assuming biaxial stretch does not induce shear is not valid for fibre reinforced material. This scenario is only possible if fibres are strictly aligned in both stretching directions without cross-fibre effects. Both are not true in real tissue tests. The assumption of no shear in the model leads to the poor outcome of predicting biaxial test data from simple shear tests, even if the general HO model is used. Indeed, we show that assuming shear-free behaviour in Sommer et al. biaxial testing produced relatively poor goodness-of-fit for both the general HO and HO-S models; however, this is significantly improved when including a small shear component as per biaxial tests of fibre-reinforced anisotropic material [57, 170](Figs. 3.6 (a)). As the shear components in the biaxial tests are not reported by [4], the maximum shear angles are assumed to be the same along the CFD and MFD, respectively, at around 6° . In Ahmad et al. data, the shear components in the biaxial tests are estimated, with the results presented here (Fig. 3.6 (b)) suggesting that measuring of shear components in biaxial testing is necessary for myocardium and, potentially, other anisotropic materials.

To determine the variability of material parameters when fitting the various HO models to the experimental data, a random initialization strategy is used with 100 samples drawn from pre-defined parameter ranges. Estimated parameters from different guesses are summarized in Table 3.3. In general, all estimated parameters for reduced HO models have small standard deviations compared to the average values, and also less than the standard deviations from the general HO model, suggesting a better determinability for reduced HO models. The large standard deviations in the general HO model can be expected because more parameters are present. It is also noted when fitting to Dokos et al. data that some parameters lie in the lower bounds, such as b_s in the HO-D model. This may be partially explained by the limited experimental data, which cannot capture some directional stress responses, or due to the inter-dependence of material parameters [13]. Since no studies exist on the quantity of experimental data required to fully capture myocardial mechanical properties, we limit this chapter to three experimental studies in our AIC analysis.

There are many other constitutive models exist, such as the “pole-zero” model [175], various Fung-type models [39, 61], and the constitutive framework with minimized cross-term covariance proposed by [176]. The AIC analysis can be readily applied to select different types of material models. For instance, we can compare the HO-D model and the Fung-type Guccione’s model [61] with Dokos et al. shear data. We find that better fitting results can be achieved using the HO-D model, which has a much lower AIC value (-559.3) than the value from the Guccione’s model (-65.8). This is because the Guccione’s model is a transversely isotropic material model, but myocardium is known to be orthotropic.

When calculating the stress responses from the mechanical tests, homogeneous strains are assumed in the biaxial and simple shear tests, and within the effective area of the uniaxial samples. It is widely accepted that the collagen fibres are in a highly layered architecture and myocardial material properties are heterogeneous in nature, thus the homogeneous strain as-

sumption in this chapter is a rough approximation. Directly using FEM simulations to fit the material models to experiments may be needed, but FEM simulations can be computationally intensive, with difficulty in achieving converging solutions. Whilst Schmid et al. [177] found that the Fung-type “Costa-Law” performs almost identically to Dokos et al. data when assuming homogeneous strain and using the FEM simulations, further studies are needed to compare the accuracy between FEM simulations and the approach we use in this chapter. Last but not least, other limitations include (1) collagen fibres are dispersed in myocardium, so an angular-based integration with fibre distributions or the general structure tensor approach may improve goodness-of-fit; (2) myocytes and collagen fibres are not modelled separately; (3) the cross-links among collagen fibres at different directions are not explicitly included, though the I_8 terms may account some cross-link effects.

3.5 Conclusion

This chapter describes an AIC-based constitutive model reduction for myocardium. We make use of three different myocardial mechanical studies, including uniaxial, biaxial and simple shear tests. We propose three different reduced HO models based on the congressing myocardial tissue studies, with all models retaining similar descriptive and predictive capabilities as the general HO model. We demonstrate the importance of accounting for the shear in the biaxial experiments, as without shear, it is not possible to describe the biaxial experiments reliably. We further demonstrate that it is necessary to consider through thickness fibre rotations in the sample, which is done by introducing the effective fibre ratio when fitting material models to the uniaxial and simple shear myocardial experiments. Finally, we use the AIC analysis to identify the best combinations of tissue tests, and our results show that the minimum one shear responses (nf) and one biaxial test with stretch ratio 1(MFD): 1(CFD) are required to capture human myocardial mechanical property in Sommer et al. study. The different reduced material models for the three experimental studies indicate that the least terms required to achieve a competent material model may depend on species, ages, and pathologies. Therefore, a combined experimental and modelling approach is important in selecting an appropriate material model for predictive biomechanical models in personalized medicine.

Experiment	Model		Parameters													
			a (kPa)	b	a_f (kPa)	b_f	a_s (kPa)	b_s	a_n (kPa)	b_n	a_{fs} (kPa)	b_{fs}	a_{fn} (kPa)	b_{fn}	a_{sn} (kPa)	b_{sn}
Dokos et al	HO-D	<i>avg</i>	0.073	15.517	26.040	9.333	4.869	0.001	-	-	0.170	16.955	-	-	-	-
		<i>std</i>	4.0E-3	2.3E-1	1.1E-1	4.3E-2	4.7E-2	5.6E-5	-	-	5.0E-3	1.2E-1	-	-	-	-
	General HO	<i>avg</i>	0.019	8.576	25.790	9.668	4.281	0.010	0.001	0.868	0.250	16.037	0.025	13.826	0.252	8.773
		<i>std</i>	1.6E-2	7.7E+0	3.4E-2	1.5E-2	3.0E-2	3.8E-2	8.3E-4	6.5E-1	1.8E-2	1.8E-1	2.0E-2	5.7E+0	1.0E-1	4.7E+0
Sommer et al	HO-S	<i>avg</i>	0.809	7.474	1.911	22.063	-	-	0.227	34.802	0.547	5.691	-	-	-	-
		<i>std</i>	9.5E-4	4.9E-3	1.2E-3	4.8E-3	-	-	1.3E-3	2.2E-2	8.8E-4	1.8E-2	-	-	-	-
	General HO	<i>avg</i>	0.180	9.762	2.204	21.597	0.098	49.878	0.508	27.719	1.291	5.295	1.345	2.017	0.947	4.514
		<i>std</i>	4.4E-3	7.8E-3	5.1E-3	1.3E-2	1.8E-2	2.6E-1	3.3E-3	1.7E-2	4.9E-3	2.2E-2	1.6E-2	7.2E-1	2.2E-3	5.2E-1
Ahmad et al	HO-A	<i>avg</i>	0.075	18.143	7.067	1.339	-	-	2.745	4.497	1.859	4.066	3.541	8.222	-	-
		<i>std</i>	2.0E-4	1.6E-2	6.4E-4	9.1E-4	-	-	2.7E-3	6.2E-3	1.1E-3	3.4E-3	2.0E-3	7.2E-3	-	-
	General HO	<i>avg</i>	0.005	0.484	7.212	1.25	2.244	13.414	3.223	3.747	1.069	8.961	3.344	11.016	0.421	5.773
		<i>std</i>	3.5E-18	6.5E-19	9.0E-4	1.3E-3	3.0E-2	8.4E-1	4.8E-3	9.8E-3	7.7E-4	4.0E-2	2.6E-3	9.5E-3	5.5E-4	1.1E-1

Table 3.3: The average value *avg* and standard deviation *std* of optimized parameters from 100 random generated initial starts in interval (0.001, 50).

Chapter 4

Myofibre architecture: mapping among different geometries and its dispersion on contraction

4.1 Introduction

Extensive research has been carried out to develop computational cardiac models to understand mechanical behaviours of the heart [12, 39, 40]. For instance, FE method has been widely used to model heart function physiologically or pathologically, and to develop novel therapies [12, 164, 178]. The remaining challenges are to deal with the complex geometry, myofibre structure and material characterization of the myocardium [11, 91].

The spatial architecture of myofibres plays a central role in electrical propagation, myocardial expansion and contraction [112]. Early studies relied on histological analysis [113] to determine local fibre structure. Currently, DT-MRI [43] can describe fibre features by tracking diffusive motion of water molecules in tissue [179]. The diffusion tensor at each unit space of DT-MRI contains the diffusion signal that reflects fibre architecture. Algorithms have been developed for assessing mean fibre orientation in each diffusion tensor, such as identifying the primary eigenvector as the mean fibre direction [30]. More recently, models separate diffusion tensor into isotropic and anisotropic fractions, and fibre orientation dispersion is estimated from the anisotropic fraction [180].

To reconstruct myofibres in computational models, two different approaches have been developed. One is directly mapping myofibres from ex/in vivo datasets to the models, i.e., reconstructing models directly from DT-MRI [91], or using atlas-based methods to warp DT-MRI data into different models [44]. The other approach is the RBM, in which myofibres rotates linearly from endocardium to epicardium with prescribed angles concerning the circumferential direction in most of the studies [7, 114, 115].

Myofibres do not align perfectly along one direction at any location within ventricular wall, but are dispersed as reported by Ahmad et al. [5], who measured in-plane and out-of-plane myofibre and collagen fibre dispersion using two-photon-excited fluorescence and second harmonic generation microscopy on neonatal heart samples. Thus, it is necessary to take into account myofibre dispersion in myocardial active stress. This also agrees with the historical experimental findings from Lin and Yin [1], who measured around 40% cross-fibre active stress in rabbit myocardium. Limited numerical studies have shown that the large myofibre dispersion in heart can greatly affect ventricular pump function [21, 90, 92]. Furthermore, there is a lack of studies on how different myofibre generation approaches, DT-MRI derived or RBM, affecting ventricular pump functions. One particular question is whether the difference between DT-MRI and RBM based models can be overcome from a proper consideration of fibre dispersion. We hypothesize that incorporating a non-symmetrical dispersed active tension model in an RBM generated myofibre architecture can approximate the DT-MRI based approach when simulating the heart pump function.

In this chapter, we develop a neonatal porcine bi-ventricle model with three different myofibre architectures for the LV. The most realistic one is derived from ex vivo DT-MRI, and other two simplifications are based on RBM: one is regionally dependent by dividing the LV into 17 segments, each with different myofibre angles, and the other is more simplified by assigning a set of myofibre angles across the whole ventricle. Results from different myofibre architectures are compared in terms of cardiac pump function.

We show that the model with the most realistic myofibre architecture can produce larger cardiac output, higher EF and larger apical twist compared to those of the rule-based models under the same pre/after-loads. Our results also reveal that when the cross-fibre contraction is included, the active stress seems to play a dual role: its sheet-normal component enhances the ventricular contraction while its sheet component does the opposite. We further show that by including non-symmetric fibre dispersion using a general structural tensor, even the most simplified rule-based myofibre model can achieve similar pump function as the most realistic one, and cross-fibre contraction components can be determined from this non-symmetric dispersion approach. Thus, our study highlights the importance of including myofibre dispersion in cardiac modelling if RBM are used, especially in personalized models in subsequent research.

This chapter is based on the published paper *Guan, D., Yao, J., Luo, X. and Gao, H., 2020. Effect of myofibre architecture on ventricular pump function by using a neonatal porcine heart model: from DT-MRI to RBMs. Royal Society Open Science, 7(4), p.191655.*

4.2 Method

4.2.1 Geometry and Fibre Construction

A 3D FE bi-ventricular model from [181] is used in this chapter (Fig.4.1 (a)), which is reconstructed from a computed tomography (CT) data of a neonatal porcine heart. Details of the data acquisition can be found in [9]. The 3D CT data is first segmented using Seg3D¹, then the boundary contours are exported into SolidWorks (Dassault Systemes, MA USA) for geometry reconstruction, and finally meshed (Fig. 4.1 (a)) using ICEM (ANSYS, Inc. PA USA).

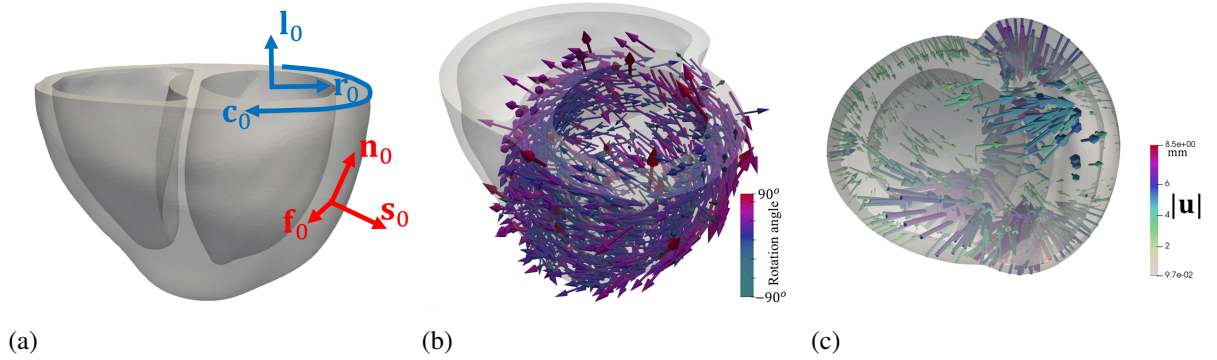


Figure 4.1: (a) The reconstructed bi-ventricle neonatal heart geometry from a 3D CT data (263,972 linear tetrahedral elements and 50,640 nodes). Local coordinate system, \mathbf{f}_0 , \mathbf{s}_0 , \mathbf{n}_0 are the conventional fibre-sheet-normal system, in which \mathbf{f}_0 is the mean fibre direction, \mathbf{s}_0 is the sheet direction in general along the transmural direction from endocardium to epicardium, and \mathbf{n}_0 is the sheet-normal direction. \mathbf{c}_0 , \mathbf{r}_0 , \mathbf{l}_0 are the local circumferential-radial-longitudinal system. (b) The reconstructed canine heart (252,713 linear tetrahedral elements and 49,460 nodes) with corresponding DT-MRI fibres. (c) Displacement vectors (\mathbf{u}) for warping the canine geometry to the porcine heart, coloured by the magnitude of \mathbf{u} .

Because the myofibre structure of the neonatal porcine heart is not available, it is interpolated from a canine heart obtained from the public dataset of Cardiovascular Research Grid² [120]. We first reconstruct a bi-ventricular geometry for the canine heart with myofibres extracted from the primary eigenvector of the DT-MRI tensors, as shown in Fig. 4.1 (b). Clearly, the neonatal bi-ventricle geometry is different from the canine geometry, as shown in Fig. 4.1. Therefore, we can not directly interpolate the measured canine myofibre structure into the neonatal bi-ventricle model. Instead, *Deformetrica*³ is then employed to register the two bi-ventricular geometries by warping a template (C_α : the canine bi-ventricle) to a target (C_β : the neonatal porcine heart) by minimizing a loss function that measures the distance between the template and target. *Deformetrica* is an open-source package based on a large deformation diffeomorphic metric mapping (LDDMM) framework [182, 183].

¹<http://www.sci.utah.edu/cibc-software/seg3d.html>

²<http://cvrgrid.org/data/ex-vivo>

³<http://www.deformetrica.org/>

To warp a template (C_α : the canine bi-ventricle) to a target (C_β : the neonatal porcine heart), we minimize the loss function

$$f(\mathbf{q}, \mu) = d(\Phi_{\mathbf{q}, \mu}(C_\alpha), C_\beta)^2 + R(\mathbf{q}, \mu) \quad (4.1)$$

where the first term measures the distance between the template and target, i.e. how well the deformed template shape is close to the target shape, and the second term acts as a regularizer. $\Phi_{\mathbf{q}, \mu}$ is a diffeomorphism mapping, which is fully parameterized by the initial control points \mathbf{q} and the momenta μ , the evolution equations for \mathbf{q} and μ follow the ‘‘Hamiltonian’’ system. For a shape represented by a triangulated surface with N_e linear triangles, the centres $(\mathbf{c}_p)_{p=1, \dots, N_e}$ and the normals $(\mathbf{n}_p)_{p=1, \dots, N_e}$ of all triangles can be readily calculated. The distance between the two triangulated surfaces (C_α and C_β) is then given by the varifold distance [184], by ignoring normal orientations,

$$d(C_\alpha, C_\beta)^2 = d((\mathbf{n}_p^\alpha, \mathbf{c}_p^\alpha)_{p=1, \dots, N_e^\alpha}, (\mathbf{n}_q^\beta, \mathbf{c}_q^\beta)_{q=1, \dots, N_e^\beta})^2 = \sum_p \sum_q K(\mathbf{c}_p^\alpha, \mathbf{c}_q^\beta) \frac{((\mathbf{n}_p^\alpha)^\top \mathbf{n}_q^\beta)^2}{|\mathbf{n}_p^\alpha| |\mathbf{n}_q^\beta|} \quad (4.2)$$

where $K(\mathbf{c}_p, \mathbf{c}_q) = \exp(-|\mathbf{c}_p - \mathbf{c}_q|^2 / \sigma^2)$ is a Gaussian kernel with width σ . Eq. (4.1) is optimized with the steepest gradient decent or the L-BFGS method implemented in the *Deformetrica* package with respect to μ to determine a diffeomorphism mapping Φ . Details of the LDDMM framework can be found in [182].

After warping C_α into C_β , the displacement fields for all nodes on the external surface of C_α are obtained, denoting $\mathbf{u}_{\text{Ex}}^{\text{LDDMM}}$ as shown in Fig. 4.1 (c). The displacement vectors on the nodes lying within the ventricular wall are then interpolated by solving a Laplace system with Dirichlet boundary conditions (Eq. 4.3) in *Fenics*⁴,

$$\begin{cases} \nabla^2 \mathbf{u} = 0, \\ \mathbf{u} = \mathbf{u}_{\text{Ex}}^{\text{LDDMM}} \end{cases} \quad \text{at external surface.} \quad (4.3)$$

Following the finite deformation theory, the deformation gradient of warping the canine bi-ventricle model into the porcine model is

$$\mathbf{F} = \nabla \mathbf{u} + \mathbf{I}, \quad (4.4)$$

in which \mathbf{I} is the identity matrix. Note that \mathbf{F} and \mathbf{u} are associated with the canine bi-ventricle model. Myofibre orientation in the warped canine model is

$$\mathbf{f}_{\text{warp}}^{\text{canine}} = \frac{\mathbf{F} \mathbf{f}_{\text{template}}^{\text{canine}}}{|\mathbf{F} \mathbf{f}_{\text{template}}^{\text{canine}}|}, \quad (4.5)$$

⁴<https://fenicsproject.org/>

where $\mathbf{f}_{\text{template}}^{\text{canine}}$ is the unit myofibre direction from the DT-MRI canine dataset. Finally myofibres in the porcine model \mathbf{f}_0 are assigned according to the nearest neighbours between the warped canine and porcine geometries, such that

$$\mathbf{f}_0 = \mathbf{f}^{\text{porcine}}(\mathbf{x}^{\text{porcine}}) = \mathbf{f}_{\text{warp}}^{\text{canine}}(\text{argmin}_{\mathbf{y}} |\mathbf{y} - \mathbf{x}^{\text{porcine}}|), \quad \mathbf{y} \in \mathbf{x}_{\text{warp}}^{\text{canine}}, \quad (4.6)$$

in which $\mathbf{x}^{\text{porcine}}$ is a position vector in the porcine model, and $\mathbf{x}_{\text{warp}}^{\text{canine}}$ is the position vector in the warped canine model. The sheet direction \mathbf{s}_0 is defined transmurally across the wall, and the sheet-normal is $\mathbf{n}_0 = \mathbf{f}_0 \times \mathbf{s}_0$.

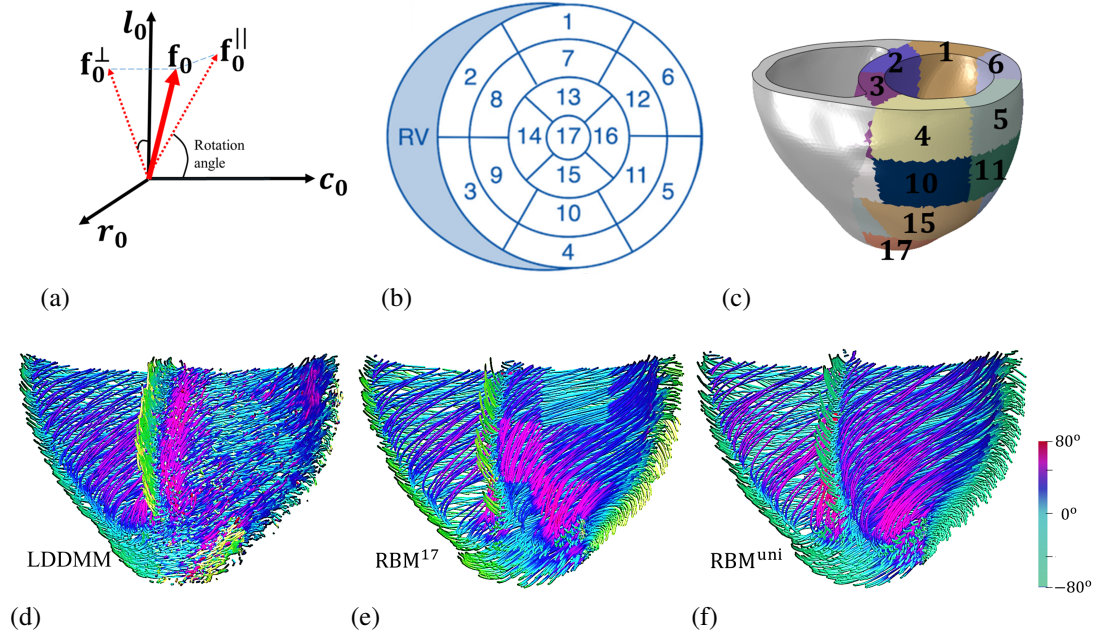


Figure 4.2: Myofibre rotation angle definition (a), which is the angle between \mathbf{f}_0^{\parallel} and \mathbf{c}_0 . \mathbf{f}_0^{\parallel} (in-plane) and \mathbf{f}_0^{\perp} (out-of-plane) are the projections of \mathbf{f}_0 in $\mathbf{c}_0 - \mathbf{l}_0$ and $\mathbf{l}_0 - \mathbf{r}_0$ planes, respectively, (b) AHA 17 segments definition in a bullseye view and (c) in the porcine model. Three different myofibre architectures are generated, they are (d) LDDMM derived, (e) RBM^{17} and (f) RBM^{uni} .

We further generate two different myofibre structures in the left side of the bi-ventricle using a rule-based approach [7], septum included. By projecting \mathbf{f}_0 into the $\mathbf{c}_0 - \mathbf{l}_0$ plane to have \mathbf{f}_0^{\parallel} , we define the myofibre angle as the angle between \mathbf{f}_0^{\parallel} and \mathbf{c}_0 , as shown in Fig. 4.2 (a). The average myofibre angles in the porcine model are then summarized at endocardium ($\theta_{\text{endo}}^{\text{ave}}$) and epicardium ($\theta_{\text{epi}}^{\text{ave}}$) in two ways: (1) across the whole LV, and (2) at each ventricular segment according to the AHA17 (American Heart Association) definition [185] as shown in Figs. 4.2 (b, c) based on RV insertion points. A rule-based approach is used to generate two different myofibre structures: (1) one set of myofibre rotation angles varies linearly from endocardium to epicardium for the whole LV; (2) for each AHA17 segment, myofibre rotates linearly based on the average rotation angles from that segment, which means myofibre angles are different at different segments. Note that the myofibre structure in the RV of the bi-ventricle model,

excluding the septum, is generated by the same rule-based approach but using one set of rotation angles due to the lack of DT-MRI data for the right side. We further assume the myofibre rotation angles at RV are the same as the angles when averaged across the whole LV.

With these three myofibre structures generated (Figs. 4.2 (d, e, f)), we consider the following cases:

- case LDDMM: the LV with the mapped ex-vivo DT-MRI acquired myofibre architecture (Eq. 4.6);
- case RBM¹⁷: myofibre rotates linearly from endocardium to epicardium for each LV segment according to the average rotation angles at 17 segments, derived from case LDDMM. Table 4.1 lists the myofibre rotation angles at each segment, including the angles for the RV;
- case RBM^{uni}: myofibre uniformly rotates between endocardium and epicardium in the whole LV with one set of the average rotation angles (endocardium:40°, epicardium:−30°), which are also derived from case LDDMM.

Note that case RBM¹⁷ has a heterogeneous myofibre structure in the whole LV but homogeneous within each segment. We also have not smoothed rotation angles between segments since those variations are within the range of local angle variations in case LDDMM as suggested in Fig. 4.4 (a). Thus, case RBM¹⁷ is a simplification of case LDDMM. Case RBM^{uni} has the same myofibre structure across the whole LV, a further simplification compared to case RBM¹⁷.

Section	1	2	3	4	5	6	7	8	9
Endocardium	20	40	30	40	60	40	40	60	30
Epicardium	-20	-40	-40	0	-20	-20	-40	-40	-30
Section	10	11	12	13	14	15	16	17	RV
Endocardium	40	60	40	60	30	80	60	10	40
Epicardium	-20	-20	-40	-40	-30	-20	-40	-10	-30

Table 4.1: Average myofibre rotation angles (°) at endocardium and epicardium according to the AHA17 definition, and the set of angles for the RV.

4.2.2 Constitutive Model

Passive stress response

The passive behaviour of myocardium is described by a strain-invariant based function [181], which is reduced from the model proposed by Holzapfel and Ogden [11] by fitting to an experimental study of neonatal porcine myocardium [9]. The SEF consists of a deviatoric (\mathcal{W}_{dev}) and

a volumetric (\mathcal{W}_{vol}) parts,

$$\begin{aligned}\mathcal{W}_{\text{dev}} &= \frac{a}{2b} \{ \exp[b(\bar{I}_1 - 3)] - 1 \} + \sum_{i=f,n} \frac{a_i}{2b_i} \{ \exp[b_i(\max(\bar{I}_{4i}, 1) - 1)^2] - 1 \} \\ &\quad + \sum_{ij=fs,fn} \frac{a_{ij}}{2b_{ij}} [\exp(b_{ij}\bar{I}_{8ij}^2) - 1], \\ \mathcal{W}_{\text{vol}} &= \frac{1}{D} \left(\frac{J^2 - 1}{2} - \ln(J) \right),\end{aligned}\tag{4.7}$$

where $a, b, a_i, b_i, a_{ij}, b_{ij}$ are material constants and D is a multiple of the reciprocal of the bulk modulus K , i.e., $D = 2/K$. $J = \det(\mathbf{F})$, $\mathbf{F} = J^{1/3}\bar{\mathbf{F}}$, and $\bar{\mathbf{C}} = \bar{\mathbf{F}}^T\bar{\mathbf{F}}$. The isochoric invariants are defined as $\bar{I}_1 = \text{trace}(\bar{\mathbf{C}})$, $\bar{I}_{4f} = \mathbf{f}_0 \cdot \bar{\mathbf{C}}\mathbf{f}_0$, $\bar{I}_{4n} = \mathbf{n}_0 \cdot \bar{\mathbf{C}}\mathbf{n}_0$, $\bar{I}_{8fs} = \mathbf{f}_0 \cdot \bar{\mathbf{C}}\mathbf{s}_0$, and $\bar{I}_{8fn} = \mathbf{f}_0 \cdot \bar{\mathbf{C}}\mathbf{n}_0$, in which $\mathbf{f}_0, \mathbf{s}_0, \mathbf{n}_0$ are the myofibre, sheet and sheet-normal directions in the reference state. In this chapter, we assume the collagen fibres follow the layered myocyte structure. Thus, myofibres represent both myocyte and collagen fibres. The $\max()$ in Eq. 4.7 will ensure the collagen fibres can only bear load when in tension. The passive Cauchy stress tensor is given by

$$\begin{aligned}\sigma^p &= p_{\text{vol}}\mathbf{I} + 2J^{-1}[\bar{\mathcal{W}}_1 \text{dev}\bar{\mathbf{B}} + \bar{\mathcal{W}}_{4f} \text{dev}(\bar{\mathbf{f}} \otimes \bar{\mathbf{f}}) + \bar{\mathcal{W}}_{4n} \text{dev}(\bar{\mathbf{n}} \otimes \bar{\mathbf{n}}) \\ &\quad + \frac{1}{2}\bar{\mathcal{W}}_{8fs} \text{dev}(\bar{\mathbf{f}} \otimes \bar{\mathbf{s}} + \bar{\mathbf{s}} \otimes \bar{\mathbf{f}}) + \frac{1}{2}\bar{\mathcal{W}}_{8fn} \text{dev}(\bar{\mathbf{f}} \otimes \bar{\mathbf{n}} + \bar{\mathbf{n}} \otimes \bar{\mathbf{f}})],\end{aligned}\tag{4.8}$$

in which $\bar{\mathcal{W}}_i = \frac{\partial \mathcal{W}_{\text{dev}}}{\partial \bar{I}_i}$, $i \in \{1, 4f, 4n, 8fs, 8fn\}$, $\bar{\mathbf{f}} = \bar{\mathbf{F}}\mathbf{f}_0$, $\bar{\mathbf{s}} = \bar{\mathbf{F}}\mathbf{s}_0$, $\bar{\mathbf{n}} = \bar{\mathbf{F}}\mathbf{n}_0$, $\bar{\mathbf{B}} = \bar{\mathbf{F}}\bar{\mathbf{F}}^T$, $p_{\text{vol}} = \partial \mathcal{W}_{\text{vol}} / \partial J$, and $\text{dev}(\bullet) = (\bullet) - (1/3)[(\bullet) : \mathbf{I}]\mathbf{I}$ denotes the deviatoric operator.

Active stress

Biaxial investigations on actively contracting rabbit myocardium [1] suggest that a large portion of active stress exists in cross-fibre directions. This has motivated computational efforts to include a proportion of the active stress to the cross-fibre directions when RBM generated myofibres are used [90, 178]. In this chapter, we employ the active stress approach for myocardial active stress along myofibre, sheet and sheet-normal directions

$$\sigma^a = n_f T_a \hat{\mathbf{f}} \otimes \hat{\mathbf{f}} + n_s T_a \hat{\mathbf{s}} \otimes \hat{\mathbf{s}} + n_n T_a \hat{\mathbf{n}} \otimes \hat{\mathbf{n}},\tag{4.9}$$

in which $\hat{\mathbf{f}} = \mathbf{f}/|\mathbf{f}|$, $\hat{\mathbf{s}} = \mathbf{s}/|\mathbf{s}|$ and $\hat{\mathbf{n}} = \mathbf{n}/|\mathbf{n}|$, n_f, n_s and n_n (all positive and sum up to 1) are the proportions of the active tension in their respective directions. T_a is the active tension generated along the myofibre direction, which is described by a time-varying elastance model that has been described extensively in the literature [89–91]

$$T_a(t, l) = \frac{T_{\text{max}}}{2} \frac{\text{Ca}_0^2}{\text{Ca}_0^2 + \text{ECa}_{50}^2(l)} (1 - \cos(\omega(t, l)))\tag{4.10}$$

where

$$ECa_{50}(l) = \frac{Ca_{0max}}{\sqrt{e^{B(l-l_0)} - 1}}$$

$$\omega(t, l) = \begin{cases} \pi \frac{t}{t_0} & \text{for } 0 \leq t \leq t_0 \\ \pi \frac{t-t_0+t_r(l)}{t_r} & \text{for } t_0 < t \leq t_0 + t_r \\ 0 & \text{for } t > t_0 + t_r \end{cases}$$

$$t_r(l) = ml + b$$

$$l = l_r \sqrt{2E_{ff} + 1}$$

where T_{max} is the isometric tension under maximal activation, Ca_0 is the peak intracellular calcium concentration; m and b are constants that govern the shape of the linear relaxation duration and sarcomere length relaxation; E_{ff} is the Lagrange strain in the fibre direction; B is a constant that governs the shape of the peak isometric tension-sarcomere length relation; l_r is the sarcomere length with the stress-free condition whilst l_0 is the sarcomere length that does not produce active stress [89]. Active parameters values [12] can be find in Table 4.2. Please note the real active tension T_a in FE simulations is around 50 kPa during cardiac systole, which locates in the normal range [186], and the T_{max} of 135 kPa and 180 kPa are comparable to the reported values in other studies [91, 95, 164]. T_{max} represents contractility, its definition is different from active tension in general.

	t_0 (ms)	m (s μm^{-1})	b (s)	l_0 (μm)	B (μm^{-1})	Ca_0 (μM)	Ca_{0max} (μM)	T_{max} (kPa)	l_r (μm)
LV	150	1048.9	-1.7	1.58	4.750	4.35	4.35	180	1.85
RV	150	1048.9	-1.7	1.58	4.750	4.35	4.35	135	1.85

Table 4.2: Parameter values for the time varying elastance active tension constitutive model.

In this chapter, we assume the cross-fibre contraction in the RV is zero, i.e. $n_f = 1$, $n_s = 0$, and $n_n = 0$. This is because RV has a much thinner wall thickness, and Ahmad et al. [5] reported the fibre dispersion in the RV is much less than in the LV (9.3° v.s. 19.2°). We also performed simulations for the RBM^{uni} case, using the LV's non-zero cross-fibre contraction for the RV. Our results show the differences of EF are 0.7% and 4.1% for the LV and RV, respectively. Thus assuming no cross-fibre contraction for the RV seems to be reasonable.

As for the LV (septum is included), since DT-MRI derived myofibres is naturally dispersed in case LDDMM (Fig. 4.2), we set $n_f = 1$, $n_s = 0$, and $n_n = 0$. But for the RBM cases, it is necessary to include cross-fibre active tension, and n_s and n_n are calculated based on a dispersed fibre structure tensor. This will be explained in the following section.

Determination of n_f , n_n and n_s using DT-MRI derived myofibres for case RBM^{uni}

We first introduce $\{\mathbf{e}_1, \mathbf{e}_2, \mathbf{e}_3\}$ to denote the axes of a Cartesian coordinate system as shown in Fig. 4.3, and then define myofibre direction of the reference configuration to be \mathbf{M} with a density distribution $\rho(\mathbf{M})$. \mathbf{M} can be further characterized by two angles $\Theta \in [0, \pi]$ and $\Phi \in [0, 2\pi]$, that is

$$\mathbf{M}(\Theta, \Phi) = \sin \Theta \cos \Phi \mathbf{e}_1 + \sin \Theta \sin \Phi \mathbf{e}_2 + \cos \Theta \mathbf{e}_3. \quad (4.11)$$

Θ is the angle between \mathbf{e}_3 and \mathbf{M} , and Φ is the angle between \mathbf{e}_1 and the projected vector of \mathbf{M} in the \mathbf{e}_1 - \mathbf{e}_2 plane.

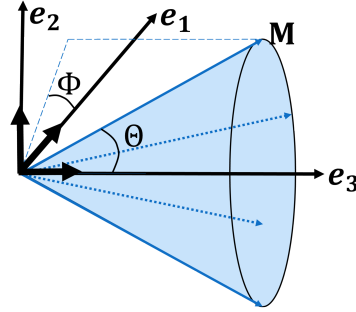


Figure 4.3: An unit vector $\mathbf{M}(\Theta, \Phi)$ representing a fibre direction defined by Θ and Φ with respect to a Cartesian system \mathbf{e}_1 , \mathbf{e}_2 and \mathbf{e}_3 . The plane spanned by \mathbf{e}_2 - \mathbf{e}_3 is in-plane whilst out-of-plane is \mathbf{e}_1 - \mathbf{e}_2 . The mean myofibre direction is along \mathbf{e}_3 .

We assume the dispersions in different planes are essentially independent [187], i.e.

$$\rho(\mathbf{M}) = \rho(\Theta, b_1, \Phi, b_2) = \rho_{\text{op}}(\Phi, b_2) \rho_{\text{in}}(\Theta, b_1), \quad (4.12)$$

in which $\rho_{\text{op}}(\Phi, b_2)$ describes the out-of-plane dispersion, and $\rho_{\text{in}}(\Theta, b_1)$ describes the in-plane dispersion. Note in the ventricular model, in-plane is the plane defined by $\mathbf{c}_0 - \mathbf{l}_0$, and out-of-plane is the plane defined by $\mathbf{l}_0 - \mathbf{r}_0$. This is consistent with experimental studies when measuring in-/out-of-plane fibre angles [4, 5]. π -periodic von Mises distribution is used for $\rho_{\text{in}}(\Theta, b_1)$ and $\rho_{\text{op}}(\Phi, b_2)$ [19], such as

$$\rho(\theta, b) = \frac{\exp(b \cos(2\theta))}{2G \int_0^\pi \exp(b \cos(x)) dx}, \quad (4.13)$$

in which θ is a variable representing Θ or Φ , $b > 0$ is the concentration parameter, G is a constant to ensure

$$\int_0^{2\pi} \int_0^\pi \rho_{\text{op}}(\Phi, b_2) \rho_{\text{in}}(\Theta, b_1) \sin \Theta d\Theta d\Phi = 1. \quad (4.14)$$

When there is no dispersion, the structure tensor $\mathbf{M} \otimes \mathbf{M}$ can be directly used for constructing $I_{4f} = \mathbf{C} : \mathbf{M} \otimes \mathbf{M}$ and active stress tensor $T_a \frac{\mathbf{M} \otimes \mathbf{M}}{I_{4f}}$. With dispersion, a GST \mathbf{H} can be defined over

an unit sphere [19–21],

$$\mathbf{H} = \int_0^{2\pi} \int_0^\pi \rho_{\text{op}}(\Phi, b_2) \rho_{\text{in}}(\Theta, b_1) \mathbf{M} \otimes \mathbf{M} \sin \Theta d\Theta d\Phi. \quad (4.15)$$

From Figs. 4.4 (a,b), we can find that in-plane angle (Θ) varies linearly from endocardium to epicardium for both RBM cases, but the fibres are much dispersed for case LDDMM, especially near the endocardium and epicardium, where myofibres align more longitudinally (\mathbf{l}_0). The out-of-plane angle (Φ) is zero for both RBM cases since RBM generated myofibres only lie in the $\mathbf{c}_0 - \mathbf{l}_0$ plane. However, out-of-plane dispersion can be seen in case LDDMM shown in Fig. 4.4 (b). We now determine the in/out-of-plane dispersions from the angle differences between case LDDMM and RBM^{uni}. Figs. 4.4 (c) and (d) show the histograms of in/out-of-plane dispersion in the LV, both Θ and Φ centre around 0° . The maximum likelihood method *mle()* from MATLAB is used to fit ρ_{ip} and ρ_{op} to the histograms of the in/out-of-plane dispersions, with $b_1 = 1.6153$ for the in-plane dispersion, and $b_2 = 1.2144$ for the out-of-plane dispersion.

Without loss of generality, we consider the mean fibre direction along \mathbf{e}_3 , the sheet direction along \mathbf{e}_1 and the sheet-normal direction along \mathbf{e}_2 . Then the in-plane distribution is $\rho_{\text{ip}}(\Theta - 0, b_1)$, the out-of-plane distribution is $\rho_{\text{op}}(\Phi - \frac{\pi}{2}, b_2)$, and

$$\begin{aligned} \mathbf{H} &= \int_0^\pi \int_0^{2\pi} \rho_{\text{ip}}(\Theta, b_1) \rho_{\text{op}}(\Phi - \pi/2, b_2) \mathbf{M} \otimes \mathbf{M} \sin \Theta d\Theta d\Phi \\ &= \begin{pmatrix} 0.086 & & \\ & 0.268 & \\ & & 0.646 \end{pmatrix} \\ &= H_{11} \mathbf{s}_0 \otimes \mathbf{s}_0 + H_{22} \mathbf{n}_0 \otimes \mathbf{n}_0 + H_{33} \mathbf{f}_0 \otimes \mathbf{f}_0. \end{aligned} \quad (4.16)$$

Similar as the active stress expression in Eq. (4.9), the active Cauchy stress with dispersed myofibres is

$$\boldsymbol{\sigma}^a = T_a \mathbf{F} \hat{\mathbf{H}}_a \mathbf{F}^T = T_a H_{11} \hat{\mathbf{s}} \otimes \hat{\mathbf{s}} + T_a H_{22} \hat{\mathbf{n}} \otimes \hat{\mathbf{n}} + T_a H_{33} \hat{\mathbf{f}} \otimes \hat{\mathbf{f}}, \quad (4.17)$$

where a corresponding dispersed structural tensor $\hat{\mathbf{H}}_a$ [21] can be introduced

$$\hat{\mathbf{H}}_a = H_{11} I_{4s}^{-1} \mathbf{s}_0 \otimes \mathbf{s}_0 + H_{22} I_{4n}^{-1} \mathbf{n}_0 \otimes \mathbf{n}_0 + H_{33} I_{4f}^{-1} \mathbf{f}_0 \otimes \mathbf{f}_0. \quad (4.18)$$

Thus we have $n_s = H_{11} = 0.086$, $n_n = H_{22} = 0.268$, and $n_f = H_{33} = 0.646$ for case RBM^{uni}.

4.2.3 Boundary conditions and implementations

The bi-ventricular model is implemented using the nonlinear FE software ABAQUS (Dassault Systemes, Johnston RI, USA). In order to simulate diastolic filling and systolic ejection, a lumped model for the pulmonary and systemic circulation systems is attached to this bi-

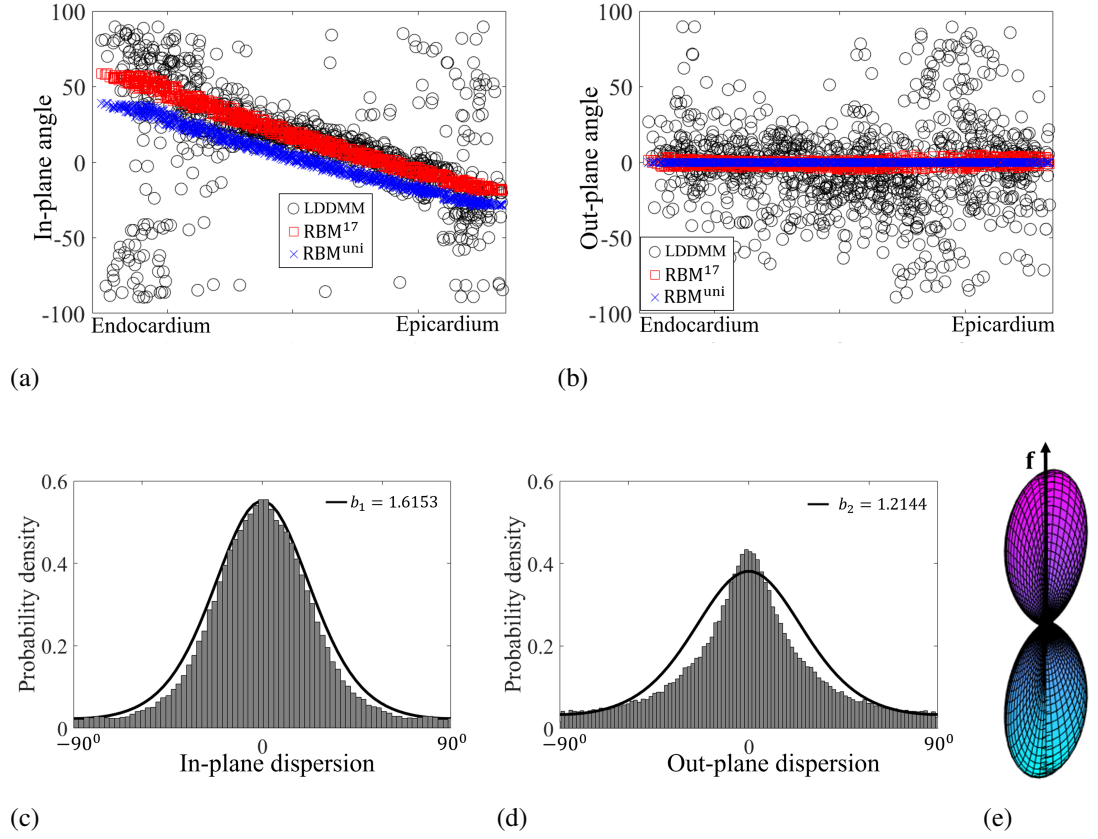


Figure 4.4: Fibre dispersion quantified from the DT-MRI dataset. (a) shows the in-plane angle Θ and (b) the out-of-plane angle Φ across the LV ventricular wall; (c) is the in-plane dispersion distribution with fitted $\rho_{ip}(\Theta, b_1)$ and (d) is the out-of-plane dispersion distribution with fitted $\rho_{op}(\Phi, b_2)$; (e) a 3D surface plot defined by the vector $\rho(\Theta, b_1, \Phi, b_2)\mathbf{f}(\Theta, \Phi)$ with $\rho(\Theta, b_1, \Phi, b_2) = \rho_{ip}(\Theta, b_1)\rho_{op}(\Phi, b_2)$. The negative angle in (a) suggests the in-plane fibre vector lies in the fourth quadrant ($+\mathbf{c}_0$ and $-\mathbf{l}_0$), and similarly in (b) for the out-of-plane fibre vector, which lies in the fourth quadrant of plane ($-\mathbf{l}_0$ and $+\mathbf{r}_0$). All values are used for determining the in-plane and out-of-plane dispersions in (c) and (d).

ventricular model, which is realized through a combination of surface-based fluid cavities and fluid exchanges [188] as shown in Fig. 4.5. We define the mass flow rate between two different cavities as

$$\dot{m} = \rho \dot{V}A, \quad (4.19)$$

where ρ is the blood density, A is the effective area between the two connected cavities, and \dot{V} is the fluid flux. \dot{m} is further related to the pressure difference

$$\Delta pA = C_V \dot{m} + C_H \dot{m}|\dot{m}|, \quad (4.20)$$

where Δp is the pressure difference between two connected cavities, C_V is viscous resistance coefficient, and C_H is hydrodynamic resistance coefficient, and $C_H = 0$ in this chapter. This type of boundary conditions is equivalent to a simplified two-element windkessel model. Parameters

for the lumped circulation system are listed in Table 4.3 and scaled from [91] by taking into account the dimensions of the neonatal porcine heart. For example, the total blood volume is around 80 mL for a newborn piglet [189], much less than in an adult porcine (67.2 ± 4.12 mL/kg) [190], and the valvular area in a newborn heart is about one-tenth of the area in an adult heart [191–193], and the diameter of blood vessel is also much smaller in the newborn piglet compared to an adult porcine [194], which suggests that under similar pressure loadings, the vessel compliance, calculated as $\frac{\Delta V}{\Delta P}$ will be much less in a newborn porcine because of much smaller ΔV in a newborn piglet.

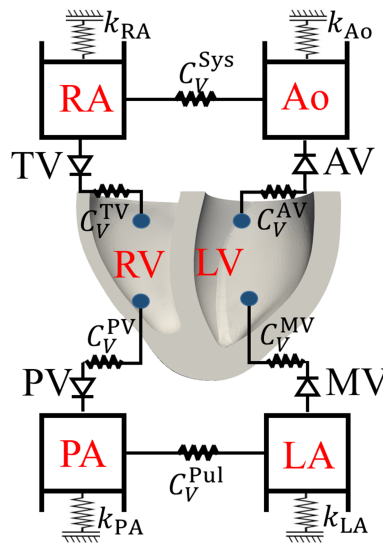


Figure 4.5: Schematic of the bi-ventricular model coupled with a circulatory system. MV: mitral valve; AV: aortic valve; RA: right atrium; TV: tricuspid valve; PV: pulmonary valve; LA: left atrium; RA: right atrium; Ao: aorta; Sys: systemic circulation; Pul: pulmonary circulation; and PA: pulmonary artery. Grounded spring with a stiffness (k) is tuned to provide the appropriate PV response (i.e., compliance) for that cavity. C_V is viscous resistance coefficient to describe resistance between cavities. One-direction flow through valves is controlled by setting fluid exchanging properties between the cavities.

Parameters for passive SEF and the maximum active tension from myocytes (T_{\max}) are listed in Table 4.4.

Using Eq. (4.7), initial values for passive response of LV are from Table 3.1 of Chapter 3, and a_i ($i \in \{1, 4f, 4n, 8fs, 8fn\}$) are further reduced by half together with chosen T_{\max} to ensure both LV and RV can achieve EF within the physiological range ($EF > 50\%$). Values of b_i ($i \in \{1, 4f, 4n, 8fs, 8fn\}$) are kept same as in Table 3.1. RV material parameters are processed in the same way, which are derived from experimental data of RV [9]. Note that because of missing measured data (wall motion, ventricular pressure) for the porcine heart, rather than constructing a personalized model [2, 91], we only aim to obtain a set of parameters with which the bi-ventricle behaves physiologically.

ABAQUS			Windkessel equivalent		
Name	Value	Unit	Name	Value	Unit
C_V^{AV}	20.0	$\text{MPa} \cdot \text{mm}^2 \cdot \text{s}/\text{tonne}$	R_{AV}	0.150	$\text{mmHg} \cdot \text{s}/\text{ml}$
C_V^{MV}	50.0	---	R_{MV}	0.375	---
C_V^{PV}	55.0	---	R_{PV}	0.412	---
C_V^{TV}	16.0	---	R_{TV}	0.120	---
C_V^{Sys}	3600.0	---	R_{Sys}	27.0	---
C_V^{Pul}	300.0	---	R_{Pul}	2.25	---
k_{Ao}	0.8	N/mm	C_{Ao}	0.061	ml/mmHg
k_{PA}	0.8	---	C_{PA}	0.065	---
k_{LA}	0.1	---	C_{LA}		---
k_{RA}	0.1	---	C_{RA}		---

Table 4.3: Parameter values for the lumped circulatory model as shown in Fig. 4.5. C_V is the viscous resistance coefficient, and k is the stiffness of the grounded spring. Corresponding values for the equivalent Windkessel model is also listed for reference including the resistance (R) and the compliance (C). Note that the compliances of the RA and LA are not constant but varied to ensure constant EDP, which are not listed here.

	a	b	a_f	b_f	a_n	b_n	a_{fs}	b_{fs}	a_{fn}	b_{fn}
	(kPa)		(kPa)		(kPa)		(kPa)		(kPa)	(kPa)
LV	0.038	18.143	3.5335	1.339	1.373	4.495	0.929	4.067	1.771	8.225
RV	0.485	7.513	2.777	1.685	0.704	9.407	0.121	15.314	1.351	17.235

Table 4.4: Parameter values for passive properties of the LV and RV myocardium.

The FE nodes on the top basal plane are constrained along the longitudinal axis but free to move within the basal plane. The longitudinal axis is defined as the line passing the LV basal centre and perpendicular to the basal plane. To start the simulation, linearly increased blood pressures from 0 to end-diastolic values are first applied to the inner surfaces of the bi-ventricular model, 8 mmHg in the LV and 4 mmHg in the RV. Typical diastolic pressures inside the pulmonary, left atrium, aorta and right atrium are also applied to those 4 cavities (10 mmHg, 8 mmHg, 67.5 mmHg, and 4 mmHg [195]). Then the bi-ventricular model starts iso-volumetric contraction ($t=0$ s), followed by systolic ejection when the ventricular pressure is higher than that of the aorta (around $t=0.045$ s), and then the iso-volumetric relaxation. Systolic ejection ends at 0.12s. 1 s is chosen for a whole cardiac cycle for computational convenience. In order to ensure the EDPs in both LV and RV are same at next cardiac cycles, EDPs in both atria are maintained constant.

4.3 Results

We first compare the heart pump function for cases LDDMM, RBM^{17} and RBM^{uni} without cross-fibre active tension. We then analyse the effect of cross-fibre active tension in case

RBM^{uni}. Finally we include dispersed active tension derived from DT-MRI myofibres in case RBM^{uni} and compared with case LDDMM.

4.3.1 No cross-fibre active tension

Fig. 4.6 (a) shows the PV loops from the three cases with no cross-fibre active tension. Although they all have the same EDP, the LV EDV from case LDDMM (2.87ml) is slightly larger than the other two rule-based cases (2.83ml), the relative difference is around 1.4%. The LV ESV in case LDDMM is also the smallest (1.38ml). Interestingly, though myofibre structures in the RV for the three cases are same, however, due to the difference in LV dynamics, the RV ESV from case LDDMM is also the smallest (0.87ml).

Fig. 4.6 (b) shows EFs for the three cases. Again, case LDDMM achieves higher EF both at LV (51.92%) and RV (55.47%) than the two rule-based cases. Furthermore, the LV EFs for cases RBM¹⁷ and RBM^{uni} are less than 50%, which are below literature reported normal range (50% – 75%), indicating the LV pump function is suboptimal in those two cases. ESPs are within the measured range as reported values of LV (80–90 mmHg) [196] and RV (23–30 mmHg) [197].

Fig. 4.6 (c) shows the average end-systolic stress for the entire LV along the circumferential, radial and longitudinal directions, respectively. Although the circumferential stress from case LDDMM is lower near endocardium and epicardium than RBM cases, it is much higher in the midwall, with the lowest value from case RBM^{uni}. Contrary to the circumferential stress, the longitudinal stress is higher in case LDDMM at endocardium and epicardium, while lowest at part of the midwall. The opposite trends of the circumferential and longitudinal stress levels in case LDDMM may compensate each other to achieve a deeper systolic contraction than cases RBM¹⁷ and RBM^{uni}. The radial stress is negative for all three cases with the lowest in case LDDMM.

Fig. 4.6 (d) is the apex twist angle within one cardiac cycle. The twist angle is defined as the rotation of the apex with respect to the basal plane at end-diastole. The apex from case LDDMM twists more compared to cases RBM¹⁷ and RBM^{uni}, with a peak value of 11°, which is well within the reported ranges in healthy hearts (10.2±7.6°) [198]. Therefore, a more efficient pump function is achieved in case LDDMM compared to the RBM cases. Difference between the two rule-based cases are subtle, only slightly improved pump function can be found in case RBM¹⁷, compared to case RBM^{uni}, but it has a reduced apex twist.

Figs. 4.7 (a-c) show the end-systolic myofibre stress distributions for the three cases. In case LDDMM, higher myofibre stress ($\hat{\mathbf{f}} \cdot (\sigma \hat{\mathbf{f}})$) can be found at both the endocardial and epicardial surfaces, especially in the LV side, while its distribution is less uniform compared to the two RBM cases. Figs. 4.7 (d-f) show the strains along myofibre at end-systole. Strain distributions are similar in the two RBM cases, but the great difference is seen from the LDDMM case. The less uniform distributions of stress and strain in case LDDMM may be partially explained by much dispersed myofibre structures. The angle between the long-axis and the longitudinal axis

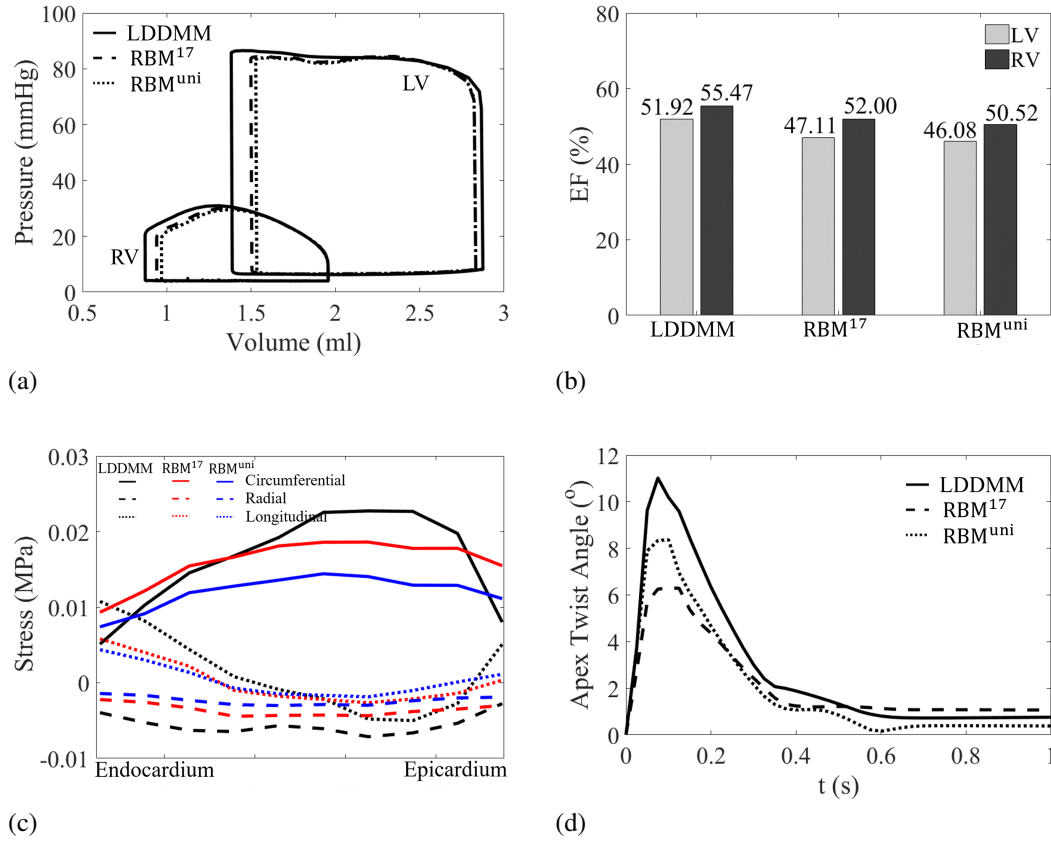


Figure 4.6: Simulated pump functions from cases LDDMM, RBM¹⁷ and RBM^{uni}, including (a) PV loops of LV and RV, (b) LV and RV EFs, (c) stress distribution across the wall at end-systole, and (d) apex twist angle.

at end-systole, defined in Figs. 4.7 (d-f), is largest in the LDDMM case (8.7°) and lowest in RBM^{uni} (4.2°), also suggesting different deformed end-systolic shapes.

4.3.2 RBM^{uni} with cross-fibre active tension

Based on case RBM^{uni}, five different sets of n_s and n_n are chosen to investigate how they affect ventricular dynamics. These are: (1) $n_s = 0, n_n = 0$, (2) $n_s = 0.2, n_n = 0$, (3) $n_s = 0.4, n_n = 0$, (4) $n_s = 0.0, n_n = 0.2$, (5) $n_s = 0.0, n_n = 0.4$. For all simulations $n_f = 1.0$. Fig. 4.8 shows the pump functions with varied n_s or n_n . If we only consider cross-fibre active tension along the sheet direction, then the PV loop enclosed area is reduced as shown in Fig. 4.8 (a), suggesting that the active tension along the sheet direction will counteract the myofibre contraction. On the other hand, non-zero n_n increases the area enclosed by the PV loop and enhances the cardiac work. For example, with $n_s = 0.4$, the LVEF is around 29.97%, which is much less than the case with $n_s = 0$ (46.08%), while with $n_n = 0.4$, LVEF is increased by 10% as shown in Fig. 4.8 (b). Therefore, active tension along the sheet-normal direction is beneficial to the pump function, but contraction along the sheet direction has the opposite effect.

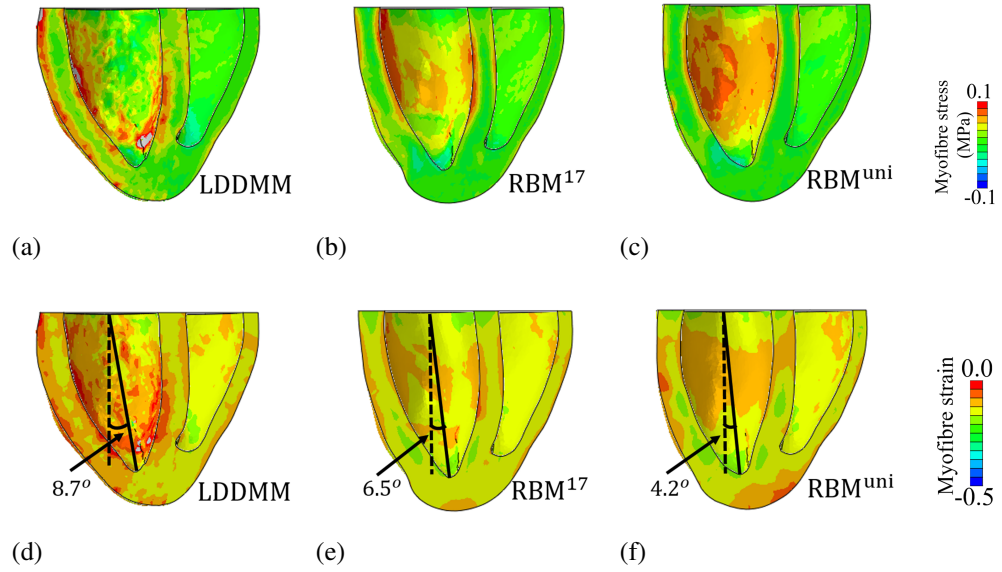


Figure 4.7: Myofibre stress and strain distributions at end-systole for cases LDDMM, RBM¹⁷ and RBM^{uni}, respectively. The solid lines in (d), (e), and (f) are the long-axis which links the LV basal centre and the LV apex, and the longitudinal axis is represented by the dash line passing the LV basal centre and perpendicular to the basal plane.

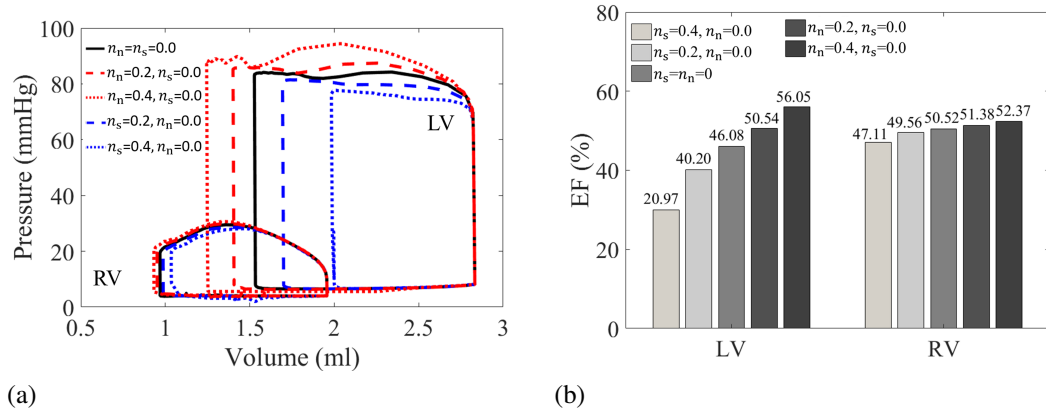


Figure 4.8: Pump functions with varied n_s and n_n in case RBM^{uni}. $n_f = 1.0$ for all simulations. (a) PV loops of LV and RV, and (b) EFs for LV and RV.

Fig. 4.9 shows results from case RBM^{uni} with dispersed active contraction, modelled by the structural tensor from Eq. (4.16). In this case, case RBM^{uni} has nearly the same LV PV loop as case LDDMM, and the apical twist is also similar to case LDDMM (Figs. 4.9 (a, b)). Only a small difference in EDV ($\approx 1.4\%$) is observed between the two models. On the other hand, Fig. 4.9 (c,d) shows that the end-systolic circumferential stress is much lower compared to case LDDMM, particularly in the midwall. The longitudinal and radial stresses are also slightly higher in the midwall because of non-zero n_n and n_s .

In summary, compared to case LDDMM, case RBM^{uni} shows a lower and more homoge-

neous stress level but achieves a similar pump function if using a suitable general structural tensor approach for the cross-fibre contraction.

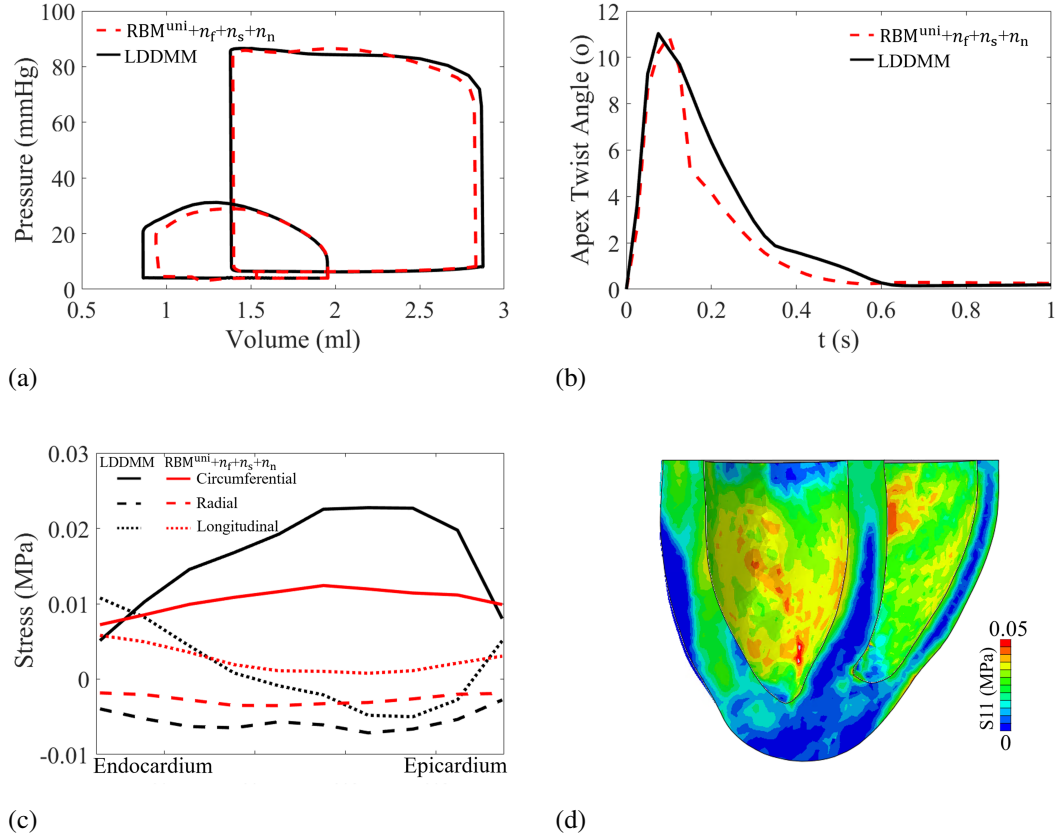


Figure 4.9: Pump function comparisons between case LDDMM and case RBM^{uni} with cross-fibre contraction. (a) PV loops, (b) apex twist angle, (c) intramural stress across the entire LV wall and (d) myofibre stress distribution from case RBM^{uni} with cross-fibre contraction at end-systole.

It is interesting to see if similar results could be obtained without any knowledge of the patient-specific fibre field. To this end, we run extra simulations based on RBM^{uni} using literature-based values for n_f , n_s , and n_n . Specifically, we consider (1) no dispersion $n_f = 1$, $n_s = n_n = 0$, (2) $n_f = 0.879$, $n_s = 0.009$, $n_n = 0.112$ [4], and (3) $n_f = 0.646$, $n_s = 0.086$, $n_n = 0.268$, derived from DT-MRI in this chapter. The fibre rotation angles are also chosen from $30^\circ \sim -30^\circ$ (exRBM¹), $45^\circ \sim -45^\circ$ (exRBM²), or $60^\circ \sim -60^\circ$ (exRBM³) [7]. The results are summarized in Fig. 4.10 in terms of the LV and RV EFs. Clearly, EFs increase with fibre rotation angles, as more myofibres align longitudinally which enhance the active contraction. Different dispersion parameters also affect the pump function. Compared to case LDDMM, the EFs are lower in exRBM¹ (39.37% (LV), 45.89% (RV)), and still lower in exRBM² (47.86% (LV), 51.72% (RV)). Only exRBM³ with DT-MRI derived dispersion parameters can achieve the similar pump functions as in case LDDMM, though the myofibre rotation angles ($60^\circ \sim -60^\circ$) are much greater than case LDDMM (mean angles $40^\circ \sim -30^\circ$). This would suggest that subject-specific my-

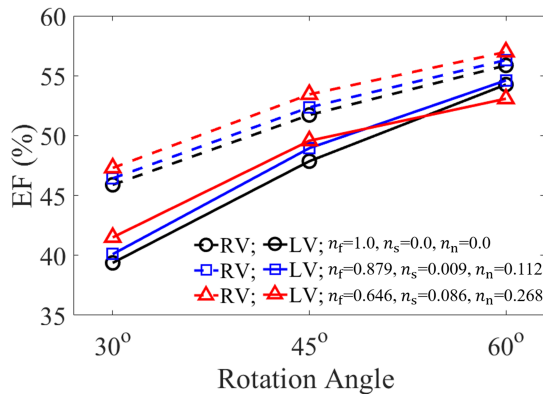


Figure 4.10: Predicted EFs with literature-based myofibre rotation angles [7] and dispersion parameters [4] using case RBM^{uni} . The results are to be compared with the LDDMM case in Fig.4.7 (b), which has the mean fibre rotation angles $40^\circ \sim -30^\circ$, and EFs of 51.92% (LV) and 55.47% (RV).

of fibre structure is necessary for cardiac mechanic modelling, as using literature-based myofibre structures seem to underestimate the pump function.

4.3.3 Parameter sensitivity and inference study of myocardial property

A sensitivity study is performed with case LDDMM. The so-called “one-point” approach is employed here by varying one parameter at a time and others kept same. Parameters (a , b , a_f , b_f , a_n , b_n , a_{fs} , b_{fs} , a_{fn} , b_{fn} and T_{\max}) are first doubled and then halved from the values in Table 4.4 . Fig. 4.11 (a,b) shows the normalized end-diastolic and ESVs with respect to case LDDMM. It can be found that EDV is mostly affected by a , b , a_f and a_n , while ESV is mostly affected by T_{\max} . Fig. 4.11 (c) further shows the changes of EFs. Both LV and RV EFs are reduced when doubling a , b , a_f , a_n , and vice versa. T_{\max} has the largest effect on LV and RV EFs, while other parameters have little influences.

In this chapter, the EDV for the LV is $(V_0 + 1)$ mL, and $(V_0 + 0.6)$ mL for the RV with V_0 being the reference volume of the LV or RV, respectively. T_{\max} is then determined by achieving targeted EFs. Fig. 4.12 illustrates how the mismatch between the targeted value and the predicted value is reduced by the passive scaling factor and T_{\max} during the inference procedure for the LV as an example. Fig. 4.12 (a) is the mismatch of LV EDV with respect to the scaling factor, which is defined as $|(\text{EDV}^{\text{predict}} - \text{EDV}^{\text{target}})/\text{EDV}^{\text{target}}|$, and Fig. 4.12 (b) is the mismatch of LV EF ($|(\text{EF}^{\text{predict}} - \text{EF}^{\text{target}})/\text{EF}^{\text{target}}|$) with respect to T_{\max} . From Fig. 4.12, it can be seen that both the passive scaling factor and myocardial contractility (T_{\max}) can be nicely determined by matching targeted values. Note that this approach will only provide one set of possible parameters, to uniquely infer each parameter of myocardial material property can be extremely challenging due to various difficulties [13], i.e. limited measured data, parameter correlation, etc.

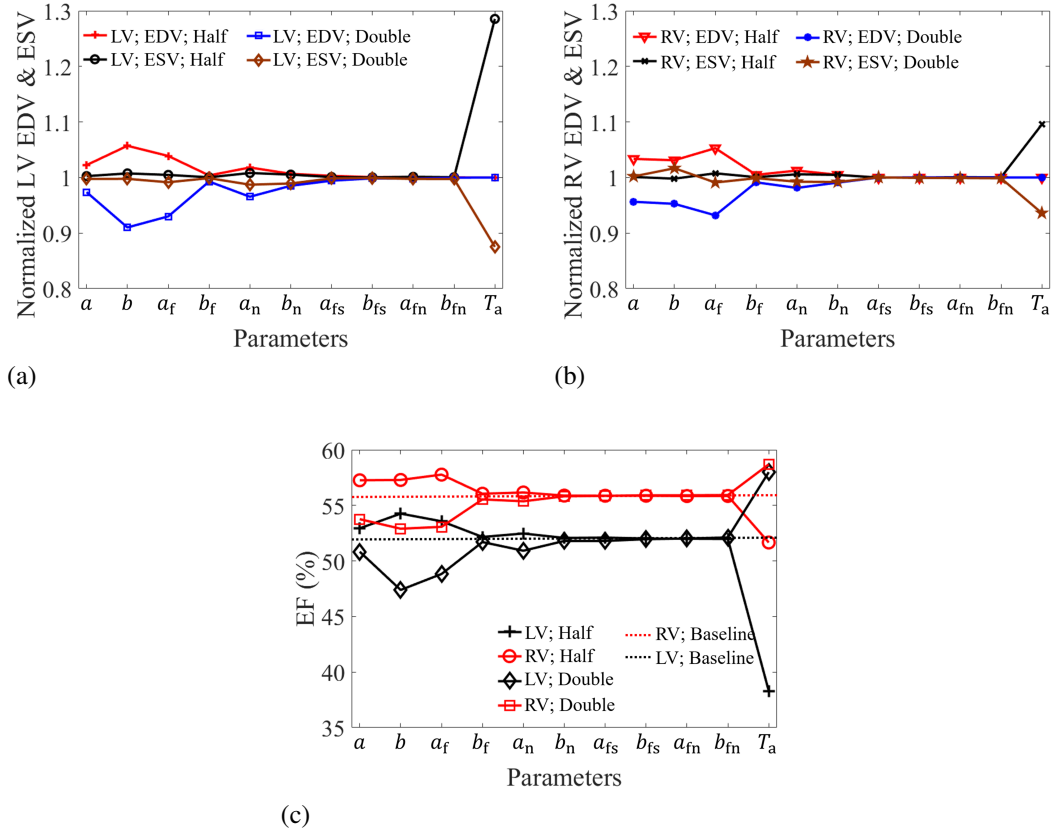


Figure 4.11: Myocardial material parameter sensitivity study, including a , b , a_f , b_f , a_n , b_n , a_{fs} , b_{fs} , a_{fn} , b_{fn}) and the active parameter (T_{max}). (a) normalized EDV and ESV values of the LV and (b) the RV with respect to the corresponding baseline values; (c) EF values. The baseline values of LV and RV are from the simulation with parameter values in Table 3 (the main text).

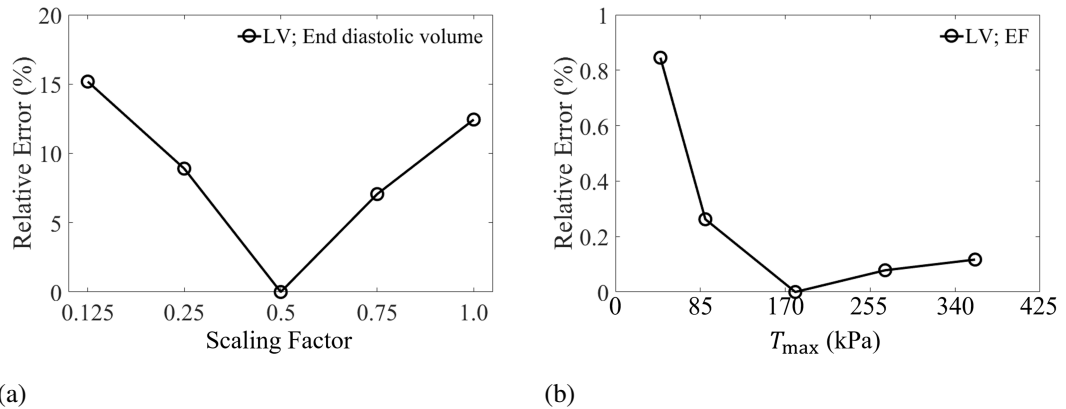


Figure 4.12: Relative errors in EDV (a) and EF (b) of the LV when inferring reasonable model parameters by matching targeted EDV ($V_0 + 1$) mL with V_0 the initial value and EF 52%.

4.4 Discussion

In this chapter, LDDMM-based *Deformetrica* [182] is used to warp a canine bi-ventricle to a neonatal porcine heart, and DT-MRI measured myofibre structure is then mapped to a porcine heart by solving a Laplace system. Base on the mapped DT-MRI measured myofibre structure, two simplified fibres are further generated using a rule-based approach. Our results show that under same pre-/after-loading conditions, both LV and RV have a higher pump function in the case with LDDMM-mapped fibres compared to the rule-based cases, while case LDDMM experiences higher myofibre stress and more heterogeneous stress pattern than rule-based cases. Large differences can be expected when using literature-based fibre structures and dispersion parameters compared to case LDDMM. Those different results highlight the necessity of use realistic myofibre structure for personalized cardiac modelling as demonstrated in other studies [7, 118, 119, 122].

In case LDDMM, the high active fibre stresses at both epicardial and endocardial surfaces (Fig. 4.7 (a)) can potentially enhance the long-axis shortening and also apical twist (Fig. 4.6 (d)). In fact, long-axis shortening in systole with respect to end-diastole is slightly higher in case LDDMM (-7.3%) than other two cases (-6.8% for RBM^{17} , -7% for RBM^{uni}). Our results show (Figs. 4.4 (a, b)) that DT-MRI derived myofibres do not lie in $\mathbf{c}_0 - \mathbf{l}_0$ plane but dispersed. Thus the active tension in case LDDMM is generated along fibres dispersed with both in-plane and out-of-plane components. In section 4.2.2, we firstly quantify myofibre dispersion with in-plane and out-of-plane distributions, and then introduce a structural tensor \mathbf{H} [20, 199] by fitting to the measured in/out-of-plane dispersions. The π -period von Mises distribution is used to describe myofibre dispersion, good agreement can be achieved as shown in Figs. 4.4 (c) and (d). While it may not be guaranteed that the von Mises distribution can be applied to pathological tissues, such as myocardial infarction [200].

We find that cross-fibre contraction is highest along the sheet-normal direction compared to that of the sheet-direction, but much lower than along mean fibre direction. Furthermore, active contraction in the sheet-normal direction can facilitate contraction, but not in sheet direction. This is because myofibres dominantly lie in $\mathbf{c}_0 - \mathbf{l}_0$ plane, in which \mathbf{f} and \mathbf{n} are defined, and contraction along \mathbf{f} and \mathbf{n} causes circumferential and long-axial shortening [201], so the wall thickens to maintain the constant wall volume if the material is incompressible. Whilst transmural contraction along \mathbf{s} causes wall thinning, which counteracts myofibre contraction. Note that in this chapter, the sheet direction is defined transmurally across the wall, which is consistent with studies from [11, 21, 113], though some studies define it as the sheet-normal direction [91]. Unlike the myofibres which rotate from endocardium to epicardium, here the sheet direction is assumed to align the radial direction in all cases. In other words, the sheet rotation angle is chosen to be zero. To evaluate this assumption, we have tested three sets of sheet rotation angles as in [7]: $30^\circ \sim -30^\circ$, $45^\circ \sim -45^\circ$, $60^\circ \sim -60^\circ$, based on case RBM^{uni} with dispersed active tension. The results show that the sheet rotation angle has little effect on ventricular pump

function, and the differences in EF between different sheet rotation angles are within 1%. This agrees with observations from other groups. For example, Wang et al. [7] found that the sheet rotation angle nearly has no influence on passive mechanics in an LV model.

We now compare our values of cross-fibre proportions ($n_s = 0.086$, $n_n = 0.268$, $n_f = 0.646$) with previous studies. Based on the experimental study by Lin and Yin [1], Guccione and co-workers introduced cross-fibre active contraction with $n_s = 0.0$, $n_n = 0.4$ and $n_f = 1.0$ [90]. In a recent study, Sack et al. [91] inversely determined cross-fibre contraction ratios (Note that in Sack's work [91] they used notation n_s for n_n due to a different definition) in a healthy porcine heart ($n_n = 0.07$) and a failure heart ($n_n = 0.14$) with $n_f = 1.0$ and $n_s = 0$. In our study n_n (0.268) is higher than that of Sack's study [91]. This could be due to (1) subject variation; (2) higher $n_f = 1.0$ used in their study (our $n_f = 0.646$), leading to a higher contraction along the averaged myofibre direction so a lower n_n could match the measured pump function; (3) they inversely determined n_n and T_a , which are not from measurements. In this chapter, proportions of cross-fibre contraction are derived directly from intrinsic fibre structures, which have a clear biological explanation. When normalized by n_f , the ratio between the sheet-normal and myofibre direction is 41%, which agrees with the ratio reported by Lin and Yin (40%) [1]. We further calculate the dispersion parameters from a recent study on neonatal porcine heart by Ahmad et al. [5], $n_f = 0.68$ and $n_n = 0.32$ with nearly negligible $n_s \approx 0.0009$, again very close to our values in this chapter. We are not aware of any available experimental measurements for estimating n_n and n_s in the myocardium.

Rodriguez-Cantano et al. [122] argued that RBM tends to exaggerate myofibre layered architecture and the passive stiffness of the ventricle, while DT-MRI measured fibres may underestimate ventricular stiffness due to measurement noise and uncertainties. We find that when taking into account the cross-fibre contraction in the case RBM^{uni}, we can achieve similar systolic contraction as case LDDMM (Fig. 4.9) with less heterogeneous stress patterns. Because of challenging of in vivo DT-MRI acquisition, rule-based myofibre structures will continue to be used when modelling cardiac mechanics, even in personalized models. Our results suggest by incorporating fibre dispersion using a structural tensor, RBM-based model can be a good approximation of the most realistic myofibre structure as derived from DT-MRI, and the structural tensor may be determined either from limited in/ex vivo DT-MRI data [202] or inversely estimated, while cautions need to be paid when myofibre structures are from different subjects or species. There is a small difference (around 1.4%) in EDV in Fig. 4.9 (a), presumably because the dispersion is not included in the passive constitutive law. Given that exclusion of compressed fibres using structural tensor approach is nontrivial in the passive modelling [17,64], we will leave the work of including dispersion in the passive model in future.

Using material parameters estimated from ex vivo measurements to describe in vivo material behaviours is a standing challenge. Published studies have suggested passive parameters estimated from ex vivo experiments can over-estimate the stiffness in vivo [7, 13, 92]. Hence,

most of the studies, ours included, scaled the parameters from ex vivo data to match the in vivo dynamics [2, 13, 91]. Here, the initial passive parameters are adopted from our previous study [181] which were inferred from ex vivo neonatal myocardial stretching experiments [9], then a , a_f , a_n , a_{fs} and a_{fn} are scaled to achieve the targeted EDVs. The myocardial contractility T_{max} is determined by matching the targeted EFs ($> 50\%$) for both the LV and RV. We further assume the passive scaling factor is same for the LV and RV. Thus only three parameters need to be determined: the passive scaling factor, T_{max} for the LV and T_{max} for the RV.

The sensitivity study on the passive parameters and T_{max} , and an illustration of their inferences are proceeded. As mentioned previously, it is not our intention to develop a personalized bi-ventricular model for this neonatal porcine heart, instead we seek to construct a general model with physiologically-correct pump function, i.e. eject fraction $> 50\%$. Currently, there is no consistent way on how to adjust parameters derived from ex-vivo experiments to in vivo models. Thus in many studies, parameters of in vivo myocardium are scaled from ex vivo experiments [13, 91] in order to match in vivo measurements. The similar approach is followed in this chapter by scaling a , a_f , a_n , a_{fs} , a_{fn} to match targeted EDVs.

The convexity of the HO type SEF requires all parameters greater than zero as suggested in [11], which is satisfied in our approach. Because the employed passive SEF (Eq. 4.7) is in a similar formulation as the original HO model, which indicates the convexity of Eq. 4.7 can be ensured if all parameters are positive. The initial values for a , b , a_f , b_f , a_n , b_n , a_{fs} , b_{fs} , a_{fn} and b_{fn} are all positive, thus the convexity will require the scaling factor greater than zero, which is 0.5 in this chapter. However, as pointed out by Giantesio et al. [104], the polyconvexity of the total energy function (passive and active) may not be ensured even though the passive SEF is convex. Although we have not experienced stability issues using the active stress approach, we must point out this approach may not be thermodynamically consistent. For generalised thermodynamically consistent approaches, the reader is referred to [103, 104, 108].

Due to lack of DT-MRI data for the RV from the canine experiment, a rule-based approach is used for generating fibre structure in the RV, and zero cross-fibre contraction is assumed. This can be readily improved if measured RV fibre structure becomes available. We notice there is a difference in the RV systolic function even though the RV model is identical in all three cases. In particular, the RV contracts more in case LDDMM than in the two RBM cases. We think this is due to the different LV contraction in the three cases. For instance, the end-systole angle between the long-axis and longitudinal axis is different in each case. Palit et al. [117] also found that there are strong interactions between the LV and RV dynamics in diastole. This highlights the importance of LV-RV interaction on cardiac pump function, which is why the bi-ventricle model is used. In addition, the LDDMM framework [182] relies on geometrical features for warping the two different geometries, a bi-ventricular model has much richer information compared to a stand-alone LV model, in particular in the RV-LV insertion regions.

It is expected that there are differences in myofibre structure between the porcine heart and

the canine heart, but this is difficult to assess as we don't have measured DT-MRI fibre structure for the porcine heart. However, despite the species difference, we find that the mapped canine myofibre structure agrees well with other studies in terms of mean values [5, 91, 121], see Table 4.1. For instance, Ahmad et al [5] measured myofibre rotation angles in left ventricle free wall (LVFW) of neonatal hearts (Anterior $51.1 \pm 3.8^\circ \sim -51.1 \pm 3.8^\circ$, Posterior $40.2 \pm 2.9^\circ \sim -40.2 \pm 2.9^\circ$). Sack et al. [91] reported fibre rotation angles for a normal adult porcine heart based on DT-MRI measurements (endocardium: $66.5 \pm 16.6^\circ$, epicardium: $-37.4 \pm 22.4^\circ$). Myofibre rotation angles from published experimental and numerical studies are also summarized in Table 4.5. The mean fibre rotation angle (endocardium: 40° , epicardium: -30°) is measured from the DT-MRI data and is still within the right range as the experimental studies in the Table 4.5. The small rotation angle may be one of the reasons for the less EF in the model with the RBM fibre structure, because the models with wider range of fibre rotation can achieve better pump functions as shown in Fig. 4.10. The coupling effects of fibre dispersion and fibre rotation on cardiac pump function are not further explored in this chapter.

	Experimental studies		Modelling studies		
	Epicardium	Endocardium		Epicardium	Endocardium
Anterior LVFW [5]	$-51.1 \pm 3.8^\circ$	$51.1 \pm 3.8^\circ$	Doste et al. [203]	-60.0°	60.0°
Anterior RVFW [5]	$-70.5 \pm 6.5^\circ$	$70.5 \pm 6.5^\circ$	Sack et al. [204]	-60.0°	60.0°
Posterior LVFW [5]	$-40.2 \pm 2.9^\circ$	$40.2 \pm 2.9^\circ$	Bayer et al. [116]	-50°	40°
Posterior RVFW [5]	$-22.1 \pm 6.2^\circ$	$22.1 \pm 6.2^\circ$	Wang et al. [7]	-60°	60°
Excluding apex [91]	$-37. \pm 22.44^\circ$	$66.5 \pm 16.6^\circ$	Gao et al. [13]	-60°	60°
Anterior [30]	$-35.7 \pm 8.6^\circ$	$38.5 \pm 6.1^\circ$	Barbarotta et al. [101]	-60°	60°
Lateral [30]	$-41.0 \pm 8.0^\circ$	$29.7 \pm 6.6^\circ$			
Posterior [30]	$-57.0 \pm 6.2^\circ$	$39.5 \pm 10.6^\circ$			

Table 4.5: Summary of fibre rotation angles from published experimental modelling studies. RVFW: right ventricle free wall.

The spatial variations of the material properties have not been considered in this chapter, and the same averaged dispersed active contraction model is applied across the whole LV for case RBM^{uni}. This approximation may be reasonable for healthy hearts, but questionable for pathological cases. For example, the myocardium is known to be more heterogeneous post myocardial infarction [200].

Finally, we would like to mention other limitations of our study. In the boundary conditions we used, the basal plane of the models is constrained along the longitudinal direction, and the rest nodes in the basal plane are free to move. This type of boundary conditions does not represent in vivo conditions due to the lack of the pericardium and great vessels. Under in vivo situation, with the constraints imposed by the pericardium, the apex does not move much. Instead, the basal plane moves downward towards the apex in systole and moves upward in diastole. In a recent study, Pfaller et al. [205] demonstrated that simulated cardiac mechanics could be much closer to the measured heart motion by including the pericardium influences, which highlights the necessary of pericardial-myocardial interaction. A simplified lumped cir-

ulation model is used to provide pressure boundary conditions, which is a simplification of pulmonary and systemic circulations. Coupling to a more realistic circulation model, such as one-dimensional systemic models [206, 207], will allow us to simulate more detailed cardiovascular function in pathological situations [208]. Furthermore, we have not coupled the blood flow inside ventricle, only applied a spatially homogeneous pressure to the endocardial surface, nor have we considered contraction delay due to the action potential propagation [103]. Tremendous efforts will be needed to address all those limitations, which is beyond the scope of this chapter.

4.5 Conclusion

In this chapter, we have developed a bi-ventricular porcine heart computational model from a neonatal dataset, with mapped myofibre architecture from an ex vivo canine DT-MRI dataset using an LDDMM framework. Different approximations of myofibre architecture based on widely used rule-based approaches are analysed in terms of cardiac pump function. Our results show that using DT-MRI derived myofibre architecture can enhance cardiac work, achieve higher EF and larger apical twist compared to rule-based myofibre models, even though they are all derived from the same DT-MRI dataset. Our work shows that the major difference between the LDDMM and RBM approaches is due to the fibre dispersion, which enables cross-fibre active tensions. These are not captured by standard RBM based models. Introducing regional dependent fibre structure in RBM is not sufficient to improve the model. However, when the myofibre dispersion is taken into consideration, a simplified RBM based cardiac model can achieve similar pump function as the LDDMM based model. We further note that in RBM based cardiac models, the cross-fibre active tension along the sheet-normal direction can enhance active contraction, but the opposite is true along the sheet direction.

Chapter 5

Fibre dispersion: its effects on cardiac mechanics from diastole to systole

5.1 Introduction

In Chapter 4, we studied the effect of myofibre architecture on ventricular pump function by using a neonatal porcine heart model from DT-MRI to rule-based methods, and proposed the dispersed active stress model [15] by following the GST approach. However, fibre dispersion in the passive response of myocardium was not considered. Furthermore, there is lack of study of how compressed fibre exclusion could affect the ventricular passive filling and further affecting to its pump function overall. Thus, there is a need to systematically quantify to which extent the dispersion can affect ventricular dynamics both at diastole and systole under physiological loadings.

Constitutive modelling of soft tissue with dispersed fibres have found that dispersed collagen fibres can have a significant effect on the overall mechanical response of the soft tissue [20, 124]. To incorporate fibre dispersion into a SEF, one way is to assume a PDF with respect to the mean fibre direction, such as using the π -periodic von Mises distribution [20, 134]. Then the total SEF for the tissue can be the summarization of each fibre contribution along with other constituents. Broadly speaking, there are two approaches for counting collagen fibre contributions: (1) the AI approach [123], in which the stress from each fibre is added together; and (2) the other one is the GST approach, which was first proposed by Gasser et al [20].

In soft tissue mechanics, it is often considered that collagen fibres will not bear load when compressed, thus excluding compressed fibres is necessary [125]. Such exclusion is simple when fibres are not dispersed by simply zeroing out fibre stress if compressed, but can be challenging when fibres are dispersed because a stretched domain needs to be determined at each loading step according to its PDF. In both the AI and GST approaches, to exclude compressed fibres under complex dynamics will generally require a 2D integration over a unit sphere at each computational location at each loading step, except for some special cases where analytical

solutions may exist. The numerical realization of this 2D integration over a unit sphere may require hundreds of integrations, thus the computational demand can be very high [136]. To improve computational efficiency of this 2D integration of stretched fibres in FE simulation, Li et al [17] developed a DFD model. The unit spherical surface of the fibre dispersion domain is divided into finite elements, and the fibre bundle at the centroid of each element is chosen as the representative fibre. If a representative fibre is stretched, then all the fibres in the element area are assumed to contribute to the total stress, and the contribution amount is estimated by the stretch of the representative fibre and corresponding probability density determined from the PDF. Li et al. [17] found that DFD method could significantly reduce the computational demand for excluding compressed fibres, for example, a speed-up of 224 times was achieved in their study than using a traditional AI approach.

In this chapter, we have focused on mathematical modelling of fibre dispersion in myocardial mechanics, and study how different fibre dispersions affect cardiac pump function. In order to exclude compressed fibres for passive response, we adopt the DFD model for approximating a continuous fibre distribution with finite fibre bundles, and then the GST approach is employed for describing dispersed active tension. The methodological approaches are shown at first simple test cases and gradually increasing in complexity. We first study the numerical accuracy of the integration of fibre contributions using the DFD approach with an unit cube model, then compare different mechanical response in an uniaxially stretched myocardial strip model with varied fibre dispersions, which serves as a preliminary concept-proof. We finally study the cardiac pump functions from diastole to systole in two heart models, a single LV model and a biventricle model that are two common heart models.

Our results show that the DFD model is preferred for excluding compressed fibres because of its high computational efficiency. Both the diastolic filling and the systolic contraction will be affected by dispersed fibres depending on the in-plane and out-of-plane dispersion degrees, especially in systolic contraction. The in-plane dispersion seems to affect myocardial mechanics more than the out-of-plane dispersion. Despite different effects in the rabbit and human models caused by the fibre dispersion, large differences in pump function exist when fibres are highly dispersed at in-plane and out-of-plane. Our results highlight the necessity of using dispersed fibre models when modelling myocardial mechanics, especially when fibres are largely dispersed under pathological conditions, such as fibrosis.

This chapter is based on the published paper *Guan, D., Zhuan, X., Holmes, W., Luo, X. and Gao, H., 2021. Modelling of fibre dispersion and its effects on cardiac mechanics from diastole to systole. Journal of Engineering Mathematics, 128(1), pp.1-24.*

5.2 Method

5.2.1 DT-MRI acquisition protocol

Diffusion-weighted images of a fixed rabbit heart were acquired on a 7T Bruker Pharmascan magnetic resonance imaging system, with a micro-imaging gradient insert (model BG-6) and 100-A gradient amplifiers that provide linear magnetic field gradient pulses of up to 300 mT/m. The heart was contained in a 50 ml syringe (Terumo, Belgium) of inner diameter 29.1 mm. The water was degassed with a slight vacuum and air bubble removed by agitation. The sample syringe was placed in a 35 mm Bruker birdcage radio frequency resonator. Using a spin-echo diffusion weighted sequence, the echo time was 27 ms, the repetition time was 2000 ms, the diffusion gradient separation was 14 ms, and the diffusion gradient duration was 7 ms. Diffusion weighted images were acquired for 6 directions with a b-value of 500 s/mm², additionally one b₀ image (with no diffusion gradients) was acquired. The field-of-view was fixed to 4.5×3.1×3.1 cm³, matrix 160×110×110, with voxel dimensions of 0.282×0.282×0.282 mm³. The total scanning time acquiring one average, along six diffusion directions, took around 47 hours. Using the DTI reconstruction software dtfit in FSL [209], freely available at <https://fsl.fmrib.ox.ac.uk/fsl/fslwiki>, the 6 DWIs and the b₀ images were corrected for eddy currents, and then the metrics of the tensor, i.e. the three eigenvalues, were computed. The radial diffusivity was then calculated by averaging of the second and third eigenvalues.

5.2.2 Passive stress

It is a common practice to model myocardium as a hyperelastic fibre-reinforced incompressible material as evidenced in various experimental studies [4, 5] and modelling studies [2, 91, 181]. Here, a reduced form of invariant-based SEF for incompressible soft tissue is used by only including the contributions from the ground matrix and the fibres (both collagen and myofibres), that is

$$\mathcal{W} = \mathcal{W}_g + \mathcal{W}_f = \frac{a}{2b} \{ \exp[b(I_1 - 3)] - 1 \} + \frac{a_f}{2b_f} \{ \exp[b_f(\max(I_{4f}, 1) - 1)^2] - 1 \}, \quad (5.1)$$

where a, b, a_f, b_f are material constants, $I_1 = \text{trace}(\mathbf{C})$ and $I_{4f} = \mathbf{f}_0 \cdot \mathbf{C} \mathbf{f}_0$ are strain invariants with $\mathbf{C} = \mathbf{F}^T \mathbf{F}$ and \mathbf{F} the deformation gradient, \mathbf{f}_0 is the mean fibre direction in the reference state. The $\max()$ in Eq. (5.1) is to ensure that only the stretched fibres can bear the loads. Eq. (5.1) has been widely used for modelling collagenous tissue [63, 64] and myocardium [65, 66].

In general, fibres do not align perfectly along the mean fibre direction, but are dispersed [5]. To describe such dispersed fibres, we first introduce a spherical polar coordinate system based on the layered fibre structure, the so-called $\mathbf{f}_0 - \mathbf{s}_0 - \mathbf{n}_0$ system, shown in Fig. 5.1 (a), thus a

single fibre can be described in terms of the two spherical polar angles Θ and Φ in the reference configuration as

$$\mathbf{M}(\Theta, \Phi) = \cos \Theta \mathbf{f}_0 + \sin \Theta \cos \Phi \mathbf{n}_0 + \sin \Theta \sin \Phi \mathbf{s}_0, \quad (5.2)$$

within the domains of Θ and Φ defined over an unit hemisphere

$\mathbb{S} = \{(\Theta, \Phi) | \Theta \in [0, \pi/2], \Phi \in [0, 2\pi]\}$ as shown in Fig. 5.1 (b). Since the two fibres lying in one line are mechanically identical, thus \mathbb{S} only needs to be defined over a unit hemisphere.

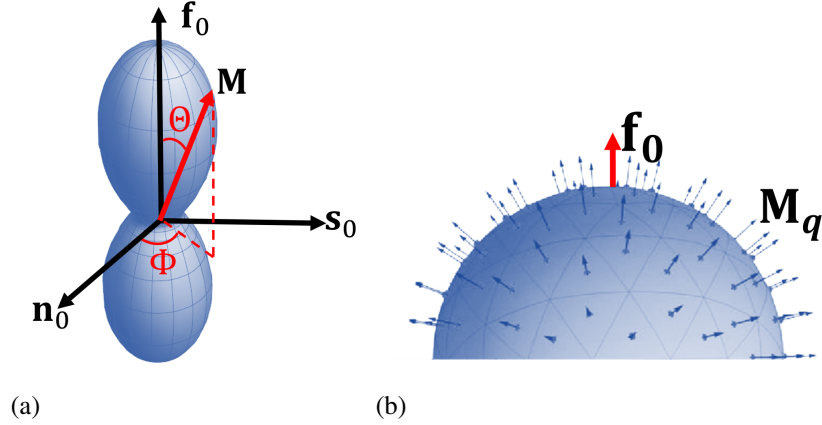


Figure 5.1: (a) Surface plot of $\rho(\Theta, b_1, \Phi, b_2)\mathbf{M}(\Theta, \Phi)$ in the fibre system \mathbf{f}_0 , \mathbf{n}_0 and \mathbf{s}_0 with an unit vector \mathbf{M} (red) representing the fibre direction defined by Θ and Φ . (b) Illustration of a discrete triangular discretization of the unit hemisphere domain centralised with the mean fibre direction \mathbf{f}_0 (the red arrow) with N representative fibre directions \mathbf{M}_q (blue arrows) at the centroid of each triangular surface.

The definition of PDF of fibre dispersion $\rho(\Theta, b_1, \Phi, b_2)$ is same as that in section 4.2.2 of Chapter 4, and the fibre dispersion domain is updated from the unit sphere to the unit hemisphere by modifying the constant G in Eq. (4.13). Note large concentration parameter b_i suggests less dispersion, and vice versa. We write \mathcal{W}_f in Eq. (5.1) as

$$\mathcal{W}_f^* = \int_{\mathbb{S}} \rho(\Theta, b_1, \Phi, b_2) \mathcal{W}_f(I_{4M}(\Theta, \Phi)) \sin \Theta d\Theta d\Phi, \quad (5.3)$$

where $I_{4M}(\Theta, \Phi) = \mathbf{M} \cdot (\mathbf{C}\mathbf{M})$, and $\mathcal{W}_f(I_{4f}) = \frac{a_f}{2b_f} \{\exp[b_f(\max(I_{4f}, 1) - 1)^2] - 1\}$.

Integrating Eq. (5.3) analytically can be very challenging because of the $\max()$ function, in other words, the exclusion of non-stretched fibres. In a recent study, Li et al [17] divided the hemisphere space domain \mathbb{S} into N spherical triangle elements using representative fibre bundles for excluding non-stretched fibres, the so-called DFD approach, shown in Fig. 5.1 (b). For detailed description of the DFD approach, please refer to [17]. In brief, the representative fibre direction of a triangle (q) in Fig. 5.1 (b) is denoted as $\mathbf{M}_q(\Theta_q, \Phi_q)$ with Θ_q and Φ_q the spherical coordinates of the centroid of the q^{th} triangle, $\Delta\mathbb{S}_q$ is the triangular area, and the fibre

density distribution at this triangle is approximated as

$$\rho_q = \int_{\Delta\mathbb{S}_q} \rho(\Theta, b_1, \Phi, b_2) \sin \Theta d\Theta d\Phi, \quad q = 1, \dots, N, \quad \text{subject to} \quad \sum_{q=1}^N \rho_q = 1, \quad (5.4)$$

in which N is the number of discretized triangles for the unit hemisphere. Thus \mathcal{W}_f^* can be further approximated as

$$\mathcal{W}_f^* \cong \sum_{q=1}^N \rho_q \mathcal{W}_f(I_{4M}^q), \quad \text{with} \quad \mathcal{W}_f(I_{4M}^q) = \begin{cases} \mathcal{W}_f(I_{4M}^q) & \text{if } I_{4M}^q > 1 \\ 0 & \text{if } I_{4M}^q \leq 1 \end{cases}, \quad (5.5)$$

where $I_{4M}^q = \mathbf{M}_q \cdot (\mathbf{C}\mathbf{M}_q)$.

Finally, the passive stress of myocardium with dispersed fibres is

$$\sigma^p = a \exp[b(I_1 - 3)] \mathbf{B} + 2 \underbrace{\sum_{q=1}^N \rho_q a_f (I_{4M}^{q*} - 1) \exp[b_f (I_{4M}^{q*} - 1)^2]}_{\sigma_f} (\mathbf{m}_q \otimes \mathbf{m}_q) - p \mathbf{I}, \quad (5.6)$$

where $\mathbf{B} = \mathbf{F}\mathbf{F}^T$, $I_{4M}^{q*} = \max(I_{4M}^q, 1)$, $\mathbf{m}_q = \mathbf{F}\mathbf{M}_q$, p is the hydrostatic-like pressure to ensure incompressibility, and \mathbf{I} is the identity matrix. Algorithm 5.1 lists the detailed steps of numerically calculating σ_f in Eq. (5.6).

5.2.3 Active stress

To take into account dispersed active stress due to dispersed myofibres, we followed the GST approach as in section 4.2.2 of Chapter 4 by introducing a structural tensor \mathbf{H} , that is

$$\mathbf{H} = \int_{\mathbb{S}} \rho(\Theta, b_1, \Phi, b_2) \sin \Theta \mathbf{M} \otimes \mathbf{M} d\Theta d\Phi, \quad (5.7)$$

in which we assume the same $\rho(\Theta, b_1, \Phi, b_2)$ as used in Eq. (5.3). Hence, the myocardial active stress is

$$\sigma^a = T_a H_{11} \hat{\mathbf{f}} \otimes \hat{\mathbf{f}} + T_a H_{22} \hat{\mathbf{n}} \otimes \hat{\mathbf{n}} + T_a H_{33} \hat{\mathbf{s}} \otimes \hat{\mathbf{s}}. \quad (5.8)$$

None zero H_{22} and H_{33} represent the cross-fibre contraction. Accordingly, the total myocardial Cauchy stress is

$$\sigma = \sigma^p + \sigma^a. \quad (5.9)$$

Note, the additive framework is employed here to model myocardial active contraction, alternative approaches exist, such as the active strain framework, please refer to [96, 101, 105] for more details on the active strain framework.

Algorithm 5.1 Excluding compressed fibres using the DFD framework for computing passive stress from stretched fibres.

Data:**F:** deformation gradient tensor**Result:** σ_f : Cauchy stress resulted from stretched fibresAll computations are performed according to the \mathbf{f}_0 – \mathbf{s}_0 – \mathbf{n}_0 systemDivide the \mathbb{S} into N spherical triangles using a freely-available Matlab code^aCalculate $\rho_q = \int_{\Delta\mathbb{S}_q} \rho(\Theta, b_1, \Phi, b_2) \sin \Theta d\Theta d\Phi$ with $\sum_{q=1}^N \rho_q = 1$ Initialization: $\sigma_f = \mathbf{0}$ $J = \det(\mathbf{F})$ $\mathbf{C} = \mathbf{F}^T \mathbf{F}$ **for** $q=1$ to N : **do** determine Θ_q and Φ_q $\mathbf{M}_q(\Theta, \Phi) = \cos \Theta \mathbf{f}_0 + \sin \Theta \cos \Phi \mathbf{n}_0 + \sin \Theta \sin \Phi \mathbf{s}_0$ $I_{4M}^q = \mathbf{M}_q \cdot (\mathbf{C} \mathbf{M}_q)$ **if** $I_{4M}^q > 1$ **then** $\mathbf{m}_q = \mathbf{F} \mathbf{M}_q$ $\sigma_f = \sigma_f + 2J^{-1} \rho_q a_f (I_{4M}^q - 1) \exp[b_f (I_{4M}^q - 1)^2] (\mathbf{m}_q \otimes \mathbf{m}_q)$ **else** $\sigma_f = \sigma_f + \mathbf{0}$ **end****end**^awww.mathworks.com/matlabcentral/fileexchange/58453-spheretri

5.2.4 Estimation in the eigenvector space: the AI approach

In Eq. (5.5), I_{4M}^q is calculated directly using \mathbf{C} and the representative fibre direction \mathbf{M}_q , an alternative approach to calculate I_{4M} is to project \mathbf{M} into the eigenvector space of \mathbf{C} , and then determine whether the fibre bundle \mathbf{M}_q should be excluded or not. The eigenvector space of the right Cauchy-Green tensor is

$$\mathbf{C} = \mathbf{F}^T \mathbf{F} = \mathbf{U}^2 = \lambda_1 \mathbf{v}_1 \otimes \mathbf{v}_1 + \lambda_2 \mathbf{v}_2 \otimes \mathbf{v}_2 + \lambda_3 \mathbf{v}_3 \otimes \mathbf{v}_3, \quad (5.10)$$

where λ_i is the i^{th} eigenvalue and \mathbf{v}_i is the corresponding i^{th} eigenvector. We choose an order such that $\lambda_1 \geq \lambda_2 \geq \lambda_3$, then use \mathbf{v}_i to form an orthonormal right-hand basis with $\mathbf{v}_3 = \mathbf{v}_1 \times \mathbf{v}_2$.

Then a fibre vector \mathbf{M} can be rewritten with respect to this eigenvector space $(\mathbf{v}_1, \mathbf{v}_2, \mathbf{v}_3)$, that is

$$\mathbf{M}(\theta, \phi) = \cos \theta \mathbf{v}_1 + \sin \theta \cos \phi \mathbf{v}_2 + \sin \theta \sin \phi \mathbf{v}_3, \quad (5.11)$$

where θ, ϕ are polar angles in $\{\mathbf{v}_1, \mathbf{v}_2, \mathbf{v}_3\}$ shown in Fig. 5.2 (a), and the squared fibre stretch is

$$I_{4M}(\theta, \phi) = \mathbf{M}(\theta, \phi) \cdot (\mathbf{C} \mathbf{M}(\theta, \phi)) = \sin^2 \theta (\lambda_2 \cos^2 \phi + \lambda_3 \sin^2 \phi) + \lambda_1 \cos^2 \theta. \quad (5.12)$$

For incompressible myocardium, when $\mathbf{F} \neq \mathbf{I}$, we have

$$\det \mathbf{C} = \lambda_1 \lambda_2 \lambda_3 \equiv 1 \quad \Rightarrow \lambda_1 > 1 > \lambda_3. \quad (5.13)$$

Replacing $a = \lambda_1 - 1$, $b = \lambda_2 - 1$, $c = \lambda_3 - 1$, and $x = \sin^2 \theta$, $y = \sin^2 \phi$ in Eq. (5.12), we have

$$\begin{aligned} I_{4M}(\theta, \phi) - 1 &= \sin^2 \theta [\cos^2 \phi (\lambda_2 - 1) + \sin^2 \phi (\lambda_3 - 1)] + (1 - \sin^2 \theta) (\lambda_1 - 1) \\ &= x[(1 - y)b + cy] + a(1 - x) = (b - a)x + a - (b - c)xy > 0, \end{aligned} \quad (5.14)$$

and it can be further simplified when $b - c \neq 0$, we arrive

$$\begin{cases} \frac{b-a}{b-c} + \frac{a}{b-c} \frac{1}{x} > y, & \text{if } x > 0, \\ a > 0 & \text{if } x = 0. \end{cases} \quad (5.15)$$

Note $0 \leq x = \sin^2 \theta \leq 1$ and $0 \leq y = \sin^2 \phi \leq 1$, $b - a = \lambda_2 - \lambda_1 \leq 0$ and $b - c = \lambda_2 - \lambda_3 \geq 0$.

Thus, from Eq. (5.15), we now consider the following 4 scenarios:

- 1): $x = 0$, $a = (\lambda_1 - 1) > 0$ is always satisfied, see Eq. (5.13)
- 2): $b \geq 0 > c$, that is $\lambda_2 \geq 1 > \lambda_3$, the $x - y$ curve defined in Eq. (5.15) is illustrated in Fig. 5.2 (b). The $x - y$ will stay above the x axis except when $b = 0$ in which the $x - y$ curve crosses the x axis at $(1,0)$, and no crossing point with the y axis. Therefore, the valid domain for stretched fibres Ω^e is the shaded region defined in Fig. 5.2 (b) with two sub-regions (Ω_1^e and Ω_2^e), that is

$$\Omega_1^e = \begin{cases} y \in [\frac{b}{b-c}, 1] \\ x \in [0, f(y)] \end{cases}, \quad \Omega_2^e = \begin{cases} y \in [0, \frac{b}{b-c}] \\ x \in [0, 1] \end{cases}, \quad \text{and} \quad \Omega^e = \Omega_1^e \cup \Omega_2^e, \quad (5.16)$$

where $f(y) = \frac{a}{(b-c)y + a - b}$. The corresponding polar angle domains Ω are

$$\Omega_1 = \begin{cases} \phi \in [\eta, \pi - \eta] \cup [\pi + \eta, 2\pi - \eta], & \text{with } \eta = \arcsin \sqrt{\frac{b}{b-c}} \\ \theta \in \left[0, \arcsin \sqrt{\frac{a}{(b-c)\sin^2 \phi + a - b}}\right] \end{cases},$$

$$\Omega_2 = \begin{cases} \phi \in [0, \eta] \cup [\pi - \eta, \pi + \eta] \cup [2\pi - \eta, 2\pi] \\ \theta \in [0, \frac{\pi}{2}] \end{cases}, \quad \text{and} \quad \Omega = \Omega_1 \cup \Omega_2; \quad (5.17)$$

- 3): $0 > b > c$, the $x - y$ curve crosses the x -axis at $(\frac{a}{a-b}, 0)$ as shown in Fig. 5.2 (c), the

valid domain for stretched fibres is

$$\Omega^e = \begin{cases} y \in [0, 1] \\ x \in [0, f(y)] \end{cases}, \quad (5.18)$$

and the corresponding domain in terms of the polar angles is

$$\Omega = \begin{cases} \phi \in [0, 2\pi] \\ \theta \in \left[0, \arcsin \sqrt{\frac{a}{(b-c)\sin^2\phi + a - b}}\right] \end{cases}; \quad (5.19)$$

- 4): $b = c < 0$, a special case of the scenario 3 by setting $f(y) = \frac{a}{a-c}$, and the domain is

$$\Omega = \begin{cases} \phi \in [0, 2\pi] \\ \theta \in \left[0, \arcsin \sqrt{\frac{a}{a-b}}\right] \end{cases}; \quad (5.20)$$

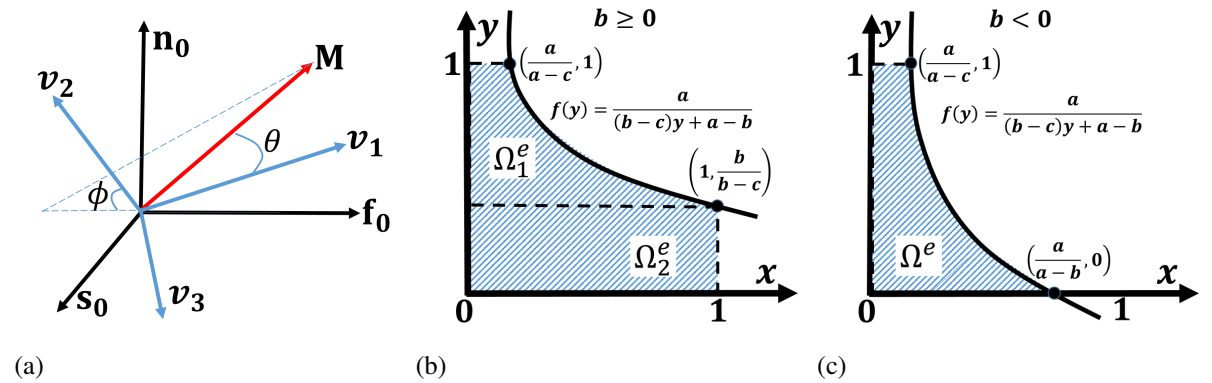


Figure 5.2: (a) Fibre directions (\mathbf{M}) defined using the eigenvectors (\mathbf{v}_1 , \mathbf{v}_2 and \mathbf{v}_3) of the right Cauchy-Green tensor \mathbf{C} with the two fibre angles θ and ϕ . (b) The stretched fibres Ω^e of (x, y) represented by the shaded area for case 2 and (c) case 3.

Alternatively, the fibre SEF per unit volume (\mathcal{W}_f) with only stretched fibres can be re-defined with respect to θ and ϕ , that is

$$\mathcal{W}_f = \int_{\Omega} \rho^*(\theta, \phi) \mathcal{W}_f(I_{4M}(\theta, \phi)) \sin \theta d\theta d\phi, \quad (5.21)$$

where $\rho^*(\theta, \phi) = \rho(\mathcal{M}(\Theta), \mathcal{M}(\Phi))$, and \mathcal{M} is a mapping between (Θ, Φ) and (θ, ϕ) using the following identity,

$$[\mathbf{v}_1 \mathbf{v}_2 \mathbf{v}_3][\cos \theta \sin \theta \cos \phi \sin \theta \sin \phi]^T = [\mathbf{f}_0 \mathbf{n}_0 \mathbf{s}_0][\cos \Theta \sin \Theta \cos \Phi \sin \Theta \sin \Phi]^T. \quad (5.22)$$

Finally, the total passive stress in terms of θ and ϕ is

$$\begin{aligned} \sigma^p = & J^{-1} a \exp[b(I_1 - 3)] \mathbf{B} - p \mathbf{I} \\ & + 2J^{-1} \int_{\Omega} \rho^*(\theta, \phi) a_f (I_{4M} - 1) \exp[b_f (I_{4M} - 1)^2] (\mathbf{m}(\theta, \phi) \otimes \mathbf{m}(\theta, \phi)) \sin \theta d\theta d\phi, \end{aligned} \quad (5.23)$$

where $\mathbf{m}(\theta, \phi) = \mathbf{F}\mathbf{M}(\theta, \phi)$. Algorithm 5.2 illustrates the numerical evaluation of the dual integration in Eq. (5.23), identical to the AI approach.

Algorithm 5.2 Calculation of Cauchy fibre stress in the eigen-space of \mathbf{C} by only counting stretched fibres.

Data:

F: deformation gradient tensor;

Result:

σ_f : Cauchy stress of collagen fibre at each Gaussian quadrature point.

Computation in the eigen-space of right Cauchy-Green tensor

eigen() is the function to compute eigenvectors and eigenvalues of a tensor;

Initialization: $\sigma_f = 0$ $\mathbf{C} = \mathbf{F}^T \mathbf{F}$ $J = \det(\mathbf{F})$;

$(\mathbf{v}_1, \mathbf{v}_2, \mathbf{v}_3, \lambda_1, \lambda_2, \lambda_3) = \text{eigen}(\mathbf{C})$;

Solving Eqs. 5.14~5.19 to find out Ω , denoted as $\theta \in (f_1(\phi), f_2(\phi))$ while $\phi \in (\phi_1, \phi_2)$ with discrete size $\Delta\theta$ and $\Delta\phi$ respectively;

for $\phi = \phi_1$ to ϕ_2 : **do**

for $\theta = f_1(\phi)$ to $f_2(\phi)$: **do**

$(\Theta, \Phi) = (\mathcal{M}(\theta), \mathcal{M}(\phi))$;

$\rho^*(\theta, \phi) = \rho(\Theta, b_1, \Phi, b_2)$;

$\mathbf{M}(\theta, \phi) = \cos \theta \mathbf{v}_1 + \sin \theta \cos \phi \mathbf{v}_2 + \sin \theta \sin \phi \mathbf{v}_3$;

$I_{4M} = \sin^2 \theta (\lambda_2 \cos^2 \phi + \lambda_3 \sin^2 \phi) + \lambda_1 \cos^2 \theta$;

$\mathbf{m} = \mathbf{F}\mathbf{M}$;

$\sigma_f = \sigma_f + 2J^{-1} \rho^*(\theta, \phi) a_f (I_{4M} - 1) \exp[b_f (I_{4M} - 1)^2] (\mathbf{m} \otimes \mathbf{m}) \sin \theta \Delta\theta \Delta\phi$.

end

end

An example of theoretical solution for a uniaxial tension test

Considering a single element, the mean fibre direction is along \mathbf{e}_1 ([1, 0, 0]), the uniaxial stretch is also along \mathbf{e}_1 . We further assume the dispersed fibres is transversely isotropic. Thus under uniaxial stretch λ along \mathbf{e}_1 , the deformation gradient tensor and right Cauchy-Green tensor are

$$\mathbf{F} = \begin{bmatrix} \lambda & 0 & 0 \\ 0 & \frac{1}{\sqrt{\lambda}} & 0 \\ 0 & 0 & \frac{1}{\sqrt{\lambda}} \end{bmatrix} \Rightarrow \mathbf{C} = \mathbf{F}^T \mathbf{F} = \begin{bmatrix} \lambda^2 & 0 & 0 \\ 0 & \frac{1}{\lambda} & 0 \\ 0 & 0 & \frac{1}{\lambda} \end{bmatrix}. \quad (5.24)$$

Therefore, the eigenvalues of \mathbf{C} are $\lambda_1 = \lambda^2$, $\lambda_2 = 1/\lambda$ and $\lambda_3 = \lambda_2$, and the corresponding eigen vectors are \mathbf{e}_1 , \mathbf{e}_2 , and \mathbf{e}_3 . The stretched fibre domain can be determined as the scenario 4 (Eq. (5.20)) in section 5.2.4, that is

$$\Omega = \begin{cases} \phi \in [0, 2\pi] \\ \theta \in \left[0, \arcsin \sqrt{\frac{\lambda^2 + \lambda}{\lambda^2 + \lambda + 1}}\right] \end{cases}. \quad (5.25)$$

The fibre direction within the eigen-vector space of \mathbf{C} can be expressed as

$$\mathbf{M}(\theta, \phi) = [\cos \theta \quad \sin \theta \cos \phi \quad \sin \theta \sin \phi]^T, \quad (5.26)$$

then

$$\mathbf{m} = \mathbf{F}\mathbf{M} = \left[\lambda \cos \theta \quad \frac{1}{\sqrt{\lambda}} \sin \theta \cos \phi \quad \frac{1}{\sqrt{\lambda}} \sin \theta \sin \phi\right]^T, \quad (5.27)$$

and

$$\mathbf{m} \otimes \mathbf{m} = \begin{bmatrix} \lambda^2 \cos^2 \theta & \sqrt{\lambda} \cos \theta \sin \theta \cos \phi & \sqrt{\lambda} \cos \theta \sin \theta \sin \phi \\ \sqrt{\lambda} \cos \theta \sin \theta \cos \phi & \frac{1}{\lambda} \sin^2 \theta \cos^2 \phi & \frac{1}{\lambda} \sin^2 \theta \cos \phi \sin \phi \\ \sqrt{\lambda} \cos \theta \sin \theta \sin \phi & \frac{1}{\lambda} \sin^2 \theta \cos \phi \sin \phi & \frac{1}{\lambda} \sin^2 \theta \sin^2 \phi \end{bmatrix} \quad (5.28)$$

For demonstration purposes, a simple SEF of fibre contribution is assumed as

$$\mathcal{W}_f = a_f (I_{4f} - 1)^2, \quad (5.29)$$

where a_f is material parameter. A simple transverse isotropic fibre distribution is also assumed,

$$\rho(\theta, \phi) = \rho(\theta)\rho(\phi) = (C_1 + C_2\theta)C_0, \quad (5.30)$$

in which C_0, C_1, C_2 are constants. According to Eq. 15 (main text), the squared fibre stretch is

$$I_{4f}(\theta, \phi) = \sin^2 \theta \left(\frac{1}{\lambda} \cos^2 \phi + \frac{1}{\lambda} \sin^2 \phi \right) + \lambda^2 \cos^2 \theta = \frac{1}{\lambda} \sin^2 \theta + \lambda^2 \cos^2 \theta. \quad (5.31)$$

Finally, the total Cauchy fibre stress is

$$\boldsymbol{\sigma}_f = 4a_f \int_{\Omega} (C_1 + C_2\theta)C_0 \left(\frac{1}{\lambda} \sin^2 \theta + \lambda^2 \cos^2 \theta - 1 \right) \mathbf{m} \otimes \mathbf{m} \sin \theta d\theta d\phi, \quad (5.32)$$

and in components

$$\begin{aligned}
\sigma_f^{11} &= \frac{a_f C_0 \pi \lambda}{450} \{240 (3\lambda^3 - 5\lambda + 2) C_1 + 450 (\lambda^3 - 2\lambda + 1) (C_2 \sin(\zeta) - (C_1 + C_2 \zeta) \cos(\zeta)) \\
&\quad + 25 (3\lambda^3 - 4\lambda + 1) (C_2 \sin(3\zeta) - 3(C_1 + C_2 \zeta) \cos(3\zeta)) \\
&\quad + 9 (\lambda^3 - 1) (C_2 \sin(5\zeta) - 5(C_1 + C_2 \zeta) \cos(5\zeta))\}, \\
\sigma_f^{22} &= \frac{a_f C_0 \pi}{900 \lambda^2} \{480 (\lambda^3 - 5\lambda + 4) C_1 + 450 (\lambda^3 - 6\lambda + 5) [C_2 \sin(\zeta) - (C_1 + C_2 \zeta) \cos(\zeta)] \\
&\quad + 25 (\lambda^3 + 4\lambda - 5) [C_2 \sin(3\zeta) - 3(C_1 + C_2 \zeta) \cos(3\zeta)] \\
&\quad + 9 (\lambda^3 - 1) [5(C_1 + C_2 \zeta) \cos(5\zeta) - C_2 \sin(5\zeta)]\}, \\
\sigma_f^{33} &= \frac{a_f C_0 \pi}{900 \lambda^2} \{480 (\lambda^3 - 5\lambda + 4) C_1 + 450 (\lambda^3 - 6\lambda + 5) [C_2 \sin(\zeta) - (C_1 + C_2 \zeta) \cos(\zeta)] \\
&\quad + 25 (\lambda^3 + 4\lambda - 5) [C_2 \sin(3\zeta) - 3(C_1 + C_2 \zeta) \cos(3\zeta)] \\
&\quad + 9 (\lambda^3 - 1) [5(C_1 + C_2 \zeta) \cos(5\zeta) - C_2 \sin(5\zeta)]\}, \\
\sigma_f^{12} &= 0, \quad \sigma_f^{21} = 0, \quad \sigma_f^{13} = 0, \quad \sigma_f^{31} = 0, \quad \sigma_f^{23} = 0, \quad \sigma_f^{32} = 0.
\end{aligned} \tag{5.33}$$

in which $\zeta = \arcsin \sqrt{\frac{\lambda^2 + \lambda}{\lambda^2 + \lambda + 1}}$. Therefore, an analytical expression of fibre Cauchy stress can be obtained for simplified fibre distribution function.

A hybrid algorithm based on algorithms 5.1 and 5.2

As has been reported by Li et al [17] and others, the dual integration in (Eq. (5.23)) can be very computationally demanding. Since the strain invariant I_{4M} will be same either evaluated at the $\mathbf{f}_0 - \mathbf{s}_0 - \mathbf{n}_0$ system or the eigen-space of \mathbf{C} , and the expression of I_{4M} according to (Eq. (5.12)) can be readily obtained, we could replace $I_{4M}^q(\Theta, \Phi)$ in Algorithm 5.1 with $I_{4M}^q(\theta, \phi)$ which is evaluated in the eigen-space of \mathbf{C} , thus an updated approach based on Algorithm 5.1 can be realized (Algorithm 5.3).

In Algorithm 5.3, instead of evaluating $I_{4M}^q(\Theta, \Phi)$ in Algorithm 5.1 in the local material coordinate system $\mathbf{f}_0 - \mathbf{s}_0 - \mathbf{n}_0$, we evaluated $I_{4M}^q(\theta, \phi)$ in the eigen-space of \mathbf{C} (Algorithm 5.2).

5.3 Results

In this section, we first studied the influences on stress distributions resulted from different fibre dispersions in a multi-element myocardial strip (section 5.3.1) under uniaxial stretching, and compared the DFD approach (Algorithm 5.1) with other two algorithms (5.2 & 5.3) in section 5.3.2. We then studied pump function in a dynamic bi-ventricular rabbit heart model (section 5.3.3) using the DFD approach for passive response and the GST approach for active response, finally in a dynamic human LV model (section 5.3.4).

Algorithm 5.3 A hybrid approach by evaluating squared fibre stretch I_{4M} in the eigen-space of \mathbf{C} within Algorithm 5.1.

Data: \mathbf{F} : deformation gradient tensor;**Result:** σ_f : Cauchy stress of collagen fibre.Computation is in the $\mathbf{f}_0 - \mathbf{s}_0 - \mathbf{n}_0$ systemDivide the \mathbb{S} into N spherical trianglesCalculate $\rho_q = \int_{\Delta\mathbb{S}_q} \rho(\Theta, b_1, \Phi, b_2) \sin \Theta d\Theta d\Phi$ with $\sum_{q=1}^N \rho_q = 1$ Initialization: $\sigma_f = \mathbf{0}$ $J = \det(\mathbf{F})$ $\mathbf{C} = \mathbf{F}^T \mathbf{F}$

eigen() is the function to compute eigenvectors and eigenvalues of a tensor;

 $(\mathbf{v}_1, \mathbf{v}_2, \mathbf{v}_3, \lambda_1, \lambda_2, \lambda_3) = \text{eigen}(\mathbf{C})$;**for** $q=1$ to N : **do**| determine Θ_q and Φ_q ;| $(\theta_q, \phi_q) = (\mathcal{M}(\Theta_q), \mathcal{M}(\Phi_q))$;| $\mathbf{M}_q(\theta_q, \phi_q) = \cos \theta_q \mathbf{v}_1 + \sin \theta_q \cos \phi_q \mathbf{v}_2 + \sin \theta_q \sin \phi_q \mathbf{v}_3$;| $I_{4M}^q = \sin^2 \theta_q (\lambda_2^2 \cos^2 \phi_q + \lambda_3^2 \sin^2 \phi_q) + \lambda_1^2 \cos^2 \theta_q$;| **if** $I_{4M}^q > 1$ **then**| | $\mathbf{m}_q = \mathbf{F} \mathbf{M}_q$;| | $\sigma_f = \sigma_f + 2J^{-1} \rho_q a_f (I_{4M}^q - 1) \exp[b_f (I_{4M}^q - 1)^2] (\mathbf{m}_q \otimes \mathbf{m}_q)$;| **else**| | $\sigma_f = \sigma_f + \mathbf{0}$;| **end****end**

5.3.1 Uniaxial test on multi-element strip

Fig. 5.3 (a) schematically illustrates different combinations of b_1 and b_2 as in [210]. Different values of N (40, 80, 160, 640) are chosen for integrating Eq. (5.4), the relative differences of the numerical integrations compared to the analytical value (1.0) is shown in Fig. 5.5 (a). The differences with $N = 640$ is almost negligible for all chosen b_1 and b_2 . While for $N = 160$, high accuracy of $\sum_{q=1}^N \rho_q$ can be achieved even for the combination of $b_1 = 8$ and $b_2 = 8$ in which fibres are highly aligned both in-plane and out-of-plane. When $N = 40$, $\sum_{q=1}^N \rho_q$ is less accurate whenever fibres are highly aligned either in-plane or out-of-plane, while good accuracy can be achieved when $b_1 \leq 2$ and $b_2 \leq 2$. Therefore, in the following studies, unless explicitly stated, $N = 160$ is used when either $b_1 = 8$ or $b_2 = 8$, otherwise $N = 40$ is chosen for the sake of computational efficiency.

Fig. 5.3 (b) is the uniaxial test sample with a dimension of $15 \times 5 \times 3 \text{ mm}^3$ as used in ex vivo experiments [4]. The fibres lie in the $\mathbf{e}_1 - \mathbf{e}_2$ plane and linearly rotate from -60° to 60° with respect to \mathbf{e}_1 . The strip was virtually stretched along \mathbf{e}_1 by 1.2 by fixing one end. Two sets

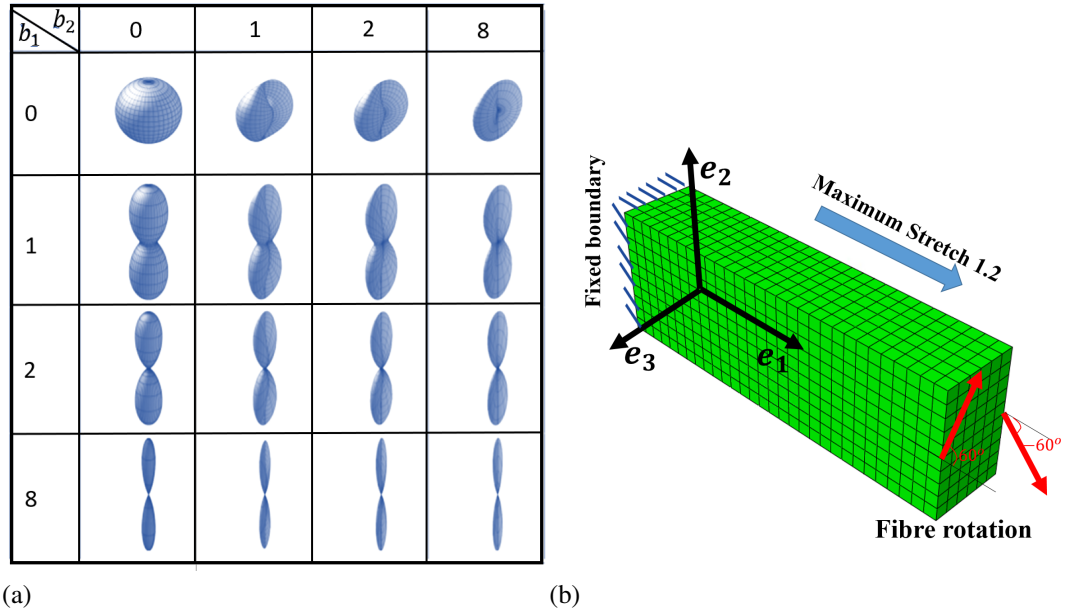


Figure 5.3: Surface plots of $\rho(\Theta, b_1, \Phi, b_2)\mathbf{M}(\Theta, \Phi)$ for different combinations of b_1 and $b_2 \in \{0, 1, 2, 4, 6, 8\}$ (a), and (b) a uniaxially stretched strip with linearly rotated fibres represented by red arrows.

of passive parameters were used in this chapter, namely the rabbit and the human myocardium. Parameter values for the rabbit myocardium were determined by fitting Eq. (5.1) to the equal-biaxial experiments from [1] using the same optimization procedure in [181].

Equibiaxial stress-strain measured data from Lin and Yin [1] was chosen as shown in Figure 5.4, the sample size is $20 \times 20 \times 2 \text{ mm}^3$ with 36° fibre rotation according to [1]. Passive material parameters were estimated by formulating a non-linear least square minimization problem, and the Matlab function *fmincon* (MatLab, MathWorks 2017) was used to minimize the loss function

$$L(\beta) = \sum_{n=1}^N [\sigma_n^{\text{simulation}}(\beta) - \sigma_n^{\text{experiment}}]^2, \quad (5.34)$$

where β denotes the set of unknown parameters, N is the total number of data points. The fitting procedure is similar as in [181]. The fitting result is shown in Fig. 5.4.

Parameter values for the human myocardium were adopted from [2] inferred by matching the measured in vivo heart dynamics. All parameter values are listed in Table 5.1. Note that fibre dispersion was not taken into account when estimating passive parameters for both the rabbit and human myocardium because of lack of experimental data.

Fig. 5.5 (b) shows σ_{11} using $N = 640$ under uniaxial stretching with four different fibre dispersions, they are

- case 1: $b_1 = b_2 = 0$, the isotropic fibre distribution;
- case 2: $b_1 = 0, b_2 = 2$, the in-plane isotropic fibre distribution;

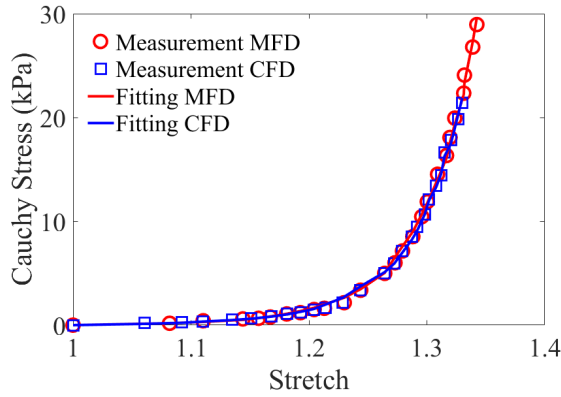


Figure 5.4: Inference of rabbit myocardial passive property from the equibiaxial experimental data of Lin and Yin [1]. Red circles and blue squares are measured data along the mean fibre direction and the cross-fibre direction, respectively, and the solid lines are the final fitted result.

Parameters	a (kPa)	b	a_f (kPa)	b_f	T_a (kPa)
Rabbit	0.2678	4.5505	0.0977	5.0855	80
Human	0.224	1.6215	2.4	1.8268	145

Table 5.1: Parameters of rabbit myocardium by fitting to the experimental data in [1] and parameters for human LV model adopted from [2]. Contractility T_a was manually determined by achieving a physiological EF within 50% ~ 75%.

- case 3: $b_1 = 2, b_2 = 0$, the transversely isotropic fibre distribution, in other words, the rotationally symmetric distribution [20];
- case 4: $b_1 = b_2 = 2$, the general fibre distribution with both in-plane and out-of-plane dispersion;

Significant differences can be found when using the human passive material parameters, with the highest stress in the transversely isotropic fibre distribution, and the lowest in the planar-isotropic distribution. Similar trend can be found for the rabbit myocardium, but with much less differences, which could be explained by much smaller a_f for the rabbit myocardium (rabbit: 0.097 kPa vs human: 2.4 kPa). Figs. 5.5 (c-d) are the contours of σ_{11} at the maximum stretch with different b_1 and b_2 for the rabbit and human myocardium, respectively. With more aligned in-plane fibres ($b_1 \rightarrow 8$), σ_{11} becomes much higher suggesting stiffening along \mathbf{e}_1 , the mean fibre direction. For example, σ_{11} is increased by 10.6% from 3.85 Pa ($b_1 = b_2 = 0$) to 4.26 Pa ($b_1 = 2, b_2 = 0$), followed by a 7.5% increment from $b_1 = 2, b_2 = 0$ to $b_1 = 8, b_2 = 0$. Similar trends can be found for the human myocardium, a 62.9% increase from $b_1 = 0, b_2 = 0$ to $b_1 = 2, b_2 = 0$, and a further 21.5% increase from $b_1 = 2, b_2 = 0$ to $b_1 = 8, b_2 = 0$. On the contrary, when $b_1 = 0$, increasing b_2 seems having little effect on σ_{11} as shown in Figs. 5.5 (c-d). Thus, a transversely isotropic fibre distribution will reinforce the material stiffness along the mean fibre direction overall, but not a planar-isotropic distribution.

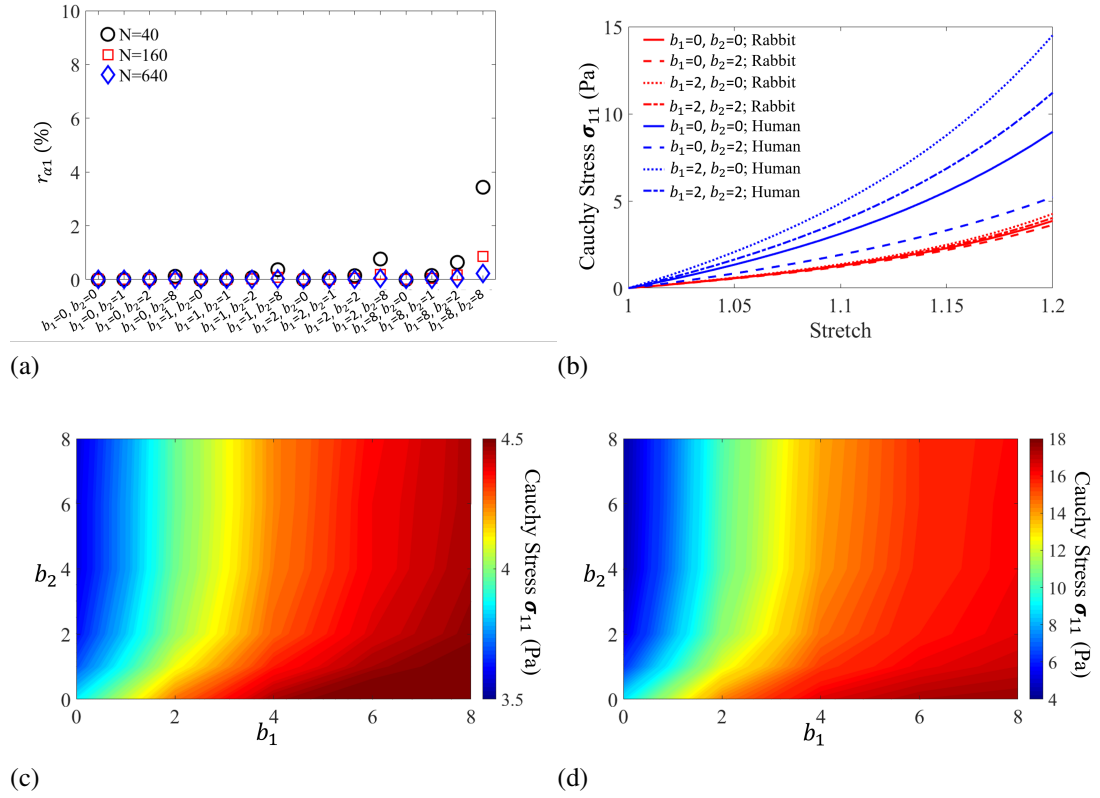


Figure 5.5: Relative errors of evaluating Eq. (5.4) using $N = 40$, $N = 160$ and $N = 640$ with different b_1 and b_2 combinations (a), the relative error is calculated in relation to the analytical value (1.0). (b) Stress-stretch responses of the uniaxial tension in four dispersion cases by using human (blue lines) and rabbit (red lines) material parameters, respectively. (c) Contours of stresses at the maximum stretch when using rabbit material parameters and (d) the human material parameters.

A compression experiment using human material parameters was further carried out with the same strip up to 20% shortening along the mean fibre direction. Two dispersions were considered here, one with $b_1 = b_2 = 1$ and the other one with $b_1 = b_2 = 2$. Fig. 5.6 shows the resultant σ_{11} . It can be found that the more dispersed fibre distribution leads to higher resultant stress in magnitude compared to the case with less dispersion. This can be explained by the more stretched dispersed fibres along the cross-fibre directions in the case with $b_1 = b_2 = 1$ compared to the case with $b_1 = b_2 = 2$, although the mean fibre direction is under compression. Therefore, dispersed fibres could lead to increased stiffness in compression.

5.3.2 Comparison between Algorithms

We first compared the computational efficiency between the DFD method (Algorithm 5.1) and the AI method with the dual integration in the eigenvector system (Algorithm 5.2), and the hybrid DFD method (Algorithm 5.3) in a single hexahedron element as shown in Fig. 5.7 (a). The mean fibre direction is along the \mathbf{e}_1 axis with a general fibre dispersion ($b_1 = b_2 = 2$).

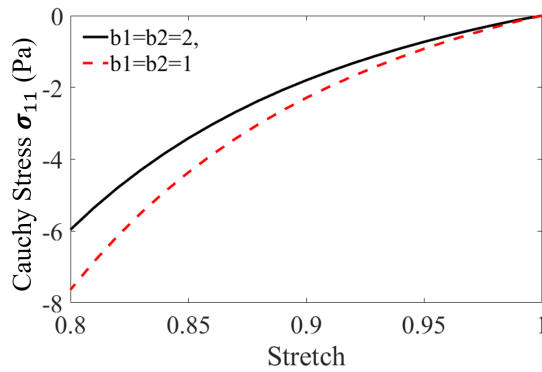


Figure 5.6: Compression tests with $b_1 = b_2 = 1$ and $b_1 = b_2 = 2$, respectively. A maximum of 20% compression is applied along the mean fibre direction, the negative values mean the resultant compressive stress.

Under a maximum stretch of 1.3, all algorithms converge to one identical stretch-stress response, shown in Fig. 5.7 (b). Algorithm 5.1 with $N = 160$ took 21.1 seconds, followed by Algorithm 5.3 ($N = 160$, 22.3 seconds), however, Algorithm 5.2 took about 75.7 seconds with $\Delta\theta = \Delta\phi = 0.0982$ in order to achieve the same accuracy as Algorithms 5.1 and 5.2. The much longer computational time used by Algorithm 5.2 agrees with the findings by Li et al [17]. All computation were performed using ABAQUS Explicit (Dassault Systemes, Johnston RI, USA) with user-coded subroutine for calculating myocardial stress in a Windows workstation (CPU E5-2680 v3@2.50 GHz and 64.0 GB memory), and only one CPU was used. Therefore, Algorithm 5.1 has been used in the following studies because of its high computational efficiency.

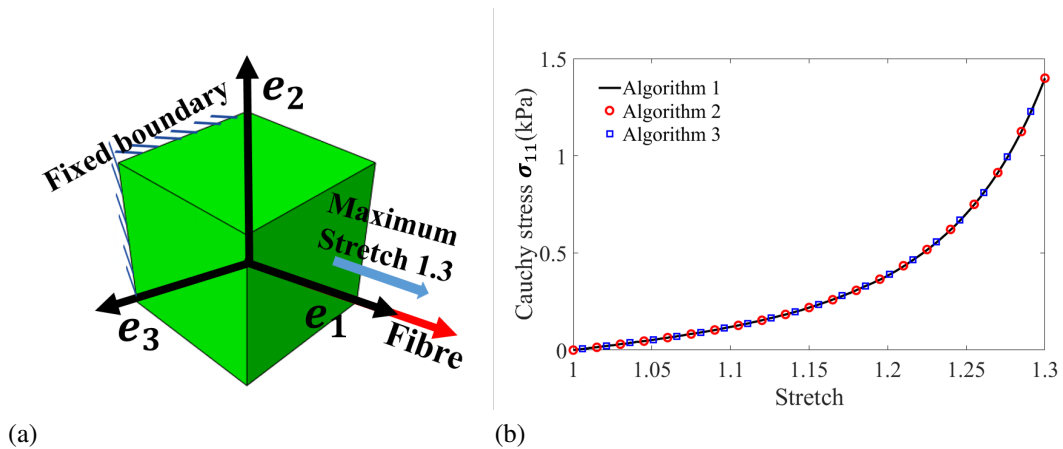


Figure 5.7: A single element model with non-rotationally symmetric fibre distribution under uniaxial stretching (a), and (b) stretch-stress responses using Algorithm 5.1 (the black line), Algorithm 5.2 (the red cycles) and Algorithm 5.3 (the blue squares).

5.3.3 The dynamic rabbit bi-ventricle model

A 3D bi-ventricle rabbit heart model was constructed from an ex-vivo dataset of a healthy rabbit heart, which was acquired using a 7 Tesla Bruker Pharmascan magnetic resonance imaging system. The acquired volumetric image had a size of $160 \times 110 \times 110$ with voxel dimensions of $0.282 \times 0.282 \times 0.282 \text{ mm}^3$. Fig. 5.8 (a) shows one processed DT-MRI image. Details of DT-MRI acquisition protocols can be found in the supplementary material. The bi-ventricular wall was first segmented from the ex-vivo DT-MRI data using ITK-SNAP¹ (Fig. 5.8 (a)), then the boundary contours were exported into SolidWorks (Dassault Systemes, MA USA) for geometry reconstruction, and finally meshed by ICEM (ANSYS, Inc. PA USA). To take into account varied fibre distribution at different regions, the rabbit geometry was further divided into four regions: the left ventricular free-wall (LVFW), the right ventricular free-wall (RVFW), the septum and the apex, as shown in Fig. 5.8 (b). The layered fibre architecture (Fig. 5.8 (c)) was generated using a RBM [15, 46], and the fibre rotation angles varied linearly from the epicardium to endocardium according to the measurements from rabbit hearts in [3], and further summarized in Table 5.2.

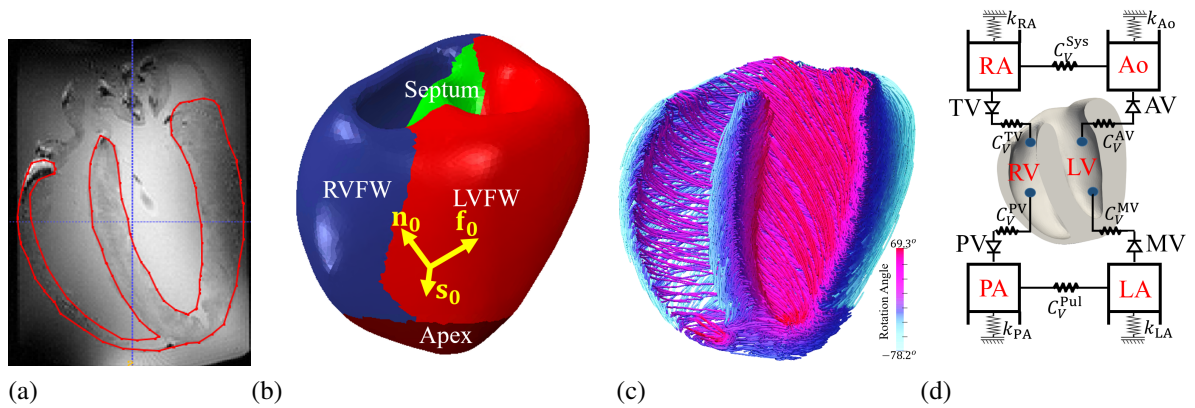


Figure 5.8: The reconstructed bi-ventricle rabbit heart geometry from a DT-MRI data (296785 linear tetrahedral elements and 55957 nodes). (a) An example DT-MRI rabbit heart with delineated ventricular wall enclosed by the red lines; (b) Four regions are defined for the rabbit heart with different colors, \mathbf{f}_0 , \mathbf{s}_0 , \mathbf{n}_0 are the fibre–sheet–normal system, in which \mathbf{f}_0 is the mean fibre direction, \mathbf{s}_0 is the sheet direction, in general along the transmural direction from endocardium to epicardium, and \mathbf{n}_0 is the sheet-normal direction; (c) Rule-based fibre architecture with fibre rotation angles defined in Table 5.2; (d) A schematic illustration of the bi-ventricular rabbit model coupled with a circulatory system. MV: mitral valve, AV: aortic valve, RA: right atrium, TV: tricuspid valve, PV: pulmonary valve, LA: left atrium, RA: right atrium, Ao: aorta, Sys: systemic circulation, Pul: pulmonary circulation and PA: pulmonary artery. Grounded spring with a stiffness of k is tuned to provide the appropriate PV response (i.e., compliance) for the corresponding cavity. C_V is the viscous resistance coefficient for describing resistance between cavities. Flow through valves is realized by only allowing uni-directional fluid exchanging between two cavities.

¹<http://www.itksnap.org>

Regions	LVFW	RVFW	Septum	Apex
Epicardium	-71.0	-78.2	-45.1	-29.6
Endocardium	59.6	28.0	51.5	69.3

Table 5.2: Fibre rotation angles at different regions of the rabbit heart adopt from [3].

The dynamic bi-ventricular rabbit model was implemented in ABAQUS Explicit. In order to simulate diastolic filling and systolic ejection, a lumped model of the pulmonary and systemic circulation systems was attached to this bi-ventricle, which was realized through a combination of surface-based fluid cavities and fluid exchanges [188] as shown in Fig. 5.8 (d). After preloading both ventricles with the prescribed EDPs (LV: 8 mmHg and RV: 3 mmHg) within 0.1 s, the iso-volumetric contraction starts and the ventricular pressures increase sharply, followed by the systolic ejection at around $t = 0.15$ s after the valves open when the LV and RV pressures exceed the pressure in the aorta (90 mmHg) and the pulmonary artery (10 mmHg), respectively. The systolic ejection ends at around $t = 0.3$ s. We further assumed myocardium contracts simultaneously across the whole wall immediately after end-diastole.

Lumped circulation models were attached to the rabbit heart model and the human LV model, which were realized through a combination of surface-based cavities in ABAQUS as introduced in section 4.2.3 of Chapter 4. Parameters for the lumped circulation model of rabbit and human heart are listed in Table 5.3. Note, values of this rabbit model are much higher than that of the human model because of human valves areas are much bigger than rabbit. For example, the aortic valve area for human is around 3.7 cm^2 [211], much larger than the rabbit aortic area, which is 0.23 cm^2 [212]. These settings ensure that both the human LV model and the rabbit biventricle model can achieve physiological values of EF, SV and ESP, which are comparable to the reported values of human heart [213] and rabbit heart [214], respectively.

Rabbit heart model			Human heart model		
Name	Value	Unit	Name	Value	Unit
C_V^{AV}	30.0	$\text{MPa} \cdot \text{mm}^2 \cdot \text{s}/\text{tonne}$	C_V^{AV}	1.2	$\text{MPa} \cdot \text{mm}^2 \cdot \text{s}/\text{tonne}$
C_V^{MV}	20.0	--	C_V^{MV}	1.2	--
C_V^{PV}	30.0	--	C_V^{PV}	--	--
C_V^{TV}	10.0	--	C_V^{TV}	--	--
C_V^{Sys}	4500.0	--	C_V^{Sys}	92.0	--
C_V^{Pul}	500.0	--	C_V^{Pul}	--	--
k_{Ao}	2.0	N/mm	k_{Ao}	1.0	N/mm
k_{PA}	0.8	--	k_{PA}	--	--
k_{LA}	0.01	--	k_{LA}	0.1	--
k_{RA}	0.01	--	k_{RA}	--	--

Table 5.3: Parameter values for the lumped circulatory model as shown in Fig. 5.8 (d) and Fig. 5.12 (c). C_V is the viscous resistance coefficient, and k is the stiffness of the grounded spring.

Cardiac dynamics were simulated with the four representative cases as mentioned in section 5.3.1, and an additional case with perfectly aligned fibres (case 5, without dispersion). Fig. 5.9 depicts the end-diastolic and end-systolic fibre stress distributions for the five representative cases. Both the end-diastolic stress distributions and the deformed shapes are very similar for all cases, but large differences can be found at end-systole. For example, nearly no contraction for case 1 with isotropic fibre distribution ($b_1 = b_2 = 0$). Excessive longitudinal shortening ($\approx -20\%$) and wall thickening ($\approx 120\%$) in case 2 with $b_1 = 0, b_2 = 2$, which has in-plane isotropic fibre distribution. The heart contracts less in case 3 with $b_1 = 2, b_2 = 0$ compared to the general fibre structure in case 4 with $b_1 = 2, b_2 = 2$, which behaves similarly to case 5 (no dispersion) at end-diastole and end-systole.

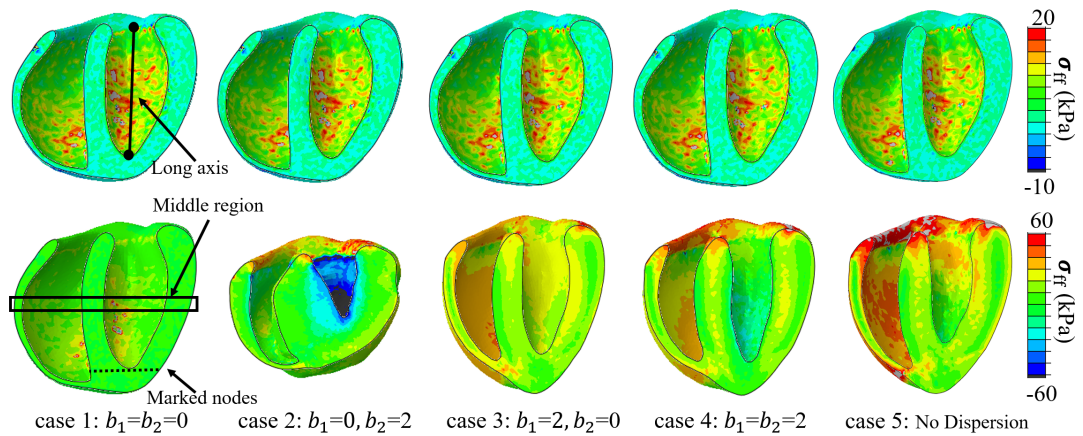


Figure 5.9: Myofibre stress (σ_{ff}) distributions with deformed shapes at end of diastole (top) and end of systole (bottom) in the rabbit bi-ventricle model for case 1 ($b_1 = b_2 = 0$), case 2 ($b_1 = 0, b_2 = 2$), case 3 ($b_1 = 2, b_2 = 0$), case 4 ($b_1 = b_2 = 2$), and case 5 without fibre dispersion.

Fig. 5.10 (a) illustrates the PV loops for all cases, again, different combinations of in-plane and out-of-plane dispersions can significantly affect the pump function of both the LV and RV. Because of no contraction in case 1, its pressure loop degenerates to a point as indicated in Fig. 5.10 (a). Case 2 has the highest cardiac work, that is the area enclosed by the PV loop, in particular in the RV. Cases 4 and 5 have similar cardiac outputs with better performance than case 3. Figs. 5.10 (b, c, d) show the long-axis shortening, average myofibre stress at mid-ventricle (σ_{ff}) and the apical twist for the five cases during systole. For case 1, due to the isotropic fibre distribution, there is little contraction in systole with the smallest long-axis shortening and the apex twist, and nearly zero myofibre stress due to the counteraction of symmetrical fibre distributions. While case 2 is on the other extreme, with the highest long-axis shortening ($\approx -20\%$), the lowest myofibre stress due to the isotropic in-plane distribution, and the highest apex twist. For cases 3, 4 and 5, the long-axis shortening, the myofibre stress and the apex twist follow similar trends as shown in Figs. 5.10 (b, c, d). Considering the largest long-axis shortening and the apex twist, and excessive wall thickening in case 2 compared to experimentally reported

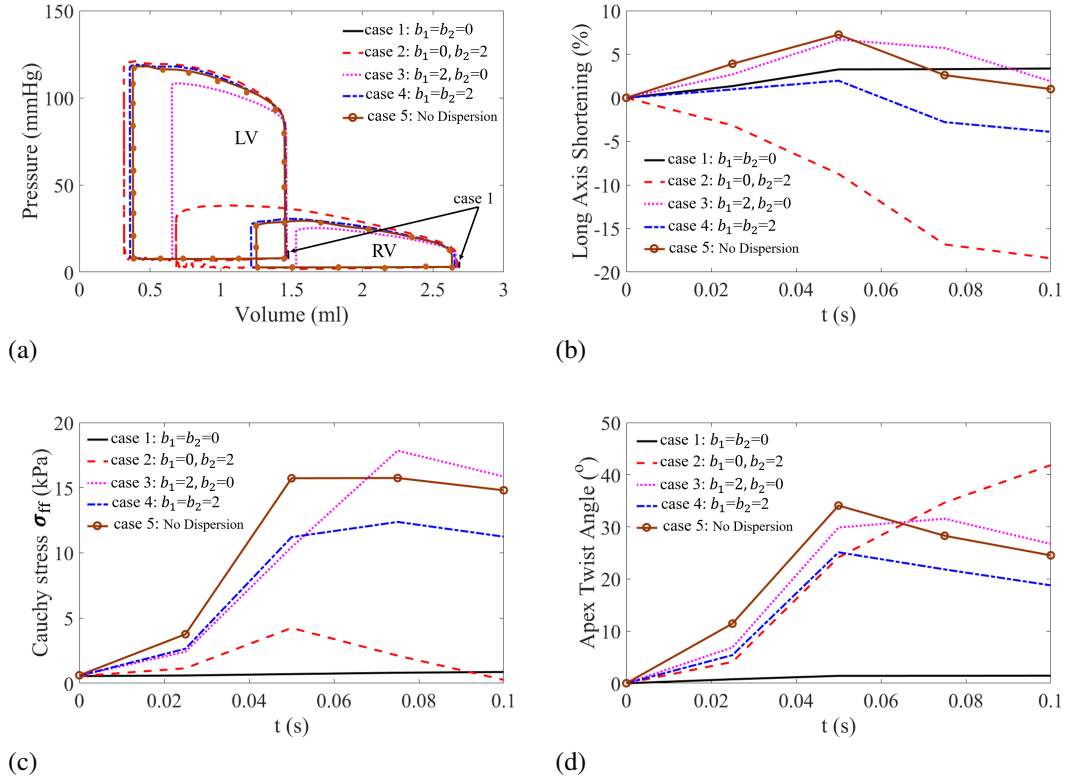


Figure 5.10: Systolic function for the five cases with different dispersed fibres in the rabbit heart model. (a) PV loops; (b) long-axis shortening, and the long axis is defined as the line segment between the LV basal centre and the apex (the black line in Fig. 5.9); (c) average myofibre stress σ_{ff} in the middle ventricle enclosed by the black rectangle in Fig. 5.9, and (d) the apex twist angles.

values (around 46% in [215], 40% in [108]), it may suggest that the dynamics of case 2 can be unphysiological, especially in systole.

Figs. 5.11 (a) and (b) show the differences of EDV of the LV and RV for different combinations of b_1 and b_2 by comparing with case 5 without fibre dispersion. It can be found that the differences in LV EDV and RV EDV are not significant compared to case 5, with a maximum difference of 2% and concentrated close to the isotropic distribution ($b_1 \rightarrow 0$ and $b_2 \rightarrow 0$). However, significant differences exist for ESV of LV and RV as shown in Figs. 5.11 (c) and (d), in particular when $b_1 \rightarrow 0$ and $b_2 \rightarrow 0$. The solid and dashed lines in Figs. 5.11 (c) and (d) indicate the differences within the 5% range compared to case 5. The b_1 - b_2 space within 5% range is much narrower in the LV than RV, indicating that including fibre dispersion in the LV is necessary for this rabbit model. Our results further suggest that fibre dispersion can significantly affect both the LV and RV systolic function for this rabbit heart model, but less in the diastolic filling. With high in-plane dispersion (small b_1) and less out-of-plane dispersions ($b_2 \rightarrow 8$), both the LV and RV can contract more, while with high in-plane and out-of-plane dispersions, both the LV and RV pump functions are reduced significantly especially when $b_1 = b_2 = 0$, despite

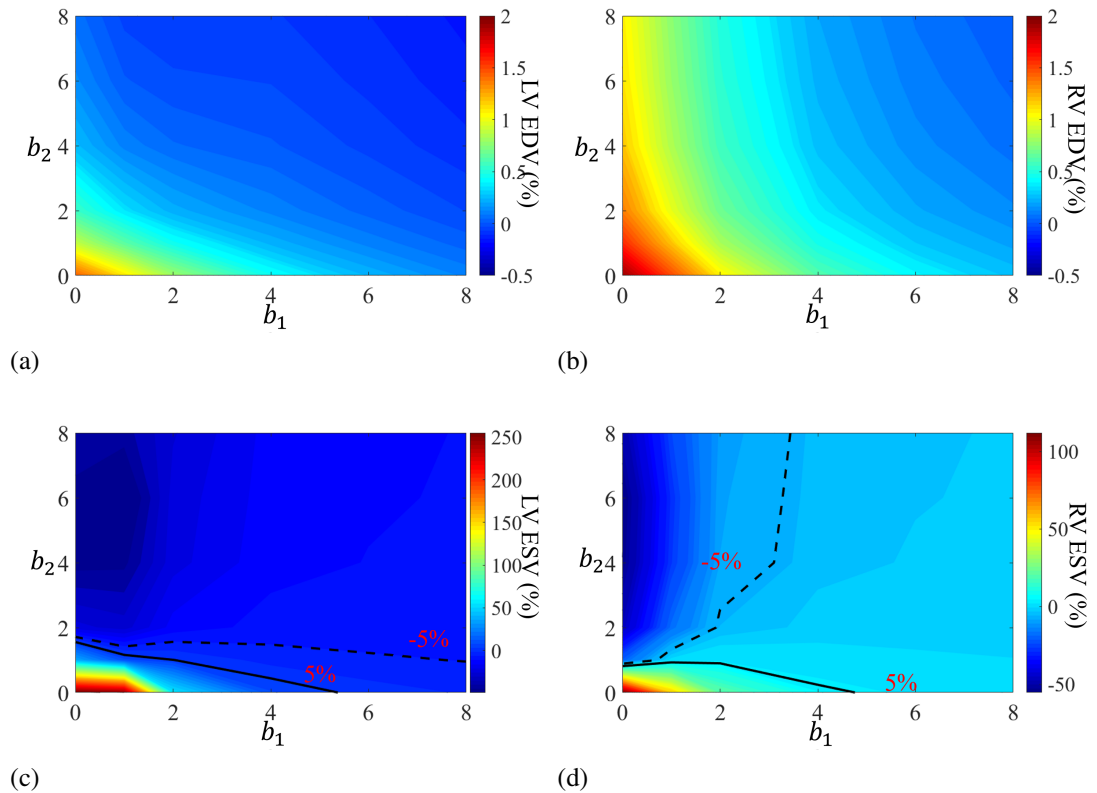


Figure 5.11: Relative differences of ESV and EDV values with different dispersion parameters compared to case 5. (a) EDV differences of the rabbit LV and (b) RV, (c) ESV differences of the rabbit LV and (d) RV, respectively.

slightly larger EDVs for both the LV and RV chambers.

5.3.4 The human LV model

A human LV model from our previous work is used here [2] to study how different fibre dispersions can affect the pump function in the human LV. Fig. 5.12 (a) shows the LV model with a rule-based fibre structure as illustrated in (b) with linearly varied fibre rotation angle from the epicardium (-60°) to the endocardium (60°). A similar simplified circulation system was attached to the LV model as in the rabbit model, whereas only the aorta and the left atrium (Fig. 5.12 (c)) were included. To simulate LV dynamics, we first preload the LV to 8 mmHg within 0.3 s, then the iso-volumetric contraction begins, followed by the systolic ejection around at $t = 0.4$ s when the LV pressure exceeds the aortic pressure (75 mmHg), and finally the ejection ends when the LV pressure is lower than the aortic pressure. We also assumed simultaneous contraction in this LV model. The same five cases with varied fibre dispersions are analysed in this section.

The end-diastolic and end-systolic fibre stress distributions for the five cases are shown in Fig. 5.13. Myofibre stresses at end-diastole are similar across the five cases with slight difference

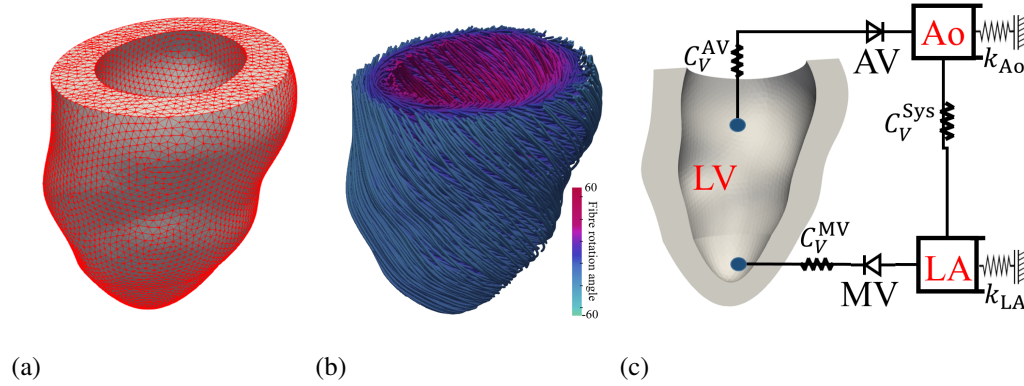


Figure 5.12: A human LV model with 133,042 linear tetrahedral elements and 26,010 nodes (a) and its fibre architecture (b) generated by the rule-based method with fibre rotation angles from -60° at epicardium to 60° at endocardium. (c) A schematic illustration of the human LV model with a circulation system, and the definitions of various symbols are same as those in Fig. 5.8 (d).

in the deformed shapes. The end-systolic shapes are largely different among the five cases. Similar as in the rabbit model, no contraction happens in case 1, and excessive contraction experienced by case 2. Although cases 3, 4 and 5 have similar end-systolic shapes, the stress distribution is different in case 3 with stress concentration near the base, which may be caused by the less long-axis shortening compared to cases 4 and 5.

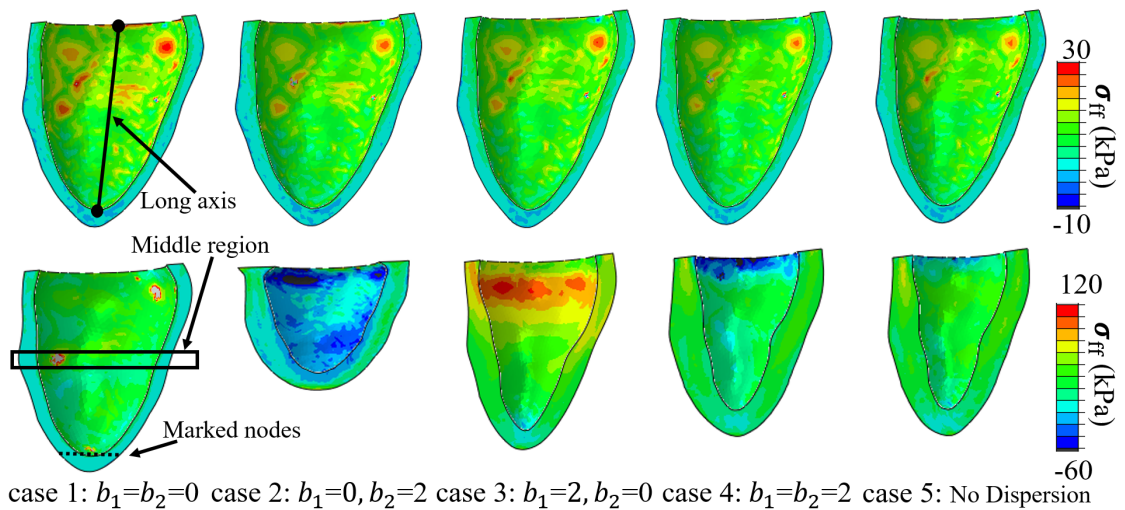


Figure 5.13: Myofibre stress distributions (σ_{ff}) at the end of diastole (top) and at the end of systole (bottom) for the human LV model with different combinations of b_1 and b_2 .

Fig. 5.14 (a) further summarizes the PV loops for the five cases. For the cases either with $b_1 = 0$ or $b_2 = 0$, a larger EDV can be achieved, suggesting an increased compliance in diastole because of dispersed fibres. But those dispersed fibres seem compromising active contraction because of the counteracting effects as in case 1 in which all fibres are equally distributed over

the unit hemisphere, resulting no contraction at all under incompressible assumption (Fig. 5.14 (a)). Interestingly, the cardiac output from case 4 with a general fibre dispersion is slightly larger than the non-dispersed case 5, that may be because of the larger EDV in case 4, which leads to higher active contraction according to the ‘Frank-Starling’ law. Figs. 5.14 (b, c, d) show the long-axial shortening, the fibre stress and the apex twist in systole, respectively. Again, an excessive long-axis shortening can be found for $b_1 = 0$ and $b_2 = 2$ with a peak value of -36.8% (case 2), nearly no shortening in case 1, and the long-axis shortening in case 4 is around 20%, higher than cases 3 and 5. The myofibre stress at mid-ventricle is extremely low in case 1 due to the counteraction of dispersed myofibres, and followed by case 2 with in-plane isotropic fibres. Similar trends can be found in cases 3, 4 and 5 but with different levels. Note because of dispersed myofibres, there are cross-active tension along the sheet and sheet-normal direction, which also affect myocardial contraction. For example, even though the myofibre stresses in cases 2 and 3 are low, because of the in-plane myofibre distribution, large contractile stress can be found along the sheet-normal direction, which will further contribute to contraction as suggested in [15]. The maximum apex twist angles are similar for cases 2, 3 and 5 (around 25°), 15° for case 4, and lowest in case 1 as expected. Thus for this human LV model, a fully dispersed myofibre structure (case 1) is non-physiological because of nearly no contraction, while an in-plane isotropic fibre structure (case 2) can lead to non-physiological dynamics in systole because of the excessive long-axis shortening.

Fig. 5.15 is the contour plot of the relative EDV and ESV differences with varied b_1 and b_2 compared to the case with non-dispersion fibres (case 5), the superimposed lines indicate the parameter space with differences in the range of $\pm 5\%$. The parameter space with $> 5\%$ difference for EDV mainly locates near the b_1 axis and b_2 axis, with a maximum difference of 18% when $b_1 = 0$ and $b_2 = 0$. The differences in ESV are much more significant as shown in Fig. 5.15 (b). Still, the regions near the b_1 and b_2 axis have reduced myocardial contraction with much larger ESV compared to case 5. In Fig. 5.15 (b), we can also find a region enclosed by the dashed line which has much less ESV compared to case 5, this can be explained by the large in-plane dispersion which can enhance pump function as found in our previous study [15]. Thus for this human LV model, when $(b_1, b_2 \in [0, 2])$, there is a need to incorporate fibre dispersion, beyond that, the differences of LV EDV and ESV are in general within 5% range compared to the case without considering fibre dispersion. In fact, the same parameter space of $b_1, b_2 \in [0, 2]$ can be found for the rabbit model, where the large difference (i.e. $> 5\%$) exists as shown in Fig. 5.11. The measured fibre dispersion in human myocardial samples from [4] is represented by the white dot in Fig. 5.15, which lies in the $< 5\%$ region of the EDV and ESV differences compared to case 5.

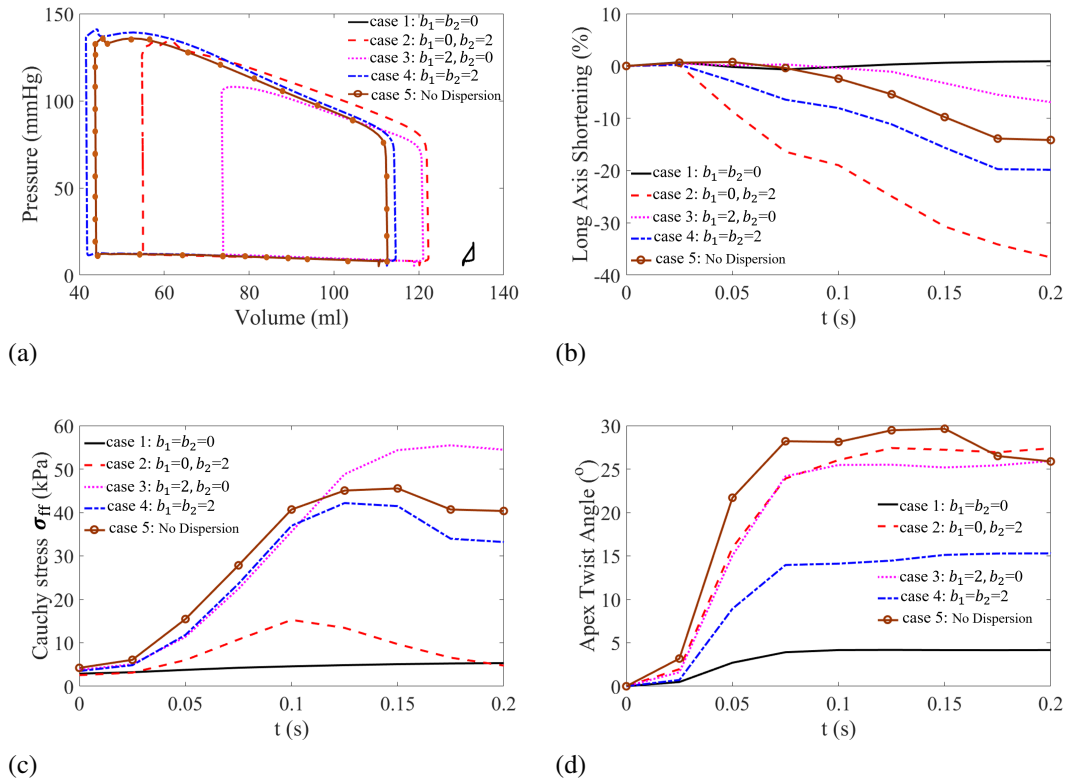


Figure 5.14: Systolic function for the five cases in the human LV model. (a) PV loops; (b) long-axis shortening, the long-axis is defined as the link between the LV basal centre and the apex (the black line in Fig. 5.13); (c) average myofibre stress σ_{ff} in the middle ventricle indicated by the black rectangle in Fig. 5.13, and (d) the apex twist angles.

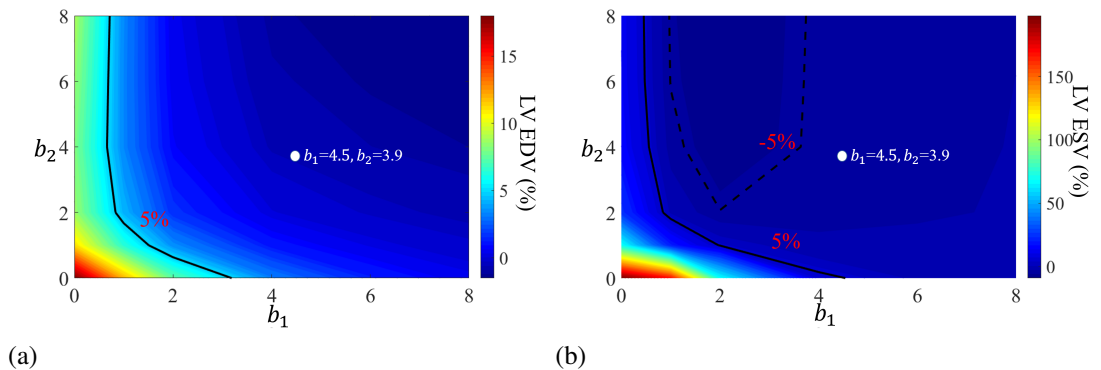


Figure 5.15: Relative differences of EDV (a) and ESV (b) with different dispersion parameters compared to case 5 for the human LV model. The contour lines indicate $\pm 5\%$ difference, and the white dot is the measured dispersion ($b_1 = 4.5, b_2 = 3.9$) from Sommer et al [4].

5.4 Discussion

In this chapter, we have focused on how different fibre dispersions will affect myocardial mechanics both passively and actively. Fibre dispersion is described by a non-rotationally sym-

metric distribution based on recent experimental studies [4, 5]. In order to exclude compressed fibres for passive response, we adopted the DFD model developed in [17], and then the general structural tensor [20] was employed for describing dispersed active tension as in our previous study [15]. We first studied the numerical accuracy of the integration of fibre contributions using the DFD approach, then studied the different mechanical response in a uniaxially stretched myocardial sample with varied fibre dispersions. Two heart models were further employed in this chapter, the rabbit bi-ventricle model and the human LV model. Cardiac dynamics from diastole to systole were simulated with different fibre dispersions. Our results show that fibre dispersion can have significant effects on myocardial mechanics and the pump function, which highlights the necessity of using appropriate dispersion models when modelling myocardial mechanics, especially when fibres are largely dispersed.

The SEF for myocardium (Eq. (5.1)) only includes two strain invariants I_1 and I_4 . We further fitted this SEF to the biaxial stretching experimental data of human tissues reported by Sommer et al [4], as shown in Fig. 5.16. The experimental is re-digitized from the Figure 9(b) in Sommer et al's study. It can be found that Eq.(1) agrees well with experimental data both along the fibre direction and the cross-fibre direction. Good agreements were achieved along the fibre direction and the cross-fibre direction. Myocardium was further assumed to be incompressible, a widely adopted assumption in literature [2, 11, 90–92]. In our human LV model, $J = 1 \pm 0.008$ at end-diastole and $J = 1 \pm 0.009$ at end-systole, which suggests myocardial incompressibility was achieved in our simulations, and the very small standard deviation is due to the numerical realization of the incompressible penalty. Interested readers can refer to [216] for a recent contemporary review of constitutive modelling of myocardium.

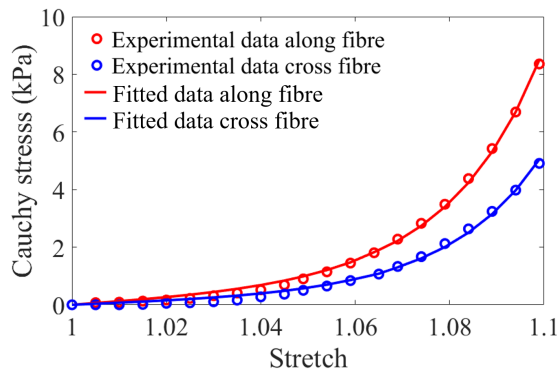


Figure 5.16: Fitting results to an equal-biaxial tension test in Sommer et al. [4] using Eq.(1).

To model fibre dispersion, the AI approach and the GST approach have been widely used in various soft tissue mechanics, such as arterial wall, myocardium, tendon, valvular tissue, and skin, etc. One striking feature of collagen fibres is that they can not bear the loading when compressed, thus it is necessary to exclude compressed fibres. In this chapter, we have adopted the DFD approach developed in [17], which is a numerical approximation of the AI approach. By discretizing an unit hemisphere into N spherical triangles, the DFD approach can then integrate

stress contributions from stretched fibre bundles in a much faster way as demonstrated by Li et al [17], and also in this chapter. The advantage of the DFD approach is that by replacing the double integration in the AI approach with finite representative fibre bundles, it preserves the straightforward compressed fibre exclusion from the AI approach.

In our previous study [15], we have determined the dispersed active tension from a DT-MRI acquired fibre structure using the GST approach along with a rule-based fibre structure. We found that this GST-based dispersed active stress model can well approximate the systolic function in a bi-ventricle model compared to the DT-MRI derived fibre structure, the most realistic fibre structure. Since there is no need to exclude any myofibre during active contraction, the GST approach is naturally convenient to take into account dispersed active tension for the sake of computational efficiency. In this chapter, we further tested the DFD approach for the active stress with one hexahedra element, and the total active tension is $\sigma^a = T_a \sum_{q=1}^N \rho_q \hat{\mathbf{m}}_q \otimes \hat{\mathbf{m}}_q$ where $\hat{\mathbf{m}}_q = \mathbf{m}_q / |\mathbf{m}_q|$. Because the active tension is much higher compared to the passive stress part at systole, a much larger N was needed compared to the value used for the passive response during the numerical integration of the fibre contribution. We then compared the DFD-based and GST-based active tension in the human LV model with $N = 160$, the ESV difference was negligible for this two approaches, while the computational time was much longer for the DFD-based active tension, which took 6 times longer for one cardiac cycle than the GST-based active tension.

According to the studies from Sommer et al [4] and Ahmad et al [5], the in-plane and out-of-plane dispersions are largely different, thus a non-rotational symmetry assumption is more appropriate than the rotationally symmetry distribution as assumed in the κ model [21]. Furthermore, the non-rotational symmetric fibre distribution allows us to study how different degrees of in-plane and out-of-plane dispersions can affect ventricular dynamics, for example from the fully isotropic to the in-plane isotropic fibres, the transversely isotropic fibres, the general dispersion, and the highly aligned fibre structures as depicted in Fig. 5.3 (a).

In the DFD approach, the dispersed fibre distribution within an hemisphere is first divided into N triangles before excluding compressed fibres, see Fig. 5.5. In Li et al's study [17], they used $N = 640$ for the hemisphere discretization when modelling the simple shear and the uniaxial tests. Because the computational demanding for the rabbit and human heart models can be very high even without fibre dispersion, usually hours for one cardiac cycle, thus we first determined the possible minimum N for integrating fibre contributions with different b_1 and b_2 . We found that in general $N = 40$ can achieve a fairly good agreement with the theoretical value if fibres are not highly aligned (Fig. 5.5 (a)), but except for $b_1 = 8$ or $b_2 = 8$ in which a larger N will be needed. A further test on the human LV model with $N = 160$ and $N = 40$ showed that the computation time with $N = 160$ was almost 3.2 times longer than with $N = 40$, while the pump function was nearly identical.

Fibre dispersion seems having little influence on the passive filling of the rabbit bi-ventricle,

but not for the human heart. This agrees with our previous work using a neonatal porcine biventricle model [15], in which the LV and RV EDV differences were around 1.4% between a rule-based fibre structure without dispersion and a DT-MRI fibre structure which is naturally dispersed. The size of the neonatal porcine heart in [15] is similar to the rabbit heart in this chapter. The possible reasons for the different impacts from fibre dispersion between the rabbit and LV models are: (1) the much thinner wall in the rabbit heart (4 mm) compared to the human heart (10 mm), thus the changing of mean fibre angle is more rapid in the rabbit heart than the human heart, which may indicate that the diastolic filling in the rabbit heart could be more sensitive to the mean fibre rotation angle; (2) different fibre structures, i.e. different fibre rotation angles; (3) different passive material properties; (4) the much smaller size of the rabbit heart compared to the human heart.

Because of the wavy structure of the collagen network in the soft tissue, collagen fibres are initially crimped, and gradually recruited to bear the loading with increased stretch [8, 126]. Only recently, Cheng et al [8] assessed collagen fibre recruitment in bladder tissue using advanced bioimaging, and experimentally demonstrated that the low resistance in the toe regime, corresponding to the low stretch regime, can be explained by the no-discernible recruitment of collagen fibres. This will support the fundamental hypothesis in this chapter, also among others [17, 127], that is a straight fibre under compression will buckle and not support load because of its crimped configuration. This assumption is also necessary for reasons of stability as discussed in [127]. Including recruitment into the SEF would be more physiologically relevant compared to the simple tension-compression switch [128]. Another way to take into account the crimped wavy collagen fibre network is to adopt a multiscale approach from nanoscale up to the macroscale using homogenisation techniques as in [129]. In this chapter, the tension-compression switch is used because of its simple numerical implementation.

The importance of convexity of a SEF has been studied in [127] for ensuing material stability and meaningful mechanical behaviour. Here we will briefly discuss the convexity of the SEF in the DFD approach when only considering myocardial passive response, see Eqs. (5.1)(5.4). The convexity of the isotropic part in Eq. (5.1) has been demonstrated in [11], thus we only discuss the convexity of the anisotropic part (Eq. (5.4)). For each fibre bundle, ρ_q is constant, thus for the local deformation tensor \mathbf{C} , we have

$$\frac{\partial \mathcal{W}_f(I_{4M}^q)}{\partial \mathbf{C}} = \mathcal{W}'_f(I_{4M}^q) \mathbf{M}_q \otimes \mathbf{M}_q, \quad \frac{\partial^2 \mathcal{W}_f(I_{4M}^q)}{\partial \mathbf{C} \partial \mathbf{C}} = \mathcal{W}''_f(I_{4M}^q) \mathbf{M}_q \otimes \mathbf{M}_q \otimes \mathbf{M}_q \otimes \mathbf{M}_q, \quad (5.35)$$

and

$$\begin{aligned} \mathcal{W}'_f(I_{4M}^q) &= a_f (I_{4M}^q - 1) \exp[b_f (I_{4M}^q - 1)^2], \\ \mathcal{W}''_f(I_{4M}^q) &= a_f \exp[b_f (I_{4M}^q - 1)^2] [1 + 2b_f (I_{4M}^q - 1)^2]. \end{aligned}$$

Because a_f and b_f are positive parameters. When the fibre bundle (\mathbf{M}_q) is under stretch, $I_{4M}^q > 1$

ensures both $\mathcal{W}'_f(I_{4M}^q) > 0$ and $\mathcal{W}''_f(I_{4M}^q) > 0$; When the fibre bundle is under compression, by setting $I_{4M}^q = 1$ or equivalently $\mathcal{W}'_f(I_{4M}^q) = 0$, then $\mathcal{W}'_f(I_{4M}^q) = \mathcal{W}''_f(I_{4M}^q) = 0$. Therefore, $\sum_{q=1}^N \mathcal{W}'_f(I_{4M}^q) > 0$ and $\sum_{q=1}^N \mathcal{W}''_f(I_{4M}^q) > 0$ ensure the convexity of Eq. (5.4). During active contraction, the adopted active stress approach may violate the thermodynamic constraints [96], and might further lead to no-convexity and instability issue. As discussed in other studies [96, 108], the active strain approach would be an alternative approach if thermodynamic constraints need to be enforced. Nevertheless, we have not met instability issue in this chapter.

We further found that active contraction is sensitive to fibre dispersions for both the human and rabbit models. For example, the isotropic fibre distribution leads to almost no contraction, while the in-plane isotropic fibre distribution results purely in-plane active stresses with a high proportion of active tension along the sheet-normal direction, which leads to excessive longitudinal contraction in the human model (-36.8%) than reported the normal range in human ($-16.7 \pm 2.2\%$ [217], and $-17.75 \pm 5.44\%$ [218]). For both the LV and rabbit models, a general dispersed fibre structure, i.e. $b_1 = 2$ and $b_2 = 2$ can achieve a slightly larger cardiac output than the non-dispersed fibre structure, that is because the cross-fibre active stress can enhance the pump function as demonstrated in our previous study [15] and other studies [1, 91].

We would like to mention limitations. First, the passive SEF only incorporates the matrix and fibre contributions, but not including the terms associated with the sheet-direction and the sheet-normal as in other studies [11, 181], that is because of lack of experimental data for identifying all parameters and dispersed fibre measurements in those two directions. Secondly, fibre dispersion is only considered along the fibre direction \mathbf{f} , it is possible to include the sheet dispersion and the sheet-normal direction as in [74], but it would make the computation very challenging. Thirdly, a lumped circulation model is used for the ventricular models to provide physiologically accurate pressure boundary conditions. This lumped circulation model is similar to the Windkessel model and realized by a combination of surface-based fluid cavities and uni-directional fluid exchanges [15, 91]. Using a more realistic circulation model, such as one-dimensional models, will allow us to systematically investigate the interactions between ventricles and blood flow in vessels [208, 219]. A further limitation is that the electrophysiology is not modelled in this chapter, but assuming all myocytes contract simultaneously following our previous studies [15, 46, 208] and other studies [91]. Reasons are that in healthy hearts (1) the action propagation in the LV is much faster than the mechanical contraction, (2) an electromechanical model will significantly increase the modelling complexity, such as the Purkinje fibre network [220], and further difficulties in parameter calibration. We refer interested readers to the review [103] for multi-physics modelling. Last but not the least, the experimental data for the rabbits were from different studies, and rule-based fibre structures were assumed for both heart models. A combined experimental measurements (bi-axial and shear mechanical tests, DT-MRI fibre acquisition, ventricular pressure measurements, in vivo dynamics imaging, etc.) with the computational modelling from the same heart will be desirable to gain a deeper understanding

of how different fibre structures affecting ventricular pump function.

Despite those above limitations, the present computational framework can be readily to be extended to subject-specific multi-physics simulations [103] by including other heart chambers, electrophysiology, ventricular blood flow, and perfusion within myocardium, etc. Future studies shall also explore state-of-art assimilation methods in computational cardiology for clinical translation [221], and fast computation using cutting-edge machine learning approaches [216, 222].

5.5 Conclusion

This chapter systematically investigates the impact of fibre dispersions on myocardial mechanics both passively and actively, first on a myocardial strip, then a rabbit bi-ventricle model, and finally a human LV model. The fibre dispersion in myocardium is characterized by a non-rotationally symmetric distribution using a π -periodic Von Mises distribution. To exclude compressed fibres, two different approaches are compared, including the DFD model and the AI based approach within the eigen-space of the right Cauchy-Green tensor. The dispersed active tension is derived from the general structural tensor approach. Our results show that the DFD model is preferred for excluding compressible fibres because of high computational efficiency as already demonstrated in the literature. Our results further suggest that both diastolic filling and systolic contraction can be largely affected by dispersed fibres depending on the in-plane and out-of-plane dispersion degrees, especially for systolic contraction. The in-plane dispersion seems affecting myocardial mechanics more than the out-of-plane dispersion, an inappropriate dispersed fibre structure will result in a non-physiological dynamics (i.e. in-plane isotropic fibres). Despite different effects in the rabbit and human models caused by the fibre dispersion, large differences in pump function exist when $b_1, b_2 \in [0, 2]$, suggesting the necessary including fibre dispersion in cardiac models when the fibre dispersion is high, especially for pathological myocardium, i.e. fibrosis.

Part II

Growth and remodelling in left ventricle

Chapter 6

Growth and remodelling: a framework based on the constrained mixture theory

6.1 Introduction

The incidence of heart failure, such as after heart attack, has remained persistently high due to the maladaptive G&R of heart. The myocardium responds to internal or external environmental changes, such as mechanical loading conditions, by adaptably altering its structure and function. These adaptation processes are generally referred to as G&R. For example, when the heart is subjected to chronic overload conditions, ventricular dysfunction occurs after initial compensatory hypertrophy failing, finally resulting in heart failure.

There are two types of overload: pressure overload and volume overload. Common causes of pressure overload are aortic stenosis or systemic hypertension, thus LV has to overcome high resistance in order to pump blood into the aorta to normalise the systemic circulation, leading higher systolic wall stress. Thus, high wall stress during active contraction is usually considered as a mechanical cue to trigger G&R in pressure overload [141]. In volume overload, increased filling volume in the LV due to mitral valve regurgitation leads to higher stretch of the myocardium. Thus stretch of fibre has been considered to be a mechanical cue to simulate G&R of LV under volume overload.

The kinematic growth theory has been widely used to study G&R in soft tissue. Rodriguez et al. [10] firstly proposed the volumetric growth by the multiplicative decomposition of the total deformation gradient tensor \mathbf{F} , such that $\mathbf{F} = \mathbf{F}_e \mathbf{F}_g$, according to the concept of plasticity. \mathbf{F}_g is an inelastic growth tensor that describes changes in shape and size of a stress-free and compatible tissue. Growth can lead the tissue into a new incompatible and stress-free intermediate configuration. In the subsequent step, elastic deformation gradient tensor \mathbf{F}_e assembles all growing and original constituents into a new compatible state, in which residual stress may be generated.

The kinematic growth theory is an elegant approach to describe or predict G&R, with advantages of simple concept and convenient computational implementation. However, there are also limitations. For example, the theory was initially applied in stress-free configuration that does not exist inside the living tissue. Additionally, a single phenomenological evolution law of \mathbf{F}_g cannot distinguish the different G&R patterns of multiple constituents in tissue. Moreover, constant tissue density is always assumed during both elastic deformation and G&R. Although the kinematic growth theory is able to characterise overall G&R progression, important information such as different biological constituents' adaptation and response are missed.

To overcome these limitations, Cyron et al. [147] introduced a homogenized constrained mixture theory to describe G&R of each constituent, in which all constituents share the same total deformation. For constituent i , the total G&R deformation tensor \mathbf{F}_{gr}^i is assumed as the product of an inelastic remodelling deformation tensor \mathbf{F}_r^i and an inelastic growth tensor \mathbf{F}_g^i , and the total deformation gradient tensor under loading is $\mathbf{F} = \mathbf{F}_e^i \mathbf{F}_r^i \mathbf{F}_g^i$ [147] where \mathbf{F}_e^i is an elastic deformation tensor. Similar growth laws can be adapted from the kinematic growth theory to estimate growth ratios of constituents in this hybrid model.

In this chapter, the homogenised constrained mixture approach is employed to describe individual G&R of each component in myocardium, specifically, the ground matrix, myofibres and collagen fibres. The reference configuration before the growth of each G&R cycle is updated following the framework proposed by Lee et al. [143]. Finally, the coupled G&R model is applied to a beating human heart to study its G&R processes under various pathological conditions, including pressure overload induced by aortic stenosis and volume overload induced by mitral regurgitation. Different biomechanical cues are considered as the onset of G&R. Effects of G&R induced residual stress are also studied. Different assumptions of G&R considerations of collagen fibre are further discussed, including elastic or inelastic remodelling, to explore the interplays between myofibres and collagen fibres.

Our simulation results show that general features of eccentric and concentric cardiac growths can be captured by using individual G&Rs of myofibre, collagen fibre and the ground matrix in this homogenised constrained mixture G&R framework. Our results also highlight the importance of G&R properties of collagen fibre. For example, elastic remodelling or excessive growing collagen fibre could act as a scaffold to limit the eccentric enlargement of LV, but not on the concentric growth. Residual stress induced by G&R may play an important role in promoting eccentric growth while preventing wall thickening, which should be included in subsequent G&R studies.

6.2 Methodology of updated Lagrangian constrained mixture G&R framework

6.2.1 Homogenised constrained mixture model

In this study, we only consider three main constituents in myocardium, i.e. the ground matrix, myofibres and collagen fibres, denoted by $\{g,m,c\}$. Following Cyron et al. [147], although deformation of each component is quantified in its own reference configuration, all components share the same geometrical configuration before and after deformation states during the G&R process, i.e. sharing same total deformation mapping tensor \mathbf{F} . Moreover, Cyron et al. [147] defined an inelastic growth tensor \mathbf{G}^i , an inelastic remodelling tensor \mathbf{F}_{ir}^i , and a homogenised elastic deformation tensor \mathbf{F}_e^i for i th constituent at each G&R step, and further assumed that the i th constituent experienced the homogenised elastic and inelastic deformations [147].

A schematic illustration of Cyron's G&R process is shown in Fig. 6.1, which consists of two time-scale steps: the growth step ($\mathcal{B}_1 \rightarrow \mathcal{B}_4$) and the loading step ($\mathcal{B}_4 \rightarrow \mathcal{B}_5$). The growth tensor for individual constituents (\mathbf{G}^i) firstly converts the compatible configuration \mathcal{B}_1 to the incompatible configuration (\mathcal{B}_2), and the inelastic remodelling (\mathbf{F}_{ir}^i) further remodels it to \mathcal{B}_3 that can be either compatible or incompatible. Until this step, there is no residual stress induced from growth. Then the elastic remodelling (\mathbf{F}_{er}^i) lumps all constituents to the compatible configuration \mathcal{B}_4 where residual stress is presented due to the growth. Finally, external loadings are applied to \mathcal{B}_4 , leading to a further elastically deformed configuration \mathcal{B}_5 .

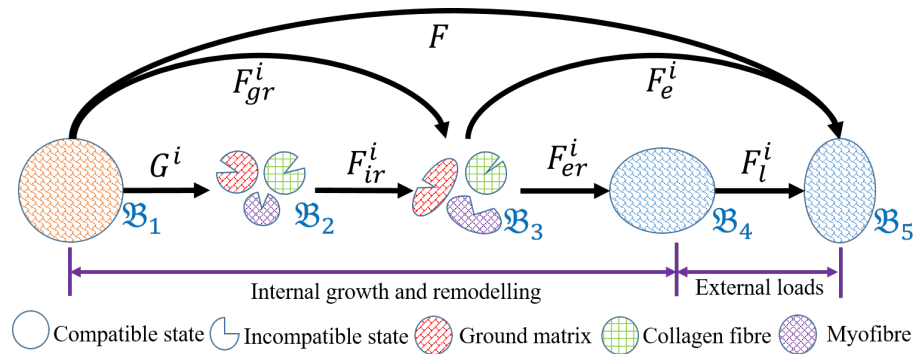


Figure 6.1: Scheme of G&R and loading process for each constituent in one numerical cycle. \mathcal{B}_1 is the updated reference configuration. Growth tensor (\mathbf{G}^i) firstly converts \mathcal{B}_1 to the incompatible configuration \mathcal{B}_2 , and inelastic remodelling (\mathbf{F}_{ir}^i) further remodels the \mathcal{B}_2 to the compatible or incompatible configuration \mathcal{B}_3 , then elastic remodelling (\mathbf{F}_{er}^i) merger all constituents to the compatible state \mathcal{B}_4 , finally the configuration \mathcal{B}_5 is the loading state according to external loads.

The total deformation in a homogenised constrained mixture model is denoted as

$$\mathbf{F} = \mathbf{F}_e^i \mathbf{F}_{ir}^i \mathbf{G}^i, \quad i \in \{g,m,c\}. \quad (6.1)$$

Note that \mathbf{F}_e^i includes two parts: the elastic remodelling deformation \mathbf{F}_{er}^i that denotes an elastic

deformation to achieve a compatible configuration after growth without external loadings, and the external elastic loading deformation \mathbf{F}_l^i that describes the elastic deformation from a grown compatible state to another deformed compatible state under external loadings. Thus, Eq. (6.1) can be written as

$$\mathbf{F} = \mathbf{F}_l^i \mathbf{F}_{er}^i \mathbf{F}_{ir}^i \mathbf{G}^i = \mathbf{F}_e^i \mathbf{F}_{gr}^i, \quad i \in \{g, m, c\}, \quad (6.2)$$

where the elastic part $\mathbf{F}_e^i = \mathbf{F}_l^i \mathbf{F}_{er}^i$ and the inelastic part $\mathbf{F}_{gr}^i = \mathbf{F}_{ir}^i \mathbf{G}^i$.

6.2.2 Updated reference configuration framework

Updated reference configuration

Reference configuration plays a crucial role in describing geometric deformation occurred in the G&R process [23] and the constrained mixture theory requires to track the evolution of reference configurations of individual constituents [138]. To overcome the difficulty of tracking all historical reference configurations, an updated reference framework is developed here. As shown in Fig. 6.2, one numerical simulation cycle includes three steps: a pre-processing step to update reference configuration (steps 1-6), a growth step to undergo G&R under no-loadings (step 7), and a loading step to simulate cardiac pump function from systole to diastole (steps 8-9). The growth step in Fig. 6.1 corresponds to step 7 in Fig. 6.2, and the loading step in Fig. 6.1 is accounted by steps 8-9 in Fig. 6.2. The residually-stressed compatible configuration \mathcal{B}_4 in Fig. 6.1 (or end of step 7 in Fig. 6.2) will be the updated reference configuration for the next growth step. Please note there are two time scales in one numerical simulation cycle, the G&R step occurs in weeks and the loading step occurs in seconds. Thus, one numerical simulation cycle can also be denoted as one growth cycle in this thesis.

Please note the residual stress in this chapter is quantified by the residual deformation tensor \mathbf{F}_r , and the growth is described by the growth tensor \mathbf{G} . They are the inputs for each new growth cycle. Details for the updated reference configuration are as following, schematically shown in Fig. 6.2, in which steps 1-6 are updated reference configuration process, step 7 is the G&R step, and steps 8-9 denote the loading step.

1. After finishing the n th growth cycle, obtaining the unloaded compatible configuration \mathcal{B}_n ;
2. Computing the residual tensor (\mathbf{F}_r^{n+1}) and the growth tensor (\mathbf{G}^{n+1}) according to mechanical clues from the n th loading cycle at configuration \mathcal{B}_n ;
3. Updating nodal positions according to the no-loading compatible geometry after G&R at n th cycle, and constructing new configuration \mathcal{B}_{n+1} ;
4. Updating fibre directions at new configuration \mathcal{B}_{n+1} ;
5. Updating growth and residual deformation tensors at new configuration \mathcal{B}_{n+1} ;

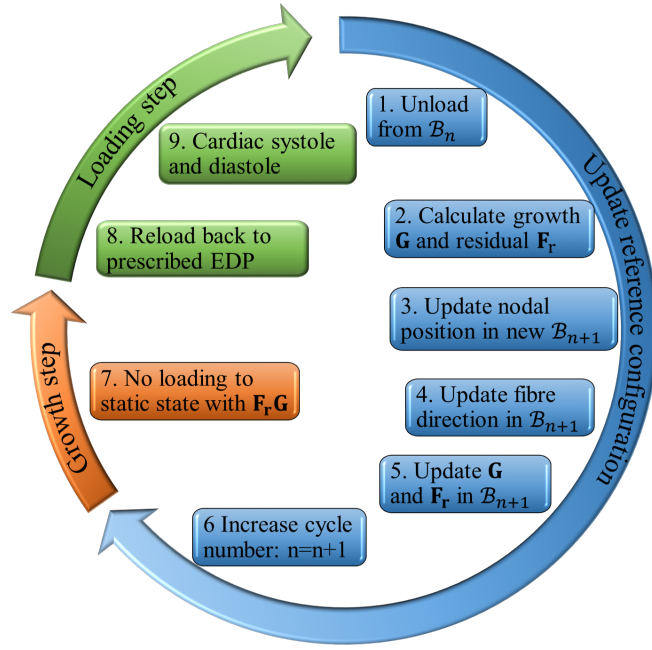


Figure 6.2: Scheme to update reference configuration and proceed a numerical simulation cycle that includes a updating reference configuration step, a growth step and a loading step.

6. Starting the new $(n + 1)$ th cardiac growth cycle;
7. Allowing heart to deform into a new static compatible geometry with \mathbf{F}_r^{n+1} and \mathbf{G}^{n+1} under no external-loadings;
8. Reloading back to prescribed EDP;
9. Starting a new cardiac systole and diastole process.

Updated growth tensors

Growths along fibre (myofibre and collagen fibre) and cross-fibre directions can result in cardiac eccentric and concentric growths, respectively. Note that cross-fibre direction is the sheet direction in this thesis, or equivalently, the transmural direction from endocardium to epicardium.

At beginning of growth (\mathcal{B}_1 in Fig. 6.1), growth tensor is designed as

$$\mathbf{G}^i = \vartheta^{f,i} \mathbf{f}_1^i \otimes \mathbf{f}_1^i + \vartheta^{s,i} \mathbf{s}_1^i \otimes \mathbf{s}_1^i + \mathbf{n}_1^i \otimes \mathbf{n}_1^i, \quad i \in \{g, m, c\}, \quad (6.3)$$

where $\vartheta^{f,i}$, and $\vartheta^{s,i}$ are growth ratios respectively along the fibre and cross-fibre directions in the current growth cycle, and they are defined relative to the fibre length in \mathcal{B}_1 , and the unit vectors \mathbf{f}_1^i , \mathbf{s}_1^i and \mathbf{n}_1^i represent the fibre, sheet and sheet-normal directions of each constituent in \mathcal{B}_1 . Descriptions of inelastic remodelling tensors will be discussed in the next subsection.

A possible evolution equation for stretch-driven fibre growth could take the following formulation [141]

$$\dot{\theta}_{n+1}^f = \frac{1}{\tau^f} \left(\frac{\theta^{\max,f} - \theta_{n+1}^f}{\theta^{\max,f} - 1} \right)^{\gamma^f} (\lambda^e - \lambda^{\text{crit}}) \mathcal{H}(\lambda^e - \lambda^{\text{crit}}) \quad \text{with} \quad \lambda^e = \frac{\|\mathbf{F} \cdot \mathbf{f}_0\|}{\vartheta_n^f}, \quad (6.4)$$

in which τ^f , γ^f are constant parameters, $\theta^{\max,f}$ is the maximum growth ratio along the fibre direction, λ^{crit} is the critical threshold of fibre stretch, and $\mathcal{H}(\cdot)$ is the Heaviside step function that is one when the elastics stretch λ^e exceeds λ^{crit} and is zero otherwise, θ_{n+1}^f is the total growth ratio from the first growth cycle (before any growth) to the current $(n+1)$ th growth cycle, $\vartheta_n^f = \theta_n^f / \theta_{n-1}^f$ is defined as the incremental growth ratio in the n th growth cycle, and $n+1, n, n-1$ represent the growth cycle numbers. Assuming the growth ratio θ_n^f is known at the end of the previous time step t_n , the following finite difference approximation of the first order time derivative is introduced as

$$\dot{\theta}_{n+1}^f = \frac{\theta_{n+1}^f - \theta_n^f}{\Delta t}, \quad (6.5)$$

where Δt denotes the growth cycle time. The Newton-Raphson method is used to solve θ_{n+1}^f when $\lambda^e > \lambda^{\text{crit}}$, such that

$$\begin{aligned} \mathcal{R}_f &= \theta_{n+1}^f - \theta_n^f - \frac{1}{\tau^f} \left(\frac{\theta^{\max,f} - \theta_{n+1}^f}{\theta^{\max,f} - 1} \right)^{\gamma^f} (\lambda^e - \lambda^{\text{crit}}) \Delta t = 0, \\ \mathcal{K}_f &= \frac{d\mathcal{R}_f}{d\theta_{n+1}^f} = 1 + \frac{\gamma^f}{\tau^f} \left(\frac{\theta^{\max,f} - \theta_{n+1}^f}{\theta^{\max,f} - 1} \right)^{\gamma^f - 1} \frac{(\lambda^e - \lambda^{\text{crit}})}{\theta^{\max,f} - 1} \Delta t, \end{aligned} \quad (6.6)$$

in which the numerical iteration can be stopped when $|\mathcal{R}_f / \mathcal{K}_f| \leq \varepsilon_s$, i.e. $\theta_{n+1}^f - \mathcal{R}_f / \mathcal{K}_f \cong \theta_{n+1}^f$.

Stress-driven cross-fibre growth [141] is estimated by

$$\dot{\theta}_{n+1}^s = \frac{1}{\tau^s} \left(\frac{\theta^{\max,s} - \theta_{n+1}^s}{\theta^{\max,s} - 1} \right)^{\gamma^s} \left(\frac{\text{tr}(J\sigma_t)}{p^{\text{crit}}} - 1 \right) \mathcal{H}(\text{tr}(J\sigma_t) - p^{\text{crit}}), \quad (6.7)$$

in which τ^s , γ^s are material parameters, $\theta^{\max,s}$ is the maximum growth ratio along sheet direction, p^{crit} is critical threshold value for active tension generated by each myocyte, σ_t is the total Cauchy stress tensor and $J = \det(\mathbf{F})$. Similarly, θ_{n+1}^s is solved by

$$\begin{aligned} \mathcal{R}_s &= \theta_{n+1}^s - \theta_n^s - \frac{1}{\tau^s} \left(\frac{\theta^{\max,s} - \theta_{n+1}^s}{\theta^{\max,s} - 1} \right)^{\gamma^s} \left(\frac{\text{tr}(J\sigma_t)}{p^{\text{crit}}} - 1 \right) \Delta t = 0 \\ \mathcal{K}_s &= \frac{d\mathcal{R}_s}{d\theta_{n+1}^s} = 1 + \frac{\gamma^s}{\tau^s} \left(\frac{\theta^{\max,s} - \theta_{n+1}^s}{\theta^{\max,s} - 1} \right)^{\gamma^s - 1} \frac{(\text{tr}(J\sigma_t) / p^{\text{crit}} - 1)}{\theta^{\max,s} - 1} \Delta t. \end{aligned} \quad (6.8)$$

in which numerical iteration also is stopped when $|\mathcal{R}_s/\mathcal{K}_s| \leq \varepsilon_s$, i.e. $\theta_{n+1}^s - \mathcal{R}_s/\mathcal{K}_s \cong \theta_{n+1}^s$. Myofibres, collagen fibres and the ground matrix all use Eq. (6.4) and Eq. (6.7) to estimate growth ratios with their respective parameter value settings.

Updated volume fractions

Myocardial volume equals to the summation of individual volumes of all constituents by assuming they are incompressible. Hence, the total volume growth amount (J_n^g) from the $(n-1)$ th to the n th growth cycle can be derived from the incremental growth ratio ϑ_n^i and the corresponding volume fraction ϕ_{n-1}^i of all constituents,

$$J_n^g = \frac{V_n}{V_{n-1}} = \frac{\sum_{i=\{g,m,c\}} \vartheta_n^i V_{n-1}^i}{V_{n-1}} = \sum_{i=\{g,m,c\}} \vartheta_n^i \frac{V_{n-1}^i}{V_{n-1}} = \sum_{i=\{g,m,c\}} \phi_{n-1}^i \vartheta_n^i, \quad (6.9)$$

where V_{n-1} and V_{n-1}^i are respective the total volume and the individual volume of constituent i in the $(n-1)$ th growth cycle. And, the updated volume fraction ϕ_n^i of each constituent after growth is inversely computed by

$$\phi_n^i = \frac{V_n^i}{V_n} = \frac{\vartheta_n^i V_{n-1}^i}{\sum_{i=\{g,m,c\}} \vartheta_n^i V_{n-1}^i} = \frac{\vartheta_n^i V_{n-1}^i / V_{n-1}}{\sum_{i=\{g,m,c\}} \vartheta_n^i V_{n-1}^i / V_{n-1}} = \frac{\phi_{n-1}^i \vartheta_n^i}{\sum_{i=\{g,m,c\}} \phi_{n-1}^i \vartheta_n^i}. \quad (6.10)$$

Updated fibre direction

The total deformation tensors between any two compatible configurations can be computed according to relative nodal displacement,

$$\mathbf{F}_{a \rightarrow b} = \nabla \mathbf{u}_{a \rightarrow b} + \mathbf{I}, \quad (6.11)$$

where $\mathbf{F}_{a \rightarrow b}$ is the total deformation tensor from a compatible configuration \mathcal{B}_a to another \mathcal{B}_b , and $\mathbf{u}_{a \rightarrow b}$ is the corresponding nodal displacements. To compute fibre rotation, for example, rotated fibre system by total deformation gradient tensor from \mathcal{B}_1 ($a=1$) to \mathcal{B}_4 ($b=4$) in Fig. 6.1 is

$$\mathbf{f}_1^{n+1'} = \mathbf{F}_{1 \rightarrow 4} \mathbf{f}_1^n, \quad \mathbf{s}_1^{n+1'} = \mathbf{F}_{1 \rightarrow 4} \mathbf{s}_1^n, \quad \mathbf{n}_1^{n+1'} = \mathbf{F}_{1 \rightarrow 4} \mathbf{n}_1^n, \quad (6.12)$$

where \mathbf{f}_1^n , \mathbf{s}_1^n and \mathbf{n}_1^n are respectively fibre, sheet and sheet-normal directions at \mathcal{B}_1 (in Fig. 6.1) in the n th growth cycle. Note that \mathbf{f}_1^n , \mathbf{s}_1^n and \mathbf{n}_1^n are unit orthogonal vectors at \mathcal{B}_1 , but $\mathbf{f}_1^{n+1'}$, $\mathbf{s}_1^{n+1'}$ and $\mathbf{n}_1^{n+1'}$ are not at \mathcal{B}_4 . Hence, we redefine fibre system as following

$$\mathbf{f}_1^{n+1} = \frac{\mathbf{f}_1^{n+1'}}{|\mathbf{f}_1^{n+1'}|}, \quad \mathbf{n}_1^{n+1} = \frac{\mathbf{f}_1^{n+1} \times \mathbf{s}_1^{n+1'}}{|\mathbf{f}_1^{n+1} \times \mathbf{s}_1^{n+1'}|}, \quad \mathbf{s}_1^{n+1} = \frac{\mathbf{n}_1^{n+1} \times \mathbf{f}_1^{n+1}}{|\mathbf{n}_1^{n+1} \times \mathbf{f}_1^{n+1}|}, \quad (6.13)$$

where \mathbf{f}_1^{n+1} , \mathbf{s}_1^{n+1} and \mathbf{n}_1^{n+1} are the updated fibre system at \mathcal{B}_1 in the $(n+1)$ th numerical simulation cycle.

6.2.3 Strain energy functions

SEFs of the three constituents are

$$\begin{aligned}\Psi_g(\mathbf{F}) &= \frac{a_g}{2b_g} \{ \exp[b_g(I_1 - 3)] - 1 \}, \\ \Psi_m(\mathbf{F}) &= \frac{a_m}{2b_m} \{ \exp[b_m(I_{4m}^* - 1)^2] - 1 \}, \\ \Psi_c(\mathbf{F}) &= \frac{a_c}{2b_c} \{ \exp[b_c(I_{4c}^* - 1)^2] - 1 \},\end{aligned}\quad (6.14)$$

where $a_g, b_g, a_m, b_m, a_c, b_c$ are material parameters, $I_1 = \text{trace}(\mathbf{C}^g)$ with $\mathbf{C}^g = (\mathbf{F}^g)^T \mathbf{F}^g$ and \mathbf{F}^g the deformation gradient of ground matrix; $I_{4i} = \mathbf{f}^i \cdot \mathbf{C}^i \mathbf{f}^i$ is the strain invariant with $\mathbf{C}^i = (\mathbf{F}^i)^T \mathbf{F}^i$ and \mathbf{F}^i is the deformation gradient tensor of myofibre ($i = m$) or collagen fibre ($i = c$), respectively, and \mathbf{f}^i is the mean fibre direction in the reference configuration; $I_{4i}^* = \max(I_{4i}, 1)$ is to ensure only the stretched fibres can bear load passively. The total volumetric part is

$$\Psi_{\text{vol}}(J) = \frac{1}{D} \left(\frac{J^2 - 1}{2} - \ln(J) \right), \quad (6.15)$$

where D is a multiple of the Bulk Modulus K , i.e., $D = 2/K$, \mathbf{F} is the total deformation tensor and $J = \det(\mathbf{F})$.

In an individual growth cycle, growth tensor \mathbf{G}^i is constant, if we further assume the inelastic remodelling tensor \mathbf{F}_{ir}^i can be defined as a constant tensor according to remodelling property of constituent i , then the elastic passive stress in one numerical simulation cycle is the function of elastic deformation tensor \mathbf{F}_e^i , such as

$$\boldsymbol{\sigma}_p^i = J_{\mathbf{F}}^{-1} \mathbf{F} \frac{\partial \Psi_i(\mathbf{F})}{\partial \mathbf{F}} = J_{\mathbf{F}}^{-1} \mathbf{F} \frac{\partial [J_{\mathbf{F}_{gr}^i} \Psi_i(\mathbf{F}_e^i)]}{\partial \mathbf{F}} = J_{\mathbf{F}}^{-1} J_{\mathbf{F}_{gr}^i} \mathbf{F} \left(\frac{\partial \mathbf{F}_e^i}{\partial \mathbf{F}} : \frac{\partial \Psi_i(\mathbf{F}_e^i)}{\partial \mathbf{F}_e^i} \right) = J_{\mathbf{F}_e^i}^{-1} \mathbf{F}_e^i \frac{\partial \Psi_i(\mathbf{F}_e^i)}{\partial \mathbf{F}_e^i}, \quad (6.16)$$

where $\mathbf{F}_{gr}^i = \mathbf{F}_{ir}^i \mathbf{G}^i$, $J_{\mathbf{F}_e^i} = \det(\mathbf{F}_e^i)$, $J_{\mathbf{F}_{gr}^i} = \det(\mathbf{F}_{gr}^i)$, and inelastic \mathbf{F}_{gr}^i makes $\partial J_{\mathbf{F}_{gr}^i} / \partial \mathbf{F}_e^i = \mathbf{0}$ and $\partial \mathbf{F}_{gr}^i / \partial \mathbf{F}_e^i = \mathbf{0}$ (4th order). Similarly, the total volumetric stress is estimated according to the total volume growth in the current numerical simulation cycle, that is

$$\boldsymbol{\sigma}_{\text{vol}} = \frac{\partial \Psi_{\text{vol}}(J)}{\partial J} \mathbf{I} = \frac{\partial \Psi_{\text{vol}}(\eta)}{\partial \eta} \mathbf{I}, \quad (6.17)$$

where $J = \det(\mathbf{F})$, and $\eta = J/J_k^g$.

Additive active stress generated by myofibre is

$$\boldsymbol{\sigma}_a^m = T_a \hat{\mathbf{f}} \otimes \hat{\mathbf{f}}, \quad (6.18)$$

Finally, the total stress at n th growth cycle is

$$\sigma_t = \left(\sum_{i=\{g,m,c\}} \phi_n^i \sigma_p^i \right) + \phi_n^m \sigma_a^m + \frac{1}{D} \left(\eta - \frac{1}{\eta} \right) \mathbf{I}. \quad (6.19)$$

6.2.4 Application to human in vivo heart model

A human LV model in section 5.3.4 of Chapter 5 is employed here to study G&R using the proposed framework. Fig. 6.3 (a) shows the meshed LV geometry with a rule-based fibre structure. Fibres linearly rotate from epicardium (-60°) to endocardium (60°). A similar simplified circulation system [15] is attached to the LV model, whereas only the aorta and the left atrium (Fig. 6.3 (b)) are included.

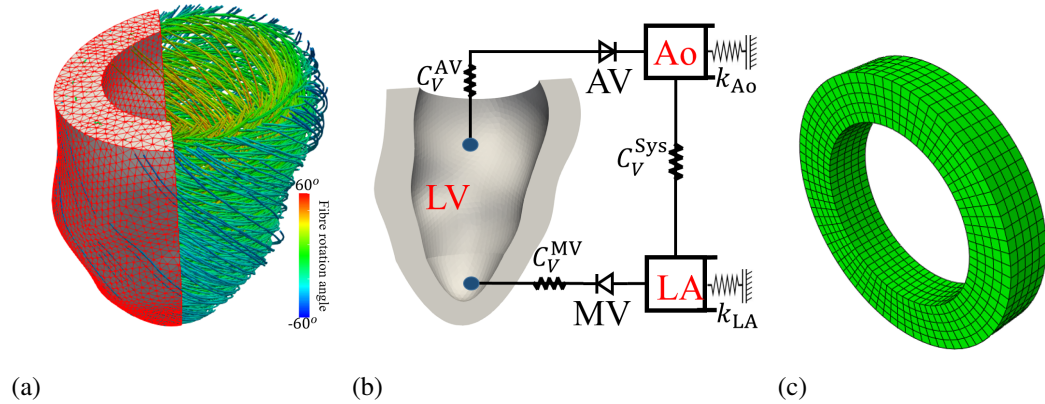


Figure 6.3: (a) Meshed network of human LV model (133,042 linear tetrahedral elements and 26,010 nodes) and three element circles at base, medium and apex positions. Inside fibre distribution was constructed by the rule based method from -60° at epicardium to 60° at endocardium. (b) Sketch of the human LV model with a circulation system, same as the Fig. 5.12 (c). (c) Meshed network of simple ring model (1,925 linear hexadecimal elements and 2,772 nodes) and fibres also rotates from endocardium (60°) to epicardium (-60°).

In normal condition without G&R, LV pressure is firstly preloaded to normal EDP (8 mmHg), and mean fibre stretch at end-diastole is the criterion (λ^{crit} in Eq. (6.4)) to determine whether to trigger fibre growth. Then, the iso-volumetric contraction begins, followed by the systolic ejection when the LV pressure exceeds the aortic pressure (80 mmHg), and finally the ejection ends when the LV pressure is lower than the aortic pressure. The mean maximum trace of Cauchy stress tensor during active contraction is the threshold (p^{crit} in Eq. (6.7)) to trigger cross-fibre growth.

In pathological growth conditions, we first simulate the growth cycle with no external loading boundary conditions, which allows the LV to grow and remodel triggered by excessive diastolic fibre stretch or active tension or both. In chronic eccentric growth, we use the increased LV cavity pressure (16 mmHg [140]) for the EDP, and no changes for active contraction same as

the model in section 5.3.4 of Chapter 5 represent no further remodelling in active contraction. In contrast, for the concentric growth, the passive diastole filling is the same as the model in section 5.3.4 of Chapter 5, instead we increase the aortic valvular stenosis from normal $C_v = 1.2$ to pathological $C_v = 50$ in Eq. (4.20). In this way, the LV systolic pressure will increase significantly to overcome the stenosis in the aortic valve.

The G&R process will stop when the sum of relative errors of loaded and unloaded LV cavity volumes with respect to these values in the previous growth cycle is less than the threshold $\mathcal{R}^{\text{crit}}$, that is

$$\mathcal{R}_{\text{error}} = \left| \frac{V_{\text{loaded}}^{n+1} - V_{\text{loaded}}^n}{V_{\text{loaded}}^n} \right| \times 100\% + \left| \frac{V_{\text{unloaded}}^{n+1} - V_{\text{unloaded}}^n}{V_{\text{unloaded}}^n} \right| \times 100\% < \mathcal{R}^{\text{crit}} \quad (6.20)$$

where $\mathcal{R}_{\text{error}}$ is the total absolute relative error, V_{loaded} is the loaded LV cavity volume and V_{unloaded} is unloaded value.

A simple meshed ring model (Fig. 6.3(c)) is further used here to study the residual stress induced by G&R. Through dividing LV wall into five layers and projecting the average stress of each layer onto the corresponding layer on the ring model, we will study how the ring will open under the effects of growth-induced residual stress, a virtual ‘open-angle’ experiment.

6.3 Verification of the homogenised constrained mixture model

To verify the homogenised constrained mixture G&R in this updated reference framework, a volumetric G&R is employed in this section. The homogenised constrained mixture growth approach is performed in section 6.3.1 with more detailed descriptions of growth tensors. The volumetric growth approach in section 6.3.2 adopts the updated reference framework described in section 6.2. Both approaches use the human LV model in section 6.2.4, and they share the same boundary conditions. Residual stress is released at the beginning of the growth cycle whilst the residual stress generated by the new growth [143] is kept in the subsequent loading step. The initial volume fractions of three constituents are $\phi^g = 0.274$, $\phi^m = 0.7$, and $\phi^c = 0.026$. For simplicity, we assume that all constituents do not experience any inelastic remodelling, i.e. $\mathbf{F}_{ir}^i = \mathbf{I}$ ($i = \{g, m, c\}$), and share the same growth tensor. Only the eccentric growth induced by volume overload is simulated in this section. The parameters in simulations are listed in Table 6.1.

6.3.1 Homogenised constrained mixture approach

As shown in Fig. 6.4, \mathcal{B}_1 is stress free because of relieving residual stress before growth in an updated reference configuration. After growth, \mathcal{B}_2 turns to be incompatible state. Then, the elastic remodelling tensor homogenise all grown constituents into new compatible state \mathcal{B}_3 , in

Passive parameters and T_{\max}						
a_g (kPa)	b_g	a_m (kPa)	b_m	a_c (kPa)	b_c	T_{\max}
0.205	6.404	4.236	2.3710	32.82	11.674	210
Eccentric growth						
τ^f	γ^f	λ^{crit}	$\theta^{\text{max},f}$	ε_f	$\mathcal{R}^{\text{crit}}$	
1.0	1.0	1.1124	1.4	1.0E-9	1.0%	
Concentric growth						
τ^s	γ^s	p^{crit}	$\theta^{\text{max},s}$	ε_s	$\mathcal{R}^{\text{crit}}$	
17.0	1.0	0.0586	2.0	1.0E-9	5.0%	

Table 6.1: Parameters in simulations of G&R

which the residual stress is presented. The compatible geometry in this configuration will be the initial geometry in the next growth cycle after discarding all residual stress. The mechanical clues to determine the growth tensor are from the loaded mechanical environments in \mathcal{B}_4 .

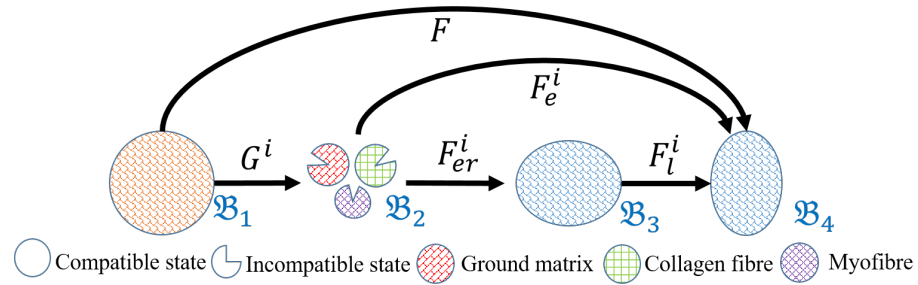


Figure 6.4: Scheme of G&R when relieving residual stress before growth at beginning of each updated growth cycle. The configuration \mathcal{B}_1 is stress-free and grows to the new stress-free and incompatible configuration \mathcal{B}_2 , which turns to be the compatible state again \mathcal{B}_3 by elastic remodelling, finally cardiac dynamics in the \mathcal{B}_4 is achieved by applying external loadings in the \mathcal{B}_3 .

Therefore, the total deformation gradient tensor \mathbf{F} in a homogenised constrained mixture model for each constituent

$$\mathbf{F} = \mathbf{F}_l^i \mathbf{F}_{er}^i \mathbf{G}^i = \mathbf{F}_e^i \mathbf{G}^i, \quad i \in \{g, m, c\} \quad (6.21)$$

where $\mathbf{F}_e^i = \mathbf{F}_l^i \mathbf{F}_{er}^i$ is the total elastic deformation that contributes to the final Cauchy stress. Myofibres and collagen fibres share same direction (\mathbf{f}_1) at begging of growth (\mathcal{B}_1), and the growth tensor is

$$\mathbf{G}^i = \vartheta^{f,i} \mathbf{f}_1^i \otimes \mathbf{f}_1^i + \mathbf{s}_1^i \otimes \mathbf{s}_1^i + \mathbf{n}_1^i \otimes \mathbf{n}_1^i, \quad (6.22)$$

thus, the total elastic tensor for i th constituent is

$$\mathbf{F}_e^i = \mathbf{F}(\mathbf{G}^i)^{-1}, \quad (6.23)$$

and the passive stresses in cardiac dynamics are

$$\begin{aligned}
 \boldsymbol{\sigma}_p^g &= J_{\mathbf{F}_e^g}^{-1} a_g \exp[b_g(I_1 - 3)] \mathbf{B}_e^g, \\
 \boldsymbol{\sigma}_p^m &= 2J_{\mathbf{F}_e^m}^{-1} a_m (I_{4m}^* - 1) \exp[b_m(I_{4m}^* - 1)^2] (\mathbf{f}_e^m \otimes \mathbf{f}_e^m), \\
 \boldsymbol{\sigma}_p^c &= 2J_{\mathbf{F}_e^c}^{-1} a_c (I_{4c}^* - 1) \exp[b_c(I_{4c}^* - 1)^2] (\mathbf{f}_e^c \otimes \mathbf{f}_e^c),
 \end{aligned} \tag{6.24}$$

in which

$$\begin{aligned}
 \mathbf{B}_e^g &= \mathbf{F}_e^g \mathbf{F}_e^{gT}, & \mathbf{C}_e^g &= \mathbf{F}_e^{gT} \mathbf{F}_e^g, & I_1 &= \text{trace}(\mathbf{C}_e^g), & J_{\mathbf{F}_e^g} &= \det(\mathbf{F}_e^g), \\
 \mathbf{C}_e^m &= \mathbf{F}_e^{mT} \mathbf{F}_e^m, & I_{4m} &= \mathbf{f}_1 \cdot \mathbf{C}_e^m \mathbf{f}_1, & \mathbf{f}_e^m &= \mathbf{F}_e^m \mathbf{f}_1, & J_{\mathbf{F}_e^m} &= \det(\mathbf{F}_e^m), \\
 \mathbf{C}_e^c &= \mathbf{F}_e^{cT} \mathbf{F}_e^c, & I_{4c} &= \mathbf{f}_1 \cdot \mathbf{C}_e^c \mathbf{f}_1, & \mathbf{f}_e^c &= \mathbf{F}_e^c \mathbf{f}_1, & J_{\mathbf{F}_e^c} &= \det(\mathbf{F}_e^c).
 \end{aligned} \tag{6.25}$$

Finally, total passive stress at n th growth cycle is

$$\boldsymbol{\sigma}_t^p = \sum_{i=\{g,m,c\}} \phi_n^i \boldsymbol{\sigma}_p^i. \tag{6.26}$$

6.3.2 Volumetric growth approach

In the volumetric growth approach, all constituents are treated as a mixture and use a common total deformation gradient tensor \mathbf{F} , total SEF is sum of three parts, the ground matrix, myofibres and collagen fibres, with respective volume fractions, such as

$$\Psi = \phi_g \frac{a_g}{2b_g} \{\exp[b_g(I_1 - 3)] - 1\} + \phi_m \frac{a_m}{2b_m} \{\exp[b_m(I_{4f}^* - 1)^2] - 1\} + \phi_c \frac{a_c}{2b_c} \{\exp[b_c(I_{4f}^* - 1)^2] - 1\}, \tag{6.27}$$

where $I_1 = \text{trace}(\mathbf{C})$, $I_{4f} = \mathbf{f}_1 \cdot \mathbf{C} \mathbf{f}_1$ are strain invariants with $\mathbf{C} = \mathbf{F}^T \mathbf{F}$ and \mathbf{F} is the total deformation gradient, and \mathbf{f}_1 is the mean fibre direction in the updated reference \mathcal{B}_1 (Fig. 6.5).

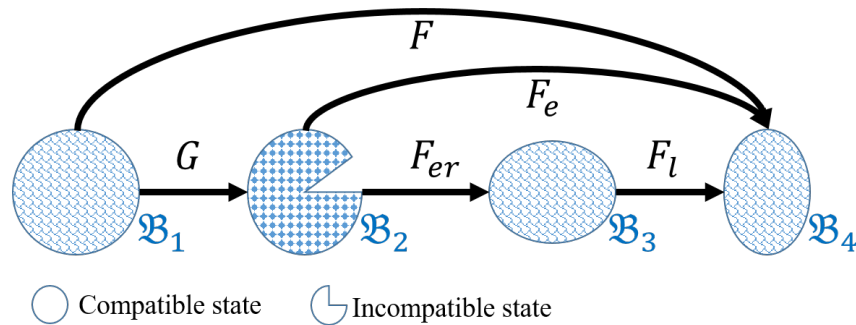


Figure 6.5: Scheme of volumetric growth without residual stress at beginning of growth. The configuration \mathcal{B}_1 is stress-free and grows to the incompatible stress-free configuration \mathcal{B}_2 . Then, it turns to be the compatible state \mathcal{B}_3 by elastic remodelling, which is finally loaded to \mathcal{B}_4 .

In Fig. 6.5, the total deformation (\mathbf{F}) consists of growing (\mathbf{G}), remodelling (\mathbf{F}_{er}) and loading

(\mathbf{F}_l) deformations, thus

$$\mathbf{F} = \mathbf{F}_l \mathbf{F}_{er} \mathbf{G} = \mathbf{F}_e \mathbf{G}, \quad (6.28)$$

where total elastic tensor $\mathbf{F}_e = \mathbf{F}_l \mathbf{F}_{er}$ is also

$$\mathbf{F}_e = \mathbf{F} \mathbf{G}^{-1}, \quad (6.29)$$

with

$$\mathbf{G} = \vartheta^f \mathbf{f}_1 \otimes \mathbf{f}_1 + \mathbf{s}_1 \otimes \mathbf{s}_1 + \mathbf{n}_1 \otimes \mathbf{n}_1. \quad (6.30)$$

Hence, the total passive stress is

$$\begin{aligned} \sigma_i^p &= J_{\mathbf{F}_e}^{-1} \mathbf{F}_e \frac{\partial \Psi}{\partial \mathbf{F}_e} \\ &= \phi_g J_{\mathbf{F}_e}^{-1} a_g \exp[b_g(I_1 - 3)] \mathbf{B}_e + \phi_m 2J_{\mathbf{F}_e}^{-1} a_m (I_{4m}^* - 1) \exp[b_m(I_{4m}^* - 1)^2] (\mathbf{f}_e \otimes \mathbf{f}_e) \\ &\quad + \phi_c 2J_{\mathbf{F}_e}^{-1} a_c (I_{4c}^* - 1) \exp[b_c(I_{4c}^* - 1)^2] (\mathbf{f}_e \otimes \mathbf{f}_e) \end{aligned} \quad (6.31)$$

in which $J_{\mathbf{F}_e} = \det(\mathbf{F}_e)$, $\mathbf{B}_e = \mathbf{F}_e^T \mathbf{F}_e$, $\mathbf{f}_e = \mathbf{F}_e \mathbf{f}_1$, $\mathbf{C}_e = \mathbf{F}_e^T \mathbf{F}_e$, $I_1 = \text{trace}(\mathbf{C}_e)$, and $I_{4f} = \mathbf{f}_1 \cdot \mathbf{C}_e \mathbf{f}_1$.

6.3.3 Verification results

The model using the homogenised constrained mixture approach is denoted as HCON and the abbreviation of the model using the volumetric growth approach is VMG. Both approaches use the same growth law. They both take 15 steps to reach a stable G&R state ($\mathcal{R}_{\text{error}} < 1.0\%$). In the grown LV, as shown in Fig. 6.6 (a), myocardium growth mainly occurs at endocardium, larger total myofibre growth ratio θ^f at inner wall, and epicardium has smaller growth increments. Overall, the smallest growth ($\theta^f = 1$) is at the apex and the largest ($\theta^f = 1.4$) locates in the middle of LV, corresponding to the enlarged LV cavity with more growth in the radial direction than the longitudinal direction. HCON and VMG have almost same grown geometric anatomies and θ^f distributions. They all present thicker and less smooth ventricular wall than the original LV with no growth (NG).

The average total myofibre growth ratio (θ^f) from the beginning of growth are depicted in Fig. 6.6 (b), where growth slows down in the later growing stage for both models and the two θ^f lines are overlapped. There are same overlaps in corresponding average incremental growth ratios (ϑ^f) of the whole LV in each updated growth cycle (Fig. 6.6 (c)), in which ϑ^f gradually decrease with LV growing. Neither θ^f increases to constant value nor ϑ^f decreases to unity, because of local growth still occurs in the model although the growth ratio almost does not change the total volume with $\mathcal{R}_{\text{error}} < 1.0\%$. For example, ϑ^f is less than 1.005 in the final growth cycle.

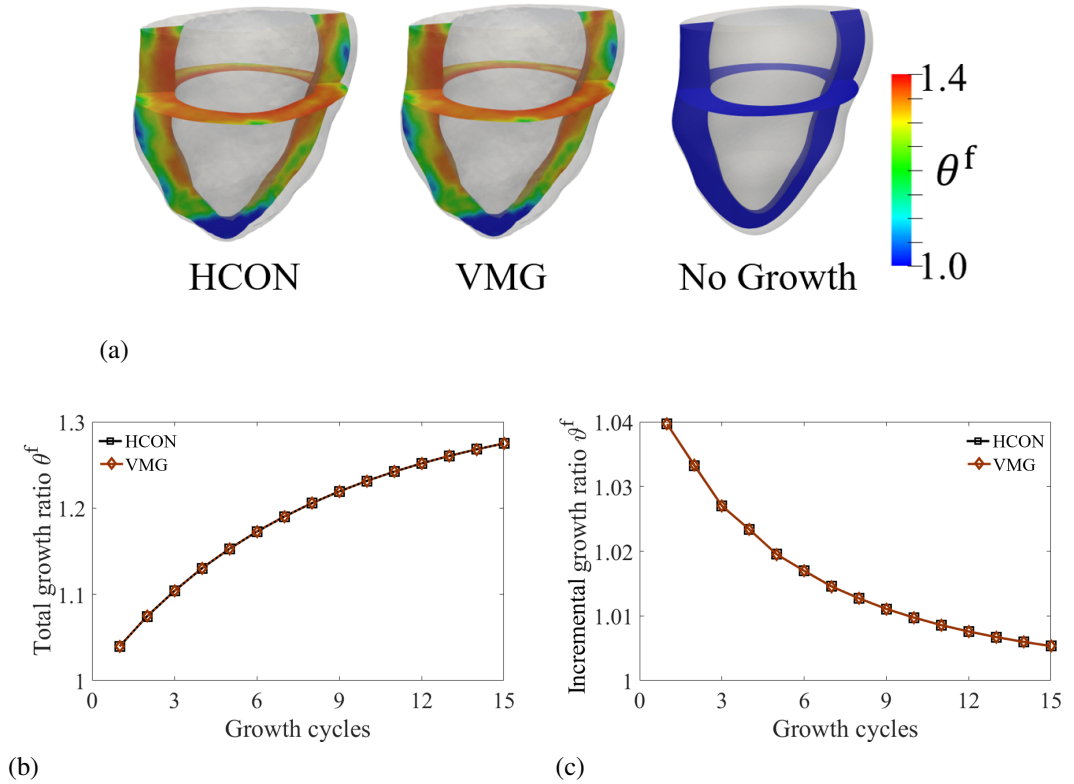


Figure 6.6: (a) Grown LV anatomical diagrams and their inside growth ratio distributions in the final growth cycle. With respect to growth cycles, average values of total growth ratio (b) and incremental growth ratio (c) of the whole LV.

Residual stress after growth in the final growth cycle is plotted in Fig. 6.7 (a), where cross-sectional view is cut from the LV midsection. There are no significant differences of residual stress distributions between HCON and VMG, and the residual stress values are around zero. Similar results can also be found in Fig. 6.7 (b) that describes transmural mean fibre stress (S_{11}) at each layer from endocardium (0%) to epicardium (100%) which are also around zero region. When mapping residual stress from Fig. 6.7 (a) to simple ring model, open angles are shown in Fig. 6.7 (c), only achieving same 3.5° , much less than the experiential value ($13 \pm 5.3^\circ$ [223]).

Updated reference configuration framework is successful coupled to the homogenised constrained mixture theorem to simulate G&R process of a heart. Almost the same results between homogenised constrained mixture theorem and volumetric growth theorem indicate the successful implementation of homogenised constrained mixture theorem in FE simulations of heart growth.

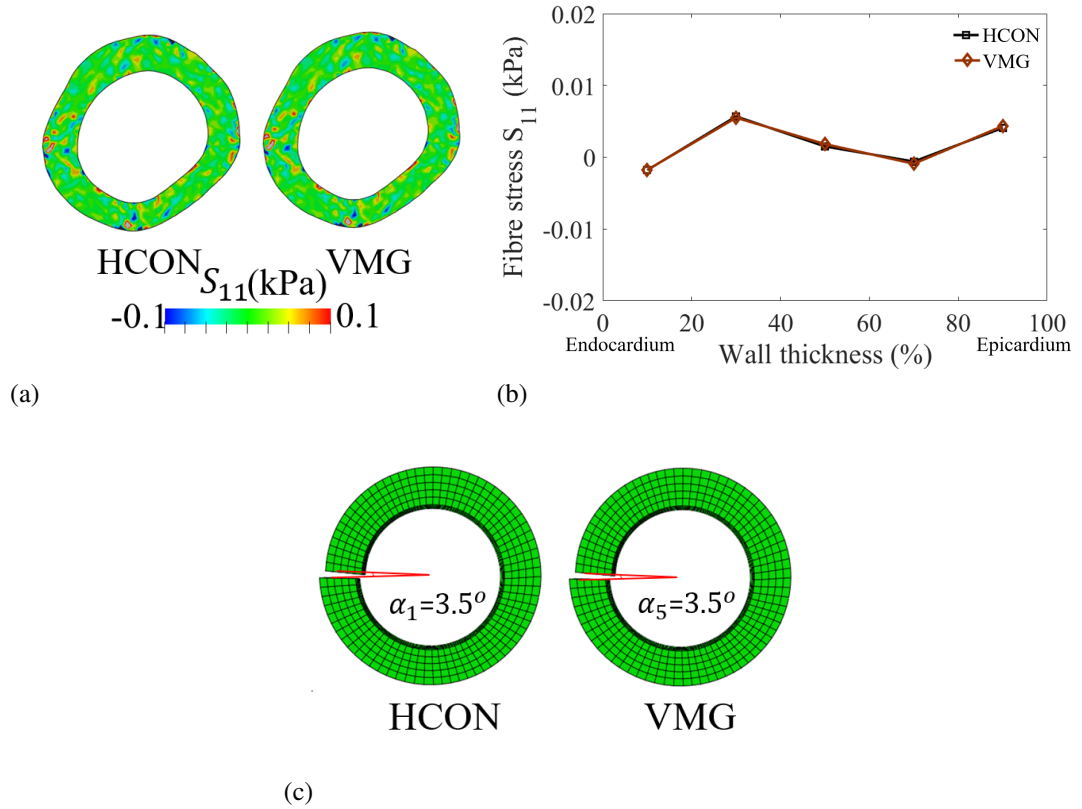


Figure 6.7: Residuals stress is estimated at compatible geometry after growth in the final growth cycle. (a) Distribution of fibre stress component along fibre S_{11} at medium of LV, (b) mean transmurals stress along wall thickness, and (c) open angle under mean residual stress in the ring model.

6.4 Comparison of maintaining and relieving residual stress during G&R

Considering the residual stress caused by G&R can adversely affect G&R [224], scenarios of maintaining or relieving the growth-induced residual stress before and after growth are compared in this section by eccentric growth under volume overload. Same as section 6.3, all constituents do not experience inelastic remodelling. Growth tensors for the ground matrix and collagen fibre are the same as the growth tensor for myofibres, thus at each growth cycle, we only determine the growth tensor for myofibres using the stretch-induced growth law (Eq. (6.4)).

6.4.1 With residual stress before and after growth

To compare the effects of the residual stress before growth for each constituent at an updated reference configuration, two fictitious incompatible stress-free configuration \mathcal{B}_0 and \mathcal{B}_{-1} are included, as shown in Fig. 6.8. Residual stress from the previous growth cycle is denoted by residual deformation tensor \mathbf{F}_{r0}^i , hence, the compatible configuration \mathcal{B}_1 with the residual stress

can be achieved by pushing \mathcal{B}_{-1} forward using \mathbf{F}_{r0}^i . Then, the G&R process can follow the growth, remodelling and loading steps ($\mathcal{B}_1 \rightarrow \mathcal{B}_2 \rightarrow \mathcal{B}_3 \rightarrow \mathcal{B}_4$). By setting \mathcal{B}_{-1} as the initial reference, the fictitious total deformation tensor ($\mathbf{F}^{i''}$) for each constituent is

$$\mathbf{F}^{i''} = \mathbf{F}_l^i \mathbf{F}_{er}^i \mathbf{G}^i \mathbf{F}_{r0}^i = \mathbf{F}_e^i \mathbf{G}^i \mathbf{F}_{r0}^i = \mathbf{F} \mathbf{F}_{r0}^i, \quad (6.32)$$

in which \mathbf{F} is total deformation tensor from the compatible configuration \mathcal{B}_1 state to the loaded compatible configuration \mathcal{B}_4 with $\mathbf{F} = \mathbf{F}_l^i \mathbf{F}_{er}^i \mathbf{G}^i$ following the homogenised constrained mixture theory. It is difficult to extract the total elastic deformation tensor from the Eq. (6.32), because both \mathbf{F}_{r0}^i and \mathbf{F}_e^i are general 2nd order tensors though \mathbf{G}^i could be diagonal.

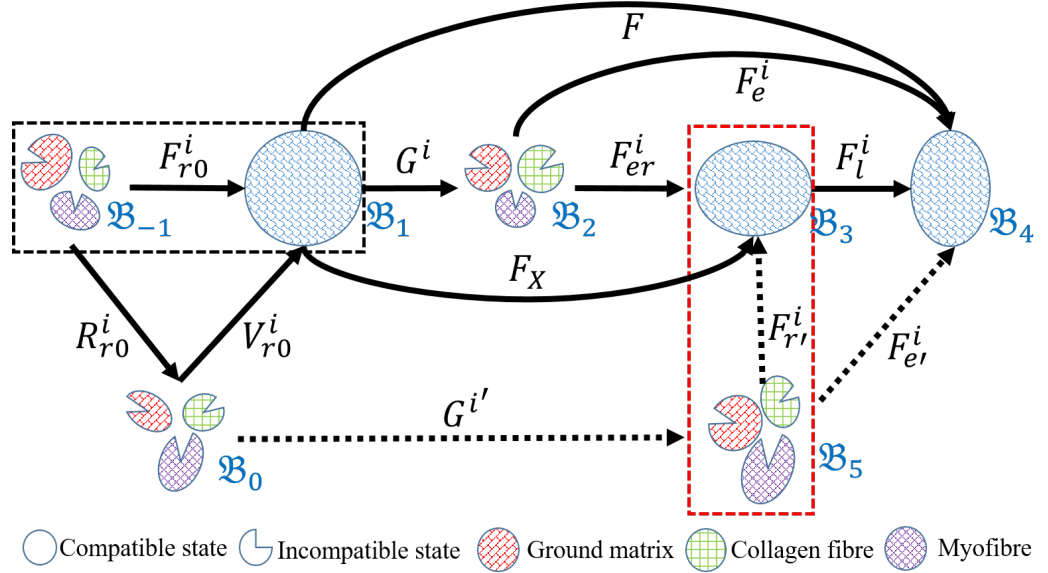


Figure 6.8: Scheme of G&R with residual stress before and after growth. \mathcal{B}_1 is real compatible state with residual stress and grows to incompatible state \mathcal{B}_2 that turns to be compatible \mathcal{B}_3 then is loaded to \mathcal{B}_4 . Fictitious incompatible stress free configurations \mathcal{B}_{-1} , \mathcal{B}_0 and \mathcal{B}_5 are included to depict equivalent fictitious G&R paths. \mathcal{B}_{-1} converts to \mathcal{B}_1 by residual deformation tensor \mathbf{F}_{r0}^i . After polar decomposition of \mathbf{F}_{r0}^i , intermediate \mathcal{B}_0 is from rotation of \mathcal{B}_{-1} then is stretched to \mathcal{B}_1 . Growing from \mathcal{B}_0 by equivalent growth, \mathcal{B}_5 merges into \mathcal{B}_3 by equivalent residual stress or turns to \mathcal{B}_4 by total equivalent elastic deformation.

Applying the polar decomposition, $\mathbf{F}_{r0}^i = \mathbf{V}_{r0}^i \mathbf{R}_{r0}^i$, we can transfer \mathcal{B}_{-1} to \mathcal{B}_1 by a rotation step (\mathbf{R}_{r0}^i) and then a stretch step (\mathbf{V}_{r0}^i) with an intermediate stress-free incompatible configuration \mathcal{B}_0 right after the rotation step. Since pure rotation dose not include elastic deformation, \mathcal{B}_0 also can be the stress-free reference configuration to compute the fictitious total deformation tensor, that is

$$\mathbf{F}^{i'} = \mathbf{F}_l^i \mathbf{F}_{er}^i \mathbf{G}^i \mathbf{V}_{r0}^i = \mathbf{F}_e^i \mathbf{G}^i \mathbf{V}_{r0}^i = \mathbf{F} \mathbf{V}_{r0}^i. \quad (6.33)$$

Even though Eq. (6.33) cannot directly provide the total elastic deformation tensor either, \mathcal{B}_0 and \mathcal{B}_1 share the same material coordinate system because pure stretch dose not change it.

To construct the equivalent fictitious growth, remodelling and loading paths, another ficti-

tious incompatible configuration \mathcal{B}_5 is proposed here and assumed as growing from \mathcal{B}_0 by an equivalent growth tensor \mathbf{G}^i . Hence, from the grown \mathcal{B}_5 state to the compatible state \mathcal{B}_4 is the equivalent fictitious total elastic deformation ($\mathbf{F}_{e'}^i$). Thus, Eq. (6.33) is rewritten as

$$\mathbf{F}^i = \mathbf{F}_{e'}^i \mathbf{G}^i. \quad (6.34)$$

According to Eq. (6.33) and Eq. (6.34), total elastic tensor is

$$\mathbf{F}_{e'}^i = \mathbf{F} \mathbf{V}_{r0}^i (\mathbf{G}^i)^{-1}, \quad (6.35)$$

which can be used for computing the Cauchy stress at \mathcal{B}_4 in Fig. 6.8,

$$\begin{aligned} \sigma_p^g &= J_{\mathbf{F}_{e'}^g}^{-1} a_g \exp[b_g(I_1 - 3)] \mathbf{B}_{e'}^g, \\ \sigma_p^m &= 2J_{\mathbf{F}_{e'}^m}^{-1} a_m (I_{4m}^* - 1) \exp[b_m(I_{4m}^* - 1)^2] (\mathbf{f}_{e'}^m \otimes \mathbf{f}_{e'}^m), \\ \sigma_p^c &= 2J_{\mathbf{F}_{e'}^c}^{-1} a_c (I_{4c}^* - 1) \exp[b_c(I_{4c}^* - 1)^2] (\mathbf{f}_{e'}^c \otimes \mathbf{f}_{e'}^c), \end{aligned} \quad (6.36)$$

where

$$\begin{aligned} \mathbf{B}_{e'}^g &= \mathbf{F}_{e'}^g \mathbf{F}_{e'}^{gT}, & \mathbf{C}_{e'}^g &= \mathbf{F}_{e'}^{gT} \mathbf{F}_{e'}^g, & I_1 &= \text{trace}(\mathbf{C}_{e'}^g), & J_{\mathbf{F}_{e'}^g} &= \det(\mathbf{F}_{e'}^g), \\ \mathbf{C}_{e'}^m &= \mathbf{F}_{e'}^{mT} \mathbf{F}_{e'}^m, & I_{4m} &= \mathbf{f}_0^m \cdot \mathbf{C}_{e'}^m \mathbf{f}_0^m, & \mathbf{f}_{e'}^m &= \mathbf{F}_{e'}^m \mathbf{f}_0^m, & J_{\mathbf{F}_{e'}^m} &= \det(\mathbf{F}_{e'}^m), \\ \mathbf{C}_{e'}^c &= \mathbf{F}_{e'}^{cT} \mathbf{F}_{e'}^c, & I_{4c} &= \mathbf{f}_0^c \cdot \mathbf{C}_{e'}^c \mathbf{f}_0^c, & \mathbf{f}_{e'}^c &= \mathbf{F}_{e'}^c \mathbf{f}_0^c, & J_{\mathbf{F}_{e'}^c} &= \det(\mathbf{F}_{e'}^c), \end{aligned} \quad (6.37)$$

Finally, the total passive stress at the n th growth cycle is

$$\sigma_t^p = \sum_{i=\{g,m,c\}} \phi_n^i \sigma_p^i. \quad (6.38)$$

From grown \mathcal{B}_5 to compatible \mathcal{B}_3 is equivalent fictitious elastic remodelling ($\mathbf{F}_{r'}^i$) that is estimated by

$$\mathbf{F}_{r'}^i = \mathbf{F}_X \mathbf{V}_{r0}^i (\mathbf{G}^i)^{-1}, \quad (6.39)$$

where \mathbf{F}_X is total deformation gradient tensor from \mathcal{B}_1 to \mathcal{B}_3 . In updated reference scheme, \mathcal{B}_{-1} is updated to \mathcal{B}_5 and \mathcal{B}_1 is updated to \mathcal{B}_3 in the next growth cycle, followed by fictitious residual tensor \mathbf{F}_{r0}^i is updated to $\mathbf{F}_{r'}^i$.

At \mathcal{B}_1 in Fig. 6.8, we assume myofibre and collagen share same direction, and \mathbf{f}_1^i , \mathbf{s}_1^i and \mathbf{n}_1^i are orthogonal. In fictitious \mathcal{B}_0 , \mathbf{f}_0^i , \mathbf{s}_0^i and \mathbf{n}_0^i may be not orthogonal because of the residual stretch tensor \mathbf{V}_{r0}^i . Based on fibre direction at \mathcal{B}_0 , we redefine sheet and sheet-normal direction

at \mathcal{B}_0 as following

$$\mathbf{f}_0^i = \frac{\mathbf{V}_{r0}^{i-1} \mathbf{f}_1^i}{|\mathbf{V}_{r0}^{i-1} \mathbf{f}_1^i|}, \quad \mathbf{s}_0^i = \frac{\mathbf{V}_{r0}^{i-1} \mathbf{s}_1^i}{|\mathbf{V}_{r0}^{i-1} \mathbf{s}_1^i|}, \quad \mathbf{n}_0^i = \frac{\mathbf{f}_0^i \times \mathbf{s}_0^i}{|\mathbf{f}_0^i \times \mathbf{s}_0^i|}, \quad \mathbf{s}_0^i = \frac{\mathbf{n}_0^i \times \mathbf{f}_0^i}{|\mathbf{n}_0^i \times \mathbf{f}_0^i|}, \quad (6.40)$$

where \mathbf{f}_0^i , \mathbf{s}_0^i and \mathbf{n}_0^i are the orthogonal fibre, sheet and sheet-normal directions at \mathcal{B}_0 . Then a diagonal growth tensor is defined as

$$\mathbf{G}^{i'} = \vartheta^{f,i'} \mathbf{f}_0^i \otimes \mathbf{f}_0^i + \mathbf{s}_0^i \otimes \mathbf{s}_0^i + \mathbf{n}_0^i \otimes \mathbf{n}_0^i. \quad (6.41)$$

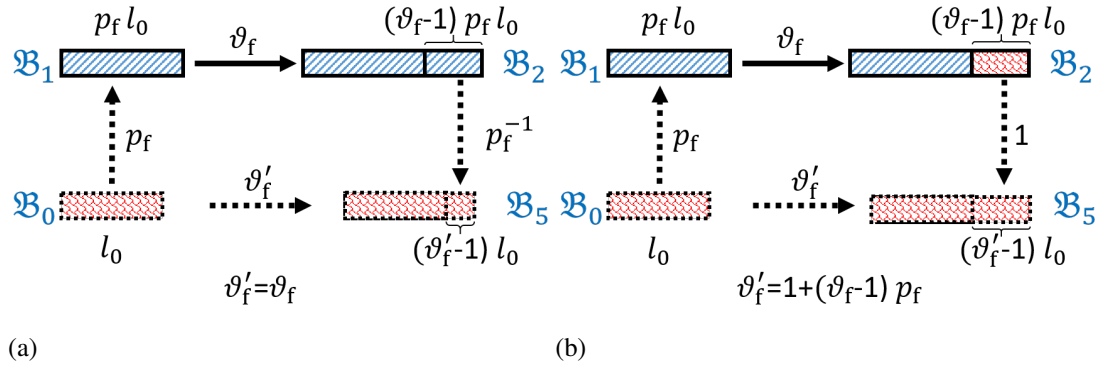


Figure 6.9: Growth increments with (a) and without (b) residual stress. Configurations \mathcal{B}_0 , \mathcal{B}_1 , \mathcal{B}_2 and \mathcal{B}_5 refer from Fig. 6.8. Red squares represent stress-free state whilst residual stress in blue squares. Fibre length in \mathcal{B}_0 is l_0 , stretch ratio from \mathcal{B}_0 to \mathcal{B}_1 is p_f , growth ratio from \mathcal{B}_1 to \mathcal{B}_2 is ϑ_f and fictitious growth ratio from \mathcal{B}_0 to \mathcal{B}_5 is ϑ_f' . When relieving residual stress from \mathcal{B}_2 to \mathcal{B}_5 , growth increment with pre-stretch induced by residual stress in (a) needs to remove the pre-stretch by p_f^{-1} , whilst stress free increment keeps same length in (b).

In this study, we assume that equivalent fictitious growth tensor $\mathbf{G}^{i'}$ is estimated from the growth tensor \mathbf{G}^i defined at the updated reference configuration \mathcal{B}_1 . Under the residual stress, the mechanical properties of the grown increment are uncertain during the growing process, therefore, only two special cases are discussed here: growing with and without the effect of the residual stress. In either case, we assume there are same pure growth increments, after relieving residual stress, along fibre between fictitious \mathcal{B}_0 and real \mathcal{B}_1 even with different fibre directions. For example, as shown in Fig. 6.9 (a), the fibre length in \mathcal{B}_0 is l_0 , the stretch ratio from \mathcal{B}_0 to \mathcal{B}_1 is p_f , the growth ratio from \mathcal{B}_1 to \mathcal{B}_2 is ϑ_f and the fictitious growth ratio from \mathcal{B}_0 to \mathcal{B}_5 is ϑ_f' , thus, the fibre length in \mathcal{B}_1 is $p_f l_0$ and the growth increment is $(\vartheta_f - 1)p_f l_0$. If the growth increment with pre-stretch induced by residual stress, to keep same stress-free increment as that in \mathcal{B}_5 , it needs to drop the pre-stretch by inverse stretch ratio p_f^{-1} ,

$$(\vartheta_f - 1)p_f l_0 p_f^{-1} = (\vartheta_f' - 1)l_0 \Rightarrow \vartheta_f' = \vartheta_f. \quad (6.42)$$

On the other hand, if the growth increment is stress free (Fig. 6.9 (b)), it keeps same length from

\mathcal{B}_2 to stress free \mathcal{B}_5 , thus

$$(\vartheta_f - 1)p_f l_0 = (\vartheta_f' - 1)l_0 \Rightarrow \vartheta_f' = 1 + (\vartheta_f - 1)p_f. \quad (6.43)$$

Therefore, the fictitious equivalent growth ratio under residual stress can be written as

$$\vartheta_f' = \omega \vartheta_f + (1 - \omega)[1 + p_f(\vartheta_f - 1)], \quad \omega \in [0, 1]. \quad (6.44)$$

We used $\omega = 1$ in this section.

6.4.2 Without residual stress before and after growth

Considering cardiac growth cycle is much longer than beat step, we assume the residual stress before and after growth may both be eliminated. As shown in Fig. 6.10, \mathcal{B}_3 is compatible state with the residual stress after G&R from stress-free \mathcal{B}_1 . \mathcal{B}_4 is the replica of \mathcal{B}_3 after relieving the residual stress and further serves as the updated reference configuration for the next growth cycle. Then all constituents share same loading deformation tensor \mathbf{F}_l to \mathcal{B}_5 .

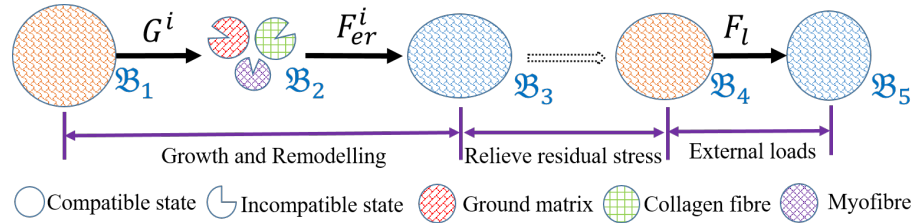


Figure 6.10: Scheme of G&R without residual stress before and after growth. Stress-free \mathcal{B}_1 grows and remodels to \mathcal{B}_3 that turns to \mathcal{B}_4 after dropping residual stress. Then, all constituents share same external loads to \mathcal{B}_5 .

Note the residual stress in \mathcal{B}_3 does not present in the loading step, thus, the total elastic tensor in dynamics is the common \mathbf{F}_l for all constituents. The passive stresses in the loading step are

$$\begin{aligned} \sigma_p^g &= J_{\mathbf{F}_l^g}^{-1} a_g \exp[b_g(I_1 - 3)] \mathbf{B}_l^g, \\ \sigma_p^m &= 2J_{\mathbf{F}_l^m}^{-1} a_m (I_{4m}^* - 1) \exp[b_m(I_{4m}^* - 1)^2] (\mathbf{f}_l^m \otimes \mathbf{f}_l^m), \\ \sigma_p^c &= 2J_{\mathbf{F}_l^c}^{-1} a_c (I_{4c}^* - 1) \exp[b_c(I_{4c}^* - 1)^2] (\mathbf{f}_l^c \otimes \mathbf{f}_l^c), \end{aligned} \quad (6.45)$$

in which

$$\begin{aligned} \mathbf{B}_l^g &= \mathbf{F}_l \mathbf{F}_l^T, & \mathbf{C}_l &= \mathbf{F}_l^T \mathbf{F}_l, & \mathbf{f}_4 &= \mathbf{F}_l \mathbf{f}_4 = \mathbf{f}_4^m \\ I_1 &= \text{trace}(\mathbf{C}_l), & I_4 &= \mathbf{f}_4 \cdot \mathbf{C}_l \mathbf{f}_4, & I_{4m}^* &= \max(I_4, 1) = I_{4c}^*, \\ J_{\mathbf{F}_l^g} &= J_{\mathbf{F}_l^m} = J_{\mathbf{F}_l^c} = \det(\mathbf{F}_l), \end{aligned} \quad (6.46)$$

where \mathbf{f}_4 is myofibre and collagen fibre direction in \mathcal{B}_4 configuration. Total passive stress at n th growth cycle is

$$\sigma_t^p = \sum_{i=\{g,m,c\}} \phi_n^i \sigma_p^i. \quad (6.47)$$

6.4.3 Comparison results

The model maintaining the residual stress takes 17 steps to reach the stable grown state ($\mathcal{R}_{\text{error}} < 1.0\%$) whilst the model relieving the residual stress takes 15 steps. In the grown LV, as shown in Fig. 6.11 (a), myocardium growth also mainly occurs at endocardium, larger total myofibre growth ratio θ^f around inner wall, and epicardium has smaller growth increments. Comparing to the model relieving residual stress, the model maintaining residual stress has smaller θ^f of myofibres whilst achieving bigger LV cavity with smooth ventricular wall.

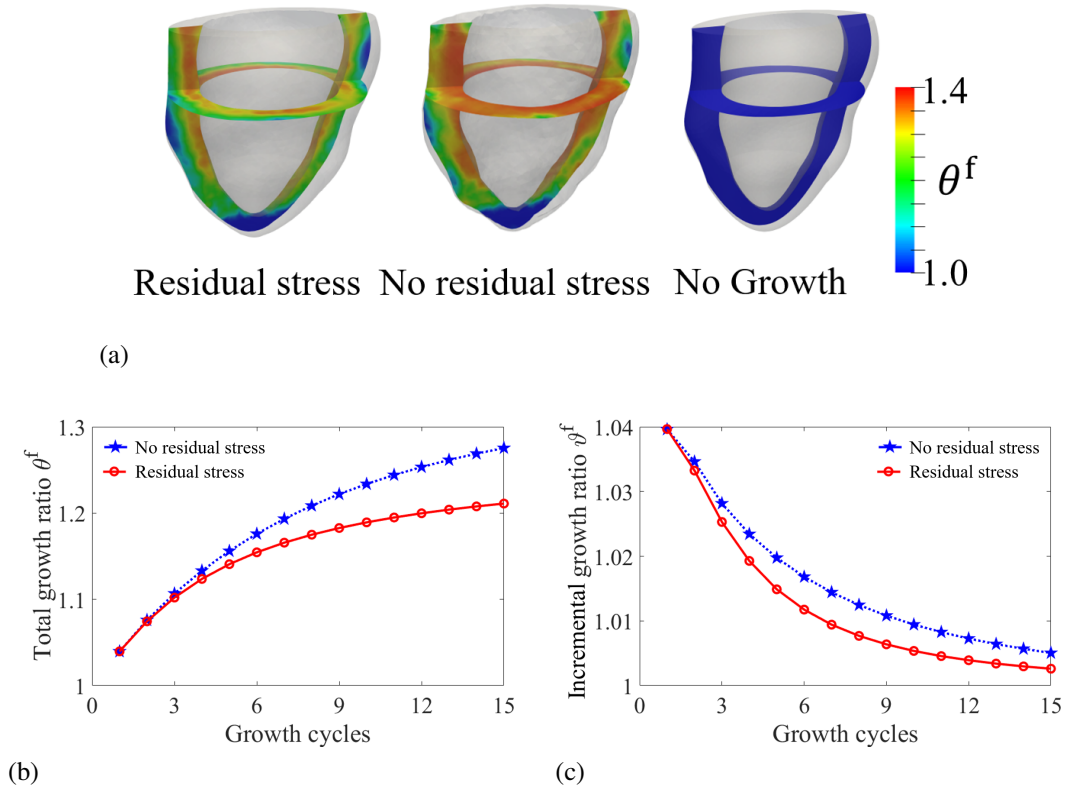


Figure 6.11: (a) grown LV anatomical diagrams and their inside growth ratio distributions in the final growth cycle. With respect to growth cycles, average values of total growth ratio (b) and incremental growth ratio (c) of the whole LV.

The variations of average total growth ratio (θ^f) and the incremental growth ratio (ϑ^f) of myofibres in the whole LV from beginning of growth are respectively depicted in Fig. 6.11 (b) and (c), where both θ^f and ϑ^f of the model with residual stress are smaller at the final growth cycle, such as $\theta^f = 1.211$ vs $\theta^f = 1.275$. In the model with residual stress, the quick decreasing ϑ^f results in a slow increase of θ^f , and two more step to reach fully grown state, indicating the

important role of residual stress in myocardial G&R.

LV wall is equally divided into five layers, and from endocardium to epicardium are denoted by 1 ~ 5. The average values of θ^f and ϑ^f at each layer are shown in Fig. 6.12. Both models present bigger θ^f and ϑ^f near the LV inner wall. Differences of θ^f between different layers are bigger in the model with residual stress (Fig. 6.12 (a)), which gradually become constant with further growth, whilst ϑ^f at each layer approaches to unity with minor difference (Fig. 6.12 (b)). Incremental growth ratios at each layer become same after the ninth growth cycle in the model without residual stress (Fig. 6.12 (d)) whose differences of θ^f at each layer almost keeps constant (Fig. 6.12 (c)).

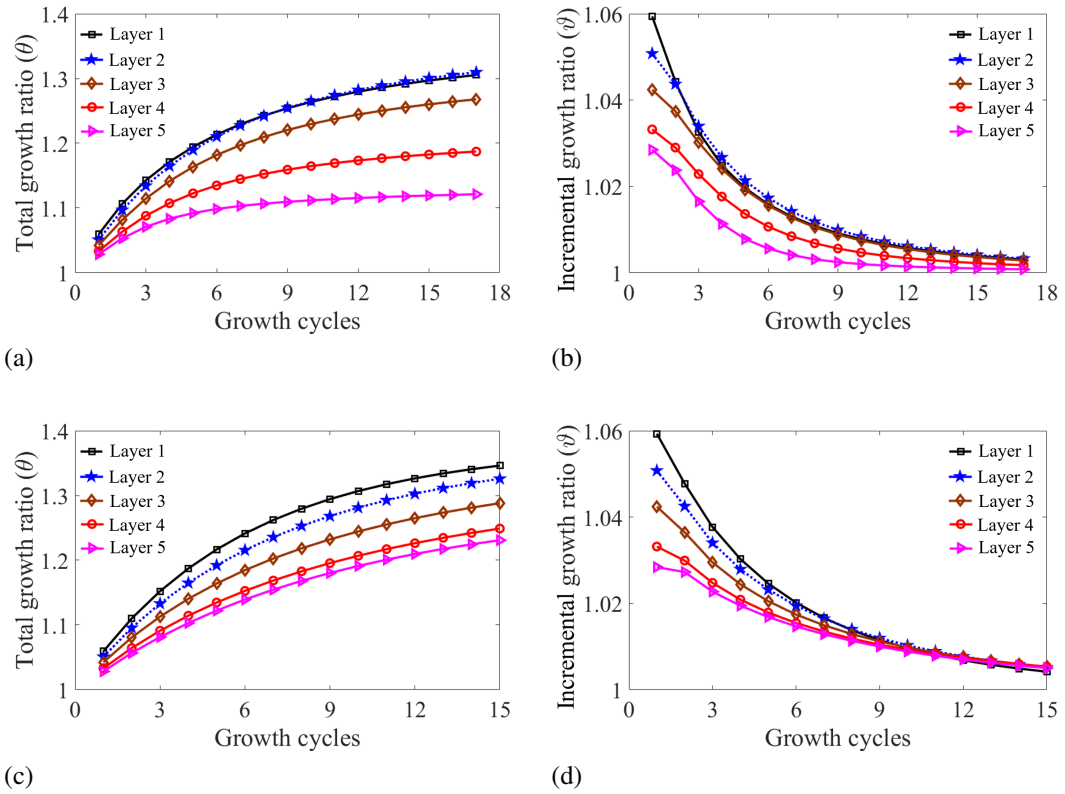


Figure 6.12: With respect to growth cycles n , average total θ^f and incremental ϑ^f growth ratios at each layers from endocardium (layer 1) to epicardium (layer 5) in maintaining residual stress model (a,b) and in relieving residual stress model (c,d).

Overall, the fibre orientation in eccentric growth does not change much and fibres still keep linear rotation along transmural direction. For example in Fig. 6.13 (a), fibres tend to circumferential direction with decreasing angles, around -2.5° at endocardium, in both models. However, epicardial fibres in the model with residual stress almost keeps constant, whilst no residual stress allows epicardial fibres to gradually decrease -7.1° in Fig. 6.13 (b).

Residual stress contributes to the bigger increments of LV cavity volume under both stress-free (Fig. 6.14 (a)) and loaded (Fig. 6.14 (b)) conditions. For example, it has the biggest unloaded LV cavity volume growth, from 50.2 ml to 71.4 ml, while the model with relieved residual

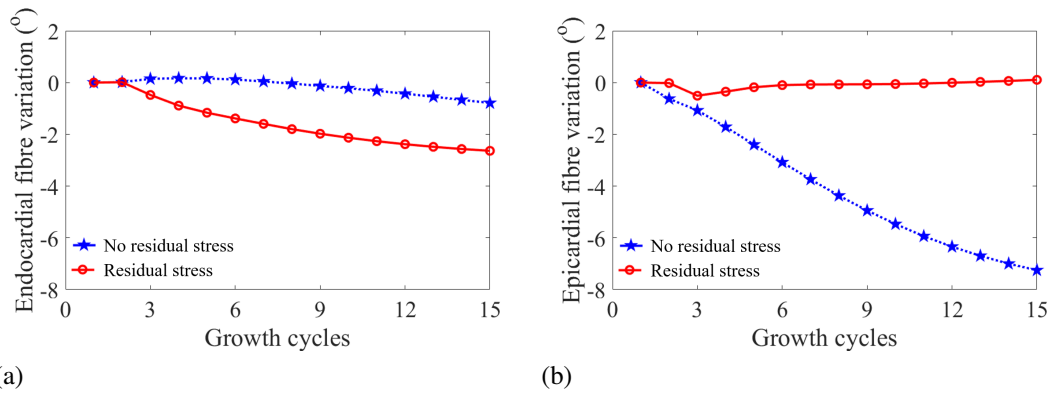


Figure 6.13: Mean fibre angles variations around endocardium (a) and epicardium (b).

stress only increases to 63.2 ml. LV cavity with normal EDP (8 mmHg) is 88.7 ml. Then, under constant EDP 16 mmHg, the EDV gradually grows from 103.1 ml to 168.8 ml, about 63.7% increase, when maintaining residual stress in model, much bigger than that in the no residuals stress model (30% increase). Additionally, after reaching the stable grown state, larger enlargement of volume (97.4 ml) from unloading to loading (16 mmHg) occurs in the model with residual stress, reflecting its softer myocardium.

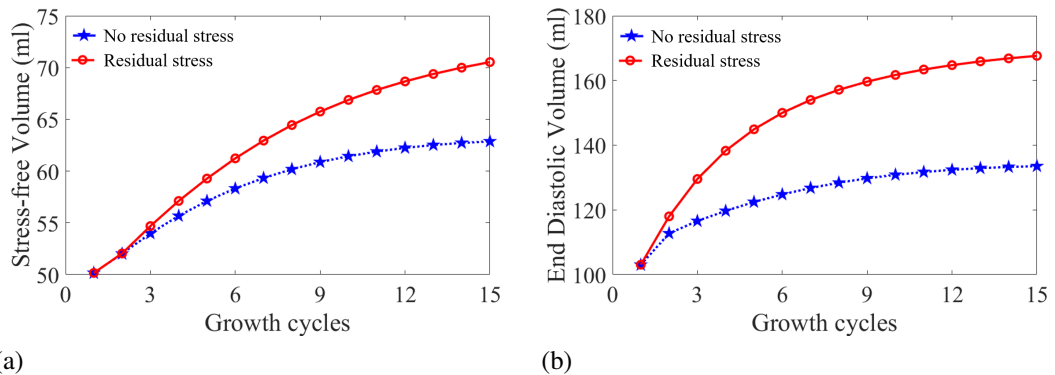


Figure 6.14: With respect to growth cycle, (a) unloaded LV volumes and (b) loaded LV volumes with EDP (16 mmHg).

Residual stress after G&R in the final growth cycle is shown in Fig. 6.15 (a). Note that the state before relieving residual stress in the model without residual stress, i.e. \mathcal{B}_3 in Fig. 6.10, is compared here. Maintaining residual stress model exhibits negative fibre stress around endocardium and positive stress around epicardium, whilst there is no significant differences in the no residual stress model whose values are around zero. This may be the reason why the cross-sectional rings in residual stress model is more like a circle (the left in Fig. 6.15 (a)) while the another is like a square (the right in Fig. 6.15 (a)). Similar results can be found in Fig. 6.15 (b) that describes transmural mean fibre stress (S_{11}) at each layer from endocardium (0%) to epicardium (100%). The S_{11} line of the non-residual stress model is around zero, whilst S_{11} of the

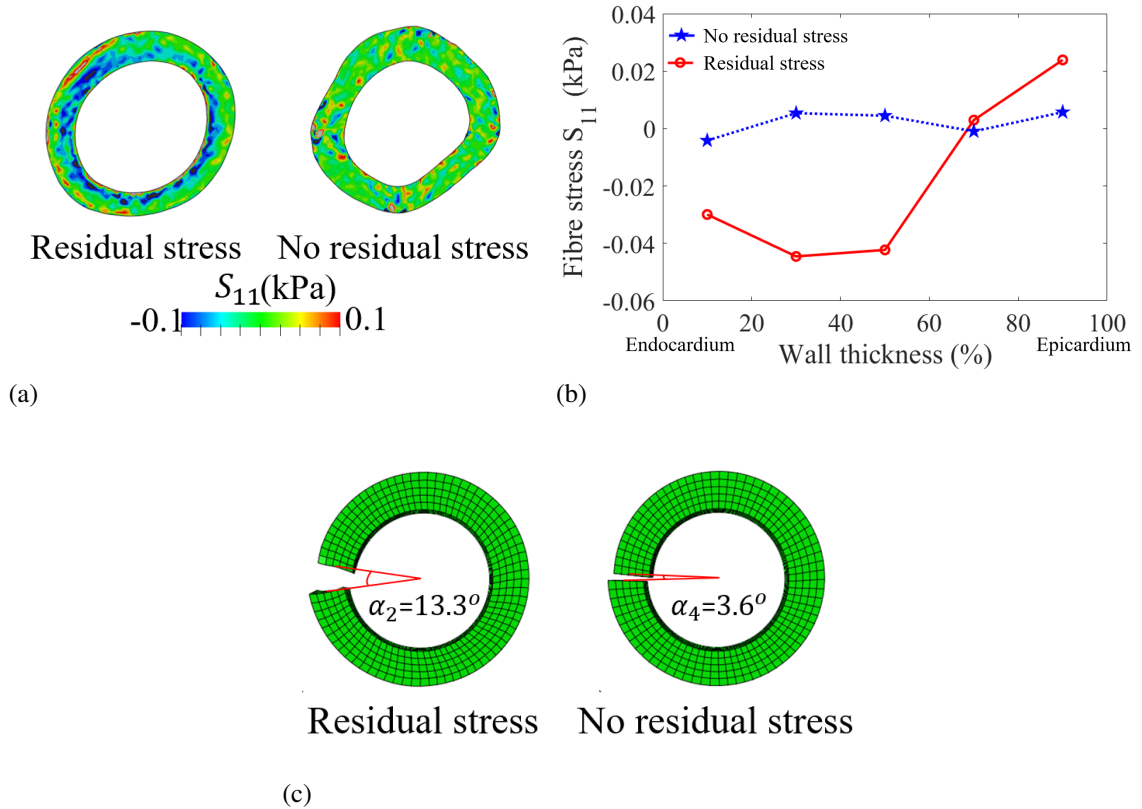


Figure 6.15: Residual stress is estimated at compatible geometry after growth in the final growth cycle. (a) Distribution of fibre stress component along fibre S_{11} at medium of LV, (b) mean transmurals stress along wall thickness, and (c) open angle under mean residual stress in the ring model.

residual stress model varies from negative (-0.0445 kPa) to positive (0.0294 kPa). After mapping residual stress from Fig. 6.15 (a) to a simple ring model, the final open angles are listed in Fig. 6.15 (c), in which the residual stress model achieves a larger opening angle (13.3°), closed to experimental data $13 \pm 5.3^\circ$ [223] with a comparison to the no residual stress model (3.6°).

6.4.4 Discussion

Residual stress is generated by converting incompatible grown constituents into a compatible state, i.e. the elastic remodelling process, and exhibits significant importance in G&R. Including residual stress at the beginning of growth makes the updated reference framework more complicated as discussed in section 6.4.1, where fictitious equivalent G&R path is developed to adapt to the numerical computations in the explicit FE solver. The updated reference in FE is still the compatible configuration after G&R, however, it is transformed from a fictitious incompatible stress-free reference by a residual deformation tensor in numerical computations of the stress response. In addition, relieving residual stress after stable G&R is also considered in section 6.4.2, which results in almost no difference from the cases with residual stress after sta-

ble G&R (section 6.3.3), indicating residual stress is much smaller than the stress responses in cardiac step. A bigger LV cavity is achieved with a smaller growth ratio when remaining residual stress accumulated by previous growth cycles, which might contribute to the remodelling process towards enlarging the cavity and preventing ventricular wall thickening, as compared in Fig. 6.11 (a).

Residual stress is generally assumed to lead the opening angles of a grown tissue, such as LV or aorta, after a radial cutting, which has been used as a common approach to check a G&R model [225]. Opening angle induced by residual stress in the heart model was achieved in [223], which agreed well with experimental measurements. We only intend to show the residual stress can cause a normal opening angle of the LV myocardium ring in our work. Therefore, for convenient operation, the mean residual stress of the entire heart model from endocardium to epicardium is mapped into the layered ring model to predict the opening angles. The simple ring model shares the same material properties and fibre structure as LV, and the opening angle is determined by the distribution of residual stress. For instance, residual stress component along with fibre orientation (σ_{11}) that changes from negative values around endocardium to positive values around epicardium will cause the ring model to splay outward. In contrast, the opposite distribution results in collapsing inward. Moreover, the larger residual σ_{11} corresponds to more numerous opening angles. Eccentric growth with residual stress achieves opening angles similar to experimental data (around 13° [223]).

6.5 Effects of different G&R properties of constituents on eccentric and concentric growths

6.5.1 Methods in eccentric and concentric G&R

The volume fractions of the three constituents will be updated as growing when they have different growth rates. In eccentric growth, the growth tensor of myofibres is

$$\mathbf{G}^m = \vartheta^{f,m} \mathbf{f}_1^m \otimes \mathbf{f}_1^m + \mathbf{s}_1^m \otimes \mathbf{s}_1^m + \mathbf{n}_1^m \otimes \mathbf{n}_1^m, \quad (6.48)$$

where $\vartheta^{f,m}$ is the growth ratio along myofibre. In contrast, for concentric growth, the growth tensor becomes

$$\mathbf{G}^m = \mathbf{f}_1^m \otimes \mathbf{f}_1^m + \vartheta^{s,m} \mathbf{s}_1^m \otimes \mathbf{s}_1^m + \mathbf{n}_1^m \otimes \mathbf{n}_1^m, \quad (6.49)$$

where $\vartheta^{s,m}$ is the growth ratio for the cross-myofibre. We still assume no inelastic remodelling, thus, the total elastic tensor for myofibre is $\mathbf{F}_e^m = \mathbf{F}(\mathbf{G}^m)^{-1}$.

Given that myofibre is the main growing component in myocardium [141], we assume that

the ground matrix dose not grow and presents inelastic properties to elongate the same amounts as grown myofibres with growth tensor $\mathbf{G}^g = \mathbf{I}$, and the inelastic remodelling is computed based on $\vartheta^{f,m}$ or $\vartheta^{s,m}$,

$$\mathbf{F}_{ir}^g = \begin{cases} \vartheta^{f,m} \mathbf{f}_1^g \otimes \mathbf{f}_1^g + \frac{1}{\sqrt{\vartheta^{f,m}}} \mathbf{s}_1^g \otimes \mathbf{s}_1^g + \frac{1}{\sqrt{\vartheta^{f,m}}} \mathbf{n}_1^g \otimes \mathbf{n}_1^g & \text{eccentric growth} \\ \frac{1}{\sqrt{\vartheta^{s,m}}} \mathbf{f}_1^g \otimes \mathbf{f}_1^g + \vartheta^{s,m} \mathbf{s}_1^g \otimes \mathbf{s}_1^g + \frac{1}{\sqrt{\vartheta^{s,m}}} \mathbf{n}_1^g \otimes \mathbf{n}_1^g & \text{concentric growth} \end{cases} \quad (6.50)$$

where $\det(\mathbf{F}_{ir}^g) = 1$ to ensure no growth in the ground matrix. The total elastic tensor turns to be $\mathbf{F}_e^g = \mathbf{F}(\mathbf{F}_{ir}^g)^{-1}$.

In terms of G&R of collagen fibre, three assumptions are proposed as following:

1. It does not grow ($\mathbf{G}^c = \mathbf{I}$), and its inelastic deformation remodels itself to have same length as grown myofibre. Similar for the ground matrix, the inelastic remodelling tensor is

$$\mathbf{F}_{ir}^c = \begin{cases} \vartheta^{f,m} \mathbf{f}_1^c \otimes \mathbf{f}_1^c + \frac{1}{\sqrt{\vartheta^{f,m}}} \mathbf{s}_1^c \otimes \mathbf{s}_1^c + \frac{1}{\sqrt{\vartheta^{f,m}}} \mathbf{n}_1^c \otimes \mathbf{n}_1^c & \text{eccentric growth} \\ \frac{1}{\sqrt{\vartheta^{s,m}}} \mathbf{f}_1^c \otimes \mathbf{f}_1^c + \vartheta^{s,m} \mathbf{s}_1^c \otimes \mathbf{s}_1^c + \frac{1}{\sqrt{\vartheta^{s,m}}} \mathbf{n}_1^c \otimes \mathbf{n}_1^c & \text{concentric growth} \end{cases} \quad (6.51)$$

and the total elastic tensor is $\mathbf{F}_e^c = \mathbf{F}(\mathbf{F}_{ir}^c)^{-1}$.

2. It does not grow ($\mathbf{G}^c = \mathbf{I}$), and subsequent an elastic deformation remodels itself to have the same length as grown myofibre. Assuming no inelastic remodelling ($\mathbf{F}_{ir}^c = \mathbf{I}$), then the total elastic tensor is $\mathbf{F}_e^c = \mathbf{F}$.
3. It grows simultaneously with myofibre with the same growth ratio, thus the growth tensor is

$$\mathbf{G}^c = \begin{cases} \vartheta^{f,m} \mathbf{f}_1^c \otimes \mathbf{f}_1^c + \mathbf{s}_1^c \otimes \mathbf{s}_1^c + \mathbf{n}_1^c \otimes \mathbf{n}_1^c, & \text{eccentric growth} \\ \mathbf{f}_1^c \otimes \mathbf{f}_1^c + \vartheta^{s,m} \mathbf{s}_1^c \otimes \mathbf{s}_1^c + \mathbf{n}_1^c \otimes \mathbf{n}_1^c, & \text{concentric growth} \end{cases} \quad (6.52)$$

Considering no inelastic remodelling ($\mathbf{F}_{ir}^c = \mathbf{I}$), the total elastic tensor is $\mathbf{F}_e^c = \mathbf{F}(\mathbf{G}^c)^{-1}$.

According to the results in section 6.4, including residual stress before and after growth can achieve more physiological eccentric growth, such as the bigger growing LV cavity and the bigger opening angle as reported in the experimental observation [223]. Therefore, the LV model with residual stress is employed to study the effects of collagen fibre with different G&R properties during the eccentric and concentric growth.

6.5.2 Eccentric growth results

Three hypothesised growth laws for collagen fibre properties exhibit different G&R patterns on eccentric growth. We denote the non-growth collagen fibre with inelastic (plastic) remodelling as CF-NG-PR and with elastic remodelling as CF-NG-ER, and the case with collagen fibre sharing the same growth as myofibre as CF-GAM. Note that θ^f and ϑ^f denote the total

and incremental growth ratios of myofibre, respectively. Fig. 6.16 (a) compares these grown geometries of LV in the final growth cycle. Common characteristics for all three cases are larger growth ratios around the inner wall than the outer wall, the most growth at the midsection and the least at apex. CF-NG-PR and CF-GAM cases both have bigger LV cavity and thinner wall than CF-NG-ER. Consistently, CF-NG-PR has biggest average total growth ratio value ($\theta^f = 1.24$), similar to that in CF-GAM ($\theta^f = 1.22$), and larger than that in CF-NG-ER ($\vartheta^f = 1.08$). Same results are also shown in Fig. 6.16 (b) where CF-NG-ER case has much smaller θ^f than CF-NG-PR and CF-GAM cases. In fact, CF-NG-ER case only takes 6 step to reach stability, however, we plot its results of 15 steps for the comparison here. Their corresponding incremental growth ratios in each growth cycle are shown in Fig. 6.16 (c), in which ϑ^f from the CF-NG-ER case drops more quickly to one than those of CF-NG-PR and CF-GAM cases.

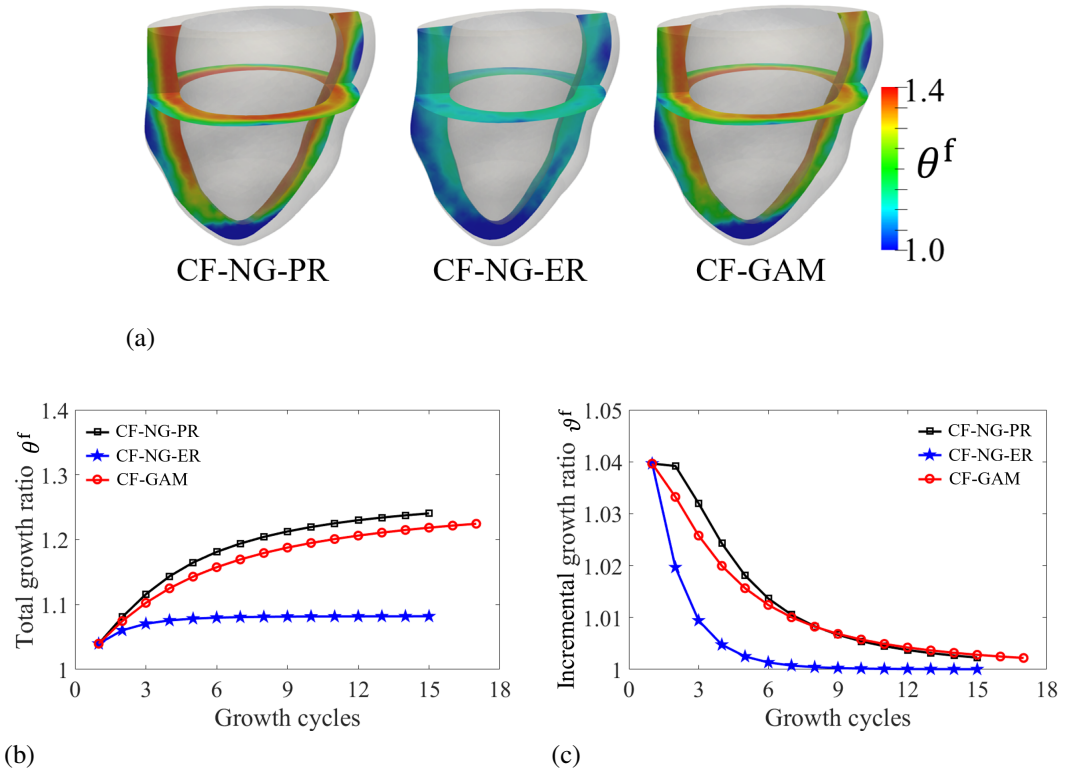


Figure 6.16: Growth of myofibre in eccentric growth. (a) Growth ratio distribution in the final grown heart models. With respect to growth cycle, (b) mean total growth ratio and (c) mean incremental growth ratio.

The average total and incremental growth ratios in each layer are listed in Fig. 6.17, which also demonstrates that the inner layer has bigger growth ratio values than outer layers. ϑ^f in all layers drops to one quickly in CF-NG-ER case while θ^f stay constant across the wall. θ^f in layer 1 and layer 2 are always overlapped in the rest two cases, whilst ϑ^f in layer 1 to layer 3 are same after the 6th step. Overall, the differences of θ^f and ϑ^f between layers are more significant in CF-NG-PR case than the others.

Due to no growth in the ground matrix and different assumptions for collagen fibre, volume

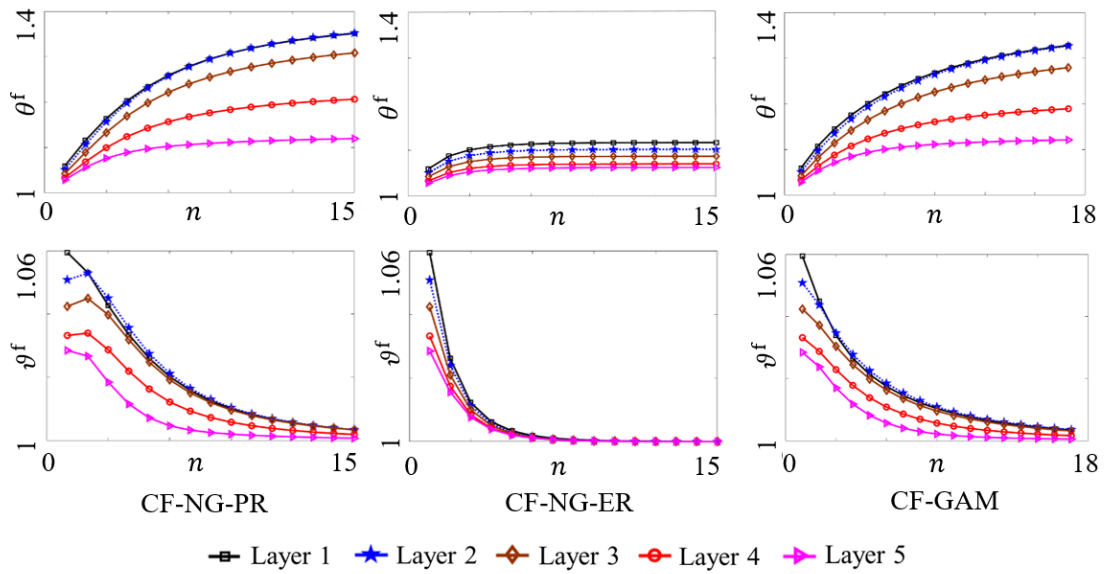


Figure 6.17: In eccentric growth, average total (top) and incremental (bottom) growth ratios of myofibre at each layers from endocardium to epicardium with respect to growth cycle (n).

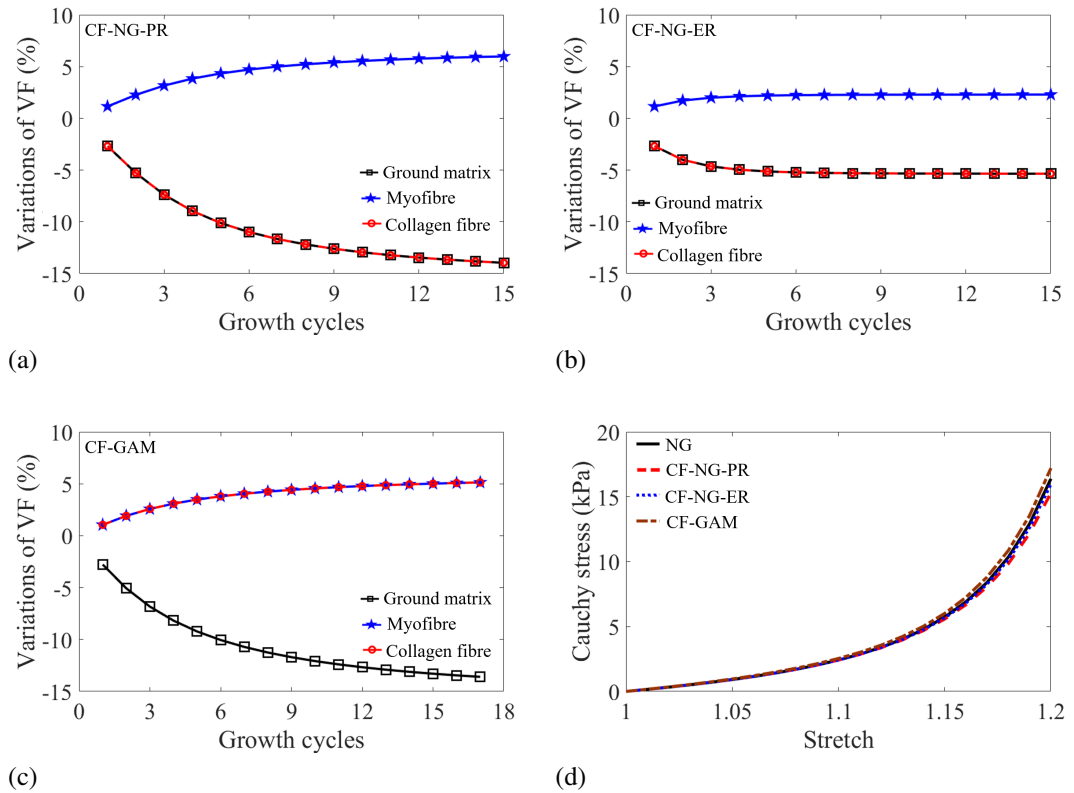


Figure 6.18: In eccentric growth, variations of volume fractions of constituents in CF-NG-PR case (a), in CF-NG-ER case (b), and in CF-GAM case (c). Using volume fractions (VF) in the final growth cycle, uniaxial tension test provides stress-stretch lines for each case comparing to no growth (NG) case.

fraction (VF) of each constituent is updated with growth. Their respective relative variations are shown in Fig. 6.18 (a) for CF-NG-PR case, Fig. 6.18 (b) for CF-NG-ER case, and Fig. 6.18 (c) for CF-GAM case. In CF-NG-PR case, ϕ^m increases by 5.98%, to 0.7419, whilst ϕ^s and ϕ^c both decrease by 13.95%, to respective 0.2358 and 0.0224. In contrast, elastic collagen fibre remodelling reduces growth of myofibre with less increment (2.29%). When myofibre and collagen fibre share the same growth ratios, both ϕ^c and ϕ^m increase by 5.13% and ϕ^s decrease to 0.2368. Variations of ϕ^s , ϕ^m and ϕ^c changes mechanical response as shown in Fig. 6.18 (d), in which volume fractions are from the final growth cycle and are used in uni-axial tension test of a unit element with the same materials properties as the LV model. Although the differences between stress-stretch curves are small with stretch from 1.0 to 1.2, CF-GAM case has highest stiffness and CF-NG-PR case present the softest property, followed by the softer CF-NG-ER case than the no growth (NG) case.

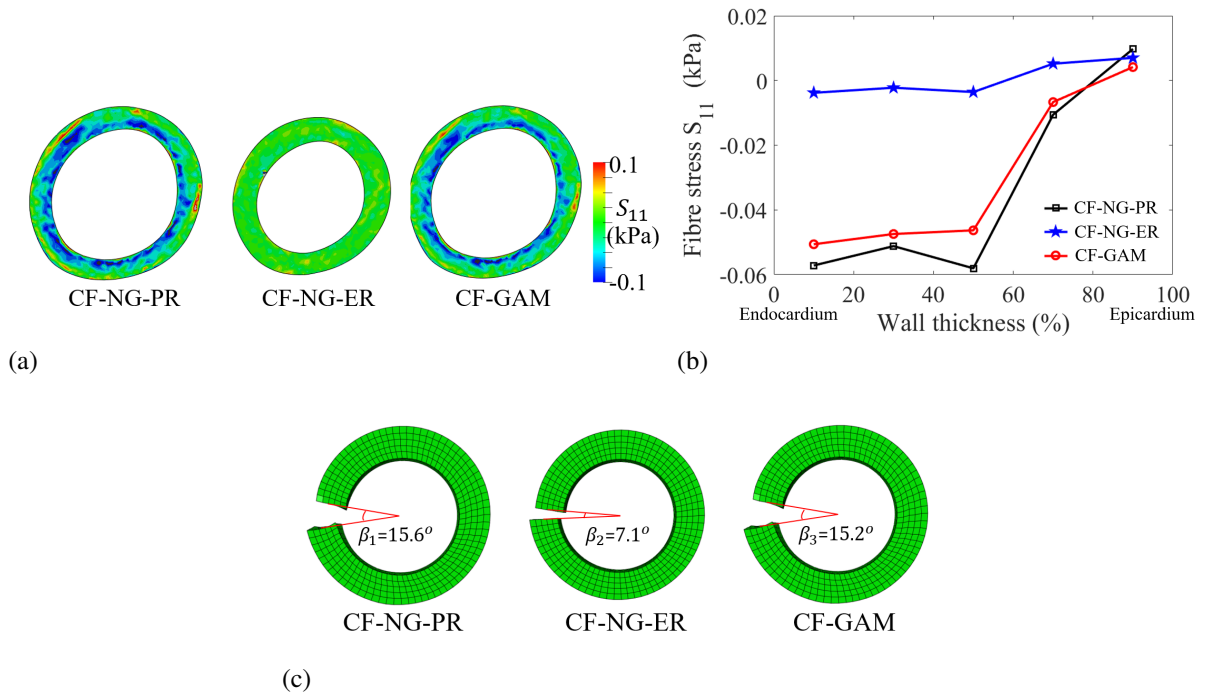


Figure 6.19: In eccentric growth, residuals stress is estimated at compatible geometry after growth in the final growth cycle. For three cases, (a) cross-sectional view of fibre stress component along fibre S_{11} distribution at the medium of LV, (b) mean transmural stress along wall thickness, and (c) opening angle under mean residual stress in the ring model.

The residual stress after growth in the final growth cycle are depicted in Fig. 6.19 (a), where these cross-sectional views are from the midsection of LV. CF-NG-PR and CF-GAM case have similar S_{11} (stress component along fibre) distribution, from negative inner value to positive outer value, whilst CF-NG-ER case almost dose not have difference with values around zero. Average S_{11} at each layer in Fig. 6.19 (b) provides similar results, and CF-NG-PR case has the biggest negative value (-0.058 kPa) at layer 3 and changes to positive value at layer 5 (0.0097

kPa). After mapping average residual stress of each layer to the simple ring model, the opening angles are shown in Fig. 6.19 (c), where CF-NG-PR case has the biggest value (15.6°), very close to 15.2° in CF-GAM case and much bigger than 7.1° in CF-NG-ER case.

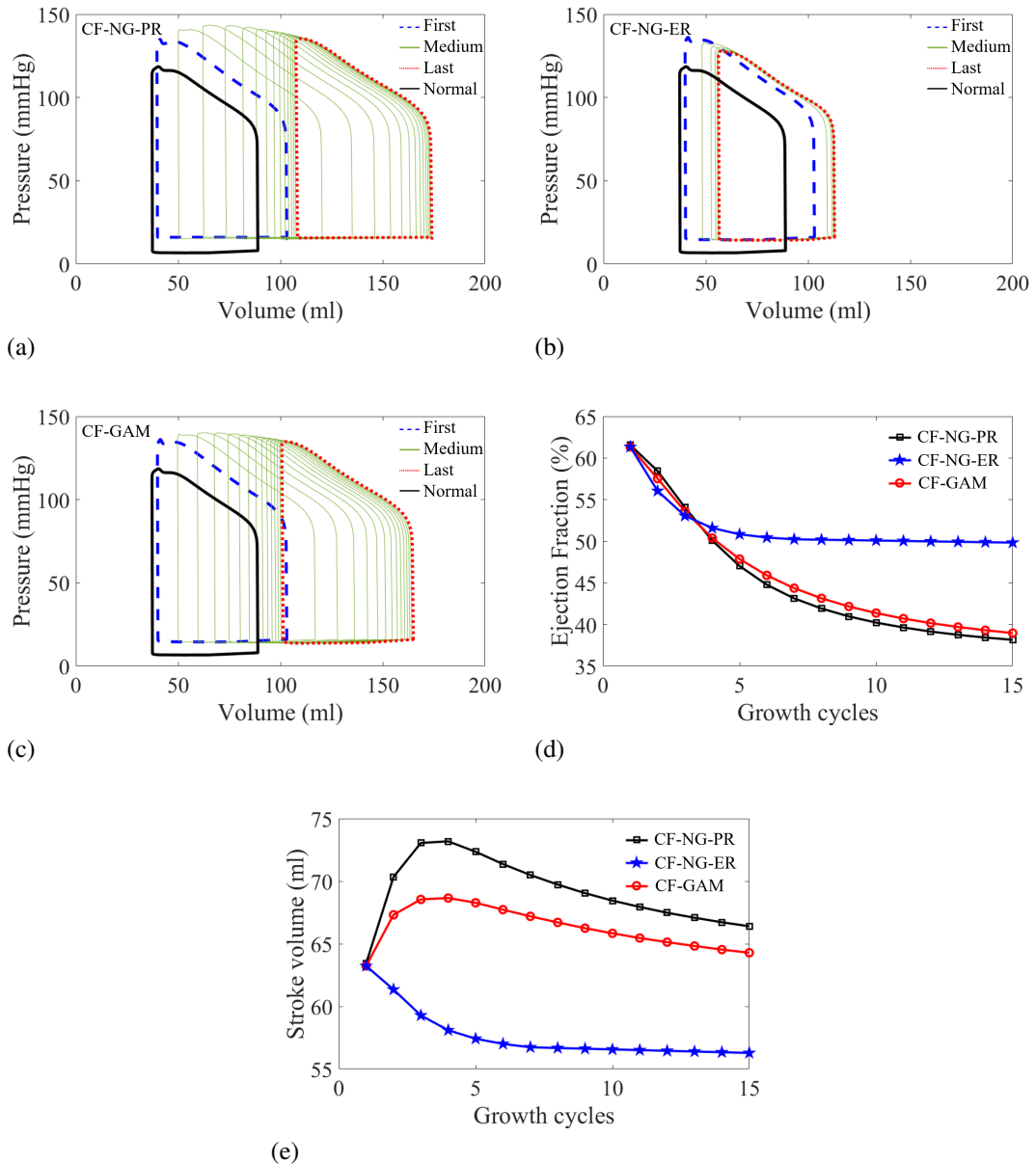


Figure 6.20: In eccentric growth, with respect to growth cycles, PV loops in (a) CF-NG-PR, (b) CF-NG-ER and (c) CF-GAM cases. Black solid line is the normal case with EDP 8 mmHg, blue dash line is the first loading step after applying volume overload with EDP 16 mmHg, red dot line is the ending of growth, and grass thin lines are medium growth cycles. Their corresponding EFs are in (d) and SVs in (e).

PV loops of three cases are shown in Fig. 6.20 (a-c) where they share the identical normal PV loop and the fist PV loop after pathological volume overload. With growing, the PV loop gradually shifts to the right, with pressure dropping in CF-NG-ER case whilst almost no change

in the other two cases. Inelastic collagen fibre without growth allows LV to grow more efficient with bigger unload cavity volume, 74.8 ml at the final step, closer to CF-GAM case (73.1 ml) while much bigger than 52.3 ml of CF-NG-ER case. EDV under constant 16 mmHg also reaches to the biggest in CF-NG-PR case with 174.0 ml, about 68.7% increase relative to beginning of growth (103.1ml), followed by 61.1% in CF-GAM case, whilst CF-NG-ER case only increases by 8.1%. Comparing EFs in normal case (58.17%), three cases' EFs (Fig. 6.20 (d)) experience a leap to 61.33% with bigger EDV, then EFs decline to 38.96% in CF-GAM case, 38.15% in CF-NG-PR case and 49.83% in CF-NG-ER case, respectively. In CF-NG-PR case, SV firstly increases to 73.2 ml at the fifth cycle from the initial 63.2 ml after overload, then gradually decreases to final 66.4 ml. Same situation occurs in CF-GAM case with a maximum SV value 68.6 ml and a final SV value of 64.3 ml. SV values have been decreasing to 56.3 ml in the CF-NG-ER case.

6.5.3 Concentric growth results

Concentric growth under three assumptions of collagen fibre properties has also been studied in this section. Similar as eccentric growth, the growth mainly occurs at endocardium with larger total growth ratio values (θ^s) of myofibres as shown in Fig. 6.21 (a). Overall, larger values of θ^s locate at midsection of LV whilst almost no growth around the apex. LV cavities all are all reduced with thicken ventricular wall, from the normal 8.7 mm to 11.8 mm for the CF-NG-PR case, to 11.6 mm for the CF-NG-ER case and to 11.5 mm for the CF-GAM case, respectively, whilst epicardial surfaces almost do not change. The mean values of θ^s of the whole LV at the final cycle are shown in Fig. 6.21 (b) where CF-NG-ER case has the largest value of 1.39, followed by $\theta^s = 1.37$ in CF-GAM case and $\theta^s = 1.34$ in CF-NG-PR case after reaching the stable grown state. While their incremental growth ratio (ϑ^s) values are very close (Fig. 6.21 (c)). Nevertheless, detailed variations of the average total and incremental growth ratios at different layers from endocardium to epicardium in Fig. 6.21 (d) also suggest three cases have very similar growth. Increments of θ^s or ϑ^s at the inner three layers (1-3) are about twice of these in the outer layers (4 and 5).

In concentric growth, Fig. 6.22 (a-c) demonstrate that volume fractions of myofibre always increase by around 8% whilst that of the ground matrix decrease by about 19% for all three case after achieving the stable grown state. Comparing to the no growth case, only in CF-GAM case, myocardium becomes stiffer while softer in the rest two case, as shown in Fig. 6.22 (d).

The residual stress at stable grown state is depicted in Fig. 6.23 (a). Three cases have similar S_{11} distributions and much smaller cross-sectional areas than eccentric growth (Fig. 6.19 (a)). Moreover, much larger negative inner values and positive outer values than eccentric growth (Fig. 6.19 (b)) are shown in Fig. 6.23 (b), where average S_{11} at each layer varies from -0.6 kPa at endocardium to 1 kPa in CF-NG-ER and CF-GAM cases and from -0.7 kPa to 1.4 kPa in CF-NG-PR case. After mapping the average residual stress of each layer to the simple ring

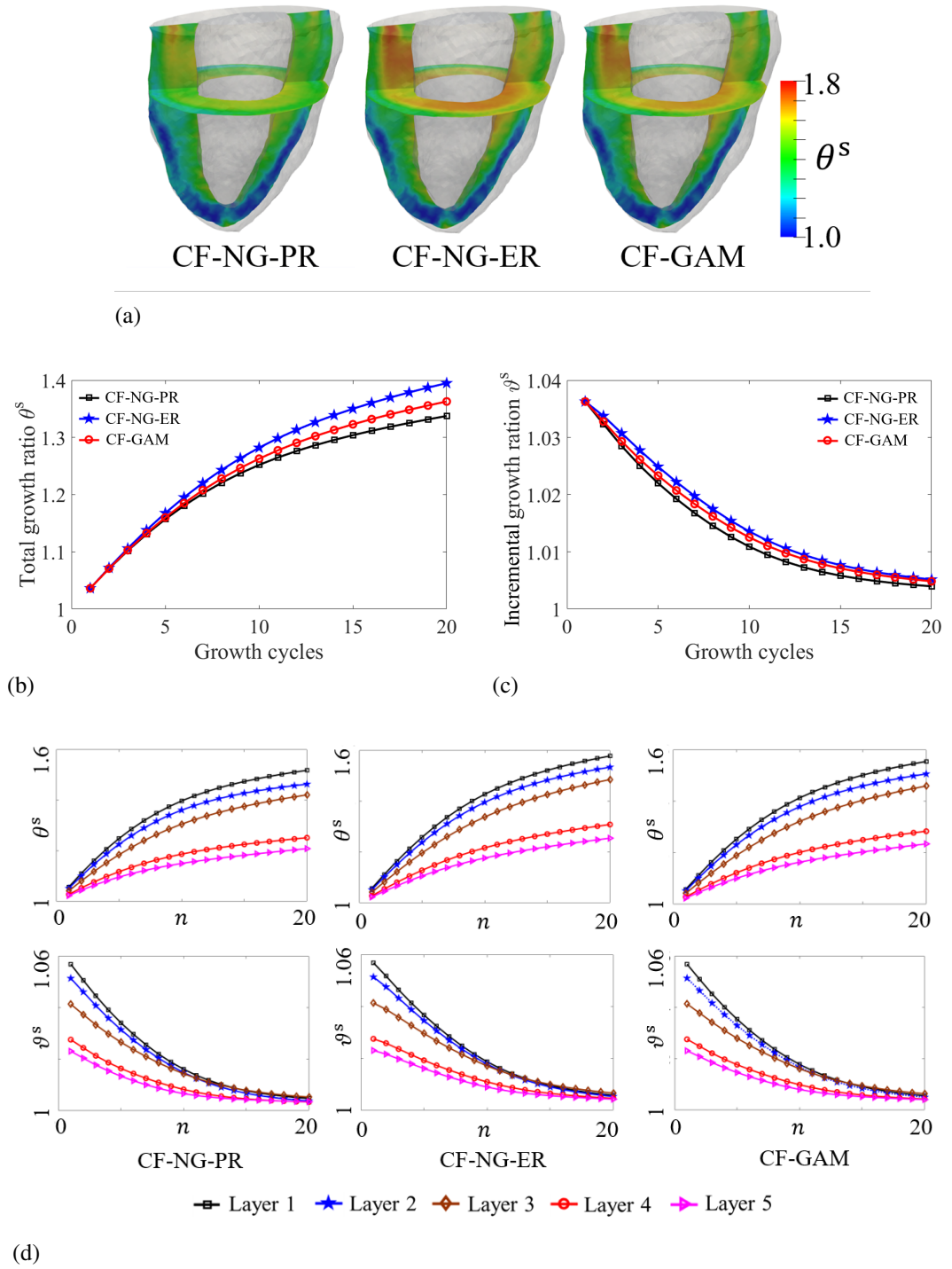


Figure 6.21: In concentric growth, for three types of G&R of collagen fibre, (a) growth ratio distributions in the final grown heart models. With respect to growth cycles, (b) mean total growth ratio and (c) mean incremental growth ratio. (d) Average total (top) and incremental (bottom) growth ratios at each layers from endocardium to epicardium with respect to growth cycles (n).

model, the opening angles are shown in Fig. 6.23 (c). All cases exhibit excessive opening angles over 100° , which may be associated with the much larger residual stress value of S_{11} . CF-NG-

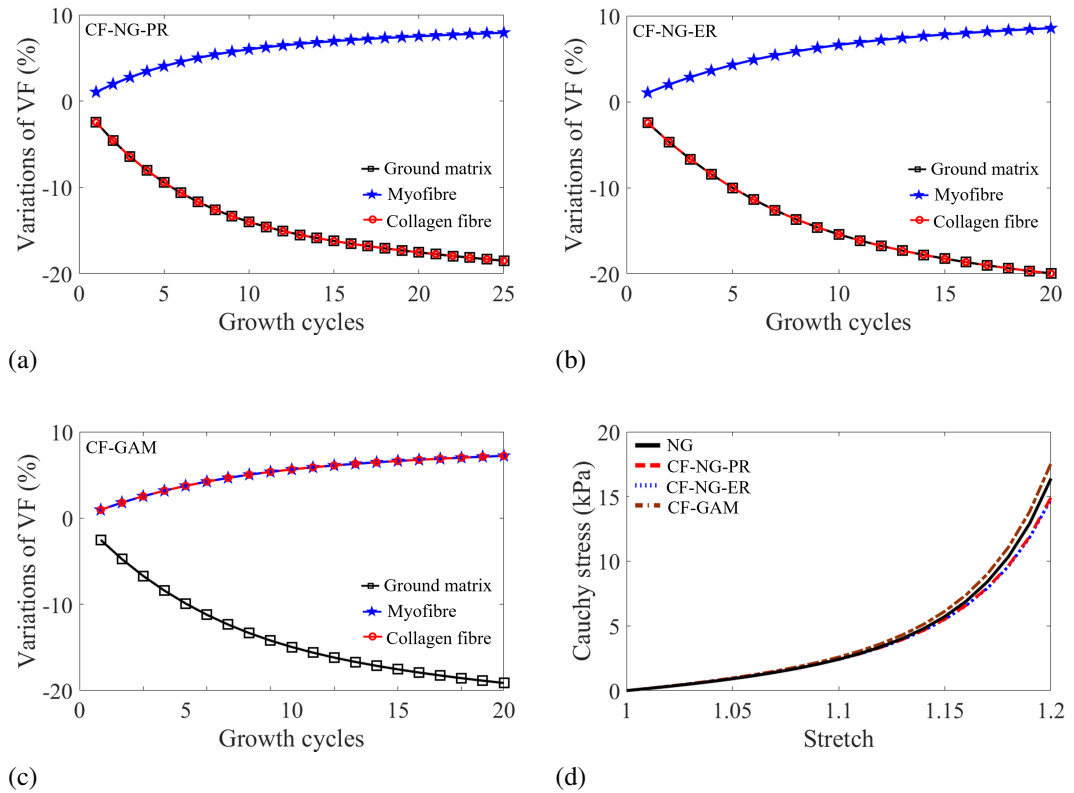


Figure 6.22: In concentric growth, variations of volume fractions of constituents in CF-NG-PR case (a), in CF-NG-ER case (b), and in CF-GAM case (c). Using volume fractions (VF) in the final growth cycle, uniaxial tension test provides stress-stretch lines for each case comparing to no growth (NG) case.

PR case has the biggest value (118.9°), followed by 115.9° in CF-NG-ER case and 116.0° in CF-GAM case.

Comparing to normal case, pressure overload induced by aortic stenosis reduces the pump function with increased peak systolic LV pressure. There are similar variations of PV loops for three cases, shifting toward left with smaller EDV and ESV, as shown in Fig. 6.24 (a-c). The largest ESP (248 mmHg) is in CF-NG-ER case, which also has biggest PV loop area at stable grown state. With growing, EDV values decrease from 88.7 ml to 38.7 ml in CF-NG-PR case, to 44.4 ml in CF-NG-ER case and to 42.2 ml in CF-GAM case, whilst all ESVs are around 20 ml. EFs of the three cases are always smaller than the EF in the normal case (58.17%). In Fig. 6.24 (d), the minimum EF (38.18%) occurs in the first loading step after the pathological pressure overload, and EF gradually increases to peak values, such as 56.82% in CF-NG-ER case or 51.21% in CF-NG-PR case, then decrease slowly. Compared to the SV in the first loading step after the pathological pressure overload, there are only minor increments of SV, such as about 4.8 ml in CF-NG-ER case at the fifth loading step, and then gradually decrease (Fig. 6.24 (e)). For each case, although the EF remains around 50% during growth, the SV is much less than normal case (51.7 ml).

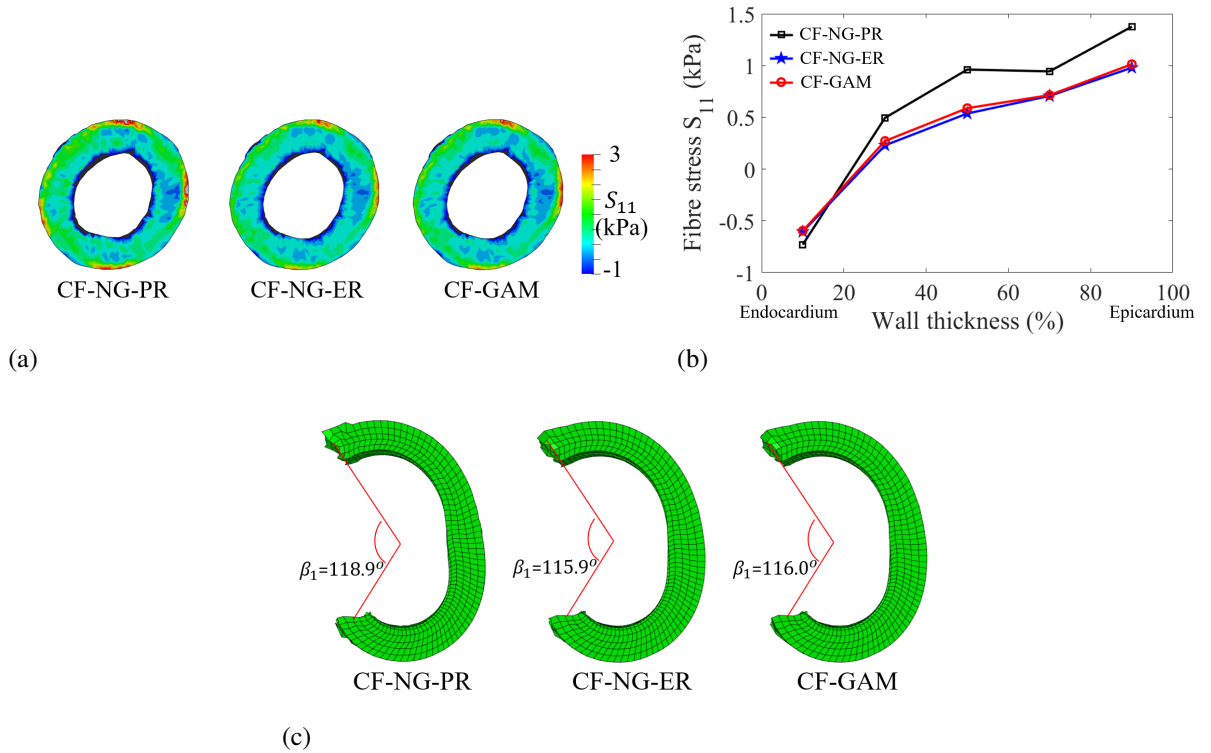


Figure 6.23: In concentric growth, residuals stress is estimated at compatible geometry after growth in the final growth cycle. For three cases, (a) cross-sectional view of fibre stress component along fibre S_{11} distribution at the medium, (b) mean transmural stress along wall thickness, and (c) opening angles under mean residual stress in the ring model.

Considering the bigger EDP always occurs in concentric growth, it is increased from normal 8 mmHg to 12 mmHg [140]. High ESP (208 mmHg) at the first loading step is also achieved by increasing T_{\max} in the active tension formulation (Eq. (4.10)), then G&R begins. Based on the CF-NG-PR case, updated PV loop is shown in (Fig. 6.24 (f)) where the final SV still decrease to 22.4 ml with EDV 41.8 ml and ESV 19.4 ml, indicating the increased EDP cannot restrain the reduction of SV.

6.5.4 Discussion

Eccentric growth of the heart model is triggered by overstretching of fibre (mainly myofibre), the so-called stretch-driven growth, whilst cross-fibre growth leads concentric growth that is usually driven by stress. The constrained mixture based cardiac G&R framework provides critical information regarding different biological constituents' adaptations under pathological conditions. For instance, different G&R properties of collagen fibre are studied to explore the individual and interactive effects between myofibres and collagen fibres. In addition, the residual stress generated by G&R is analysed here, including its contributions to G&R.

Upon slight modifications of the growth law and growth tensor, our model can also capture

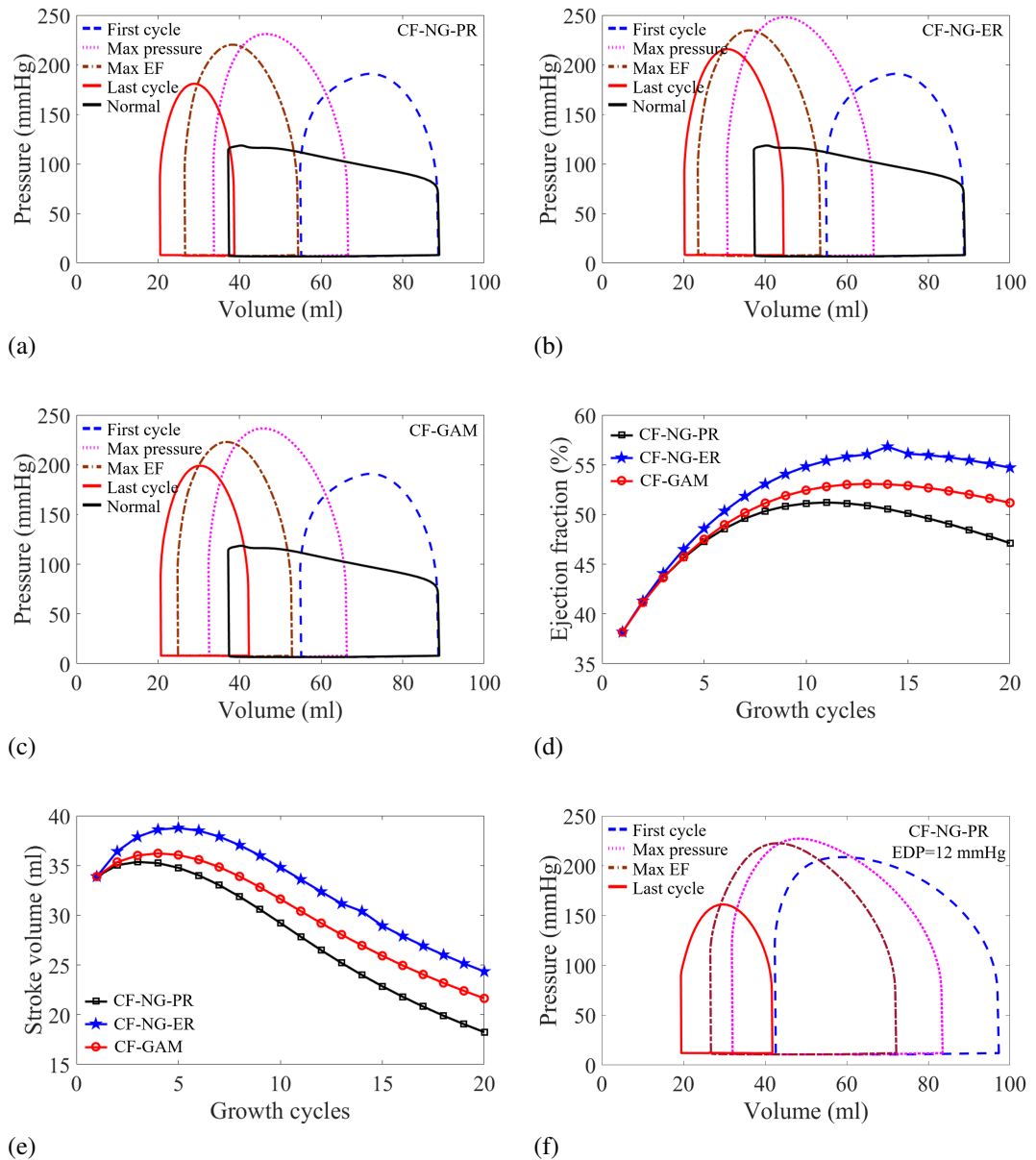


Figure 6.24: In concentric growth, with respect to growth cycles, PV loops in (a) CF-NG-PR, (b) CF-NG-ER and (c) CF-GAM cases. Black solid line is the normal case, blue dash line is the first loading step after applying pressure overload by aortic stenosis, pink dot line is the step with maximum pressure, brown dash-dot line is the step with maximum EF and red line is ending of growth. Their corresponding EFs are in (d) and SV in (e). (f) Updated PV loop with bigger EDP 12 mmHg in the CF-NG-PR case.

the pathological concentric growth with an accumulation of myocytes in parallel or eccentric growth with new myocytes accumulation in series. The current model is to explore general characteristics of eccentric or concentric growth with constrained mixture theorem under update reference framework. Thus, the parameters in growth laws are not estimated by fitting experimental data as done in [141]. The patient-specific model will be the future work. We have presented a multi-scale model for pathological eccentric growth, which finally achieves

increased LV cavity and reduced pump function (Fig. 6.20) as clinic measurement. Evolution of concentric growth is determined by diagonal values of Cauchy stress tensor ($\text{tr}(\boldsymbol{\sigma})$), rather than Mandel stress [141], because we suppose the current stress state governs the G&R of tissue.

Myofibre takes the most largest account in myocardium and is the mainly growth components, whilst the ground matrix can be assumed to inelastic self-remodelling to surround myofibre and collagen fibre. The growth ratios of collagen fibre and myofibre may be different. To study the interplays between collagen fibres and myofibres, we assume different G&R properties of collagen fibres by adjusting its growth tensor and remodelling tensor. For instance, we consider there is no growth in the collagen fibre with either elastic or inelastic remodelling itself to keep up with grown myofibres. In fact, it is not clear whether this remodelling process is inelastic or elastic or both. Remodelling potentially plays an important role when growth ratios of constituents are different. We expect the interplays of these individual G&R processes in myocytes and collagen have the potential to shed light on the biomechanical mechanism which is responsible for the transition from the compensation stage (myocyte G&R mainly) to the decompensation stage (excessive collagen G&R), and eventually guide us to predict the onset of heart failure.

Here we consider two extreme conditions for collagen fibre, sharing the same growth as myofibre and no growth. When they share the same growth, their relative variations of volume fraction are the same (Fig. 6.18 (c) and Fig. 6.22 (c)) and both increase, resulting in stiffer myocardium. If collagen fibre does not grow and only remodels to surround myofibre, two extreme conditions are also studied, elastic or inelastic remodelling. In the inelastic eccentric growth scenario, collagen fibre perhaps produces less stress constraint for myofibre when all grown tissues merging into a compatible state. Moreover, collagen fibre with reduced volume fractions generates a smaller stress response under external loads, allowing myofibre to have more considerable deformation and contributing to more growth amount (Fig. 6.16). In contrast, although the myocardium becomes softer, the elastic remodelling of collagen fibre in eccentric growth acting as a scaffold that limits the deformation of myofibre, causing growth quickly reaching the stable grown state with a much smaller growth ratio. Less new tissue accumulating on the endocardium generates less residual stress that results a smaller opening angle in the simple ring model. The similar results between the two scenarios, CF-GAM and CF-NG-PR, demonstrate that the myofibre growth plays the critical role in heart hypertrophy and residual stress.

In concentric growth, no growth along fibre direction limits the outward expansion of LV, resulting in ventricular thickening wall as G&R. The stable grown LV with different G&R properties of collagen fibre are similar (Fig. 6.21) in both shapes and growth ratios, indicating collagen fibre plays a less critical role in concentric growth than eccentric growth. Opposite to growth speeds in eccentric growth, the case with the elastic remodelling of collagen fibre has the biggest mean total growth ratios, whilst collagen fibre with inelastic remodelling causes the

smallest values in concentric growth. The reason may be that elastic stretch of collagen fibre along the sheet direction contributes to the bigger diastolic filling volume, in which collagen fibre returns to stretch along the fibre direction and compression along the sheet direction. Then, an improved contractile capability is also achieved according to ‘Frank-Starling’ Law (Fig 6.24 (b)).

In eccentric growth, a grown heart can maintain enough SV (Fig. 6.20 (e)) although EF is less than 50%, which can be treated as compensated growth. Excepting the scenario CF-NG-ER, a smaller growth ratio of myofibre can also be induced by excessive growth collagen fibre that will make myocardium stiffer and reduce the stretch of myofibre. Insufficient growth of myofibre perhaps cannot ensure a diseased heart having enough SV for a body’s need, resulting in decompensated growth. Therefore, the interplays of myofibre and collagen fibre may have the potential to elaborate the biomechanical mechanism of adverse G&R of the myocardium. In concentric growth, even though the compensated conditions occurs at the initial growth cycles with more considerable SV, smaller and smaller LV cavity reduces SV (Fig 6.24 (e)) with growth and leads to heart failure in the end. In addition, increased EDP in concentric growth cannot save heart failure (Fig 6.24 (f)).

Residual stress is mainly occurs in concentric growth, i.e. cross-fibre growth driven by stress, after comparing Fig. 6.19 (b) in eccentric growth (-0.05 kPa \sim 0.03 kPa) and Fig. 6.23 (b) in concentric growth (-0.8 kPa \sim 1.4 kPa). Residual stress is negative at endocardium where grown tissues are most in compressive state, and positive at epicardium where grown tissues are most in a stretched state. The reason why concentric growth cause higher residual stress may also be associated with the compressive grown tissue. The epicardial surface almost does not change, and cross-fibre growth accommodates new tissue inward as wall thickening, leading to a high-stress state of the myocardium. On the contrary, the residual stress can be partially relieved as the ventricular wall expanding outward with constant or thinner thickness during eccentric G&R. Our results show that residual stress in eccentric growth results in opening angles similar to the published experimental data (around 13° [223]) whilst with excessive opening angles (around 118°) occurs in concentric growth.

Although our models can qualitatively predict the features of pathological cardiac growths shown in these published simulation studies [23, 141, 143], the primary limitation is the lack of validation using clinical data. The measuring cardiac pump functions (including pressures, EFs and SVs) [140], opening angles [223] and growth speeds [146] quantitatively justify our outcomes are in the right range of values, but more patient-specific data, such as in-vivo ventricular wall motions and PV loops, ex-vivo histological analysis etc., are required in subsequent research to validate the simulations are sufficiently realistic. Secondly, there are few assumptions in this chapter which are used to simplify the model, for example, one pathological growth is only driven by one cue. Pathological cardiac G&R should be a multi-factor driven process. Different combinations of stress/strain driven constituent G&R laws shall be tested in future studies

against measurements at different stage of cardiac disease to identify the biomechanical driven factors and quantify the roles of different constituents.

6.6 Conclusion

The constrained mixture theorem establishes the link between G&R of components and total deformation of tissue, providing a simple concept to elaborate the G&R of constituents and an efficient approach to proceed numerical simulations. In this concept, different constituents have their G&R properties and interact during G&R. An updated reference framework is employed to track the evolution of reference configuration. This approach offers many permissions to modify the model during G&R process, such as updating fibre structure and SEFs. Individual G&Rs of myofibre, collagen fibre and ground matrix under pathological conditions are taken into account in this novel approach. Both eccentric growth and concentric growth have been studied using strain-driven and stress-driven growth laws, respectively, and the results agree with clinical observations. Collagen fibre after elastic remodelling or excessive growth acts as a scaffold to limit the enlargement of LV in eccentric growth, however, elastic remodelling of collagen fibre along the sheet direction contributes little to concentric growth. Modelling interaction between constituents shows the potential to study adverse G&R of the myocardium. Our results also show that residual stress contributes to LV G&R and prevents wall thickening in eccentric growth.

Chapter 7

Growth and remodelling in infarcted left ventricle

7.1 Introduction

MI indicates the death of myocytes in an area of myocardium induced by insufficient supply of oxygen, such as occlusion or pathology of coronary arteries. MI is a heart disease remaining high mortality, 8.1% in-hospital deaths in UK [150]. Survivors from MI still have high incidences of heart failure, which are resulted from maladaptive G&R of the heart with MI scar.

LV with a MI scar generally has diminished contractility that significantly impairs the LV pump function, with reduced EF and increased ESV. After acute MI, LV will experience compensatory remodelling as the initial response by increasing EDP and active contractility to maintain sufficient normal SV and blood pressures. If the pump function is maintained in the normal physiological range and absent of excessive LV cavity enlargement and wall thinning, then the G&R is adaptive and compensatory, for example the EDV increase is less than 20% compared to the value at acute-MI [226]. With time, the diseased heart may enter into the maladaptive remodelling phase with reduced EF and cardiac output, and eventually lead to heart failure. One of the reasons for this adverse G&R is the persistent imbalanced stress/stretch in myocardium [141]. As for the geometric features, the wall in the MI zone progressively becomes thinner with G&R [158], whilst the LV cavity grows larger.

In the MI zone, myofibre is gradually replaced by collagen fibre with the same mean fibre orientation, whilst collagen fibre structure becomes more dispersed [227]. However, a consistent conclusion about collagen fibre structure in the MI zone has not been reached, which may be caused by the differences in measurement methods, experimental species and observation time, etc. For example, based on histological analysis, collagen fibre orientations varied with growth in the MI zones of rabbit hearts [152]. Grown collagen fibres were orientated circumferentially because of the MI scar near the equator of the LV was stretched mainly along the circumferential direction. In contrast, collagen fibres kept same fibre structure after MI according to the DT-MRI

analysis of the rat heart at four weeks after MI [156]. The newly grown collagen fibres in the MI zone were along the myofibres orientations they replaced, which were similar to the myofibres in the remote healthy zone.

In the published mathematical models, myocardium in the MI zone is much stiffer than that in the remote healthy region, while the border zone is the transition zone [143]. Passive material properties of the infarcted and remote healthy myocardium are usually described by phenomenological constitutive laws, such as a strain-based Fung-type SEF or an invariant-based Holzapfel-Ogden SEF [12]. The MI zone is usually modelled as a pure passive soft tissue without contractility, the border zone has diminished contractility depending on the distance to the MI zone [46], and normal contractile capability is in remote healthy and border regions. However, constitution-based structural constitutive laws to describe the different roles of constituents in the infarcted myocardium have not been studied in detail, especially their evolutions with growth. Different fibre dispersion structure at the MI and non-MI zones are also needed to be considered to investigate the effects of evolving fibrosis structure.

In this chapter, we will study how the LV adapts its structure and function after MI using the developed G&R framework, which is served as a proof-of-concept study, rather than a patient-specific study. The MI model is based on a normal human LV with a large MI zone in the middle section of the LV, and a border zone is included between the remote healthy region and the MI zone. In the MI zone, all myofibres are replaced by collagen fibre, and the volume fraction of myofibres linearly varies from zero to a normal value in the border zone. After acute-MI, we consider both myocardial contractility and EDP will increase to compensate the loss of contractile function in the MI zone [161], and we assume both the eccentric and concentric G&R are activated simultaneously in the MI model. We also consider the effect of fibre dispersion on the G&R process in this MI heart. Different fibre dispersion structures are used in the MI zone, whilst non-MI zones remains a constant fibre dispersion structure.

Our model is able to reproduce main G&R features after the MI, such as the dilated LV cavity, the thickening ventricular wall in the non-MI zones, and the wall thinning in the MI zone. Our results show that the leading growth pattern at initial G&R after MI is eccentric growth whilst concentric growth gradually becomes the primary growth pattern at the late growth stage. More dispersed fibre structure in the MI zone results in border zone having more complicated stress responses and reduces the diastolic and systolic capabilities of heart. The border zone has the most complicated stress responses and growth patterns, which need further investigations. Our simulations including fibre dispersion in the MI zone show that more dispersed fibre structure results in worse cardiac pump functions with G&R.

7.2 G&R of MI model without fibre dispersion

7.2.1 Definition of the MI region

The MI model is modified from the previous human LV model in Chapter 5. As shown in Fig. 7.1, the whole LV is divided into three zones: an infarcted zone, and the remote healthy zone, and a border zone in-between. The volume fraction of the ground matrix ($\phi_g = 0.274$) is constant for the whole LV. In the remote healthy region, we consider $\phi_c = 0.026$, and $\phi_m = 0.7$. In the MI zone, all myocytes are dead ($\phi_m = 0.0$) and replaced by collagen fibre, thus, the volume fraction of collagen fibres increases to $\phi_c = 0.726$. Linear variations of ϕ_c and ϕ_m are designed in the border zone to avoid abrupt change. Specifically, we introduce \mathcal{I} to represent the degree of infarction, such that $\mathcal{I} = 1$ in the MI zone and $\mathcal{I} = 0$ in the remote healthy region, hence, the volume fractions of collagen fibre (ϕ_c) and myofibre (ϕ_m) in border zone can be expressed as

$$\phi_m = 0.7(1 - \mathcal{I}), \quad \text{and} \quad \phi_c = 0.7\mathcal{I} + 0.026. \quad (7.1)$$

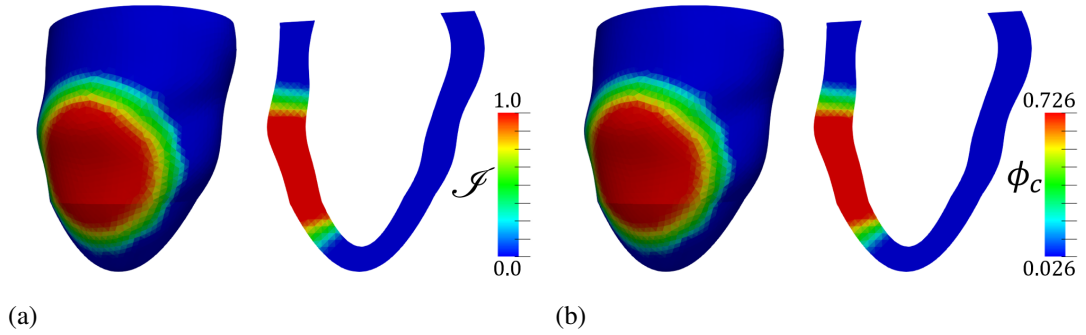


Figure 7.1: LV model and its medium cross-section where MI region is denoted by the red color and remote healthy region is in blue color. (a) Infarction degree (\mathcal{I}) distribution in LV where $\mathcal{I} = 1$ is the infarction zone and $\mathcal{I} = 0$ is remote healthy zone. Medium border zone connects infarcted zone and remote healthy zone with linear varying volume fractions of myofibre and collagen fibre (b).

The implementation in ABAQUS is same as the settings in Chapter 5 (section 5.3.4), excepting the increased LV EDP from 8 mmHg to 23 mmHg [161] and increased contractility (increasing T_{\max} in Eq. (4.10) from 210 kPa to 250 kPa) to maintain $EF > 50\%$ in response to infarcted myocardium.

7.2.2 Growth and remodelling patterns in MI model

After acute-MI, changes of mechanical indexes in diastole and systole trigger G&R of LV, which could be a comprehensive result of eccentric and concentric growths. Although we discussed different remodelling properties of collagen fibre and ground matrix in Chapter 6 (section 6.5),

for simplicity, in this chapter, we only study one scenario that the ground matrix and collagen fibres do not grow but proceed inelastic self-remodelling around the growing myofibres. Hence, in the remote healthy zone and the border zone, the growth and the inelastic remodelling tensors of each constituent are

- the ground matrix:

$$\begin{aligned} \mathbf{G}^g &= \mathbf{I}, \\ \mathbf{F}_{ir}^g &= \vartheta^{f,m} \mathbf{f}_1^g \otimes \mathbf{f}_1^g + \vartheta^{s,m} \mathbf{s}_1^g \otimes \mathbf{s}_1^g + \frac{1}{\vartheta^{s,m} \vartheta^{f,m}} \mathbf{n}_1^g \otimes \mathbf{n}_1^g, \end{aligned} \quad (7.2)$$

- the myofibres:

$$\begin{aligned} \mathbf{G}^m &= \vartheta^{f,m} \mathbf{f}_1^m \otimes \mathbf{f}_1^m + \vartheta^{s,m} \mathbf{s}_1^m \otimes \mathbf{s}_1^m + \mathbf{n}_1^m \otimes \mathbf{n}_1^m, \\ \mathbf{F}_{ir}^m &= \mathbf{I}, \end{aligned} \quad (7.3)$$

- the collagen fibres:

$$\begin{aligned} \mathbf{G}^c &= \mathbf{I}, \\ \mathbf{F}_{ir}^c &= \vartheta^{f,m} \mathbf{f}_1^c \otimes \mathbf{f}_1^c + \vartheta^{s,m} \mathbf{s}_1^c \otimes \mathbf{s}_1^c + \frac{1}{\vartheta^{s,m} \vartheta^{f,m}} \mathbf{n}_1^c \otimes \mathbf{n}_1^c. \end{aligned} \quad (7.4)$$

In the MI region, collagen fibres further remodel themselves along sheet direction to lead a thinner wall due to the reduction of intercellular space of collagen fibres, which is denoted by a multiplier $\gamma^{s,c}$. A simple linear function of $\gamma^{s,c}$ is assumed as

$$\gamma^{s,c} = \begin{cases} 1.0 - 0.05n & \text{for } n \leq 6, \\ 0.7 & \text{for } n > 6, \end{cases} \quad (7.5)$$

where n is the growth cycle number. $\gamma^{s,c}$ will result a 30% reduction of wall thickness in the MI zone, which is the value reported by Jugdutt et al. [158]. The shrinkage is a synthetic process of both collagen fibre and the ground matrix, which can be expressed as a negative growth. Therefore, the negative growth tensors and inelastic remodelling tensors respective for the ground matrix and collagen fibres are

- the collagen fibres:

$$\begin{aligned} \mathbf{G}^c &= \mathbf{f}_1^c \otimes \mathbf{f}_1^c + \gamma^{s,c} \mathbf{s}_1^c \otimes \mathbf{s}_1^c + \mathbf{n}_1^c \otimes \mathbf{n}_1^c, \\ \mathbf{F}_{ir}^c &= \mathbf{I}, \end{aligned} \quad (7.6)$$

- the ground matrix:

$$\begin{aligned}\mathbf{G}^c &= \mathbf{f}_1^g \otimes \mathbf{f}_1^g + \gamma^{s,c} \mathbf{s}_1^g \otimes \mathbf{s}_1^g + \mathbf{n}_1^g \otimes \mathbf{n}_1^g, \\ \mathbf{F}_{ir}^g &= \mathbf{I}.\end{aligned}\quad (7.7)$$

7.2.3 Results

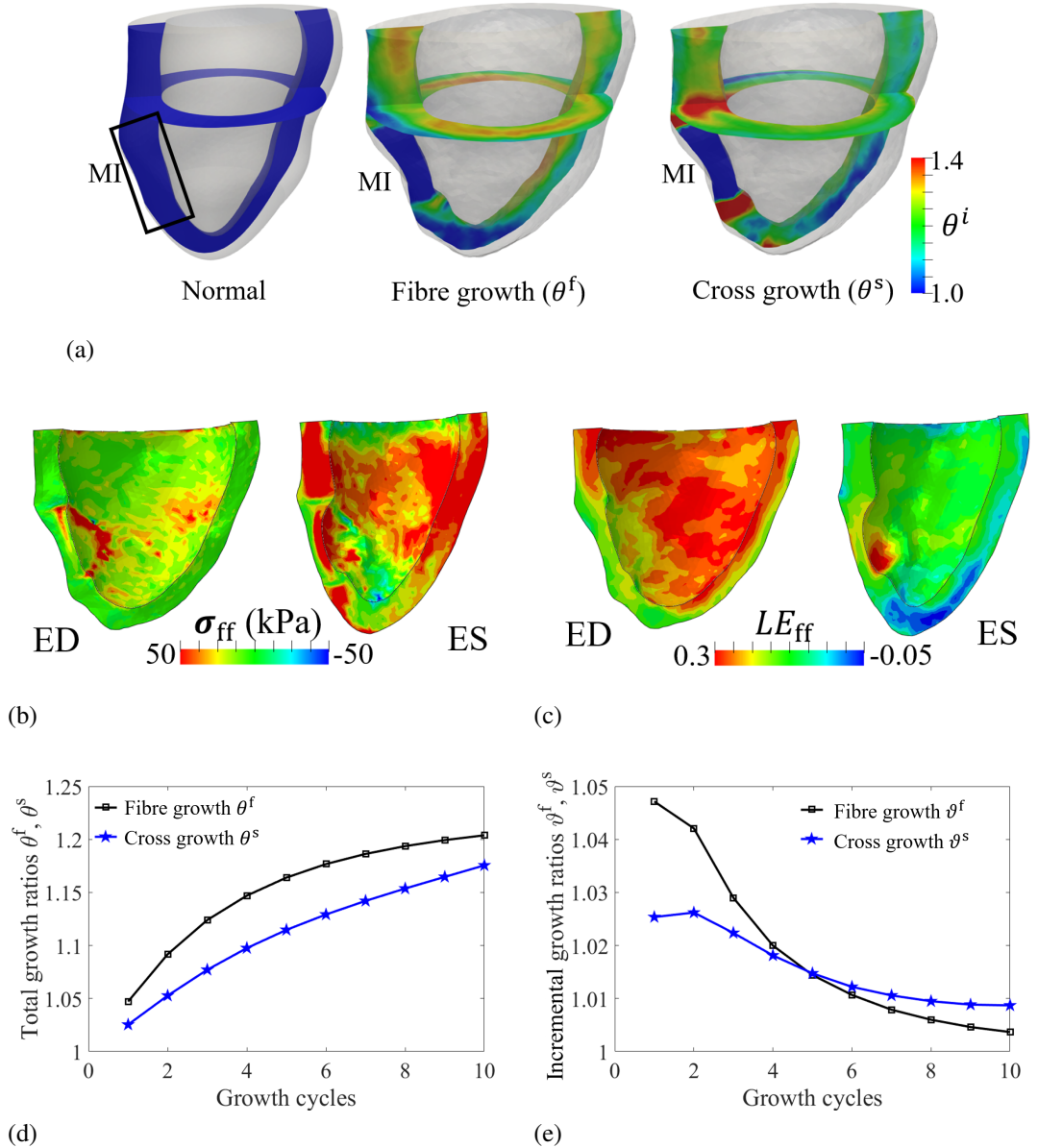


Figure 7.2: G&R of MI model without fibre dispersion. Comparing to the initial LV before growth, grown geometry and distributions of total growth ratios of myofibres along fibre (θ^f) and sheet (θ^s) direction are shown in (a). Cauchy stress component along fibre in (b), and logarithm strain component along fibre in (c) at ED and ES at the final numerical cycle. Average total (θ^i) and incremental (ϑ^i) growth ratios of the non-MI zone with respect to growth cycles are plotted in (d) and (e), respectively.

We report G&R of the MI model for ten numerical simulation cycles, corresponding to 10 weeks post-MI, and final grown geometry is shown in Fig. 7.2 (a) where distributions of total myofibre growth ratios along fibre and sheet directions are also separately plotted. Comparing to the normal heart, there are significant shrinkage in MI zone and thickening in non-MI zones (the remote healthy and the border zones), in particular around the border zone. Myofibre growth mainly locates at endocardium, and medium region has the maximum growth ($\theta^f = 1.4$) while no growth around the apex region. However, cross-fibre growth mainly appears at the border zone with much bigger θ^s than other zones, indicating significantly higher active stress response at the border zone due to persistent large stretch of myocytes in the border zone.

Distributions of stress component along the fibre direction (σ_{ff}) at end diastole (ED) and end systole (ES) are shown in Fig. 7.2 (b), where the border zone has the most complicated stress response, higher stress at ED and lower stress at ES than other zones. According to the logarithm strain along fibre direction (LE_{ff}) in Fig. 7.2 (c), during diastolic filling, excepting stretched healthy zone, border zone is also in stretching state and its higher volume fraction of collagen fibres causes stronger stress response than healthy zone. The stiffest MI zone limits itself stretch. Active contraction results in much higher σ_{ff} in the healthy ventricular wall, which stretches the MI zone to produce a high equivalent passive σ_{ff} . The smaller σ_{ff} in border zone may be caused by the interplay between the passive stretch and the active contraction.

The average total (θ^i) and incremental (ϑ^i) growth ratios of myofibres are computed from non-MI zones, and their variations with respect to growth cycles are shown in Fig. 7.2 (d) and (e), respectively. The total fibre growth (θ^f) initially has higher increasing speed and bigger values than cross-fibre growth (θ^s), and then approaches a constant value, whilst θ^s keeps increasing (Fig. 7.2 (d)). It is consistent with the data in Fig. 7.2 (e) where the incremental fibre growth increment ϑ^f gradually approaches 1 whilst the incremental cross growth ϑ^s almost reaches stable around 1.01. The results show that the total growth at the beginning is mainly the fibre growth which is larger than the cross-fibre growth, and later the cross-fibre growth plays the main role.

The variations of LV pumping function during G&R is described by the progressive PV loops shown in Fig. 7.3 (a). Comparing to the normal PV loop, in the first growth cycle ($n = 1$), the increased EDP results much larger EDV (105.3 ml), and the increased active tension contributes to higher ESP (137.2 mmHg) although ESV is larger than that in the normal condition. The maximum ESP (143.1 mmHg) occurs at the second growth cycle with both bigger ESV and EDV than those in the first cycle. After achieving the maximum EDV (129.0 ml) at the fourth cycle, ESV only has minor variation from cycle $n = 4$ to $n = 10$, less than 1.9%, whilst EDV and ESP gradually reduce to 111.5 ml and 121.5 mmHg, respectively.

Corresponding EF of LV gradually reduces from the initial 58.9% to the final 43.7% in Fig. 7.3 (b), whilst compensatory improvement of SV is maintained during the first eight growth cycles, bigger than the normal 51.7 ml, although its values keeps decreasing after the peak value

(68.6 ml) at the 2nd growth cycle, as shown in Fig. 7.3 (c).

In Fig. 7.3 (d), the ventricular wall thickness of the non-MI zones gradually increases as growing from 8.6 mm to 10.0 mm, mainly induced by the cross-fibre growth of myofibres. In the MI zone, the shrinkage of collagen fibre is determined by negative growth during the first six cycle, resulting in the thinner wall. However, the thinning of wall begins at the second cycle and continues until the eighth cycle, about 12.7% reduction from the initial 9.2 mm, after which the wall thickness remains almost constant because the MI zone neither grows nor shrinks.

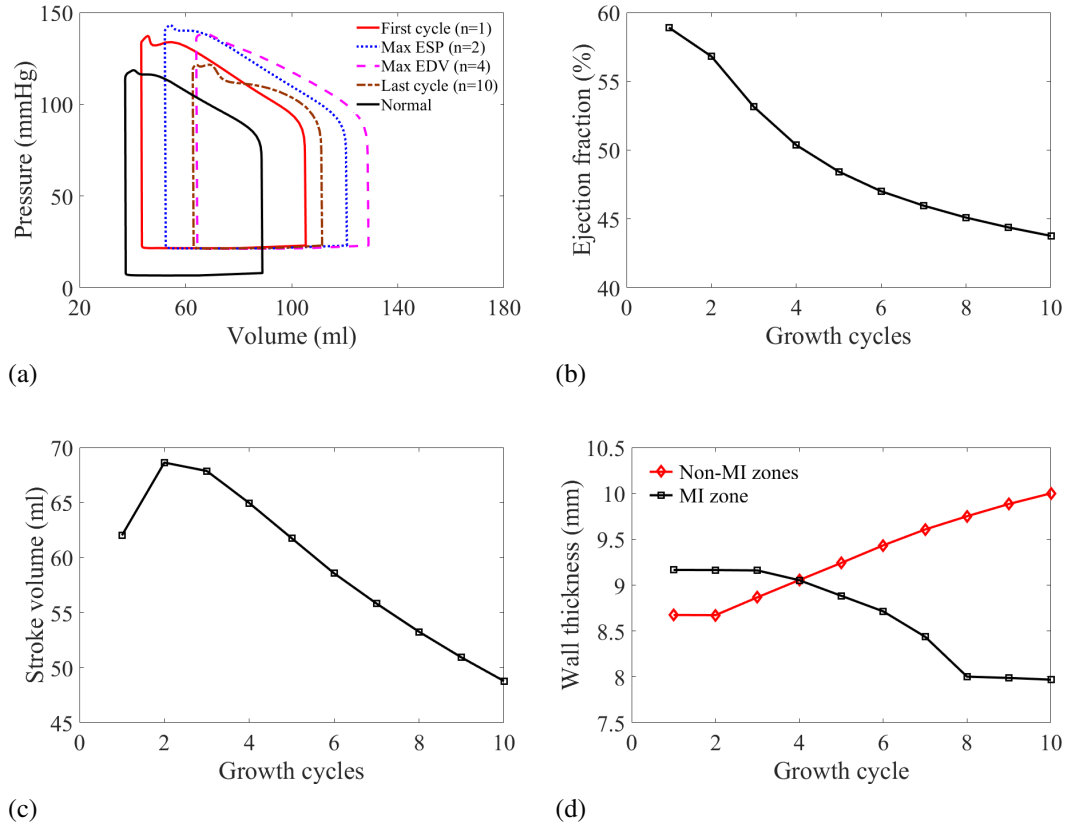


Figure 7.3: Variations of PV loop, EF, SV and wall thickness with G&R. Comparing to the normal PV loop, four representative loops are adopted in (a), which are the first cycle, the second cycle having the maximum ESP, the fourth cycle having the maximum EDV, and the last cycle. EF in (b), and SV in (c). Wall thickness in (d) covers the average thickness of the non-MI zones and the MI zone.

Residual stress induced by G&R is remained in this MI model, and the distributions of its component along the fibre direction orientation (σ_{ff}) at the remote healthy, border and MI zones are shown in Fig. 7.4 (a). It can be found that negative σ_{ff} locates at the inner wall and positive σ_{ff} is at outer wall at the healthy zone, especially in cross-section of the entire healthy zone, whilst much bigger negative σ_{ff} in border zone, followed by positive σ_{ff} in MI zone. Similar results can also be found in Fig. 7.4 (b) that describes the transmural variation of σ_{ff} within ventricular wall at these three zones. Healthy zone maintains grown myofibre compressed

around endocardium (negative σ_{ff}) and stretched around epicardium (positive σ_{ff}), however, always negative σ_{ff} in border zone demonstrates the most grown myofibre are in compression. In contrast, positive residual σ_{ff} in MI zone may be induced by shrinkage along sheet direction.

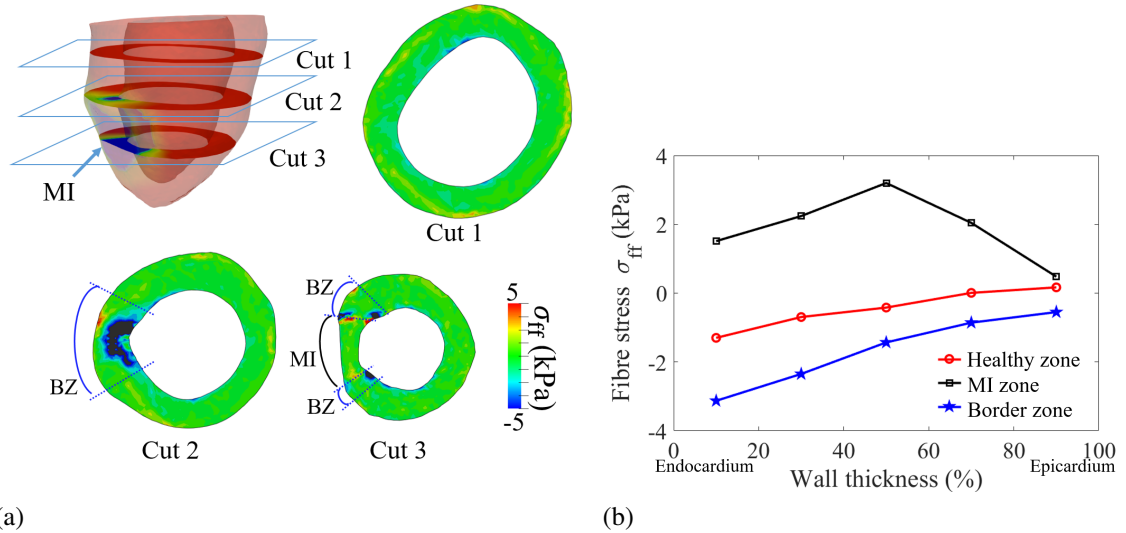


Figure 7.4: Residual stresses at healthy, border, and MI zones, respectively. Three transverse cutting positions pass through the healthy, the border, and the MI zones, respectively. (a) Cross-sections with distribution of Cauchy stress component along fibre. (b) Average transmural residual stress distributions at the three zones.

7.2.4 Discussion

The division of different zones is based on the volume fraction of collagen fibres or myofibres in myocardium. In this section, the fibre structure in the MI zone keeps constant for simplicity. In fact, the unchanged fibre orientations in MI zone was reported by DT-MRI study [156], whilst other studies have reported more circumferential or random collagen fibre direction [152], indicating the necessary of patient-specific in future studies. In addition, reduced volume fraction of myofibre indicates the reduction of active contractile capability, and replaced collagen fibres makes heart wall stiffer [143].

This MI model is adapted from the LV model that has achieved concentric and eccentric G&R in Chapter 6, and it incorporates the fibre growth driven by stretch and cross-fibre growth driven by stress simultaneously in this chapter. Thus a synthetic G&R is achieved with both LV dilation and wall thickening, similar to realistic pathological conditions. Our results (Fig. 7.3 (a)) suggest that fibre growth, i.e. eccentric growth, plays the key role in the first four growth cycle, which may be caused by the bigger EDV induced by increased EDP, then, wall thickening induced by cross-fibre growth, i.e. concentric growth, turns to be the main characteristics of G&R, which will reduce EDV and ESV. According to the 'Frank-Starling' law, increased EDV contributes stronger contractile capability, which further stimulates the cross-fibre growth,

resulting thicker ventricular wall in non-MI zones and smaller EDV with smaller LV cavity.

The shrinkage of MI tissue can be treated as a negative growth driven by chemical clues, and it is described by a simple and linear negative growth law with respect to the growth cycle here. Although the negative growth law is applied to computations, the observed shrinkage occurs after the third cycle and stops after the eighth cycle. Moreover, 30% shrinkage in the definition of negative growth in the MI zone is only achieved around 13% reduction of thickness in FE computation (Fig. 7.3 (d)). This delay and reduction perhaps are caused by a mechanical interaction between finite elements in the model. It further suggests the importance of experimental data that helps to propose more physically-accurate growth laws or quantifies the parameters in the current growth laws. Moreover, the shrinkage also may be the reason for high positive residual stress in the MI zone, the incompressible properties of myocardium making collagen fibre and the ground matrix in tension along with fibre orientation while shrinkage along sheet direction.

The border zone connects the relatively soft healthy zone and the stiff MI zone, and has both collagen fibres and myofibres with varied volume fractions, causing the most complicated mechanical response. For instance, the biggest cross-fibre growth occurs at the border zone (Fig. 7.2 (a)), whilst smaller fibre stress component σ_{ff} in the border zone at ES (Fig. 7.2 (b)). During active contraction, the healthy zone has bigger σ_{ff} to stretch MI zone by border zone, in which the passive stress in collagen fibres may be interactively cancelled by active stress generated by myofibres. In addition, the residual stress in the border zone is always negative, indicating most grown fibres are in compression.

7.3 G&R of MI model with fibre dispersion

7.3.1 Fibre dispersion structure after MI

DT-MRI technique has been used to quantify the transmural fibre rotation within myocardium in the MI region, which is similar to that in the remote healthy zone [156]. Moreover, smaller fractional anisotropy occurs in fibrotic infarcted region [227], reflecting higher fibre dispersion in MI region. In the MI model, while no change in the mean fibre orientations, we use varying fibre dispersions in the MI zone and constant fibre dispersion in the remote healthy region and the border zone. Fibre dispersion indicates the spacial distribution of fibres around the mean fibre direction in each material point, as discussed in Chapter 5. Considering effects of fibre dispersion on cardiac contractility in Chapter 5, two general and representative scenarios are respectively applied into the fibre structure in the MI zone, which are

- Scenario 1: $b_1 = 2.0$, and $b_2 = 2.0$ (intermediate dispersion),
- Scenario 2: $b_1 = 1.0$, and $b_2 = 1.0$ (highly dispersed),

while the non-infarcted zones use the normal in-plane and out-of-plane dispersion parameters

$b_1 = 4.5$ and $b_2 = 3.9$ [4]. Please note b_1 and b_2 are parameters that control in-plane and out-of-plane fibre dispersions, respectively, as discussed in Chapters 4 and 5.

In addition, we made two hypothesis: (a) myofibres and collagen fibres share the same fibre dispersion distribution, and (b) the probability density distribution remains the constant around the mean fibre direction while the mean fibre direction will change during the G&R process due to the changed LV geometry.

Dispersed fibre direction \mathbf{M}_q can be determined by polar angles around the mean fibre direction as demonstrated in Chapter 5 (section 5.2.2). Please note that, when keeping the residual stress during G&R, the variation of mean fibre direction occurs from realistic configuration \mathcal{B}_1 to fictitious equivalent configurations \mathcal{B}_0 (see Fig. 6.8 at Chapter 6). The local fibre direction \mathbf{M}_q can be rotated from one configuration to another one following the Rodrigues' rotation formula, that is

$$\mathbf{M}'_q = \mathbf{M}_q \cos \theta + (\mathbf{k} \times \mathbf{M}_q) \sin \theta + \mathbf{k} (\mathbf{k} \cdot \mathbf{M}_q) (1 - \cos \theta), \quad (7.8)$$

where \mathbf{M}_q and \mathbf{M}'_q are disperse fibre direction before and after rotation, respectively, and \mathbf{k} is a unit vector describing an axis of rotation, around which \mathbf{f}_1 rotates by an angle θ according to the right hand rule. They can be derived by mean fibre orientations before (\mathbf{f}_1) and after (\mathbf{f}'_1) stretch, such as

$$\mathbf{k} = \frac{\mathbf{f}_1 \times \mathbf{f}'_1}{|\mathbf{f}_1 \times \mathbf{f}'_1|}, \quad \text{and} \quad \theta = \arccos \left(\frac{\mathbf{f}_1 \cdot \mathbf{f}'_1}{|\mathbf{f}_1| |\mathbf{f}'_1|} \right). \quad (7.9)$$

7.3.2 Numerical implementation

In computation, the total deformation gradient tensor is decomposed into the growth part and the elasticity part, then the mechanical effect of fibre dispersion is analysed based on the elastic tensor. According to the Chapter 6 (section 6.4.1), we conclude the expression of equivalent elastic tensor ($\mathbf{F}^i_{e'}$) for each constituent in fictitious reference configuration, that is

$$\mathbf{F}^i_{e'} = \mathbf{F}^i (\mathbf{G}^i)^{-1}, \quad (7.10)$$

where \mathbf{F}^i is the fictitious equivalent total deformation gradient tensor including the stretch induced by residual stress, and \mathbf{G}^i is the fictitious equivalent growth tensor that is

$$\mathbf{G}^i = \vartheta_f^i \mathbf{f}'_1 \otimes \mathbf{f}'_1 + \vartheta_s^i \mathbf{s}'_1 \otimes \mathbf{s}'_1 + \mathbf{n}'_1 \otimes \mathbf{n}'_1, \quad (7.11)$$

where ϑ_f^i , and ϑ_s^i are growth ratios respectively along the fibre and cross-fibre directions in the current growth cycle. According to the evolution equations for stretch-driven fibre growth (Eq. (6.4)) and for stress-driven cross-fibre growth (Eq. (6.7)) in Chapter 6, we make minor modifications in the concept of fibre dispersion. For instance, for the growth driven by stretch, the total effective stretch of disperse fibres is the sum of fibre stretch multiplying corresponding

probability value ρ_q , such as

$$\dot{\theta}_{n+1}^f = \frac{1}{\tau^f} \left(\frac{\theta^{\max,f} - \theta_{n+1}^f}{\theta^{\max,f} - 1} \right)^{\gamma^f} (\lambda^e - \lambda^{\text{crit}}) \mathcal{H}(\lambda^e - \lambda^{\text{crit}}) \quad \text{with} \quad \lambda^e = \sum_{q=1}^N \rho_q |\mathbf{F}_{e'}^i \mathbf{M}'_q|, \quad (7.12)$$

and for growth driven by stress, the trace of Cauchy stress tensor ($\text{tr}(\boldsymbol{\sigma})$) is replaced by active tension T_a in each element,

$$\dot{\theta}_{n+1}^s = \frac{1}{\tau^s} \left(\frac{\theta^{\max,s} - \theta_{n+1}^s}{\theta^{\max,s} - 1} \right)^{\gamma^s} \left(\frac{T_a}{p^{\text{crit}}} - 1 \right) \mathcal{H}(T_a - p^{\text{crit}}). \quad (7.13)$$

λ^{crit} is the mean value of λ^e at end of diastole and p^{crit} is the mean value of maximum T_a during systole under normal conditions. Note that θ^f or θ^s describes a growth ratio for each element.

The passive response of the ground matrix without fibre dispersion is

$$\boldsymbol{\sigma}_p^g = J_{\mathbf{F}_{e'}^g}^{-1} a_g \exp[b_g(I_1^g - 3)] \mathbf{B}_{e'}^g, \quad (7.14)$$

where $\mathbf{B}_{e'}^g = \mathbf{F}_{e'}^g (\mathbf{F}_{e'}^g)^T$, $\mathbf{C}_{e'}^g = (\mathbf{F}_{e'}^g)^T \mathbf{F}_{e'}^g$, $I_1^g = \text{trace}(\mathbf{C}_{e'}^g)$, and $J_{\mathbf{F}_{e'}^g} = \det(\mathbf{F}_{e'}^g)$. In DFD approach, the myofibres SEF for the passive response is

$$\Psi^{m*} \cong \sum_{q=1}^N \rho_q \Psi^m(I_{4m}^{q'}), \quad \text{with} \quad \Psi^m(I_{4m}^{q'}) = \begin{cases} \Psi^m(I_{4m}^{q'}) & \text{if } I_{4m}^{q'} > 1 \\ 0 & \text{if } I_{4m}^{q'} \leq 1 \end{cases}, \quad (7.15)$$

where $I_{4m}^{q'} = \mathbf{M}'_q \cdot (\mathbf{C}_{e'}^m \mathbf{M}'_q)$, and $\mathbf{C}_{e'}^m = (\mathbf{F}_{e'}^m)^T \mathbf{F}_{e'}^m$. Then, the passive stress of dispersed myofibres is

$$\boldsymbol{\sigma}_p^m = 2J_{\mathbf{F}_{e'}^m}^{-1} \sum_{q=1}^N \rho_q a_m (I_{4m}^{q'} - 1) \exp[b_m(I_{4m}^{q'} - 1)^2] (\mathbf{m}_q^{m'} \otimes \mathbf{m}_q^{m'}) \mathcal{H}(I_{4m}^{q'} - 1), \quad (7.16)$$

where $J_{\mathbf{F}_{e'}^m} = \det(\mathbf{F}_{e'}^m)$, and $\mathbf{m}_q^{m'} = \mathbf{F}_{e'}^m \mathbf{M}'_q$. Similarly, the collagen fibres SEF is

$$\Psi^{c*} \cong \sum_{q=1}^N \rho_q \Psi^c(I_{4c}^{q'}), \quad \text{with} \quad \Psi^c(I_{4c}^{q'}) = \begin{cases} \Psi^c(I_{4c}^{q'}) & \text{if } I_{4c}^{q'} > 1 \\ 0 & \text{if } I_{4c}^{q'} \leq 1 \end{cases}, \quad (7.17)$$

where $I_{4c}^{q'} = \mathbf{M}'_q \cdot (\mathbf{C}_{e'}^c \mathbf{M}'_q)$, and $\mathbf{C}_{e'}^c = (\mathbf{F}_{e'}^c)^T \mathbf{F}_{e'}^c$. Corresponding passive stress of dispersed collagen fibres is

$$\boldsymbol{\sigma}_p^c = 2J_{\mathbf{F}_{e'}^c}^{-1} \sum_{q=1}^N \rho_q a_c (I_{4c}^{q'} - 1) \exp[b_c(I_{4c}^{q'} - 1)^2] (\mathbf{m}_q^{c'} \otimes \mathbf{m}_q^{c'}) \mathcal{H}(I_{4c}^{q'} - 1), \quad (7.18)$$

where $J_{\mathbf{F}_{e'}^c} = \det(\mathbf{F}_{e'}^c)$, and $\mathbf{m}_q^{c'} = \mathbf{F}_{e'}^c \mathbf{M}'_q$.

The dispersed myocardial active stress is developed by the GST approach demonstrated in section 4.2.2 of Chapter 4, that is

$$\sigma_a^m = T_a H_{11} \hat{\mathbf{f}}^{m'} \otimes \hat{\mathbf{f}}^{m'} + T_a H_{22} \hat{\mathbf{n}}^{m'} \otimes \hat{\mathbf{n}}^{m'} + T_a H_{33} \hat{\mathbf{s}}^{m'} \otimes \hat{\mathbf{s}}^{m'}, \quad (7.19)$$

in which T_a is the total active tension along the myofibre direction ($\mathbf{f}_1^{m'}$), $\mathbf{s}_1^{m'}$ and $\mathbf{n}_1^{m'}$ are respective sheet and sheet-normal directions of myofibre in equivalent fictitious reference configuration, then, $\hat{\mathbf{f}}^{m'} = \mathbf{F}_{e'}^m \mathbf{f}_1^{m'} / |\mathbf{F}_{e'}^m \mathbf{f}_1^{m'}|$, $\hat{\mathbf{s}}^{m'} = \mathbf{F}_{e'}^m \mathbf{s}_1^{m'} / |\mathbf{F}_{e'}^m \mathbf{s}_1^{m'}|$ and $\hat{\mathbf{n}}^{m'} = \mathbf{F}_{e'}^m \mathbf{n}_1^{m'} / |\mathbf{F}_{e'}^m \mathbf{n}_1^{m'}|$. Finally, the total Cauchy stress at the n th growth cycle is

$$\sigma_t = \left(\sum_{i=\{g,m,c\}} \phi_n^i \sigma_p^i \right) + \phi_n^m \sigma_a^m. \quad (7.20)$$

7.3.3 Results

Due to numerical convergence issue in the border zone, in which the extreme complex stress/strain pattern causes excessive distortion of finite elements, in particular at late growth cycles. Thus we only show the results from the first five growth cycles as preliminary results. In the future, the border zone will be studied with a more realistic G&R model due to the complex stress/strain patterns.

In the three cases, the non-MI zones have the identical normal fibre dispersion ($b_1 = 4.5$, $b_2 = 3.9$), and MI zones have varied fibre dispersion, which are $b_1 = 1.0$, $b_2 = 1.0$ (case 1), $b_1 = 2.0$, $b_2 = 2.0$, and $b_1 = 4.5$, $b_2 = 3.9$ (case 3). Their grown geometries and distributions of total myofibre growth ratios (θ^i) are plotted in Fig. 7.5 (a). All three cases have shown the features of eccentric growth with cavity dilation ($\theta^f > 1$), features of concentric growth with wall thickening ($\theta^s > 1$) in the remote healthy zone, and shrinkage in the MI zone. In case 1, the cross-fibre growth (θ^s) is bigger than the fibre growth (θ^f) but not in cases 2 and 3. We notice the border zone has much bigger θ^s than the MI zone and the remote healthy zone, with a value of 1.4.

In contrast, the difference of fibre growth is negligible, which are supported by the average θ^f of myofibre in the non-MI zones in Fig. 7.5 (b-d). At the final growth cycle, at the non-MI zones, three cases have same mean fibre growth amounts $\theta^f = 1.12$ that is smaller than that of MI model without fibre dispersion ($\theta^f = 1.17$). Case 2 and case 3 also share same mean $\theta^s = 1.13$ at the non-MI zones, smaller than that of case 1 ($\theta^s = 1.23$), but they are all larger than $\theta^s = 1.11$ of the MI model without fibre dispersion. The comparison shows that fibre dispersion structure may limit eccentric growth but promote concentric growth. Highly dispersed fibres in the MI zone can cause a large cross-fibre growth ratio, whilst no more difference appears when b_1 and b_2 are both bigger than 2.0. θ^f and θ^s at the end of the fifth simulation cycle are summarized in Table 7.1.

Fig. 7.6 shows that case 2 and case 3 have similar fibre stress (σ_{ff}) distributions at both ED

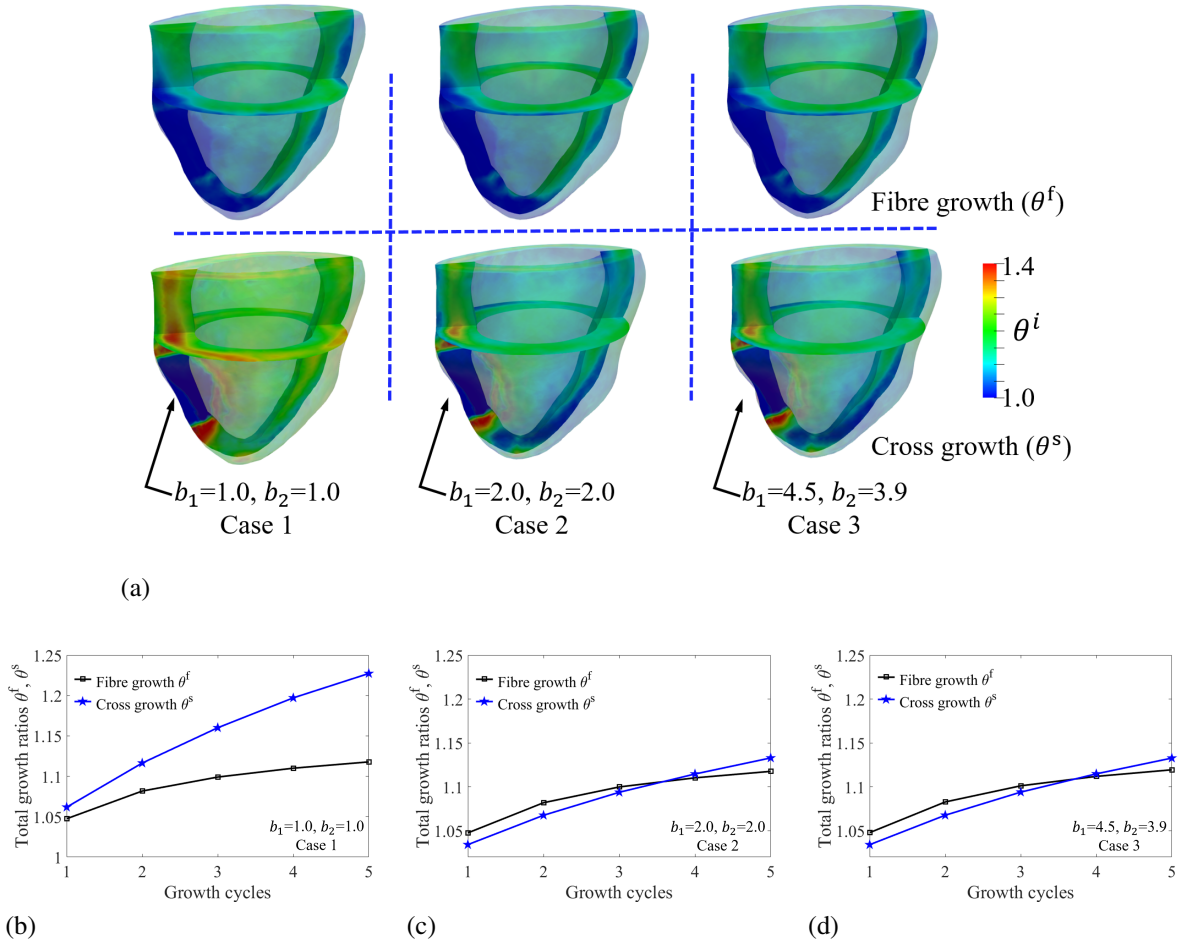


Figure 7.5: G&R of MI model with fibre dispersion. All non-MI zones use the same dispersion ($b_1 = 4.5, b_2 = 3.9$), and three general cases are in the MI zone, which are $b_1 = 1.0$ & $b_2 = 1.0$, $b_1 = 2.0$ & $b_2 = 2.0$, and $b_1 = 4.5$ & $b_2 = 3.9$. (a) Their distributions of total growth ratios along fibre (θ^f) direction on the top and along sheet (θ^s) direction on the bottom. Average growth ratios θ^f and θ^s of non-MI zones in three case1 (b), case 2 (c), and case 3 (d), respectively.

	Normal	No dispersion	$b_1 = 1.0$ $b_2 = 1.0$	$b_1 = 2.0$ $b_2 = 2.0$	$b_1 = 4.5$ $b_2 = 3.9$
θ^f	1.0	1.164	1.118	1.117	1.119
θ^s	1.0	1.115	1.227	1.133	1.133
EF (%)	58.2	48.49	36.27	44.73	45.20
SV (ml)	51.7	61.9	26.4	40.8	41.6
EDV (ml)	89.0	127.6	72.8	91.2	92.2
ESV (ml)	37.2	65.7	46.4	50.4	50.5
EDP (mmHg)	8.0	23.0	23.0	23.0	23.0
ESP (mmHg)	118.5	134.9	96.2	112.5	113.5
T_{\max} (kPa)	210	250	250	250	250

Table 7.1: Summary of main indices associated with G&R and cardiac pumping function in MI models without and with fibre dispersions at the fifth growth cycle.

and ES in the fifth cycle, very different from case 1. The highly dispersed fibre structure in cases 1 makes the stress response at the border zone very complicated, for example, dramatic changes from 50 kPa to -50 kPa, which may be partially caused by the diminished contractility towards the MI zone and different dispersions between the MI zone and the border zone. At ES, σ_{ff} distribution in the border zone becomes more homogenous and mean σ_{ff} in the MI zone becomes larger when the difference of fibre dispersions between the MI zone and the non-MI zones reducing.

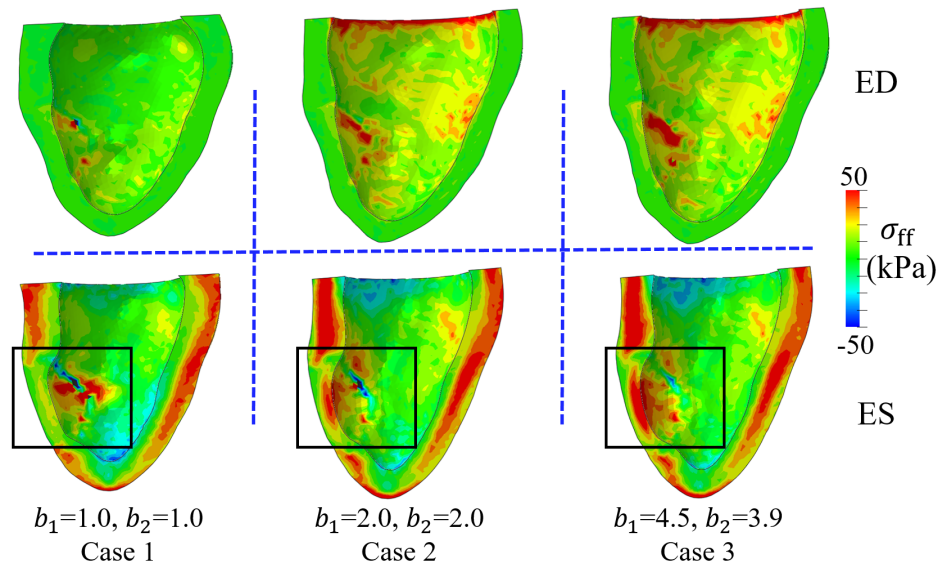


Figure 7.6: Fibre stress distributions at ED (the top) and ES (the bottom) after G&R of MI model with three cases of fibre dispersion.

Fig. 7.7 (a) describes the residual σ_{ff} distributions at three cross-sections in three cases, in which case 1 experiences more significant variations of σ_{ff} at different positions than other two cases, such as bigger positive σ_{ff} in the MI zone, while negative σ_{ff} in the border zone. Comparing to case 1, σ_{ff} distribution is more homogenous in case 2 and case 3 with bigger dispersion parameters b_1 and b_2 . The average transmural σ_{ff} distributions from endocardium to epicardium of three cases are compared at the MI zone (Fig. 7.7 (b)), the border zone (Fig. 7.7 (c)), and the remote healthy zone (Fig. 7.7 (d)), respectively. The σ_{ff} curves of case 2 and case 3 are not overlapped in the MI and border zones whilst are same in the remote healthy zone. In terms of transmural distributions of σ_{ff} in MI and border zones, case 1 and case 2 are similar in shape and close in value, indicating that the residual stress may be associated with the different fibre dispersion structures between the MI zone and the non-MI zones.

PV loops of three cases are listed in Fig. 7.8 (a-c). EDV, ESV and ESP of those three case increase in the first three growth cycles, and then decrease at the fourth and fifth growth cycles. The decreased EDV may be caused by thickening ventricular wall due to the dominated concentric growth at later growth stage. The variations in case 1 are more significant than the

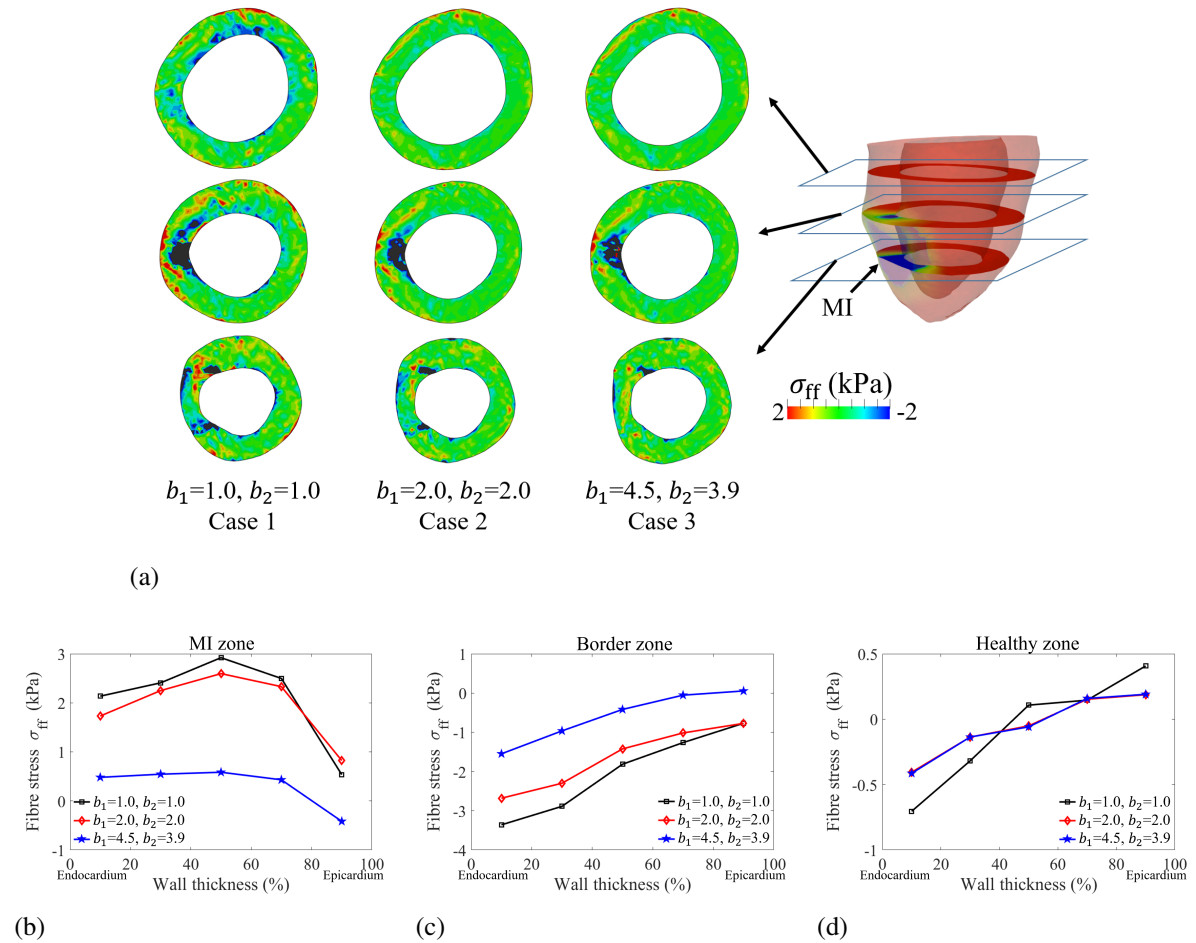


Figure 7.7: (a) Comparison of residual stress between MI models with three cases of fibre dispersion, at the healthy zone (the top), at the border zone (the medium), and at the MI zone (the bottom). The right denotes positions of the three cross-sections. (b) Three cases' average transmural residual stress distributions at the three zones.

other two cases who almost have the same PV loops with growth. For instance, EDV of case 1 increases to 107.7 ml at the second cycle and then decreases to 72.8 ml at the fifth cycle, the corresponding ESP decreases from 128.4 mmHg to 96.2 mmHg, whilst case 2 and case 3 achieve much higher ESP 112.5 mmHg and 113.5 mmHg, respectively. Finally, the pumping function of case 1 at the fifth cycle has a much smaller PV loop than that of case 2 or case 3.

In Fig. 7.8 (d) and (e), EF and SV in case 1 are both less than those of other two cases. For minor dispersed case 2 and case 3, EF decrease from 58.8% to 45.2%, and SV is from 59.7 ml to 41.7 ml, comparing to those in case 1 from 53.7% to 36.3% for EF and 54.5 ml to 26.4 ml for SV, respectively. Their pump functions are summarized in Table 7.1.

As for ventricular wall thickness, a considerable increment in the non-MI zones and decrement in the MI zone are resulted by the more dispersed fibres in the MI zone as shown in Fig. 7.8 (f). Case 1 with highest dispersed fibres causes significant wall thickening in the non-MI zones and wall thinning in the MI zone than other two cases. Fibre dispersion also affects on the

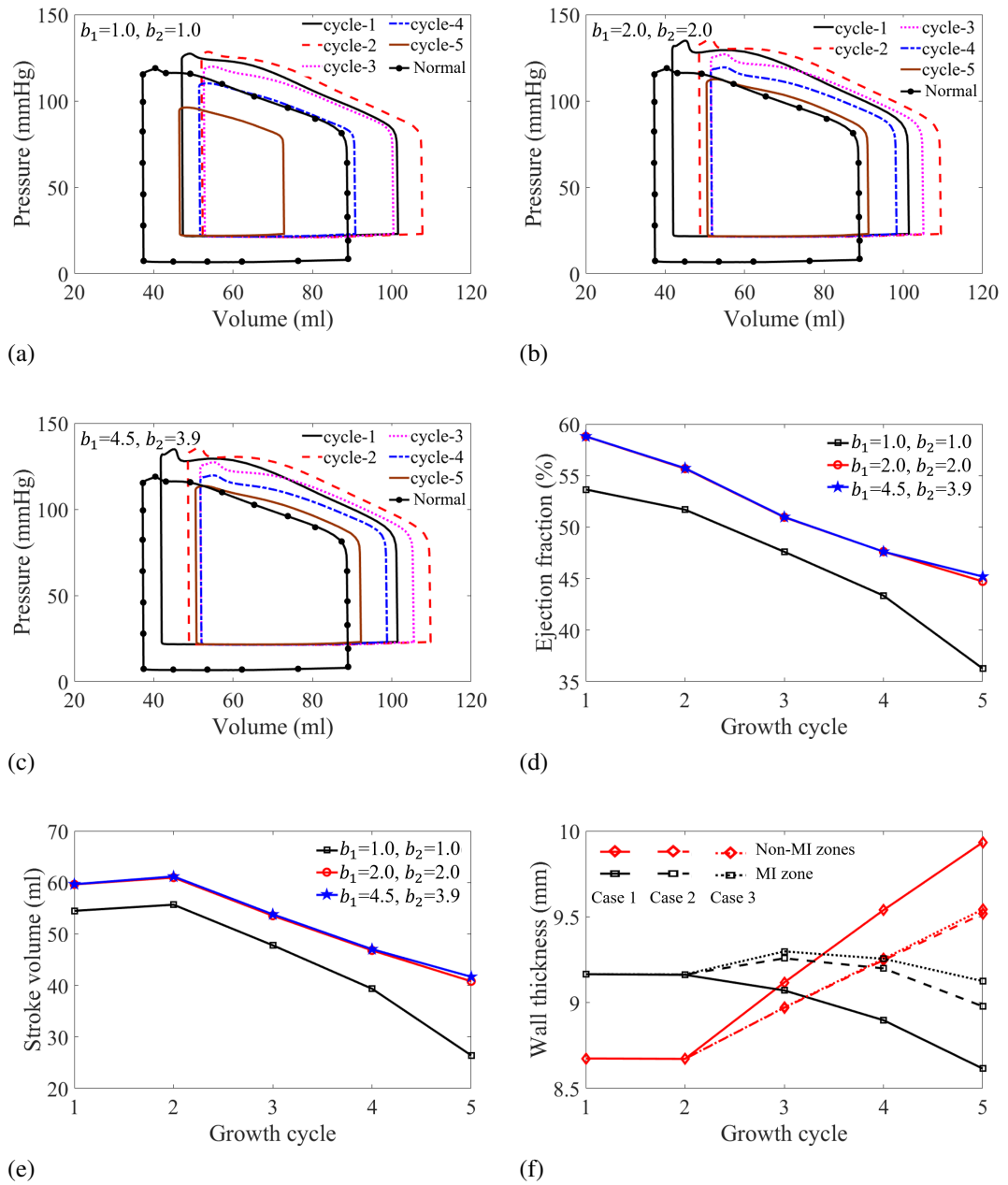


Figure 7.8: Variations of PV loop, EF, and SV using the MI models with fibre dispersion in the first five cycles. (a) PV loops of case $b_1 = 1.0$ & $b_2 = 1.0$, (b) PV loops of case $b_1 = 2.0$ & $b_2 = 2.0$, and (c) PV loops of case $b_1 = 4.5$ & $b_2 = 3.9$. Their EFs in (d), SVs in (e), and wall thickness in (f).

shrinkage of the MI zone. For instance, between case 2 and case 3, the thickness curves in the non-MI zones are overlapped whilst have deviation in the MI zone.

7.3.4 Discussion

Three cases of fibre dispersion in the MI zone are studied here, while a identical normal fibre dispersion is used in the non-MI zones. Including fibre dispersion can alter the mechanical re-

sponse of LV, which further changes the G&R of LV, such as less fibre growth and more cross growth (Table 7.1) comparing to the no dispersion case. Less fibre growth may be associated with the definition of growth law where the total effective elastic stretch along mean fibre direction is the probability sum of each dispersed fibre as in the DFD approach, which may result in a small growth ratio. The difference of PV loops between the two cases with b_1 and b_2 bigger than 2 is negligible, consistent with the previous results in Chapter 5, in which almost no differences in pump function exist when b_1 and b_2 bigger than 2. In contrast, the GST-based active stress model causes slightly more cross growth with worse cardiac function, such as less EF and SV comparing to the no dispersion case.

The comprehensive G&R of the MI model is a preliminarily combination of eccentric and concentric growths. We compute fibre growth and cross growth using two independent growth laws in this Chapter. However, the coupling growth maybe requires a new growth law that includes two types of growth together, which can be a future topic to study. Our results show that eccentric growth plays the primary role during the initial growth, then concentric growth gradually becomes the dominated characteristics, which merits further studies on the interplays between eccentric and concentric G&R in LV post-MI. The thickening wall in our results does not always occur in clinic MI measurements, in other words, eccentric growth perhaps remains as the dominant feature after acute-MI. Future studies shall identify the correct growth laws for the remote region, the border zone and the MI zone with inferred patient-specific parameters for prediction of LV G&R post-MI. Our current model only serves a proof-of-concept study of the application of constrained mixture G&R framework developed in Chapter 6 to the MI patients.

Dispersion of collagen fibre in the MI zone has a significant effect on residual stress at the border zone. For instance, more dispersed collagen fibre causes more significant negative and positive stress at the border zone, causing distorted shape. The varied stress response in the MI zone further affects the stress response of the whole LV (Fig. 7.6). The difference of residual stress will be accumulated during G&R and finally lead to different grown states. Even though the whole LV with little dispersion ($b_1 = 4.5$ and $b_2 = 3.9$ in case 3), the results of G&R is much different from that of no dispersion case (section 7.2.3), such as smaller SV and lower ESP. Therefore, the effect of fibre dispersion in G&R cannot be ignored, especially in the MI zone.

The limitations should be mentioned. Firstly, the models in this chapter shall be considered to be a proof-of-concept study, which can qualitatively reproduce the G&R characteristics of the LV with MI [151]. Due to the lack of validations of patient-specific experimental data, our models manage to produce physiological outcomes that are comparable to measured values, such as the fibre structure [156], wall thinning [158] in the MI zone and physiological index (including EDP, ESP, etc.) [161]. Secondly, eccentric and concentric growths occur together in this chapter, whilst their growth laws are independent. The leading growth pattern (eccentric or concentric) at different simulation stage may be further affected by the parameter values in growth laws.

Therefore, More clinical or measured data are required to identify the interaction between two growth patterns and quantify the roles of myofibres and collagen fibres at different stages of MI. Last but not the least, the limited growth cycle in these simulations with fibre dispersions may be caused by dramatically different stress responses in different zones, in particular the complex stress variation in the border zone.

7.4 Conclusion

G&R of MI model is achieved in this study, reproducing the main characteristics such as LV dilation, wall thickening at the non-MI zones and shrinkage at the MI zone. Eccentric and concentric G&R in the non-MI zones and negative growth in the MI zone occurs simultaneously. Our results show that eccentric growth with LV dilation plays the primary role during the initial growth of LV, then concentric growth with wall thickening turns to be the main characteristics. The border zone has the most complicated mechanical response during diastole and systole, and always has negative residuals stress whilst that of the MI zone is always positive. When including the same fibre dispersion in the non-MI zones and different fibre dispersion in the MI zone, more dispersed collagen fibre in the MI zone causes a more complicated stress response in the border zone and reduces active and passive stress in the whole LV, finally causing worse cardiac pumping functions. Moreover, residual stress in the MI and the border zones is more sensitive to fibre dispersion variation in the MI zone.

Chapter 8

Summary and future work

8.1 Summary

This thesis covers three researching topics in the biomechanics of heart, which are constitutive law, fibre structure and G&R. It is a coherent process to conduct studies of cardiac mechanisms. Studying G&R of heart requires the constitutive laws to determine the strain-stress response in myocardium and the fibre structure to control deformation of the 3D FE heart model. Therefore, this thesis includes two parts: constitutive laws and fibre structures of myocardium (Chapters 3-5) and G&R based on LV (Chapters 6&7).

Firstly, we study the classic general HO constitutive law in Chapter 3 and proposed an AIC-based constitutive model reduction for myocardium, basing on three sets of experimental tests that include uniaxial tension, biaxial tension and simple shear. The reduced model maintains similar descriptive and predictive capabilities as the general HO model. Shear in biaxial tension and fibre rotation along the thickness of samples show significant importance to fitting goodness. We find that the effective fibre ratio is also essential when fitting data of uniaxial tension and simple shear. Our results show that a component material model requires a combination of different types of experimental tests.

Secondly, a bi-ventricular porcine heart is reconstructed using DT-MRI images, and inside DT-MRI fibre structure is warped from an ex vivo canine heart using an LDDMM framework in Chapter 4. Two simple RBM fibre structures are designed according to DT-MRI fibre structure, and then the effects of three fibre structures on cardiac pumping function are compared. We find DT-MRI fibre structure can achieve better cardiac work, and the primary reason is its more dispersed distribution of fibres, which enables cross-fibre active tensions. To bridge their difference in pumping function, we propose a GST-based active tension model that includes respective fractional active tensions along three orthogonal fibre directions. Finally, an RBM fibre model with dispersed active tension achieves similar contractile capability as the model with DT-MRI fibre structure. Moreover, cross-fibre active tension along the sheet-normal direction can enhance active contraction, but the opposite is true along the sheet direction.

To further study the effect of fibre dispersion on both passive and active mechanical responses, different fibre dispersion cases are applied on a myocardial strip model, a rabbit bi-ventricular model, and a human LV model in Chapter 5. To exclude compressed fibre during passive diastole, DFD based approach is chosen because of its much higher computational efficiency than the AI-based approach. GST-based active tension is also used here. Our results show that both diastolic filling and systolic contraction can be largely affected by dispersed fibres, and in-plane dispersion exhibits a stronger influence than out-of-plane dispersion. Comparing to the model without fibre dispersion, more significant differences in pumping function occur when the fibre dispersion is high, suggesting the necessary including fibre dispersion.

Based on the cardiac mechanics in the last three chapters, the second part of this project (G&R) is explored in Chapter 6 where the constrained mixture theory is employed to investigate different G&R characteristics of constituents in myocardium. The traction of reference configurations during growth in the theory is solved using an updated reference framework, which also allows us to update fibre structure and strain energy functions. We find residual stress plays an important role in G&R, such as contributing to enlarge LV cavity and preventing wall thickening in eccentric growth, and cannot be ignored, especially in concentric growth. Our model correctly predicts the eccentric growth driven by stretch and the concentric growth driven by stress. Our results suggest properties of collagen fibre have a significant influence on G&R, for instance, elastic remodelling of collagen fibre works as a scaffold to prevent excessive enlargement of LV in eccentric growth, whilst elastic remodelling along sheet direction promotes concentric growth.

We further carry out G&R of heart with pathological MI in Chapter 7 and also include fibre dispersion in the model. Here, we only proceed with a brief exploration and predict the correct G&R pattern. For instance, the main features of G&R after MI, including LV dilation, wall thickening at non-MI zones and shrinkage at MI zone, are reproduced when eccentric and concentric G&R in non-MI zones and negative growth in MI zone are performed simultaneously. Eccentric growth plays the leading role during the initial G&R stage, then, concentric growth progressively becomes the primary pattern. Similar results also occur in the models with fibre dispersion. The border zone has the most complicated mechanical response during diastole and systole, and more dispersed collagen fibre in the MI zone makes it further complicated, resulting in worse cardiac pumping functions.

Finally, this PhD project has been completed on time, and the initial research proposal has been achieved. I have received training in systemic methodology to carry out academic research and become skilled at modifying constitutive laws, reconstructing heart geometries, designing fibre structures, coupling fibre dispersions, and implementing G&R theory to simulate pathologic growths. On the other hand, there are few limitations in this project, for instance, there is limited experimental data to validate the mathematical models, in particular for structural constitutive laws, the active stress model should be updated with more detailed biophysical in-

formation, and G&R is only implemented to qualitatively predict pathological conditions, but not patient-specific.

8.2 Future work

As the research progresses, we always find some exciting and meaningful reaching topics. They are ignored in this project due to limited time, even though we have put some efforts to perform preliminary investigations. Here, we briefly introduce three main future plans associated with a constitutive model from *ex vivo* to *in vivo*, biophysically detailed active tension model, and validation of G&R based on experimental data.

8.2.1 Constitutive modelling of myocardium from *ex vivo* to *in vivo*

The kinematics of soft tissue can be quantitatively measured by various experimental techniques [4,40,55]. However, direct measurements of *in vivo* solid stress have not been achieved, and it is still challenging in the case of the body. To overcome this difficulty, a common alternative way is using constitutive models to estimate stress response, which characterize the relation between kinematics and stress. In this respect, there is a critical need for accurate quantification of the biomechanical micro-environment in soft tissue through mathematical modelling, which is essentially dependent on constitutive models. Constitutive models are mathematical descriptions that approximate the mechanical behaviours of material under specific conditions, which can further take into account information from different scales [11]. In most soft biological tissue, collagen is the major component of the extracellular matrix and largely determines the material property (stiffness).

In the past several decades, many constitutive models have been proposed for myocardium [11]. Myocardium is usually treated as an anisotropic, hyper-elastic material with layered collagen network [13, 15, 181]. One of very widely used model is the HO model and its variations [11]. To account for fine structures of collagen fibres, general structural tensors were further introduced to describe fibre dispersion by Eriksson et al. [21]. Calibrating unknown parameters in the HO model has been investigated in [181] using three different sets of *ex vivo* experiment data. However, the estimated parameters in constitutive laws by fitting *ex vivo* experimental data are always scaled smaller to achieve enough EF or SV in 3D FE models [15,91], indicating the gap between *ex vivo* and *in vivo* constitutive modellings. Inverse estimation of unknown parameters in constitutive laws from *in vivo* data was first reported in [13] by using MRI. We will use myocardium as an example to show how we can develop an *in vivo* constitutive law from various *ex vivo* experiments and further show the applications to real patient data by encompassing a wide range of cross-scale soft tissue mathematical models.

8.2.2 A biophysically detailed active tension model based on Hill model

Mathematical models provide novel insights to understand mechanisms of cardiac tissues at different spatial scales, ranging from cells to muscles. Phenomenological approaches to model active contraction can be divided into three categories that are active stress, active strain, and hybrid approaches. However, active contraction does produce force simultaneously with elastic deformation as exhibited in an isometric contraction experiment of muscle [111]. The force in muscle rose when it was activated, and the contractile component would contract to stretch the series elastic component [111]. In other words, the active unit contracts and pulls elastic passive unit to produce stress, i.e. active stress, in myofibre. This fact suggests that a biophysically detailed active tension model may demonstrate a more realistic active tension generation process. Nevertheless, if assuming active force only depends on myofibre direction, no components in the transverse plane, it is possible to replace the 3D active strain tensor with one-dimensional stretches of interval units to avoid the interference to transverse deformation.

Myofibre is composed of myocytes whose inside unit is sarcomere to generate active tension, moreover, spatial distributions of main functional elements in sarcomere have been demonstrated in [228, 229]. The whole sarcomere has a symmetric structure where thin actin filaments are parallel to myosin. Z-bands at both ends are anchored to only one end of the thin filament and connect to both ends of myosin by elastic protein titin. Myosin also connects to actin filament by cross bridges that are controlled by active potential. In the absence of potential stimulation, cross bridges slide freely over actin filament, and the passive response of myofibre is produced by stretched titin. Once active contraction is activated, cross bridges bind actin filaments and myosin in series together and contracted myosin stretches actin filament to produce the same force. Therefore, it is feasible to separately estimate passive and active tensions, where the passive response is associated with the stretch of sarcomere in the phenomenological approach, and active tension is evaluated by the stretch of actin filaments in a biophysically detailed approach. As the three-element Hill's model in [105, 106], they both separate active and passive responses into two parallel branches, in which passive stress is the synthetic response of ground matrix, myofibre and collagen fibre in one branch, active stress is derived by active strain tensor in another branch, and total stress is the sum of active and passive stresses. Physical arrangements and lengths of main elements are demonstrated in [228] to account for the effects of sarcomere elongation on active dynamics, which also contributes to the accurate descriptions of elements involved in the generation process of active tension. In this concept, the main features of active contraction, force-velocity and length-dependent relationship are correctly predicted by a multiscale electromechanical model [230].

According to the structural analysis of principal units in sarcomeres [228–230], such as myosin and actin filament, we present a hybrid model according to the micro and macrostructure of myofibre, where a three-element Hill model is employed to illustrate the evolution of the stress response. Active stress is produced by internal actin filament stretched by contracted myosin in

series, and passive stress remains from the elongation of myofibre and collagen fibre. Moreover, length-dependent and force-velocity relationships are considered in our active tension model.

8.2.3 Patient-specific G&R model based on experimental data

Our G&R model provides important information such as different biological constituents' adaptations and responses, which are missed by the current medical technology. It also presents the potential for integrating big data of clinical measurements into a virtual twin system for understanding the mechanics of heart failure and reveal the hidden roles of different constituents. This is an essential step towards the mechanistic understanding of individual patient's risk of heart failure and the development of new treatments, and saving lives ultimately.

Experimental data during growth is essential for identifying appropriate growth laws under specific pathological conditions. Measurable data can be divided into image data, mechanical indexed data, and physiological indexed data. Based on image data, we can proceed reconstruction of geometry model by segmentation and quantification. In particular for MI growth, the division of MI zone and non-MI zone is vital to track the variations MI tissue. Mechanical indexed data are necessary to validate the computational cardiac model, such as correct kinematic deformation with similar stress and strain as measurements. Also, it provides data to calibrate parameters in constitutive laws. Physiological indexes data, such as pressure or other personalized biomarkers, contributes to designing boundary conditions for mathematical models and performing follow-up monitoring and risk stratification.

It will be a coherent and complex process, from the first image to the final disease prediction. Machine-learning and statical inference may be able to improve efficiencies, such as deep-learning for model reconstruction and emulator for fast parameter inference. It is feasible to construct a patient-specific model with high accuracy and efficiency in the future.

Bibliography

- [1] DHS Lin and FCP Yin. A multiaxial constitutive law for mammalian left ventricular myocardium in steady-state barium contracture or tetanus. *Journal of biomechanical engineering*, 120(4):504–517, 1998.
- [2] Hao Gao, Andrej Aderhold, Kenneth Mangion, Xiaoyu Luo, Dirk Husmeier, and Colin Berry. Changes and classification in myocardial contractile function in the left ventricle following acute myocardial infarction. *Journal of The Royal Society Interface*, 14(132):20170203, 2017.
- [3] Frederick J Vetter and Andrew D McCulloch. Three-dimensional analysis of regional cardiac function: a model of rabbit ventricular anatomy. *Progress in biophysics and molecular biology*, 69(2-3):157–183, 1998.
- [4] Gerhard Sommer, Andreas J Schriefl, Michaela Andrä, Michael Sacherer, Christian Viertler, Heimo Wolinski, and Gerhard A Holzapfel. Biomechanical properties and microstructure of human ventricular myocardium. *Acta biomaterialia*, 24:172–192, 2015.
- [5] Faizan Ahmad, Shwe Soe, N White, R Johnston, I Khan, J Liao, Michael Jones, R Prabhu, I Maconochie, and Peter Theobald. Region-specific microstructure in the neonatal ventricles of a porcine model. *Annals of biomedical engineering*, 46(12):2162–2176, 2018.
- [6] Reza Avazmohammadi, Michael R Hill, Marc A Simon, Will Zhang, and Michael S Sacks. A novel constitutive model for passive right ventricular myocardium: evidence for myofiber–collagen fiber mechanical coupling. *Biomechanics and modeling in mechanobiology*, 16(2):561–581, 2017.
- [7] HM Wang, H Gao, XY Luo, C Berry, BE Griffith, RW Ogden, and TJ Wang. Structure-based finite strain modelling of the human left ventricle in diastole. *International journal for numerical methods in biomedical engineering*, 29(1):83–103, 2013.
- [8] Fangzhou Cheng, Lori A Birder, F Aura Kullmann, Jack Hornsby, Paul N Watton, Simon Watkins, Mark Thompson, and Anne M Robertson. Layer-dependent role of collagen recruitment during loading of the rat bladder wall. *Biomechanics and modeling in mechanobiology*, 17(2):403–417, 2018.

- [9] Faizan Ahmad, Jun Liao, Shwe Soe, Michael D Jones, Jonathan Miller, Parker Berthelsson, Daniel Enge, Katherine M Copeland, Samar Shaabeth, Richard Johnston, et al. Biomechanical properties and microstructure of neonatal porcine ventricles. *Journal of the mechanical behavior of biomedical materials*, 88:18–28, 2018.
- [10] Edward K Rodriguez, Anne Hoger, and Andrew D McCulloch. Stress-dependent finite growth in soft elastic tissues. *Journal of biomechanics*, 27(4):455–467, 1994.
- [11] Gerhard A Holzapfel and Ray W Ogden. Constitutive modelling of passive myocardium: a structurally based framework for material characterization. *Philosophical Transactions of the Royal Society A: Mathematical, Physical and Engineering Sciences*, 367(1902):3445–3475, 2009.
- [12] Kevin L Sack, Neil H Davies, Julius M Guccione, and Thomas Franz. Personalised computational cardiology: Patient-specific modelling in cardiac mechanics and biomaterial injection therapies for myocardial infarction. *Heart failure reviews*, 21(6):815–826, 2016.
- [13] H Gao, WG Li, L Cai, C Berry, and XY Luo. Parameter estimation in a holzapfel–ogden law for healthy myocardium. *Journal of engineering mathematics*, 95(1):231–248, 2015.
- [14] Debao Guan, Xin Zhuan, William Holmes, Xiaoyu Luo, and Hao Gao. Modelling of fibre dispersion and its effects on cardiac mechanics from diastole to systole. *Journal of Engineering Mathematics*, 128(1):1–24, 2021.
- [15] Debao Guan, Jiang Yao, Xiaoyu Luo, and Hao Gao. Effect of myofibre architecture on ventricular pump function by using a neonatal porcine heart model: from dt-mri to rule-based methods. *Royal Society Open Science*, 7(4):191655, 2020.
- [16] Kewei Li, Ray W Ogden, and Gerhard A Holzapfel. Computational method for excluding fibers under compression in modeling soft fibrous solids. *European Journal of Mechanics-A/Solids*, 57:178–193, 2016.
- [17] Kewei Li, Ray W Ogden, and Gerhard A Holzapfel. A discrete fibre dispersion method for excluding fibres under compression in the modelling of fibrous tissues. *Journal of The Royal Society Interface*, 15(138):20170766, 2018.
- [18] Gerhard A Holzapfel and Ray W Ogden. Comparison of two model frameworks for fiber dispersion in the elasticity of soft biological tissues. *European Journal of Mechanics-A/Solids*, 66:193–200, 2017.
- [19] Gerhard A Holzapfel, Justyna A Niestrawska, Ray W Ogden, Andreas J Reinisch, and Andreas J Schriefl. Modelling non-symmetric collagen fibre dispersion in arterial walls. *Journal of the Royal Society Interface*, 12(106):20150188, 2015.

- [20] T Christian Gasser, Ray W Ogden, and Gerhard A Holzapfel. Hyperelastic modelling of arterial layers with distributed collagen fibre orientations. *Journal of the royal society interface*, 3(6):15–35, 2006.
- [21] Thomas SE Eriksson, Anton J Prassl, Gernot Plank, and Gerhard A Holzapfel. Modeling the dispersion in electromechanically coupled myocardium. *International journal for numerical methods in biomedical engineering*, 29(11):1267–1284, 2013.
- [22] Justyna A Niestrawska, Christoph M Augustin, and Gernot Plank. Computational modeling of cardiac growth and remodeling in pressure overloaded hearts—linking microstructure to organ phenotype. *Acta Biomaterialia*, 106:34–53, 2020.
- [23] Wilco Kroon, Tammo Delhaas, Theo Arts, and Peter Bovendeerd. Computational modeling of volumetric soft tissue growth: application to the cardiac left ventricle. *Biomechanics and modeling in mechanobiology*, 8(4):301–309, 2009.
- [24] GA Ateshian and JD Humphrey. Continuum mixture models of biological growth and remodeling: past successes and future opportunities. *Annual review of biomedical engineering*, 14:97–111, 2012.
- [25] Ce Xi, Ghassan S Kassab, and Lik Chuan Lee. Microstructure-based finite element model of left ventricle passive inflation. *Acta biomaterialia*, 90:241–253, 2019.
- [26] Bridget Louise Leonard, Bruce Henry Smaill, and Ian John LeGrice. Structural remodeling and mechanical function in heart failure. *Microscopy and Microanalysis*, 18(1):50, 2012.
- [27] JB Caulfield and TK Borg. The collagen network of the heart. *Laboratory investigation; a journal of technical methods and pathology*, 40(3):364, 1979.
- [28] Thomas F Robinson, Leona Cohen-Gould, and Stephen M Factor. Skeletal framework of mammalian heart muscle. arrangement of inter-and pericellular connective tissue structures. *Laboratory investigation; a journal of technical methods and pathology*, 49(4):482–498, 1983.
- [29] Paul P Lunkenheimer, Klaus Redmann, Natalie Kling, Xiaoji Jiang, Kai Rothaus, Colin W Cryer, Frank Wübbeling, Peter Niederer, Philipp U Heitz, Siew Yen Ho, et al. Three-dimensional architecture of the left ventricular myocardium. *The Anatomical Record Part A: Discoveries in Molecular, Cellular, and Evolutionary Biology: An Official Publication of the American Association of Anatomists*, 288(6):565–578, 2006.

- [30] Patrick A Helm, Hsiang-Jer Tseng, Laurent Younes, Elliot R McVeigh, and Raimond L Winslow. Ex vivo 3d diffusion tensor imaging and quantification of cardiac laminar structure. *Magnetic Resonance in Medicine: An Official Journal of the International Society for Magnetic Resonance in Medicine*, 54(4):850–859, 2005.
- [31] Damien Rohmer, Arkadiusz Sitek, and Grant T Gullberg. Reconstruction and visualization of fiber and laminar structure in the normal human heart from ex vivo diffusion tensor magnetic resonance imaging (dtmri) data. *Investigative radiology*, 42(11):777–789, 2007.
- [32] Matthew W Curtis and Brenda Russell. Micromechanical regulation in cardiac myocytes and fibroblasts: implications for tissue remodeling. *Pflügers Archiv-European Journal of Physiology*, 462(1):105–117, 2011.
- [33] Mathieu Couade, Mathieu Pernot, Emmanuel Messas, Alain Bel, Maguette Ba, Albert Hagège, Mathias Fink, and Mickael Tanter. In vivo quantitative mapping of myocardial stiffening and transmural anisotropy during the cardiac cycle. *IEEE transactions on medical imaging*, 30(2):295–305, 2010.
- [34] Nick Merna, Claire Robertson, Anh La, and Steven C George. Optical imaging predicts mechanical properties during decellularization of cardiac tissue. *Tissue Engineering Part C: Methods*, 19(10):802–809, 2013.
- [35] Thomas K Borg, Lewis D Johnson, and Patsy H Lill. Specific attachment of collagen to cardiac myocytes: in vivo and in vitro. *Developmental biology*, 97(2):417–423, 1983.
- [36] Guido Macchiarelli, O Ohtani, Stefania A Nottola, T Stallone, A Camboni, IM Prado, and PM Motta. A micro-anatomical model of the distribution of myocardial endomysial collagen. *Histology and histopathology*, 2002.
- [37] Benedetto Intrigila, Igor Melatti, Alberto Tofani, and Guido Macchiarelli. Computational models of myocardial endomysial collagen arrangement. *Computer methods and programs in biomedicine*, 86(3):232–244, 2007.
- [38] Michael R Zile, Catalin F Baicu, and William H Gaasch. Diastolic heart failure—abnormalities in active relaxation and passive stiffness of the left ventricle. *New England Journal of Medicine*, 350(19):1953–1959, 2004.
- [39] K.D. Costa, J.W. Holmes, and A.D. McCulloch. Modelling cardiac mechanical properties in three dimensions. *Philosophical transactions of the Royal Society of London. Series A: Mathematical, physical and engineering sciences*, 359(1783):1233–1250, 2001.
- [40] Kenneth Mangion, Hao Gao, Dirk Husmeier, Xiaoyu Luo, and Colin Berry. Advances in computational modelling for personalised medicine after myocardial infarction. *Heart*, 104(7):550–557, 2018.

- [41] H. Schmid, M. P. Nash, A. A. Young, and P. J. Hunter. Myocardial material parameter estimation—a comparative study for simple shear. *Journal of biomechanical engineering*, 128(5):742, 2006.
- [42] Holger Schmid, YK Wang, Jesse Ashton, AE Ehret, SBS Krittian, MP Nash, and PJ Hunter. Myocardial material parameter estimation: a comparison of invariant based orthotropic constitutive equations. *Computer methods in biomechanics and biomedical engineering*, 12(3):283–295, 2009.
- [43] Nicolas Toussaint, Christian T Stoeck, Tobias Schaeffter, Sebastian Kozerke, Maxime Sermesant, and Philip G Batchelor. In vivo human cardiac fibre architecture estimation using shape-based diffusion tensor processing. *Medical image analysis*, 17(8):1243–1255, 2013.
- [44] Jean-Marc Peyrat, Maxime Sermesant, Xavier Pennec, Hervé Delingette, Chenyang Xu, Elliot R McVeigh, and Nicholas Ayache. A computational framework for the statistical analysis of cardiac diffusion tensors: application to a small database of canine hearts. *IEEE transactions on medical imaging*, 26(11):1500–1514, 2007.
- [45] Herve Lombaert, Jean-Marc Peyrat, Pierre Croisille, Stanislas Rapacchi, Laurent Fanton, Farida Cheriet, Patrick Clarysse, Isabelle Magnin, Hervé Delingette, and Nicholas Ayache. Human atlas of the cardiac fiber architecture: study on a healthy population. *IEEE transactions on medical imaging*, 31(7):1436–1447, 2012.
- [46] Hao Gao, David Carrick, Colin Berry, Boyce E Griffith, and Xiaoyu Luo. Dynamic finite-strain modelling of the human left ventricle in health and disease using an immersed boundary-finite element method. *IMA journal of applied mathematics*, 79(5):978–1010, 2014.
- [47] Eoin McEvoy, Gerhard A Holzapfel, and Patrick McGarry. Compressibility and anisotropy of the ventricular myocardium: Experimental analysis and microstructural modeling. *Journal of Biomechanical Engineering*, 140(8):081004, 2018.
- [48] LINDA L Demer and FC Yin. Passive biaxial mechanical properties of isolated canine myocardium. *The Journal of physiology*, 339(1):615–630, 1983.
- [49] Sotirios Kakaletsis, William D Meador, Mrudang Mathur, Gabriella P Sugerman, Tomasz Jazwiec, Marcin Malinowski, Emma Lejeune, Tomasz A Timek, and Manuel K Rausch. Right ventricular myocardial mechanics: Multi-modal deformation, microstructure, modeling, and comparison to the left ventricle. *Acta Biomaterialia*, 2020.
- [50] Shari E Langdon, Robert Chernecky, Christopher A Pereira, David Abdulla, and J Michael Lee. Biaxial mechanical/structural effects of equibiaxial strain during

- crosslinking of bovine pericardial xenograft materials. *Biomaterials*, 20(2):137–153, 1999.
- [51] Frank CP Yin, Robert K Strumpf, Paul H Chew, and Scott L Zeger. Quantification of the mechanical properties of noncontracting canine myocardium under simultaneous biaxial loading. *Journal of biomechanics*, 20(6):577–589, 1987.
- [52] Hwa Soon Choi and RP Vito. Two-dimensional stress-strain relationship for canine pericardium. *Journal of biomechanical engineering*, 112(2):153–159, 1990.
- [53] Michael R Hill, Marc A Simon, Daniela Valdez-Jasso, Will Zhang, Hunter C Champion, and Michael S Sacks. Structural and mechanical adaptations of right ventricle free wall myocardium to pressure overload. *Annals of biomedical engineering*, 42(12):2451–2465, 2014.
- [54] Daniela Vélez-Rendón, Erica R Pursell, Justin Shieh, and Daniela Valdez-Jasso. Relative contributions of matrix and myocytes to biaxial mechanics of the right ventricle in pulmonary arterial hypertension. *Journal of Biomechanical Engineering*, 141(9), 2019.
- [55] Socrates Dokos, Bruce H Smaill, Alistair A Young, and Ian J LeGrice. Shear properties of passive ventricular myocardium. *American Journal of Physiology-Heart and Circulatory Physiology*, 283(6):H2650–H2659, 2002.
- [56] John G Pinto and YC Fung. Mechanical properties of the heart muscle in the passive state. *Journal of biomechanics*, 6(6):597–616, 1973.
- [57] Gerhard Sommer, Daniel Ch Haspinger, Michaela Andrä, Michael Sacherer, Christian Viertler, Peter Regitnig, and Gerhard A Holzapfel. Quantification of shear deformations and corresponding stresses in the biaxially tested human myocardium. *Annals of biomedical engineering*, 43(10):2334–2348, 2015.
- [58] JD Humphrey, RK Strumpf, and FCP Yin. Determination of a constitutive relation for passive myocardium: II.—parameter estimation. *Journal of biomechanical engineering*, 112(3):340–346, 1990.
- [59] JD Humphrey and FCP Yin. On constitutive relations and finite deformations of passive cardiac tissue: I. a pseudostrain-energy function. 1987.
- [60] RCP Kerckhoffs, PHM Bovendeerd, JCS Kotte, FW Prinzen, K Smits, and T Arts. Homogeneity of cardiac contraction despite physiological asynchrony of depolarization: a model study. *Annals of biomedical engineering*, 31(5):536–547, 2003.

- [61] Julius M Guccione, Andrew D McCulloch, and LK Waldman. Passive material properties of intact ventricular myocardium determined from a cylindrical model. *Journal of biomechanical engineering*, 113(1):42–55, 1991.
- [62] PJ Hunter, MP Nash, and GB Sands. Computational electromechanics of the heart computational biology of the heart ed av panfilov and av holden, 1997.
- [63] Kewei Li, Ray W Ogden, and Gerhard A Holzapfel. An exponential constitutive model excluding fibres under compression: Application to extension–inflation of a residually stressed carotid artery. *Mathematics and mechanics of solids*, 23(8):1206–1224, 2018.
- [64] Alessio Gizzi, Anna Pandolfi, and Marcello Vasta. Statistical characterization of the anisotropic strain energy in soft materials with distributed fibers. *Mechanics of Materials*, 92:119–138, 2016.
- [65] Myrianthi Hadjicharalambous, Liya Asner, Radomir Chabiniok, Eva Sammut, James Wong, Devis Peressutti, Eric Kerfoot, Andrew King, Jack Lee, Reza Razavi, et al. Non-invasive model-based assessment of passive left-ventricular myocardial stiffness in healthy subjects and in patients with non-ischemic dilated cardiomyopathy. *Annals of biomedical engineering*, 45(3):605–618, 2017.
- [66] Xin Zhuan, Xiaoyu Luo, Hao Gao, and Ray W Ogden. Coupled agent-based and hyperelastic modelling of the left ventricle post-myocardial infarction. *International Journal for Numerical Methods in Biomedical Engineering*, 35(1):e3155, 2019.
- [67] JG Murphy. Transversely isotropic biological, soft tissue must be modelled using both anisotropic invariants. *European Journal of Mechanics-A/Solids*, 42:90–96, 2013.
- [68] Ian J LeGrice, BH Smaill, LZ Chai, SG Edgar, JB Gavin, and Peter J Hunter. Laminar structure of the heart: ventricular myocyte arrangement and connective tissue architecture in the dog. *American Journal of Physiology-Heart and Circulatory Physiology*, 269(2):H571–H582, 1995.
- [69] Theo Arts, Kevin D Costa, Jim W Covell, and Andrew D McCulloch. Relating myocardial laminar architecture to shear strain and muscle fiber orientation. *American Journal of Physiology-Heart and Circulatory Physiology*, 280(5):H2222–H2229, 2001.
- [70] Brian Baillargeon, Nuno Rebelo, David D Fox, Robert L Taylor, and Ellen Kuhl. The living heart project: a robust and integrative simulator for human heart function. *European Journal of Mechanics-A/Solids*, 48:38–47, 2014.
- [71] S Göktepe, SNS Acharya, J Wong, and E Kuhl. Computational modeling of passive myocardium. *International Journal for Numerical Methods in Biomedical Engineering*, 27(1):1–12, 2011.

- [72] HM Wang, XY Luo, H Gao, RW Ogden, BE Griffith, C Berry, and TJ Wang. A modified holzapfel-ogden law for a residually stressed finite strain model of the human left ventricle in diastole. *Biomechanics and modeling in mechanobiology*, 13(1):99–113, 2014.
- [73] Liya Asner, Myrianthi Hadjicharalambous, Radomir Chabiniok, Devis Peresutti, Eva Sammut, James Wong, Gerald Carr-White, Philip Chowienczyk, Jack Lee, Andrew King, et al. Estimation of passive and active properties in the human heart using 3d tagged mri. *Biomechanics and modeling in mechanobiology*, 15(5):1121–1139, 2016.
- [74] Andrey V Melnik, Xiaoyu Luo, and Ray W Ogden. A generalised structure tensor model for the mixed invariant i8. *International Journal of Non-Linear Mechanics*, 107:137–148, December 2018.
- [75] Amir Nikou, Shauna M Dorsey, Jeremy R McGarvey, Joseph H Gorman, Jason A Burdick, James J Pilla, Robert C Gorman, and Jonathan F Wenk. Computational Modeling of Healthy Myocardium in Diastole. *Annals of Biomedical Engineering*, pages 1–13, July 2015.
- [76] Arnab Palit, Sunil K Bhudia, Theodoros N Arvanitis, Glen A Turley, and Mark A Williams. In vivo estimation of passive biomechanical properties of human myocardium. *Medical & biological engineering & computing*, pages 1–17, 2018.
- [77] Michel Destrade, Giuseppe Saccomandi, and Ivonne Sgura. Methodical fitting for mathematical models of rubber-like materials. *Proceedings of the Royal Society A*, 473(2198):20160811, 2017.
- [78] Michael S Sacks. Biaxial mechanical evaluation of planar biological materials. *Journal of elasticity and the physical science of solids*, 61(1):199–246, 2000.
- [79] Martyn Nash. *Mechanics and material properties of the heart using an anatomically accurate mathematical model*. PhD thesis, ResearchSpace@ Auckland, 1998.
- [80] Reza Avazmohammadi, João S Soares, David S Li, Samarth S Raut, Robert C Gorman, and Michael S Sacks. A contemporary look at biomechanical models of myocardium. *Annual review of biomedical engineering*, 21:417–442, 2019.
- [81] A Horowitz, Y Lanir, FCP Yin, M Perl, I Sheinman, and RK Strumpf. Structural three-dimensional constitutive law for the passive myocardium. 1988.
- [82] JD Humphrey and FCP Yin. Biomechanical experiments on excised myocardium: theoretical considerations. *Journal of biomechanics*, 22(4):377–383, 1989.
- [83] YT Lanir. Constitutive equations for fibrous connective tissues. *Journal of biomechanics*, 16(1):1–12, 1983.

- [84] MS Sacks and CJ Chuong. A constitutive relation for passive right-ventricular free wall myocardium. *Journal of biomechanics*, 26(11):1341–1345, 1993.
- [85] JD Humphrey, RK Strumpf, and FCP Yin. Determination of a constitutive relation for passive myocardium: I. a new functional form. 1990.
- [86] Adarsh Krishnamurthy, Benjamin Coppola, Jared Tangney, Roy CP Kerckhoffs, Jeffrey H Omens, and Andrew D McCulloch. A microstructurally based multi-scale constitutive model of active myocardial mechanics. In *Structure-based mechanics of tissues and organs*, pages 439–460. Springer, 2016.
- [87] Michael S Sacks, Will Zhang, and Silvia Wognum. A novel fibre-ensemble level constitutive model for exogenous cross-linked collagenous tissues. *Interface focus*, 6(1):20150090, 2016.
- [88] Kewei Li and Gerhard A Holzapfel. Multiscale modeling of fiber recruitment and damage with a discrete fiber dispersion method. *Journal of the Mechanics and Physics of Solids*, 126:226–244, 2019.
- [89] JM Guccione and AD McCulloch. Mechanics of active contraction in cardiac muscle: part i—constitutive relations for fiber stress that describe deactivation. *Journal of biomechanical engineering*, 115(1):72–81, 1993.
- [90] J F Wenk, D Klepach, L C Lee, Z Zhang, L Ge, E E Tseng, A Martin, S Kozerke, J H Gorman, R C Gorman, and J M Guccione. First Evidence of Depressed Contractility in the Border Zone of a Human Myocardial Infarction. *The Annals of Thoracic Surgery*, 93(4):1188–1193, apr 2012.
- [91] Kevin L Sack, Eric Aliotta, Daniel B Ennis, Jenny S Choy, Ghassan S Kassab, Julius M Guccione, and Thomas Franz. Construction and validation of subject-specific biventricular finite-element models of healthy and failing swine hearts from high-resolution dt-mri. *Frontiers in physiology*, 9, 2018.
- [92] Martin Genet, Lik Chuan Lee, Rebecca Nguyen, Henrik Haraldsson, Gabriel Acevedo-Bolton, Zhihong Zhang, Liang Ge, Karen Ordovas, Sebastian Kozerke, and Julius M Guccione. Distribution of normal human left ventricular myofiber stress at end diastole and end systole: a target for in silico design of heart failure treatments. *Journal of applied physiology*, 117(2):142–152, 2014.
- [93] Yongheng Wang, Li Cai, Xiaoyu Luo, Wenjun Ying, and Hao Gao. simulation of action potential propagation based on the ghost structure method. *Scientific reports*, 9(1):1–18, 2019.

- [94] RH Clayton and AV Panfilov. A guide to modelling cardiac electrical activity in anatomically detailed ventricles. *Progress in biophysics and molecular biology*, 96(1-3):19–43, 2008.
- [95] Julius M Guccione, LK Waldman, and Andrew D McCulloch. Mechanics of active contraction in cardiac muscle: Part ii—cylindrical models of the systolic left ventricle. *Journal of biomechanical engineering*, 115(1):82–90, 1993.
- [96] D Ambrosi and S Pezzuto. Active stress vs. active strain in mechanobiology: constitutive issues. *Journal of Elasticity*, 107(2):199–212, 2012.
- [97] VI Kondraurov and LV Nikitin. Finite strains of viscoelastic muscle tissue. *Journal of Applied Mathematics and Mechanics*, 51(3):346–353, 1987.
- [98] Larry A Taber and Renato Perucchio. Modeling heart development. *Journal of elasticity and the physical science of solids*, 61(1-3):165–197, 2000.
- [99] C Cherubini, S Filippi, P Nardinocchi, and L Teresi. An electromechanical model of cardiac tissue: Constitutive issues and electrophysiological effects. *Progress in biophysics and molecular biology*, 97(2-3):562–573, 2008.
- [100] Davide Ambrosi, Gianni Arioli, Fabio Nobile, and Alfio Quarteroni. Electromechanical coupling in cardiac dynamics: the active strain approach. *SIAM Journal on Applied Mathematics*, 71(2):605–621, 2011.
- [101] Luca Barbarotta, Simone Rossi, Luca Dedè, and Alfio Quarteroni. A transmurally heterogeneous orthotropic activation model for ventricular contraction and its numerical validation. *International Journal for Numerical Methods in Biomedical Engineering*, 34(12):e3137, 2018.
- [102] Ricardo Ruiz-Baier, Alessio Gizzi, Simone Rossi, Christian Cherubini, Aymen Laadhari, Simonetta Filippi, and Alfio Quarteroni. Mathematical modelling of active contraction in isolated cardiomyocytes. *Mathematical medicine and biology: a journal of the IMA*, 31(3):259–283, 2014.
- [103] Alfio Quarteroni, Toni Lassila, Simone Rossi, and Ricardo Ruiz-Baier. Integrated heart—coupling multiscale and multiphysics models for the simulation of the cardiac function. *Computer Methods in Applied Mechanics and Engineering*, 314:345–407, 2017.
- [104] Giulia Giamtesio, Alessandro Musesti, and Davide Riccobelli. A comparison between active strain and active stress in transversely isotropic hyperelastic materials. *Journal of Elasticity*, pages 1–20, 2019.

- [105] Serdar Göktepe, Andreas Menzel, and Ellen Kuhl. The generalized hill model: A kinematic approach towards active muscle contraction. *Journal of the Mechanics and Physics of Solids*, 72:20–39, 2014.
- [106] Barış Cansız, Hüsnü Dal, and Michael Kaliske. Computational cardiology: A modified hill model to describe the electro-visco-elasticity of the myocardium. *Computer Methods in Applied Mechanics and Engineering*, 315:434–466, 2017.
- [107] Archibald Vivian Hill. The heat of shortening and the dynamic constants of muscle. *Proceedings of the Royal Society of London. Series B-Biological Sciences*, 126(843):136–195, 1938.
- [108] Simone Rossi, Toni Lassila, Ricardo Ruiz-Baier, Adélia Sequeira, and Alfio Quarteroni. Thermodynamically consistent orthotropic activation model capturing ventricular systolic wall thickening in cardiac electromechanics. *European Journal of Mechanics-A/Solids*, 48:129–142, 2014.
- [109] Anna Pandolfi, Alessio Gizzi, and Marcello Vasta. Coupled electro-mechanical models of fiber-distributed active tissues. *Journal of biomechanics*, 49(12):2436–2444, 2016.
- [110] Sjur Gjerald, Johan Hake, Simone Pezzuto, Joakim Sundnes, and Samuel T Wall. Patient-specific parameter estimation for a transversely isotropic active strain model of left ventricular mechanics. pages 93–104, 2014.
- [111] CS Cook and MJ McDonagh. Force responses to constant-velocity shortening of electrically stimulated human muscle-tendon complex. *Journal of Applied Physiology*, 81(1):384–392, 1996.
- [112] Kevin D Costa, Yasuo Takayama, Andrew D McCulloch, and James W Covell. Laminar fiber architecture and three-dimensional systolic mechanics in canine ventricular myocardium. *American Journal of Physiology-Heart and Circulatory Physiology*, 276(2):H595–H607, 1999.
- [113] PM Nielsen, IJ Le Grice, BH Smaill, and PJ Hunter. Mathematical model of geometry and fibrous structure of the heart. *American Journal of Physiology-Heart and Circulatory Physiology*, 260(4):H1365–H1378, 1991.
- [114] Mark Potse, Bruno Dubé, Jacques Richer, Alain Vinet, and Ramesh M Gulrajani. A comparison of monodomain and bidomain reaction-diffusion models for action potential propagation in the human heart. *IEEE Transactions on Biomedical Engineering*, 53(12):2425–2435, 2006.

- [115] Jonathan Wong and Ellen Kuhl. Generating fibre orientation maps in human heart models using poisson interpolation. *Computer methods in biomechanics and biomedical engineering*, 17(11):1217–1226, 2014.
- [116] Jason D Bayer, Robert C Blake, Gernot Plank, and Natalia A Trayanova. A novel rule-based algorithm for assigning myocardial fiber orientation to computational heart models. *Annals of biomedical engineering*, 40(10):2243–2254, 2012.
- [117] Arnab Palit, Sunil K Bhudia, Theodoros N Arvanitis, Glen A Turley, and Mark A Williams. Computational modelling of left-ventricular diastolic mechanics: Effect of fibre orientation and right-ventricle topology. *Journal of biomechanics*, 48(4):604–612, 2015.
- [118] Marieke Pluijmert, Tammo Delhaas, Adrián Flores Parra, Wilco Kroon, Frits W Prinzen, and Peter H M Bovendeerd. Determinants of biventricular cardiac function: a mathematical model study on geometry and myofiber orientation. *Biomechanics and Modeling in Mechanobiology*, 16(2):721–729, August 2016.
- [119] Debora Gil, Ruth Aris, Agnès Borrás, Esmitt Ramírez, R Sebastian, and Mariano Vazquez. Influence of fiber connectivity in simulations of cardiac biomechanics. *International journal of computer assisted radiology and surgery*, 14(1):63–72, 2019.
- [120] Patrick A Helm, Laurent Younes, Mirza F Beg, Daniel B Ennis, Christophe Leclercq, Owen P Faris, Elliot McVeigh, David Kass, Michael I Miller, and Raimond L Winslow. Evidence of structural remodeling in the dyssynchronous failing heart. *Circulation Research*, 98(1):125–132, 2006.
- [121] Daniel D Streeter Jr, Henry M Spotnitz, Dali P Patel, JOHN ROSS Jr, and Edmund H Sonnenblick. Fiber orientation in the canine left ventricle during diastole and systole. *Circulation research*, 24(3):339–347, 1969.
- [122] Rocío Rodríguez-Cantano, Joakim Sundnes, and Marie E Rognes. Uncertainty in cardiac myofiber orientation and stiffnesses dominate the variability of left ventricle deformation response. *International Journal for Numerical Methods in Biomedical Engineering*, 6(2):e3178–20, January 2019.
- [123] Yoram Lanir. Multi-scale structural modeling of soft tissues mechanics and mechanobiology. *Journal of Elasticity*, 129(1-2):7–48, 2017.
- [124] Gerhard A Holzapfel, Ray W Ogden, and Selda Sherifova. On fibre dispersion modelling of soft biological tissues: a review. *Proceedings of the Royal Society A*, 475(2224):20180736, 2019.

- [125] Gerhard A Holzapfel and Ray W Ogden. On the tension–compression switch in soft fibrous solids. *European Journal of Mechanics-A/Solids*, 49:561–569, 2015.
- [126] Margot R Roach and Alan C Burton. The reason for the shape of the distensibility curves of arteries. *Canadian journal of biochemistry and physiology*, 35(8):681–690, 1957.
- [127] Gerhard A Holzapfel, Thomas C Gasser, and Ray W Ogden. Comparison of a multi-layer structural model for arterial walls with a fung-type model, and issues of material stability. *Journal of biomechanical engineering*, 126(2):264–275, 2004.
- [128] Michael R Hill, Xinjie Duan, Gregory A Gibson, Simon Watkins, and Anne M Robertson. A theoretical and non-destructive experimental approach for direct inclusion of measured collagen orientation and recruitment into mechanical models of the artery wall. *Journal of biomechanics*, 45(5):762–771, 2012.
- [129] Michele Marino and Giuseppe Vairo. Stress and strain localization in stretched collagenous tissues via a multiscale modelling approach. *Computer methods in biomechanics and biomedical engineering*, 17(1):11–30, 2014.
- [130] Gerard A Ateshian, Vikram Rajan, Nadeen O Chahine, Clare E Canal, and Clark T Hung. Modeling the matrix of articular cartilage using a continuous fiber angular distribution predicts many observed phenomena. *Journal of biomechanical engineering*, 131(6), 2009.
- [131] Salvatore Federico and T Christian Gasser. Nonlinear elasticity of biological tissues with statistical fibre orientation. *Journal of the Royal Society Interface*, 7(47):955–966, 2010.
- [132] Andrey V Melnik, Hudson Borja Da Rocha, and Alain Goriely. On the modeling of fiber dispersion in fiber-reinforced elastic materials. *International Journal of Non-Linear Mechanics*, 75:92–106, 2015.
- [133] Luigi Vergori, Michel Destrade, Patrick McGarry, and Ray W Ogden. On anisotropic elasticity and questions concerning its finite element implementation. *Computational Mechanics*, 52(5):1185–1197, 2013.
- [134] Gerhard A Holzapfel and Ray W Ogden. On fiber dispersion models: exclusion of compressed fibers and spurious model comparisons. *Journal of elasticity*, 129(1-2):49–68, 2017.
- [135] Kewei Li, Ray W Ogden, and Gerhard A Holzapfel. Modeling fibrous biological tissues with a general invariant that excludes compressed fibers. *Journal of the Mechanics and Physics of Solids*, 110:38–53, 2018.

- [136] V Alastrué, MA Martinez, M Doblaré, and Andreas Menzel. Anisotropic micro-sphere-based finite elasticity applied to blood vessel modelling. *Journal of the Mechanics and Physics of Solids*, 57(1):178–203, 2009.
- [137] Writing Group Members, Thomas Thom, Nancy Haase, Wayne Rosamond, Virginia J Howard, John Rumsfeld, Teri Manolio, Zhi-Jie Zheng, Katherine Flegal, Christopher O’Donnell, et al. Heart disease and stroke statistics—2006 update: a report from the american heart association statistics committee and stroke statistics subcommittee. *Circulation*, 113(6):e85–e151, 2006.
- [138] JD Humphrey and KR Rajagopal. A constrained mixture model for growth and remodeling of soft tissues. *Mathematical models and methods in applied sciences*, 12(03):407–430, 2002.
- [139] WILLIAM Grossman, DONALD Jones, LP McLaurin, et al. Wall stress and patterns of hypertrophy in the human left ventricle. *The Journal of clinical investigation*, 56(1):56–64, 1975.
- [140] Roy CP Kerckhoffs, Jeffrey H Omens, and Andrew D McCulloch. A single strain-based growth law predicts concentric and eccentric cardiac growth during pressure and volume overload. *Mechanics research communications*, 42:40–50, 2012.
- [141] Serdar Göktepe, Oscar John Abilez, Kevin Kit Parker, and Ellen Kuhl. A multiscale model for eccentric and concentric cardiac growth through sarcomerogenesis. *Journal of theoretical biology*, 265(3):433–442, 2010.
- [142] Lik Chuan Lee, Martin Genet, Gabriel Acevedo-Bolton, Karen Ordovas, Julius M Guccione, and Ellen Kuhl. A computational model that predicts reverse growth in response to mechanical unloading. *Biomechanics and modeling in mechanobiology*, 14(2):217–229, 2015.
- [143] Lik Chuan Lee, Joakim Sundnes, Martin Genet, Jonathan F Wenk, and Samuel T Wall. An integrated electromechanical-growth heart model for simulating cardiac therapies. *Biomechanics and modeling in mechanobiology*, 15(4):791–803, 2016.
- [144] Martin Genet, Lik Chuan Lee, Brian Baillargeon, Julius M Guccione, and Ellen Kuhl. Modeling pathologies of diastolic and systolic heart failure. *Annals of biomedical engineering*, 44(1):112–127, 2016.
- [145] Colleen M Witzenburg and Jeffrey W Holmes. Predicting the time course of ventricular dilation and thickening using a rapid compartmental model. *Journal of cardiovascular translational research*, 11(2):109–122, 2018.

- [146] Mathias Peirlinck, F Sahli Costabal, KL Sack, JS Choy, GS Kassab, JM Guccione, M De Beule, Patrick Segers, and E Kuhl. Using machine learning to characterize heart failure across the scales. *Biomechanics and modeling in mechanobiology*, 18(6):1987–2001, 2019.
- [147] CJ Cyron, RC Aydin, and JD Humphrey. A homogenized constrained mixture (and mechanical analog) model for growth and remodeling of soft tissue. *Biomechanics and modeling in mechanobiology*, 15(6):1389–1403, 2016.
- [148] William Wan, Laura Hansen, and Rudolph L Gleason. A 3-d constrained mixture model for mechanically mediated vascular growth and remodeling. *Biomechanics and modeling in mechanobiology*, 9(4):403–419, 2010.
- [149] Fabian Albert Braeu, Roland C Aydin, and Christian J Cyron. Anisotropic stiffness and tensional homeostasis induce a natural anisotropy of volumetric growth and remodeling in soft biological tissues. *Biomechanics and modeling in mechanobiology*, 18(2):327–345, 2019.
- [150] Oras A Alabas, Tomas Jernberg, Mar Pujades-Rodriguez, Mark J Rutherford, Robert M West, Marlous Hall, Adam Timmis, Bertil Lindahl, Keith AA Fox, Harry Hemingway, et al. Statistics on mortality following acute myocardial infarction in 842 897 europeans. *Cardiovascular research*, 116(1):149–157, 2020.
- [151] Martin G St John Sutton and Norman Sharpe. Left ventricular remodeling after myocardial infarction: pathophysiology and therapy. *Circulation*, 101(25):2981–2988, 2000.
- [152] Gregory M Fomovsky, Andrew D Rouillard, and Jeffrey W Holmes. Regional mechanics determine collagen fiber structure in healing myocardial infarcts. *Journal of molecular and cellular cardiology*, 52(5):1083–1090, 2012.
- [153] Peter Whittaker, Derek R Boughner, and RA Kloner. Analysis of healing after myocardial infarction using polarized light microscopy. *The American journal of pathology*, 134(4):879, 1989.
- [154] RICHARD J McCormick, TIMOTHY I Musch, BRYAN C Bergman, and D PAUL Thomas. Regional differences in lv collagen accumulation and mature cross-linking after myocardial infarction in rats. *American Journal of Physiology-Heart and Circulatory Physiology*, 266(1):H354–H359, 1994.
- [155] Samuel A Wickline, Edward D Verdonk, Andrew K Wong, Richard K Shepard, and James G Miller. Structural remodeling of human myocardial tissue after infarction. quantification with ultrasonic backscatter. *Circulation*, 85(1):259–268, 1992.

- [156] Junjie Chen, Sheng-Kwei Song, Wei Liu, Mark McLean, J Stacy Allen, Jie Tan, Samuel A Wickline, and Xin Yu. Remodeling of cardiac fiber structure after infarction in rats quantified with diffusion tensor mri. *American Journal of Physiology-Heart and Circulatory Physiology*, 285(3):H946–H954, 2003.
- [157] Wenguang Li. Biomechanics of infarcted left ventricle—a review of experiments. *Journal of the mechanical behavior of biomedical materials*, 103:103591, 2020.
- [158] Bodh I Jugdutt and Roger WM Amy. Healing after myocardial infarction in the dog: changes in infarct hydroxyproline and topography. *Journal of the American College of Cardiology*, 7(1):91–102, 1986.
- [159] RAYMOND G McKay, MARC A Pfeffer, RICHARD C Pasternak, JOHN E Markis, PATRICIA C Come, SHOICHIRO Nakao, JAMES D Alderman, JAMES J Ferguson, ROBERT D Safian, and WILLIAM Grossman. Left ventricular remodeling after myocardial infarction: a corollary to infarct expansion. *Circulation*, 74(4):693–702, 1986.
- [160] Sean D Pokorney, José F Rodriguez, José T Ortiz, Daniel C Lee, Robert O Bonow, and Edwin Wu. Infarct healing is a dynamic process following acute myocardial infarction. *Journal of Cardiovascular Magnetic Resonance*, 14(1):1–7, 2012.
- [161] Lisa M Mielniczuk, Gervasio A Lamas, Greg C Flaker, Gary Mitchell, Sidney C Smith, Bernard J Gersh, Scott D Solomon, Lemuel A Moyé, Jean L Rouleau, John D Rutherford, et al. Left ventricular end-diastolic pressure and risk of subsequent heart failure in patients following an acute myocardial infarction. *Congestive Heart Failure*, 13(4):209–214, 2007.
- [162] Jonathan F Wenk, Parastou Eslami, Zhihong Zhang, Chun Xu, Ellen Kuhl, Joseph H Gorman III, J Daniel Robb, Mark B Ratcliffe, Robert C Gorman, and Julius M Guccione. A novel method for quantifying the in-vivo mechanical effect of material injected into a myocardial infarction. *The Annals of thoracic surgery*, 92(3):935–941, 2011.
- [163] Gregory M Fomovsky, Jesse R Macadangdang, Gorav Ailawadi, and Jeffrey W Holmes. Model-based design of mechanical therapies for myocardial infarction. *Journal of cardiovascular translational research*, 4(1):82–91, 2011.
- [164] Hao Gao, Kenneth Mangion, David Carrick, Dirk Husmeier, Xiaoyu Luo, and Colin Berry. Estimating prognosis in patients with acute myocardial infarction using personalized computational heart models. *Scientific reports*, 7(1):1–14, 2017.
- [165] Andrew D Rouillard and Jeffrey W Holmes. Coupled agent-based and finite-element models for predicting scar structure following myocardial infarction. *Progress in biophysics and molecular biology*, 115(2-3):235–243, 2014.

- [166] Patrick Ten Eyck and Joseph E Cavanaugh. Model selection criteria based on cross-validatory concordance statistics. *Computational Statistics*, 33(2):595–621, 2018.
- [167] Reza Avazmohammadi, Michael Hill, Marc Simon, and Michael Sacks. Transmural remodeling of right ventricular myocardium in response to pulmonary arterial hypertension. *APL Bioengineering*, 1(1):016105, 2017.
- [168] RW Ogden, Giuseppe Saccomandi, and Ivonne Sgura. Fitting hyperelastic models to experimental data. *Computational Mechanics*, 34(6):484–502, 2004.
- [169] Kenneth P Burnham and David R Anderson. *Model selection and multimodel inference: a practical information-theoretic approach*. Springer Science & Business Media, 2003.
- [170] Kristen L Billiar and Michael S Sacks. Biaxial mechanical properties of the native and glutaraldehyde-treated aortic valve cusp: part ii—a structural constitutive model. *Journal of biomechanical engineering*, 122(4):327–335, 2000.
- [171] Alan D Freed, Daniel R Einstein, and Michael S Sacks. Hypoelastic soft tissues. *Acta mechanica*, 213(1-2):205–222, 2010.
- [172] Will Zhang, Rana Zakerzadeh, Wenbo Zhang, and Michael S Sacks. A material modeling approach for the effective response of planar soft tissues for efficient computational simulations. *Journal of the Mechanical Behavior of Biomedical Materials*, 89:168–198, January 2019.
- [173] Thomas J Snowden, Piet H van der Graaf, and Marcus J Tindall. Methods of model reduction for large-scale biological systems: a survey of current methods and trends. *Bulletin of mathematical biology*, 79(7):1449–1486, 2017.
- [174] Y Lanir. A structural theory for the homogeneous biaxial stress-strain relationships in flat collagenous tissues. *Journal of biomechanics*, 12(6):423–436, 1979.
- [175] Martyn P Nash and Peter J Hunter. Computational mechanics of the heart. *Journal of elasticity and the physical science of solids*, 61(1-3):113–141, 2000.
- [176] John C Criscione, Andrew D McCulloch, and William C Hunter. Constitutive framework optimized for myocardium and other high-strain, laminar materials with one fiber family. *Journal of the Mechanics and Physics of Solids*, 50(8):1681–1702, 2002.
- [177] Holger Schmid, P O’Callaghan, MP Nash, W Lin, IJ LeGrice, BH Smaill, AA Young, and PJ Hunter. Myocardial material parameter estimation. *Biomechanics and modeling in mechanobiology*, 7(3):161–173, 2008.

- [178] Brian Baillargeon, Ivan Costa, Joseph R Leach, Lik Chuan Lee, Martin Genet, Arnaud Toutain, Jonathan F Wenk, Manuel K Rausch, Nuno Rebelo, Gabriel Acevedo-Bolton, et al. Human cardiac function simulator for the optimal design of a novel annuloplasty ring with a sub-valvular element for correction of ischemic mitral regurgitation. *Cardiovascular engineering and technology*, 6(2):105–116, 2015.
- [179] Jeroen Mollink, Michiel Kleinnijenhuis, Anne-Marie van Cappellen van Walsum, Stamatios N Sotiropoulos, Michiel Cottaar, Christopher Mirfin, Mattias P Heinrich, Mark Jenkinson, Menuka Pallegage-Gamarallage, Olaf Ansorge, et al. Evaluating fibre orientation dispersion in white matter: Comparison of diffusion mri, histology and polarized light imaging. *Neuroimage*, 157:561–574, 2017.
- [180] Maira Tariq, Torben Schneider, Daniel C Alexander, Claudia A Gandini Wheeler-Kingshott, and Hui Zhang. Bingham–noddi: mapping anisotropic orientation dispersion of neurites using diffusion mri. *Neuroimage*, 133:207–223, 2016.
- [181] Debao Guan, Faizan Ahmad, Peter Theobald, Shwe Soe, Xiaoyu Luo, and Hao Gao. On the aic-based model reduction for the general holzapfel–ogden myocardial constitutive law. *Biomechanics and modeling in mechanobiology*, pages 1–20, 2019.
- [182] Stanley Durrleman, Marcel Prastawa, Nicolas Charon, Julie R Korenberg, Sarang Joshi, Guido Gerig, and Alain Trouvé. Morphometry of anatomical shape complexes with dense deformations and sparse parameters. *NeuroImage*, 101:35–49, 2014.
- [183] Alexandre Bône, Maxime Louis, Benoît Martin, and Stanley Durrleman. Deformetrica 4: an open-source software for statistical shape analysis. In *International Workshop on Shape in Medical Imaging*, pages 3–13. Springer, 2018.
- [184] Nicolas Charon and Alain Trouvé. The varifold representation of nonoriented shapes for diffeomorphic registration. *SIAM Journal on Imaging Sciences*, 6(4):2547–2580, 2013.
- [185] Manuel D Cerqueira, Neil J Weissman, Vasken Dilsizian, Alice K Jacobs, Sanjiv Kaul, Warren K Laskey, Dudley J Pennell, John A Rumberger, Thomas Ryan, et al. Standardized myocardial segmentation and nomenclature for tomographic imaging of the heart: a statement for healthcare professionals from the cardiac imaging committee of the council on clinical cardiology of the american heart association. *Circulation*, 105(4):539–542, 2002.
- [186] D HAWKINS and M BEY. A comprehensive approach for studying muscle-tendon mechanics. *Journal of biomechanical engineering*, 116(1):51–55, 1994.
- [187] Andreas J Schriefl, Georg Zeindlinger, David M Pierce, Peter Regitnig, and Gerhard A Holzapfel. Determination of the layer-specific distributed collagen fibre orientations in

- human thoracic and abdominal aortas and common iliac arteries. *Journal of the Royal Society Interface*, 9(71):1275–1286, 2011.
- [188] Abaqus Documentation and User Manual. Version 6.14-2. *Dassault systemes*, 2014.
- [189] Otwin Linderkamp, Klaus Betke, Monika Güntner, Giok H Jap, Klaus P Riegel, and Kurt Walser. Blood volume in newborn piglets: effects of time of natural cord rupture, intra-uterine growth retardation, asphyxia, and prostaglandin-induced prematurity. *Pediatric research*, 15(1):53, 1981.
- [190] John P Hannon, CAROL A Bossone, and WILLIAM G Rodkey. Splenic red cell sequestration and blood volume measurements in conscious pigs. *American Journal of Physiology-Regulatory, Integrative and Comparative Physiology*, 248(3):R293–R301, 1985.
- [191] MV Zilberman, PR Khoury, and RT Kimball. Two-dimensional echocardiographic valve measurements in healthy children: gender-specific differences. *Pediatric cardiology*, 26(4):356–360, 2005.
- [192] L DeRoth and A Bisaillon. Determination of body surface area in neonatal swine. *Laboratory animal science*, 29(2):249–250, 1979.
- [193] MM Swindle, A Makin, AJ Herron, FJ Clubb Jr, and KS Frazier. Swine as models in biomedical research and toxicology testing. *Veterinary pathology*, 49(2):344–356, 2012.
- [194] Drude Fugelseth, Saulius Satas, Martin Runde, Per Hågå, and Marianne Thoresen. Cardiac function and morphology studied by two-dimensional doppler echocardiography in unsedated newborn pigs. *Experimental physiology*, 84(1):69–78, 1999.
- [195] Mariann Gyöngyösi, Noemi Pavo, Dominika Lukovic, Katrin Zlabinger, Andreas Spannauer, Denise Traxler, Georg Goliash, Ljubica Mandic, Jutta Bergler-Klein, Alfred Gugerell, et al. Porcine model of progressive cardiac hypertrophy and fibrosis with secondary postcapillary pulmonary hypertension. *Journal of translational medicine*, 15(1):202, 2017.
- [196] Xufeng Wei, Tieluo Li, Shuying Li, Ho Sung Son, Pablo Sanchez, Shuqiong Niu, A Claire Watkins, Christopher DeFilippi, Robert Jarvik, Zhongjun J Wu, et al. Pre-clinical evaluation of the infant jarvik 2000 heart in a neonate piglet model. *The Journal of Heart and Lung Transplantation*, 32(1):112–119, 2013.
- [197] Lily Q Lin, Sanaz Hatami, James Yashu Coe, Timothy M Colen, Consolato Sergi, Richard Thompson, Elena S Di Martino, Walter Herzog, Ziad Abu Sara, Darren H Freed, et al. A novel right ventricular volume and pressure loaded piglet heart model for the study of tricuspid valve function. *JoVE (Journal of Visualized Experiments)*, (161):e61251, 2020.

- [198] J Andrade, LD Cortez, O Campos, AL Arruda, J Pinheiro, L Vulcanis, TS Shiratsuchi, R Kalil-Filho, and GG Cerri. Left ventricular twist: comparison between two- and three-dimensional speckle-tracking echocardiography in healthy volunteers. *European Journal of Echocardiography*, 12(1):76–79, 2010.
- [199] Gerhard A Holzapfel and Ray W Ogden. On the tension-compression switch in soft fibrous solids. *European Journal of Mechanics / A Solids*, 49(C):561–569, jan 2015.
- [200] Geoffrey L Kung, Marmar Vaseghi, Jin K Gahm, Jane Shevtsov, Alan Garfinkel, Kalyanam Shivkumar, and Daniel B Ennis. Microstructural infarct border zone remodeling in the post-infarct swine heart measured by diffusion tensor mri. *Frontiers in physiology*, 9:826, 2018.
- [201] Takafumi Kato, Nobuyuki Ohte, Kazuaki Wakami, Toshihiko Goto, Hidekatsu Fukuta, Hitomi Narita, and Genjiro Kimura. Myocardial fiber shortening in the circumferential direction produces left ventricular wall thickening during contraction. *The Tohoku journal of experimental medicine*, 222(3):175–181, 2010.
- [202] Chiara Giordano and Svein Kleiven. Connecting fractional anisotropy from medical images with mechanical anisotropy of a hyperviscoelastic fibre-reinforced constitutive model for brain tissue. *Journal of the Royal Society Interface*, 11(91):20130914, 2014.
- [203] Ruben Doste, David Soto-Iglesias, Gabriel Bernardino, Alejandro Alcaine, Rafael Sebastian, Sophie Giffard-Roisin, Maxime Sermesant, Antonio Berruezo, Damian Sanchez-Quintana, and Oscar Camara. A rule-based method to model myocardial fiber orientation in cardiac biventricular geometries with outflow tracts. *arXiv preprint arXiv:1809.08297*, 2018.
- [204] Kevin L Sack, Yaghoub Dabiri, Thomas Franz, Scott D Solomon, Daniel Burkhoff, and Julius M Guccione. Investigating the role of interventricular interdependence in development of right heart dysfunction during lvad support: A patient-specific methods-based approach. *Frontiers in physiology*, 9, 2018.
- [205] Martin R Pfaller, Julia M Hörmann, Martina Weigl, Andreas Nagler, Radomir Chabiniok, Cristóbal Bertoglio, and Wolfgang A Wall. The importance of the pericardium for cardiac biomechanics: From physiology to computational modeling. *Biomechanics and modeling in mechanobiology*, 18(2):503–529, 2019.
- [206] Mette S Olufsen, Charles S Peskin, Won Yong Kim, Erik M Pedersen, Ali Nadim, and Jesper Larsen. Numerical simulation and experimental validation of blood flow in arteries with structured-tree outflow conditions. *Annals of biomedical engineering*, 28(11):1281–1299, 2000.

- [207] Debao Guan, Fuyou Liang, and Pierre A Gremaud. Comparison of the windkessel model and structured-tree model applied to prescribe outflow boundary conditions for a one-dimensional arterial tree model. *Journal of biomechanics*, 49(9):1583–1592, 2016.
- [208] W W Chen, H Gao, X Y Luo, and N A Hill. Study of cardiovascular function using a coupled left ventricle and systemic circulation model. *Journal of Biomechanics*, 49(12):2445–2454, aug 2016.
- [209] Stephen M Smith, Mark Jenkinson, Mark W Woolrich, Christian F Beckmann, Timothy EJ Behrens, Heidi Johansen-Berg, Peter R Bannister, Marilena De Luca, Ivana Drobnjak, David E Flitney, et al. Advances in functional and structural mr image analysis and implementation as fsl. *Neuroimage*, 23:S208–S219, 2004.
- [210] Alessio Gizzi, Anna Pandolfi, and Marcello Vasta. A generalized statistical approach for modeling fiber-reinforced materials. *Journal of Engineering Mathematics*, 109(1):211–226, 2018.
- [211] Catherine M Otto, Alan S Pearlman, Keith A Comess, Robyn P Reamer, Carolyn L Janko, and Lee L Huntsman. Determination of the stenotic aortic valve area in adults using doppler echocardiography. *Journal of the American College of Cardiology*, 7(3):509–517, 1986.
- [212] Luis A Cuniberti, Pablo G Stutzbach, Eduardo Guevara, Gustavo G Yannarelli, Rubén P Laguens, and Roberto R Favaloro. Development of mild aortic valve stenosis in a rabbit model of hypertension. *Journal of the American College of Cardiology*, 47(11):2303–2309, 2006.
- [213] Asbjørn Støylen, Håvard Dalen, and Harald Edvard Molmen. Left ventricular longitudinal shortening: relation to stroke volume and ejection fraction in ageing, blood pressure, body size and gender in the hunt3 study. *Open heart*, 7(2):e001243, 2020.
- [214] Christophe Heymes, Marc Vanderheyden, Jean GF Bronzwaer, Ajay M Shah, and Walter J Paulus. Endomyocardial nitric oxide synthase and left ventricular preload reserve in dilated cardiomyopathy. *Circulation*, 99(23):3009–3016, 1999.
- [215] Junjie Chen, Wei Liu, Huiying Zhang, Liz Lacy, Xiaoxia Yang, Sheng-Kwei Song, Samuel A Wickline, and Xin Yu. Regional ventricular wall thickening reflects changes in cardiac fiber and sheet structure during contraction: quantification with diffusion tensor mri. *American Journal of Physiology-Heart and Circulatory Physiology*, 289(5):H1898–H1907, 2005.
- [216] Mark Alber, Adrian Buganza Tepole, William R Cannon, Suvranu De, Salvador Dura-Bernal, Krishna Garikipati, George Karniadakis, William W Lytton, Paris

- Perdikaris, Linda Petzold, et al. Integrating machine learning and multiscale modeling—perspectives, challenges, and opportunities in the biological, biomedical, and behavioral sciences. *NPJ digital medicine*, 2(1):1–11, 2019.
- [217] Nisha Arenja, Johannes H Riffel, Thomas Fritz, Florian André, Fabian aus dem Siepen, Matthias Mueller-Hennessen, Evangelos Giannitsis, Hugo A Katus, Matthias G Friedrich, and Sebastian J Buss. Diagnostic and prognostic value of long-axis strain and myocardial contraction fraction using standard cardiovascular mr imaging in patients with nonischemic dilated cardiomyopathies. *Radiology*, 283(3):681–691, 2017.
- [218] Jonathan Chan, Lizelle Hanekom, Chiew Wong, Rodel Leano, Goo-Yeong Cho, and Thomas H Marwick. Differentiation of subendocardial and transmural infarction using two-dimensional strain rate imaging to assess short-axis and long-axis myocardial function. *Journal of the American College of Cardiology*, 48(10):2026–2033, 2006.
- [219] Fuyou Liang, Debao Guan, and Jordi Alastruey. Determinant factors for arterial hemodynamics in hypertension: Theoretical insights from a computational model-based study. *Journal of biomechanical engineering*, 140(3):031006, 2018.
- [220] Mikel Landajuela, Christian Vergara, Antonello Gerbi, Luca Dedè, Luca Formaggia, and Alfio Quarteroni. Numerical approximation of the electromechanical coupling in the left ventricle with inclusion of the purkinje network. *International journal for numerical methods in biomedical engineering*, 34(7):e2984, 2018.
- [221] Radomir Chabiniok, Vicky Y Wang, Myrianthi Hadjicharalambous, Liya Asner, Jack Lee, Maxime Sermesant, Ellen Kuhl, Alistair A Young, Philippe Moireau, Martyn P Nash, et al. Multiphysics and multiscale modelling, data–model fusion and integration of organ physiology in the clinic: ventricular cardiac mechanics. *Interface focus*, 6(2):20150083, 2016.
- [222] Umberto Noè, Alan Lazarus, Hao Gao, Vinny Davies, Benn Macdonald, Kenneth Mangion, Colin Berry, Xiaoyu Luo, and Dirk Husmeier. Gaussian process emulation to accelerate parameter estimation in a mechanical model of the left ventricle: a critical step towards clinical end-user relevance. *Journal of the Royal Society Interface*, 16(156):20190114, 2019.
- [223] Martin Genet, MK Rausch, Lik Chuan Lee, S Choy, X Zhao, Ghassan S Kassab, Sebastian Kozerke, Julius M Guccione, and Ellen Kuhl. Heterogeneous growth-induced prestrain in the heart. *Journal of biomechanics*, 48(10):2080–2089, 2015.
- [224] Yangkun Du, Chaofeng Lü, Michel Destrade, and Weiqiu Chen. Influence of initial residual stress on growth and pattern creation for a layered aorta. *Scientific Reports*, 9(1):1–9, 2019.

- [225] Larry A Taber and Jay D Humphrey. Stress-modulated growth, residual stress, and vascular heterogeneity. *J. Biomech. Eng.*, 123(6):528–535, 2001.
- [226] Heerajnarain Bulluck, Yun Yun Go, Gabriele Crimi, Andrew J Ludman, Stefania Rosmini, Amna Abdel-Gadir, Anish N Bhuva, Thomas A Treibel, Marianna Fontana, Silvia Pica, et al. Defining left ventricular remodeling following acute st-segment elevation myocardial infarction using cardiovascular magnetic resonance. *Journal of Cardiovascular Magnetic Resonance*, 19(1):1–13, 2017.
- [227] Farhad Pashakhanloo, Daniel A Herzka, Susumu Mori, Muz Zviman, Henry Halperin, Neville Gai, David A Bluemke, Natalia A Trayanova, and Elliot R McVeigh. Submillimeter diffusion tensor imaging and late gadolinium enhancement cardiovascular magnetic resonance of chronic myocardial infarction. *Journal of Cardiovascular Magnetic Resonance*, 19(1):1–14, 2017.
- [228] Takumi Washio, Jun-ichi Okada, Seiryu Sugiura, and Toshiaki Hisada. Approximation for cooperative interactions of a spatially-detailed cardiac sarcomere model. *Cellular and molecular bioengineering*, 5(1):113–126, 2012.
- [229] Francesco Regazzoni, Luca Dedè, and Alfio Quarteroni. Biophysically detailed mathematical models of multiscale cardiac active mechanics. *PLoS computational biology*, 16(10):e1008294, 2020.
- [230] Francesco Regazzoni, Luca Dedè, and Alfio Quarteroni. Active contraction of cardiac cells: a reduced model for sarcomere dynamics with cooperative interactions. *Biomechanics and modeling in mechanobiology*, 17(6):1663–1686, 2018.